EXPERIMENTAL STUDY OF LOW REYNOLDS NUMBER MULTIROTOR AERODYNAMIC INTERACTIONS

A Dissertation
Presented to
The Academic Faculty

By

Dhwanil P. Shukla

In Partial Fulfillment
of the Requirements for the Degree
Doctor of Philosophy in the
School of Aerospace Engineering

Georgia Institute of Technology

August 2019

EXPERIMENTAL STUDY OF LOW REYNOLDS NUMBER MULTIROTOR AERODYNAMIC INTERACTIONS

Approved by:

Dr. Narayanan Komerath, Advisor
School of Aerospace Engineering
Georgia Institute of Technology

Dr. J V R Prasad
School of Aerospace Engineeringg
Georgia Institute of Technology

Dr. Lakshmi Sankar
School of Aerospace Engineering
Georgia Institute of Technology

Dr. John McIntyre
Scheller College of Business
Georgia Institute of Technology

Dr. Thomas Thompson
AED Aeromechanics Division
US Army, CCDC Aviation and Missile Center

Date Approved: May 22, 2019

Dedicated to those who strive to make a positive difference..

ACKNOWLEDGEMENTS

This thesis is a result of support and selfless efforts by several people. I am immensely grateful to Prof. Komerath for seeing the potential in me and accepting me as his student. He has been on my side in all stages of the five-year journey not just as a mentor, but also as a guardian. His encouragement and amazing sense of humor made the difficult times a breeze. I thank Dr. Tom Thompson, Prof. Lakshmi Sankar, Prof. J.V.R Prasad, and Prof. John McIntyre for helping me shape this thesis well through their involvement since its proposal.

I thank other graduate students in the lab: Nandeesh Hiremath, Nikolaus Thorell, and Nicholas Motahari for helping me learn fast and making the work and academics more fun. I also thank all the undergraduate students who assisted me during various stages of the research.

I am grateful to Mr. Greg Rogerson, Mr. Miller Russell, and Mr. Charles Mosely for teaching me machine shop tools and helping me fabricate parts for the test setups. I thank Mr. Juan Pablo for his guidance on using drone components for making rotor setups.

I would like to thank my parents for their unwavering support and trust in everything I have done so far. Finally, my acknowledgement will not be complete without thanking my friends from Asha for Education at Georgia Tech for helping me grow as a person and making my stay in Atlanta very memorable.

TABLE OF CONTENTS

LIST OF TABLES

LIST OF FIGURES

SUMMARY

In recent years, Vertical Take-off and Landing(VTOL) unmanned aerial vehicles (UAVs) have gained importance in various applications suited to their small size and relatively cheap construction. These include aerial videography, search and rescue missions, surveillance, construction, package/food delivery etc. In such VTOL UAVs, the multirotor arrangement is preferred over conventional single rotor arrangements. The simpler control technique based on varying rotor speeds bypasses the need for a swashplate mechanism. Small size UAVs have low aerodynamic efficiency, affecting their payload, range, and endurance. The poor aerodynamic performance can be attributed to viscosity-dominated losses at low Reynolds number (low-Re), and due to yet to be understood rotor-rotor and rotor-airframe aerodynamic interactions.

Some of the existing research areas relevant to the low-Re multirotor aerodynamics are: low-Re airfoil analysis, design and optimization, low-Re single rotor, and high-Re multirotors with focus on coaxial and tandem arrangements. Unfortunately, the findings from high-Re multirotor studies cannot be directly applied to low-Re multirotor cases because viscous forces in low-Re rotors cases have been seen to have strong effects on the wake. The changes in rotor wake due to viscous effects are expected to cause unique flow interaction phenomena in low-Re multirotor cases which are not observed in their high-Re counterparts. Predicting flow phenomena specific to low-Re cases is not possible using rotor codes based on methods such as the free wake model which assume potential flow. A full-fledged Navier-Stokes simulation on a multirotor case is very expensive and still not dependable, as even the current state of the art CFD codes fail to predict torques and side forces on rotors.

The sheer number of possible rotor arrangements in multirotor UAVs makes it neces-

sary to understand all the prominent flow phenomena. This is to be able to develop models to augment rotor analysis codes so that they can be used for better analysis, design and optimization of small scale rotor UAVs for performance. The interaction study is also relevant to addressing another issue associated with UAVs, which will gain importance with their prevalence in near future: namely noise. Every day more and more rotor UAVs are being flown for some application or other. UAV noise has been known to cause annoyance to many people, with an increase in the number of UAVs flying in inhabited areas, the imposition of stricter noise regulations on UAVs may be expected.

The approach taken in this thesis for studying rotor interactions is through laser flow visualization, and hi-speed stereo particle image velocimetry (SPIV), along with thrust and torque measurements on rotors. Five different setups were built and tested in this effort, which have been described in detail in this thesis. Seeing that there are innumerable ways in which multiple rotors can be arranged, the problem of characterizing the flow seems unending. It is reasoned that all the key flow phenomena to be found in almost all multirotor configurations should be observable between just a pair of rotors too if their relative positions are chosen thoughtfully. Experiments done in the present effort cover an adequate range of relative rotor positions and test conditions. The thesis also presents exploratory work on low-Re rotor wake interaction with a duct and with a bluff body underneath which mimic the protective duct around UAV rotors and fuselage/payload below UAVs respectively.

Analysis of instantaneous hi-speed SPIV data gives insights on interactions of a rotor's tip vortices and vortex sheets with the duct, another rotor, other rotor's wake features, and bluff bodies. Tip vortex features such as vortex core size, vortex trajectory, and vortex strength have been tracked for most cases.

The thesis is organized into chapters based on test setups and multirotor configurations on which the experiments were run. Each such chapter includes objectives of the experiments, analysis, and interpretation of results. Conclusions from the whole effort and suggested future work are summarized in the last chapter.

Nomenclature

Variables

Re	Rotor tip Reynolds number
C_T	Coefficient of thrust
C_Q	Coefficient of torque
ω	Vorticity
r	Radial location

Constants

R	Rotor radius
c	Rotor blade chord length
Ω	Rotor angular speed
μ	Absolute Viscosity of air
ρ	Density of ambient air

Abbreviations

AS	Axis shift (distance between the axes of two rotors)
VS	Vertical separation (vertical distance between rotor planes)
HD	Horizontal Distance (distance between the rotor axis and vertical box surface)
VD	Horizontal Distance (distance between the rotor plane and horizontal box surface)
FM	Figure of Merit
PIV	Particle Image Velocimetry
SPIV	Stereo Particle Image Velocimetry
RMS	Root Mean Square

CHAPTER 1
INTRODUCTION

1.1 Background

The idea of having more than one lift generating rotor for a helicopter is not new. Mikhail Lomonosov was the first person to develop a helicopter model with coaxial rotors in 1754 and demonstrate it to the Russian Academy of Sciences [1]. The first coaxial rotor helicopters, "D'AT3" and "Gyroplane Laboratoire" were developed in the early 1930s [2]. Following these, the other multirotor configurations to get developed were tandem and intermeshing rotors. The first successful tandem rotor helicopter to be mass produced was the HRP rescuer (also known as "Flying Banana") [3] which made its first flight in 1947. The Flettner FL 265 was the first intermeshing-rotor helicopter developed; it was built in 1938 [4]. These multirotor configurations were mostly developed with the motivation of improving stability, and payload capacity and to avoid the use of tail rotors to provide counter torque.

Though the above multirotor configurations performed well, they did not become as popular as the conventional single main rotor helicopter because of their much higher mechanical complexity. Having multiple rotors meant a need for more complicated transmission and blade pitching mechanisms. With advancements in electronics, controls and wireless information transfer in the 1990s, it became possible to control a rotorcraft remotely, hence much smaller unmanned rotorcraft could be developed. These small rotorcraft could easily change rotor RPM to change thrust instead of having to change blade pitch, due to the low rotor inertia. The absence of complex mechanical components made multirotor configurations more attractive as flight control could be achieved by simply varying

speeds of the different rotors. They are cheaper and more durable compared to a single rotor UAV with similar size and capabilities. Quadrotors became the most popular among all rotor UAVs. They have found their use in aerial videography, surveillance, package delivery, and as research platforms to test out new flight control and navigation algorithms. Innumerable conference and journal articles on quadrotor and multirotor control have been published in the last decade. Figure 1.1 shows a few commercially available multirotor UAV configurations.

Figure 1.1: Various multirotor UAV configurations

The total drones sales in the year 2016 were $ 8.5 billion and is expected to increase up to $12 billion by the year 2021 [5]. The industries in which the drones are being used, or are projected to be used in near future are: infrastructure, agriculture, transport, security, media/entertainment, insurance, telecommunication, and mining.

1.2 Motivation and Objective

Despite many benefits and applications of multirotor UAVs, they still lack in giving satisfactory performance in terms of payload capacity, range, and endurance. One reason is the low energy density of batteries or other energy storage devices currently feasible for such small size application. The other reason is their poor aerodynamic performance. Small rotors operating at low Reynolds number encounter more dominant viscous effects. The contribution of viscous skin friction drag becomes significant, which is generally not the case in full-scale helicopters where most of the losses are through pressure drag or lift-induced drag. The boundary layers are thick and undergo several complex phenomena. The separation bubble often spans the whole chord of a blade, adversely affecting the lift generating capability further. Small rotors with airfoils and blade geometries similar to those found in full-scale vehicles have Figures of Merit of the order of 0.35 which is very low compared to 0.7 for full-scale rotors [6].

The rotors in multirotor vehicles are almost always tightly spaced. Thus a lot of aerodynamic interactions such as those between wake-wake and blade-wake are expected. For instance, the lower rotor blade in a coaxial rotor gets continuously impinged by the wake of the upper rotor which contains tip vortices and trailing edge vortex sheet. Such blade-wake interaction is likely to cause very different angle of attacks along the span of the lower rotor at periodic time intervals, contributing to noise, vibration, and low aerodynamic efficiency. Apart from blade-vortex interactions, coaxial rotors also see significant wake-wake interaction when wake features due to the upper rotor interact with wake features of the lower rotor. Coaxial rotors are still the simplest special case of overlapping rotor configurations. Here the blade-wake and wake-wake interactions are axisymmetric. These interactions are more difficult to predict in non-axisymmetric multirotor cases. The problem gets even more

challenging in the case of small scale UAVs due to the Reynolds number range in which they operate.

Most of the present knowledge on rotorcraft aerodynamics is based on full-scale helicopters operating at very high Reynolds numbers. Typically high Reynolds number flows are perceived to be difficult to solve using CFD due to uncertainty on which turbulence model to use, need of finer grids in boundary layers and hence having to deal with very small time steps for numerical stability. However, in the case of rotor blades, it is often assumed that the flow is inviscid (Reynolds number tending to infinity) for simplifying thrust and induced drag computations, accounting for viscous parasitic drag through models. This simplifying assumption of inviscid flow makes it possible to apply potential flow methods such as prescribed and free wake models for rotor aerodynamics computations. This approach works well for the high Reynolds number rotor flow field which can be treated as being induced by the strong vortices and thin shear layers present in the wake. However, at low Reynolds number, the airfoil characteristics, nature of the tip vortex, flow separation, etc. are significantly different, and also very sensitive to small changes in geometry and Reynolds number. Viscous effects extend far from the surface. Vortices are diffused more quickly as opposed to those found due to full-size rotors.

At present, most of the low Reynolds number rotor analyses used in studying interactions still rely on high Reynolds number potential flow methods with ad-hoc empirical correction factors to account for deviations due to viscous effects. One cannot trust results obtained by such empirical fits for situations where there is more than just a rotor in the flow field. This problem requires considering the use of a full unsteady Navier Stokes equation solver because simplifying assumptions are not valid. But unfortunately that approach is often too computationally intensive for multirotor scenarios, and thus it cannot be used for the repeated runs necessary for design and optimization of multirotor UAVs to alleviate

performance problems.

Questions to address

Some important and intriguing questions regarding the low-Re multirotor flow field are: Does the concept of vortex-dominated wakes apply when Re is low, considering that the vortex is much more diffused? Are optimal blade geometries for this Re range very different from those for large scales? Are there any more efficient alternatives to full Navier-Stokes computations to obtain efficient, accurate predictions, as there are at high Re such as the free wake method? What aerodynamic interactions occur with ducts, structure, payload, other rotors, etc.? Can a strategic placement of these help improve performance? These issues are much larger than the scope of the present study, but a beginning is made here.

Motivation

The motivation behind studying low-Re multirotor aerodynamics is to identify and characterize all the dominant flow phenomena present in the interactive flow field. Once characterized, it should be possible to take those phenomena into account while designing multirotor UAVs. Physics-based or empirical models can be developed for the observed flow phenomena, to be used in rotor codes for use in design and optimization. The knowledge of dominant flow phenomena will be instrumental in the understanding of UAV noise too, which will help in developing noise abatement strategies, to keep the noise due to UAVs under annoyance limit.

Objectives

The objective of this thesis is to explore the flow field for discovering such interaction phenomena, through a wide range of multirotor experiments. This work is intended to serve as a guide for future researchers to know what needs to be investigated in further detail. The work itself does not go into a detailed study of each and every discovered flow phenomenon.

Though the primary motivation of this study is low-Reynolds number multirotor UAVs, some of the findings can be applied to large-Reynolds number cases too if a proper scaling function for the observed phenomena is developed based on the experimental findings over a good range of Reynolds numbers. That can enable the design of large scale multirotor vehicles based on much cheaper small scale multirotor experiments.

To summarize:

The primary objectives of this thesis are:

- To identify and quantify wake features and aerodynamic interactions between rotors and payloads that exists in multirotor UAVs, through experiments in Reynolds range of 10,000 to 300,000.
- To use the knowledge obtained about the flow field to provide guidance on how analysis methods can be developed or modified from existing traditional helicopter technology for estimating or predicting a multirotor UAV design's characteristics.

The basic issues that the thesis seeks to address are:

1. Low-Reynolds number regime phenomena that cause simplifying assumptions to fail.
2. Difficult to estimate the nature of highly interacting flow-field.
3. Vast number of possible multirotor configurations exhibiting a variety of flow phenomena.

1.3 Prior work

There are four distinct areas in which research progressed over the past few decades for the development of rotorcraft UAVs. One is the study and design of low Reynolds number airfoils. The second is the aerodynamic study and design of small rotors. The third is UAV design, and the fourth is full-scale multirotor vehicles.

1.3.1 Airfoil Studies

Airfoil research has been an important part of aviation and aerospace field since the beginning of the 20^{th} century when airfoils were tested in wind tunnels so that better aircraft wings could be developed. Now, after the advent of computers about 70 years ago, airfoils have been studied computationally too. Traditionally, the focus of these studies stayed in high Reynolds number flows as a majority of heavier than air flying machines are big enough to carry people and cargo. Low Reynolds number airfoil study picked up pace after the need and feasibility of small unmanned aircraft were realized.

Study of low Reynolds number airfoils started sometime in the 1970s. Researchers such as Miley, Leibeck, Selig, Kroo, Kunz and a few others designed airfoils specifically for the low Reynolds number regime using different approaches. [7, 8, 9, 10, 11, 12, 13]. Eppler *et al.* wrote a computer program for design and analysis of low-speed airfoils in 1980 [14]. Selig *et al.* came up with the multipoint inverse method for airfoil design in 1992 [15, 16, 17].

Many experimental studies have been performed on airfoils at low Reynolds number to test lift, drag and pitching moment characteristics [18, 19, 20, 10, 21, 22, 23, 24, 25]. Mueller *et al.* [26, 27] studied boundary layer separation and transition on a 2D airfoil at

low Reynolds number, and its effect on hysteresis in C_l and C_d characteristics Brendel *et al.* did boundary layer measurements [28] and Guglielmo *et al.* studied spanwise variation in profile drag for airfoils at low Reynolds number [29].

Some low-Re wing studies were also performed by Mueller, Laitone, Pelletier, Sunada, and few others [30, 31, 32, 33, 34]. Althaus [35] published a comprehensive airfoil catalog containing lift and drag coefficients of 30 airfoils. In 1981, Carmichael [36] compiled low Reynolds number flow physics studies done until that time. Van [37] also wrote a review on theoretical and experimental work in low-Re aerodynamics. Miley published a catalog of low-Re airfoils for use in the design of small wind turbines [38]. Selig performed wind tunnel tests of more than 200 airfoils in the Reynolds number range of 40,000 to 500,000. The results were compiled and published as a book "Summary of Low-Speed Airfoil Data " [39]. Laitone did pressure distribution and flow visualization tests along with force and moment measurements to explain why thin curved plates with sharp leading edges are aerodynamically superior to round-nosed airfoils at Re less than 70,000 [40, 31]. He showed that the Kutta-Joukowsky trailing edge condition does not apply for certain airfoils. Lowson [41] discussed why low Re flows are very sensitive to experimental conditions, causing large uncertainty in results from different experimental facilities. Ellington and Okamoto studied unsteady flows at low Re [42, 43, 44]. Dickinson identified the main unsteady aerodynamic mechanisms which are responsible for better lift generation: wake capture, delayed stall, and rotational circulation, through experiments on a dynamically scaled flapping insect model [45, 46].

On the computational side, Kunz and Kroo [10, 11] analyzed and designed low Re airfoils using a 2D incompressible N-S solver, INS2d developed by Rogers and Kwak [47]. Singh and Kellogg [48, 49] did parametric studies on thin cambered airfoils in Re range of 60,000 to 15,000 using XFOIL [50]. Shum [51] developed a computational model to in-

vestigate laminar separation bubbles and to predict separation, transition and reattachment locations on a 2-D airfoil.

1.3.2 Rotor Studies

Bohorquez and Hein tested hover performance of rotors at low Reynolds number for rotary wing MAVs [52, 6, 53]. Kunz analyzed and designed rotors for the ultra-low Re regime [54]. Sunada Kawachi studied effects of Reynolds number on rotor characteristics [34]. Lakshminarayan did a CFD study on a micro-rotor in hover [55, 56]. Schroeder did flow validation and prediction for MAVs using TURNS (Transonic Unsteady Rotor N-S) [57] in 2005 [58, 59]. Rubio approached the low Re rotor design and optimization problem by generating 3D blades using a set of Bezier curves as airfoils and modifying them based on BEM (Blade Element Theory) and VPM (Vortex Panel Method) analysis [60]. Bohorquez too did rotor design optimization using BEM theory and hover experiments [61].

1.3.3 Vehicle Design

Some of the earliest low Reynolds number fixed winged vehicles came around the mid-1980s [62, 63, 64]. But here we focus on rotor UAVs only. There have been numerous rotary winged UAV / MAV design studies performed and vehicles built since the late 1990s. In early 2000, a preliminary design study of a micro-coaxial rotorcraft, "MICOR'', was done by Samuel and Sirohi [65]. Other such reports are by Lipera on "iSTAR'' MAV [66], "Micro STAR'' and "Black Widow'' by Morris and Grasmeyer [67, 68], and by Bohorquez [69]. Sirohi and Tischenko designed and made a ducted single rotor vehicle with vanes in the wake for counter torque[70]. Kroo presented an aerodynamic design of the Mesicopter, which is a very small multirotor vehicle [71, 72]. Young et al [73] explored many hovering MAV configurations and did some aerodynamic performance measurements on some of

them. Woods and Baxter [74, 75] computed energy and power requirement in different low Re UAV configurations.

1.3.4 Multirotor studies

Out of all multirotor configurations, the most studied is the coaxial rotor, partly due to the number of coaxial helicopters developed and made until now. Until lately, the interest has always been in full-scale coaxial rotors. Harrington [76] and Dingeldein [77] did performance tests on coaxial rotors in the 1950s in the Langley full-scale wind tunnel. Nagashima studied coaxial rotor wake geometry [78], and a recent experimental work by Sunada *et al.* aims at maximizing thrust-torque ratio [79].

Coleman wrote a survey on theoretical and experimental research on coaxial rotors [80]. Leishman too worked on optimizing the aerodynamic performance of coaxial proprotor [81]. Researchers like Saito[82], Andrew[83] and Zimmer[84] have attempted to model coaxial rotors. Bagai used a free wake model to study tandem, tilt-rotor, and coaxial rotor configurations [85]

Griffiths studied interactions between two separated rotors and ground effect using a free vortex method [86]. Radhakrishnan *et al.* did experiments on a scaled model of a quad tilt rotor in slow forward flight [87]. Gupta did a computational study on a simplified quad tilt rotor using a time-averaged rotor model in place of rotors in a compressible N-S CFD code [88], and compared the downwash velocity and pressure distribution on wings with experimental results. Lee analyzed the aerodynamic characteristics of multirotor arrangements using the free-wake method [89]. Rajagopalan developed a computational tool, RotCFD, for efficient calculations of aerodynamic interference between rotors [90].

Driessens came up with a totally new quadrotor configuration for small rotor UAVs featuring one big thrusting rotor and three rotors for control. The configuration is claimed to be 20% more efficient compared to traditional equal size rotor quadrotors [91]. Yoon simulated XV-15 rotor in hover using OVERFLOW [92], and analyzed multirotor flows [93]. Brazinskas *et al.* performed an empirical study of overlapping rotor interference for small UAVs [94]. Young presented conceptual design aspects of three general sub-classes of multirotor configurations: Distributed, Modular, and Heterogeneous. [95]

1.4 Approach

The multirotor aerodynamic interactions phenomena such as wake-wake and blade-wake interactions were observed by capturing 3-dimensional velocity field using high-speed stereo Particle Image Velocimetry (high-speed sPIV). Five different setups were designed and built to address specific goals. They are: Single rotor, coaxial rotor for high advance ratio flight, quadrotor, modular bi-rotor, and a rotor-box. The single rotor setup was used for studying the baseline case without interactions with other rotors and effect of an annular duct. A Reynolds number sweep was done to understand Reynolds number effect on the rotor wake and performance. A larger, but low RPM coaxial rotor setup was built for conducting high advance ratio experiments, observing the interaction of tip vortices due to the two rotors and measuring performance. The quad-rotor setup was made to study the flow field of the side-by-side rotors, with and without the presence of a duct surrounding each rotor. The modular bi-rotor setup was developed to be able to achieve almost any possible relevant configuration between two rotors such as overlapping (coaxial being a special case) and side-by-side with a good range of axis shift, vertical separation, and tilt adjustments. The rotor-box setup comprised of the single rotor setup along with an instrumented box to study rotor wake interactions with a box.

Note: Intermeshed rotor configurations could not be considered because of the difficulty in getting such small rotors at high RPM to synchronize reliably enough. The wake interactions expected there can be glimpsed from the cases done.

All of the above setups have thrust measurement capability, whereas the single rotor and modular bi-rotor setups have individual rotor torque sensing too. Further details on each of the above setups and the test cases are provided in the respective chapters. The high-speed stereo PIV experiments on the test cases were very useful in observing the evolution of wake features such as the tip vortex and trailing edge vortex sheet with the passage of rotor blades and time.

1.5 Experimental Facilities

This section describes in detail the experimental facilities used in this investigation, which includes the low-speed wind tunnel and the diagnostic equipment.

1.5.1 Low Speed Wind Tunnel

The experiments were conducted in the John J. Harper closed circuit low-speed wind tunnel with the test section dimensions of $2.13m \times 2.74m$ ($7' \times 9'$) at the Georgia Institute of Technology to emulate flight conditions ranging from hover to high speed forward flight. The wind tunnel was built in 1930 and is located in the basement of the Guggenheim building. The contraction ratio between the cross-sectional area of the settling chamber to the cross-sectional area of the test section is approximately 5:1.

The tunnel is powered by a three-phase 600hp induction motor coupled to a fixed pitch single stage 4 bladed fan via a gearing mechanism with an 8:3 gear ratio. The wind tunnel speed is controlled by a variable frequency drive which is a closed loop controller with

0.1% tolerance in RPM setting. The test section wind speeds are derived from dynamic pressure (q) measured using a 10 Torr Baratron, a differential pressure transducer connected to a pitot-static tube located near the ceiling of the middle of the test section. The highest wind speed that can be obtained in the test section is about 32 m/s (71 mph/ Mach 0.1) when totally empty. The schematic diagram and photo of a scaled model of the wind tunnel is given in Figure 1.2.

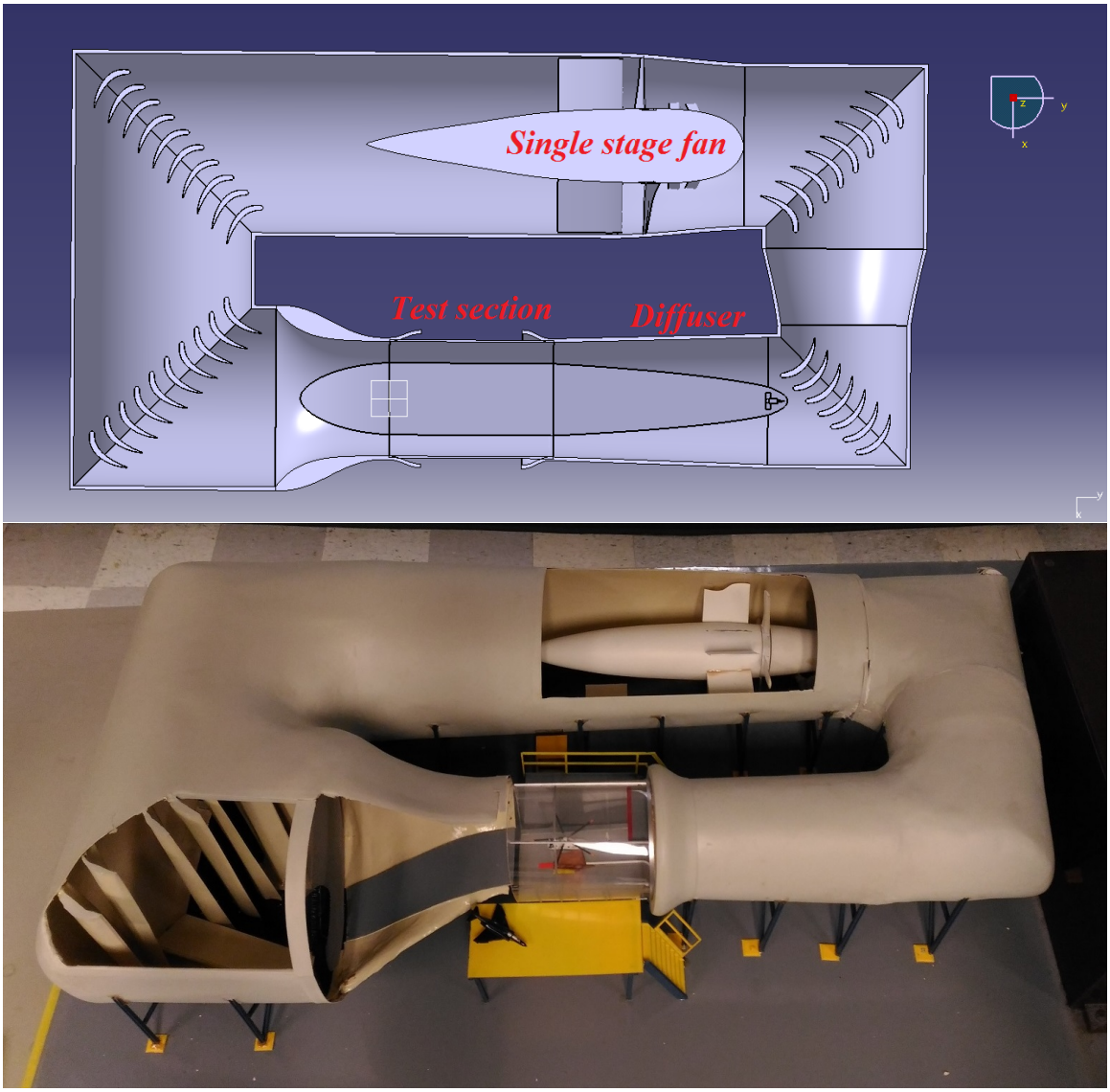

Figure 1.2: Schematic and a photo of the scaled model of the John Harper wind tunnel at Georgia Institute of Technology

Table 1.1: Expressions for computation of derived state quantities.

Quantity	Expression	Units
ρ	$\frac{P}{R_g T}$	kg/m^3
μ	$\frac{C_1 T^{3/2}}{T+S}$	$Ps-s$
V_∞	$\sqrt{\frac{2q}{\rho}}$	m/s
Re	$\frac{\rho V_\infty c}{\mu}$	

Temperature and static pressure are measured near the test section to compute air density and viscosity, which are necessary for wind speed and Reynolds number computations. The expressions used for the computations are listed in Table 1.1

The turbulence intensity of the empty wind tunnel, defined by the ratio of the standard deviation to the mean free stream velocity, is 0.05% measured at a free stream velocity of 31.29 m/s using a Constant Temperature Hot Film Anemometer. However, with support structure and models generating wakes, the turbulence intensity values observed during experiments are around 0.3%.

1.5.2 High-Speed Stereo PIV system

The flow diagnostics were performed on the rotor using PIV. The equipment used with the LaVision setup included a dual head Nd:YLF Photonics laser PIV laser (DM30-527), two Phantom v341 cameras, high-speed programmable timing unit (PTU) and the DaVis imaging software. The laser heads are run by a control unit which takes in trigger signals from the PTU and settings such as diode current from the computer and controls the laser head based on the information. A separate chiller is used to maintain the diode temperatures at about 15 to 18 degrees Celsius. The laser beam from the heads is channeled up to the lo-

Table 1.2: Specifications of the DM30-527 Laser.

Wavelength	527 nm
Average Power @ 3 kHz	45 W
Pulse Energy @ 1 kHz	30 mJ
Pulse Width @ 1 kHz	150 ns
Repetition Rate	Single Shot to 10 kHz
Nominal Beam Diameter	5.0 mm
Beam divergence	8.0 $mrad$
Beam pointing stability	$<$ 2.5 μrad

cation of interest through a closed optical path (laser arm). Sheet optics attached at the end of the laser arm spread the beam into a plane of laser sheet using a cylindrical concave lens.

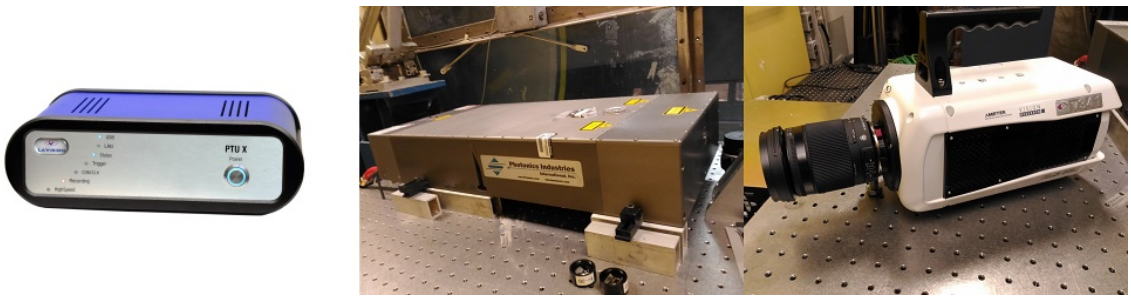

Figure 1.3: Photos of Programmable Timing Unit, the high-speed double cavity Nd:YLF laser head, and a Phantom v341 high-speed camera

The programmable timing unit used in the high-speed PIV system was LaVision PTU X. PTU synchronizes cameras and laser triggers with sub-nanosecond jitter. Figure 1.3 contains photos of the PTU, the laser and a camera. PIV data acquisition using the PTU, the laser, and the cameras is done through the DaVis 8.3 software. The software lets the user control laser intensity, frequency of image acquisition, the time difference between two frames for PIV, trigger method, camera resolution, etc. necessary for taking PIV data. The

Table 1.3: Specifications of the Phantom v341 cameras.

Sensor Type	CMOS
Resolution	2560×1600 pixels
Pixel size	10 μm
Intensity resolution	12 bit
Repetition Rate	Single Shot to 10 kHz
Minimum Exposure	1 μs
Shutter type	Global electronic shutter
Timing Resolution	20 ns
Max speed @ full resolution	800 fps
Max speed @ 256$\times 8 resolution$	130,000 fps
Min speed	10 fps

software also does calibration to find orientation and distance of the cameras with respect to the target plane to make sense of physical dimensions from images using a calibration plate. The software performs cross-correlation between images from the two cameras to compute velocity vectors at each interrogation window of a specified size.

For all the PIV measurements, vector computations were done in four passes. The first two passes used an interrogation window size of 64×64 pixels with 50% overlap, and the next two passes used 32×32 pixels window with 50% overlap. Doing multiple passes reduces uncertainty. Reducing interrogation window size with passes causes the resultant velocity vectors to represent more local velocity instead of an average over a large region. Small interrogation window size and overlap help in generating denser (higher spatial resolution) vector field, often necessary to study small size flow features. Postprocessing of the vector images consisted of an applied median filter and light smoothing for better visualization (3×3).

Uncertainty in the velocity vector computation is also found using the DaVis software which computes positional disparity of image of seeder particles in two interrogation windows which have been mapped back onto each other[96]. Upper bounds to the uncertainties in in-plane and out-of-plane velocity vectors for each test case are mentioned in respective chapters.

1.5.3 Load Cells

Daytronic uniaxial load cells

Three Daytronic uniaxial load cells (400-100) were used to measure thrust on the coaxial rotor setup described in chapter 3. The signals from the load cells were passed through a low pass filter and an amplifier before feeding them to NI USB 6361 DAQ. A LabView program to visualize and record thrust data through the DAQ was created.

Table 1.4: Specifications of the Daytronic 400-100 uniaxial load cells

Nominal Load Capacity	$\pm 500N$
Excitation	20 V maximum
Nominal output	2mV/V $\pm 0.25\%$ of full scale
Operating temperature range	-54^oC to $+93^oC$

ATI Nano 6 DOF load cell

An ATI Nano load cell was used for measuring overall thrust due to the quad-rotor setup in hover, described in chapter 4. The sensing range of the load cell along the load cell axis (z) is $\pm 75N$ and the resolution is 0.028 N.

Beam type uniaxial load cells

One kgf and 0.1 kgf load cells were used for thrust and torque measurements respectively in the single rotor and modular bi-rotor setups. No formal specifications for these load cells are available. The signals through these load cells were filtered, amplified and then read through the NI USB 6361 DAQ. Calibration of these was done using standard weights. All the load cells used over all the experiments are shown in Figure 1.4

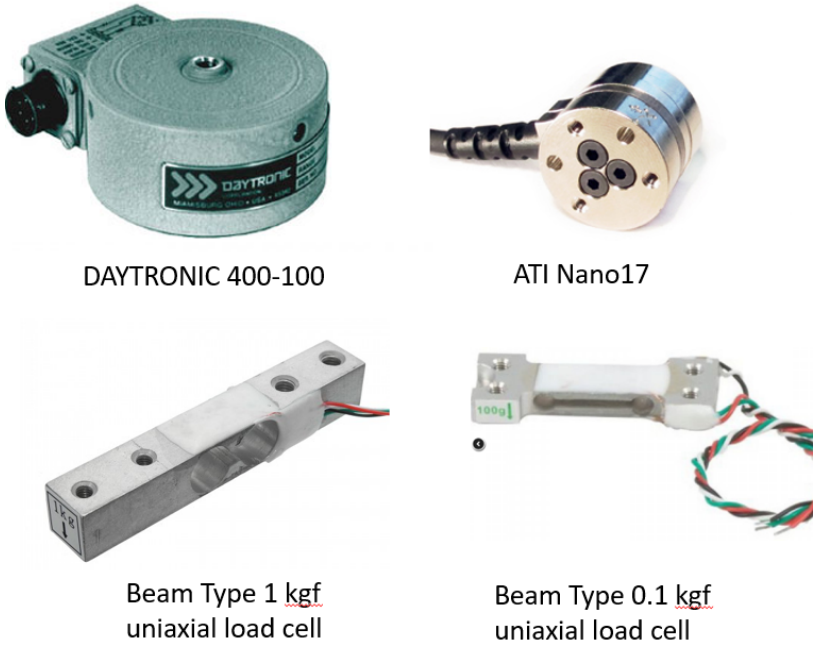

Figure 1.4: Photos of the load cells used in different setups for thrust and torque measurements

1.5.4 Laser Tachometers

Rotor RPMs for all the cases were measured using non-contact laser tachometers which could be placed far from the rotors to avoid interactions with the rotor wakes. The tachometers give out TTL outputs which are read by the DAQ (for the case of low RPM coaxial rotor setup) or by micro-controller (for the single rotor and modular bi-rotor setup). The LabView and the micro-controller program compute the RPM by timing the interval between two consecutive LOW to HIGH logic shifts from the tachometers, which happen when the

Table 1.5: Specifications of the Monarch PLT200 laser tachometers

Max measuring distance	760 cm
Min RPM	5
Max RPM	200,000
RPM Accuracy	$\pm 0.01\%$ of reading

laser gets reflected off the reflecting tape attached the rotor shaft. The laser tachometers used are MONARCH PLT200. Figure 1.5 is a photo of the laser tachometer.

Figure 1.5: Laser tachometer used for RPM measurements

CHAPTER 2
SINGLE ROTOR: EFFECT OF REYNOLDS NUMBER AND DUCT ON THE ROTOR WAKE AND PERFORMANCE

This chapter described current work on understanding the flow and performance characteristics of a low *Re* rotor in isolated and ducted/shrouded configurations. The primary focus here is to study rotor-duct interactions and their effects. The results from low *Re* isolated rotor tests are also used for comparison with some previous high *Re* rotor tests to demonstrate the role of *Re* on flight performance and rotor wakes.

2.1 Previous Single Rotor Studies

There have been numerous high Reynolds number rotor flow measurement studies dating back to the 1960s by Landgrebe *at al.*[97]. Donald W. Boatwright [98] measured inflow and near field wake velocity profile using a 3 component hot wire anemometer on a 10.2 m OH-23B rotor. Yamauchi *et al.* did 3 component PIV measurements on a 2.29m diameter rotor in hover in 2000 [99]. P. Martin *et al.* studied tip vortices and wake velocity profiles using 3 component LDV and laser flow visualization on a 0.8m diameter 1 bladed rotor in 2001 [100]. Kenneth McAlister studied rotor wake development over a rotor revolution through PIV in 2003 [101]. Wadcock *et al.* did PIV measurements on a UH-60 full scale rotor in forward flight at the National Full-Scale Aerodynamics complex in 2011 [102].

The low Reynolds number single rotor flow visualization and velocity measurement studies till date are fewer in number. M. Ramasamy and J. Leishman did PIV measurements at a range of Reynolds number and came up with a Reynolds number based tip-vortex model to estimate how properties of blade tip vortices advance with time [103, 104]. They also performed flow visualization and 2D PIV measurements on a MAV scale rotor

[105, 106]. They reported thicker, more turbulent trailing edge vortex sheet and larger vortex core size compared to high Reynolds number cases.

In the pursuit of obtaining better performance out of a low-Re rotor, there have been efforts to minimize the induced losses by applying ducts around the rotors. This also helps improve the crashworthiness of these small vehicles, which are likely to encounter impacts at low speeds since they often operate in confined spaces or with less-trained operators. The Mass Helispy, I-Star, Honeywall MAV, BAE IAV 2 are a few examples of ducted single rotor Micro Air Vehicles (MAVs) available in the market.

Martin et. al. [100] studied the performance of a ducted rotor model with varying tip clearance for a range of forward speeds and angle of attack, going from pure hover to propeller mode. Pereira [107] studied the effect of different duct shapes on the hover performance and claimed an increase in thrust up to 94%, at the same power consumption, or reductions in power by up to 62% at the same thrust for the best case. The study reported consistent improvement in performance with increasing duct lip radius and decreasing tip clearance. Akturk et. al. [108] presented mean wake measurements on a ducted rotor using PIV and used that to validate RANs simulation. Hrishikeshavan ([109]) designed a single rotor MAV with shroud weighing 280 grams and reported 20-30 grams of increase in payload capacity over the baseline case of an un-ducted rotor, accounting for the added vehicle weight due to the shroud.

2.2 Scope

From prior work[100], it is well known that ducts with low tip clearance improve rotor efficiency. In these cases, the ducts play an active role in thrust generation through the design of the inlet lip. Many multirotor UAVs seen in the market come with a thin duct

around the rotors to improve crashworthiness and operational safety, without special consideration of performance. A large thrust-assisting duct is not practical for all vehicles due to mission or size requirements. In such cases, the duct design may or may not contribute to performance. Some understanding of the basics of rotor-duct aerodynamic interactions can serve as a guide for designers to improve performance even by small modifications to ducts designed for safety.

This chapter focuses on understanding wakes of low *Re* rotors and the effect of an annular duct. A small UAV-scale rotor setup is operated with and without ducts for a range of *Re* at two constant thrust coefficients (C_T) and constant thrust through measurements of the loads, time and space-resolved velocity fields and acoustics. The purpose of the constant thrust experiments was to separate out the effects due to thrust loading from the *Re* effect. The instantaneous high-speed PIV results help in observing the evolution of the wake as well as any unsteady effects. The rotor performance and acoustic measurements aid in building confidence on the arguments made regarding vortex-duct interactions. The averaged inflow and outflow velocity profiles explain the performance measurement outcomes from momentum considerations. Here, the comparison of high vs low *Re* rotor characteristics is also done using data from some of the mentioned prior studies and the isolated (unducted) single rotor experiments from the current work.

2.3 Experimental Setup

2.3.1 Facility and Diagnostics

The experimental and flow diagnostic facility used here is the same as that detailed in chapter 1. The acoustic measurements were performed to compare ducted and un-ducted rotor acoustic signatures using a Bruel Kjaer microphone of sensitivity 12.5 milliVolt/Pascal. The signal was further amplified using a preamplifier and Stanford Research Systems ana-

log filter and amplifier. The low-pass filter was set to 15kHz and the high-pass filter was set to 5Hz. The signals were sampled at the rate of 50kHz for 15 seconds.

2.3.2 Setup description

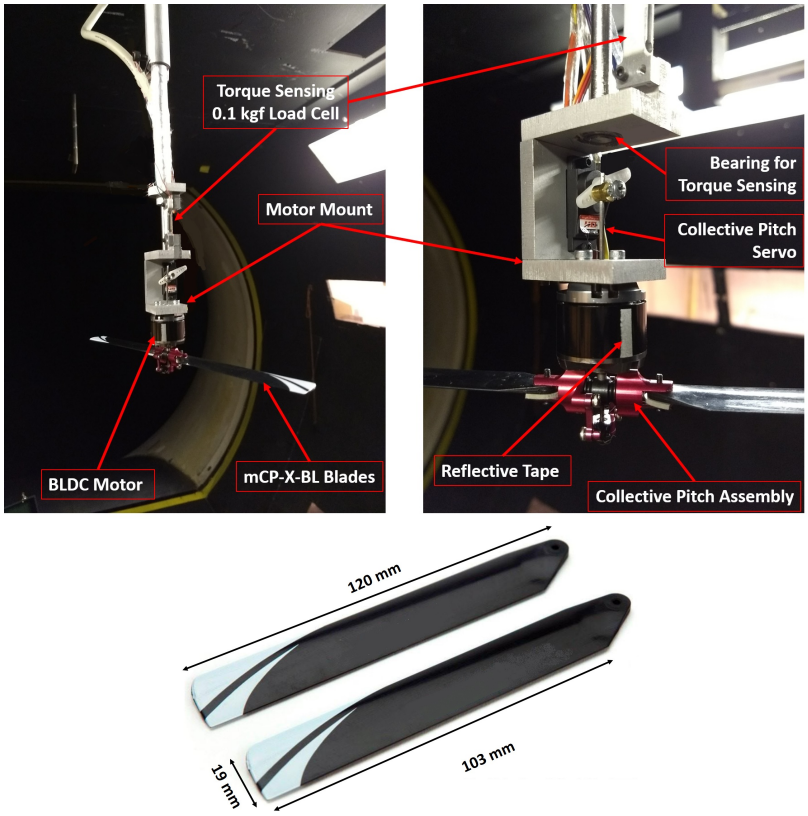

Figure 2.1: Labeled photograph of the single rotor setup

The two-bladed rotor in the single rotor tests setup was suspended from the wind tunnel ceiling to approximately the center of the test section, as shown in Figure 2.1. This arrangement was chosen to ensure that the rotor wake does not interact with any rotor support structure for reliable measurements. The test stand features thrust and torque measurement using the 1 kgf and the 0.1 kgf load cells described in chapter 1, respectively. The brushless DC (BLDC) motor is retrofitted with a variable pitch assembly allowing for adjustable collective pitch setting. The collective pitch is controlled through a pitch link running from the center of the shaft, attached to a servo motor. The blades used in this setup are from an

off the shelf model helicopter UAV (mCP-X-BL). The blades have un-tapered, untwisted planform. The rotor diameter after attaching the blades with the variable collective pitch hub is 272 mm.

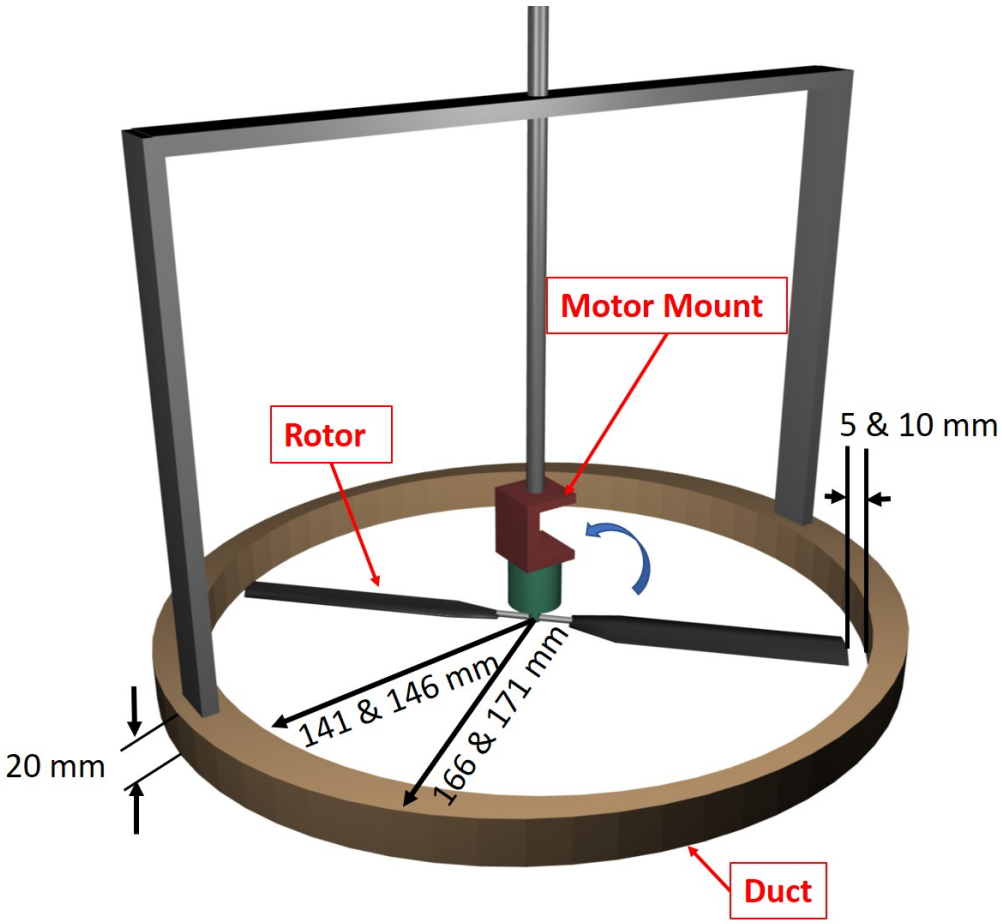

Figure 2.2: Duct dimensions and mounting

For ducted rotor experiments, two ducts with different rotor tip clearances were used. PIV and acoustic measurements are presented only for the larger tip clearance duct, whereas performance measurements are presented for both. The circular duct's radial thickness was 2.5 cm and the height was 2 cm. The ducts were supported using a lightweight structure pinned to the base of the rod away from the rotor to avoid affecting rotor inflow. Non-rigid members used to pin the support structure isolated the duct from rotor vibrations to avoid high amplitude oscillations of the duct in an event of accidental resonance of the structure with some sub-harmonic of the rotor. As the aluminum rod is suspended from the thrust

load cell, any lift force generated on the duct is also accounted for in the thrust measurements made by the thrust load cell. The shape, mounting method and the dimensions of the duct are shown in Figure 2.2. The setup specifications are listed in Table 2.1.

Table 2.1: Single rotor experiments setup specifications and test conditions

Rotor Specifications	
Number of blades	2
Rotor radius (R)	136 mm
Root cutout radius	21 mm
Blade planform	untapered, untwisted rectangular blades
Blade chord length	19 mm
Airfoil	NACA 0010
Hub type	rigid/hingeless
Pitch control	collective only
Duct Dimensions	
Inner radius, Outer radius, Tip clearance	Wider: [146 mm, 166 mm, 10mm], Narrower: [141 mm, 161 mm, 5mm]*
Height	20 mm
Test Conditions	
Blade tip *Re* tested	40k, 60k, 80k
C_T for constant C_T experiments	0.004, 0.006*
T for constant T experiments	0.27 N
	*[Performance measurements only]

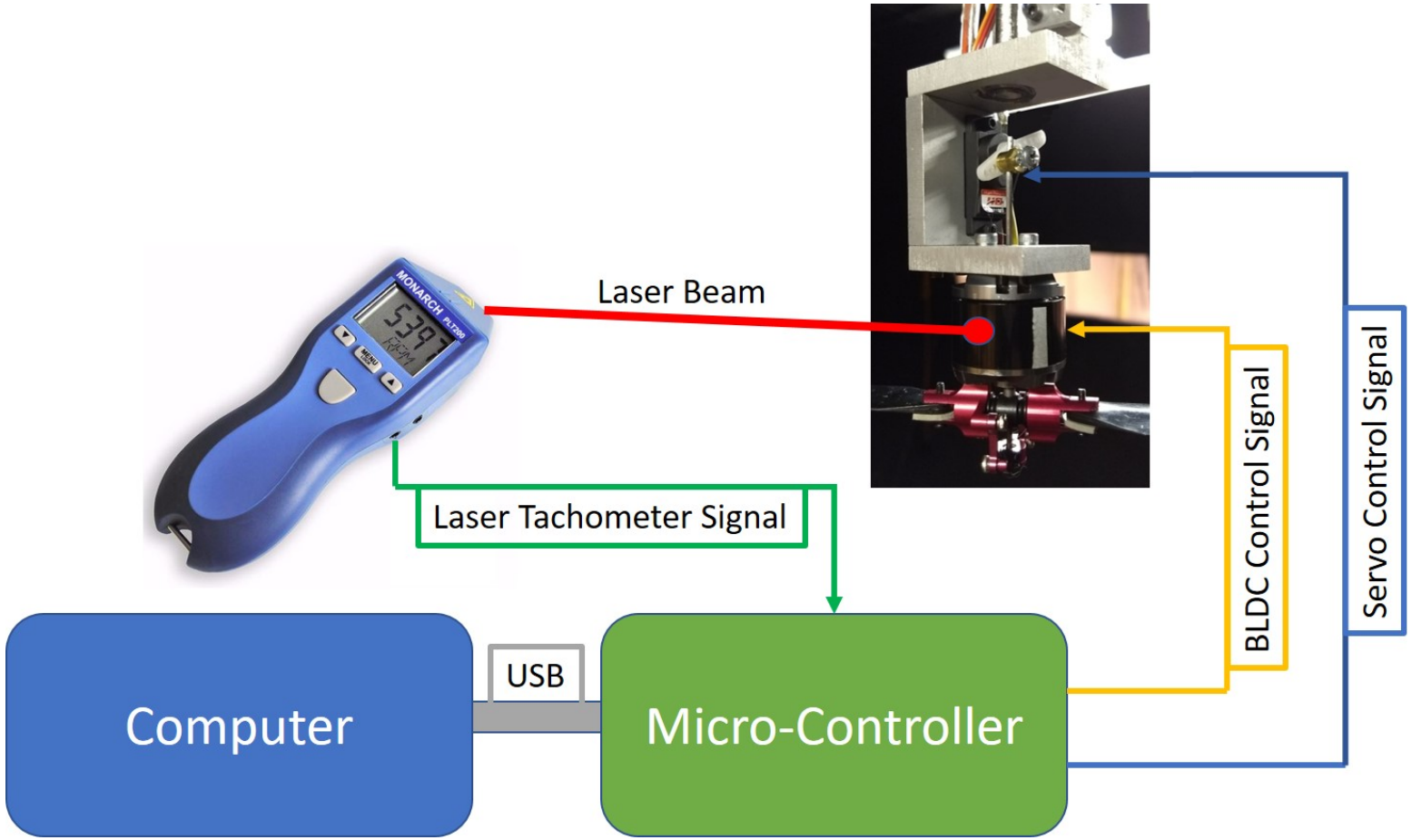

Figure 2.3: Rotor RPM and pitch control signal diagram

Figure 2.3 is a pictorial representation of the rotor RPM and pitch control signals. The Electronic speed controller (ESC) used for controlling and supplying power to the BLDC motor, and the servo motor, receive commands through an Atmel Atmega168 micro-controller embedded onto Arduino USB board. A reflective tape strip is glued to the BLDC motor rotor and a laser tachometer (described in chapter 1) is set up pointing towards the motor. The output of the laser tachometer is fed to the micro-controller which computes RPM from the time interval between two consecutive rotations. A basic proportional controller is implemented on the micro-controller to keep the rotor speed within ± 10 RPM of the set value at steady state. The micro-controller displays current RPM on, and takes its commands on RPM setting, servo position, etc. from a PC through serial communication.

2.3.3 Test conditions

The high-speed PIV and performance measurement experiments were performed for ducted and un-ducted single rotor arrangements at a constant coefficient of thrust (C_T)) as well as constant thrust (T) settings at three tip Reynolds numbers. The tip Reynolds number was varied by varying rotor RPM. Constant C_T and constant T test sets were performed to separate out the effects of rotor loading from those due to tip Reynolds number on rotor performance and flow features. The test matrix for ducted and un-ducted rotor experiments is included in Table 2.1.

2.3.4 Measurements and uncertainty

The single rotor tests involved high-speed stereo PIV, acoustic, rotor thrust, and torque measurements. The collective pitch angle for each test case was known through servo input as collective pitch and servo input were mapped onto each other through a calibration curve.

Collective pitch calibration and measurement

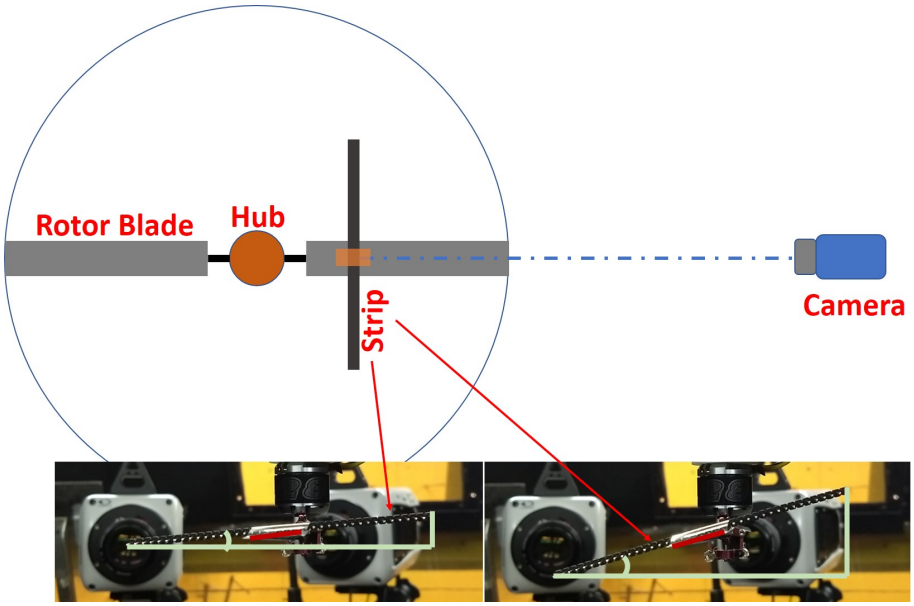

Figure 2.4: Schematic diagram explaining pitch calibration procedure

Due to the very small size of the rotors, it was not possible to reliably measure blade pitch angles using traditional contact tools such as protractors. Hence, a non-contact method employing a camera was used, as shown in Figure 2.4. A thin, light, stiff strip was applied with tape to one of the two rotor blades along the chord. A camera was placed along the blade pitch axis, on a stand, focusing on the strip. Photos of the strip were captured at six different servo motor settings, which were then uploaded to a computer to measure the angle of the strip with respect to zero pitch condition using an on-screen protractor. The procedure was performed 2-3 times to ensure the repeatability of the results and to build confidence in the obtained calibration curve.

To prevent introducing absolute errors in the process of identifying the zero pitch condition, the rotor was spun at the required rotational speed and the pitch was adjusted until the measured thrust approached zero. The photo taken at this pitch condition was considered as zero pitch. During this process of pitch calibration, the problem of 'pitch hysteresis'

due to some mechanical play in the variable pitch assembly was discovered. Servo inputs in a direction opposite to the previous input failed to provide the expected amount of pitch change due to play in variable pitch assembly link joints. This caused significant uncertainty in the actual pitch angle for a given servo position. The workaround for this problem was to return the servo to the zero pitch position before changing to a servo position that was in the opposite direction to the previous position. With this practice, the uncertainty in the collective pitch angle was brought down to ± 0.5 degrees.

High-speed SPIV measurements

The laser sheet was placed in a plane normal to the rotor disc plane, offset from the rotor axis by 32 mm towards the PIV cameras to avoid the shadow of the motor and hub in PIV data images, as shown in Figure 2.5. The two high-speed PIV cameras focused on a region covering half of the rotor, 30 mm above it to capture inflow and 110 mm below it to capture the wake from 2-3 rotor rotations. The two cameras were equally and symmetrically spaced from the plane of interest, on the same side of the plane. As all the experiments were performed on the rotor in hover condition, only one-half of the rotor is captured under the assumption of symmetry to best utilize the available camera resolution.

The high-speed PIV data were captured at the rate of 400 frames per second at the full camera resolution of 4 Mega Pixels. Hence, the instantaneous PIV data frames are 2.5 ms apart. The resultant physical resolution of the images by the cameras was 0.087 mm $\times$ 0.087 mm. The computed vector field after all passes has the resolution of 1.392 mm $\times$ 1.392 mm (16 $\times$ 16 pixels).

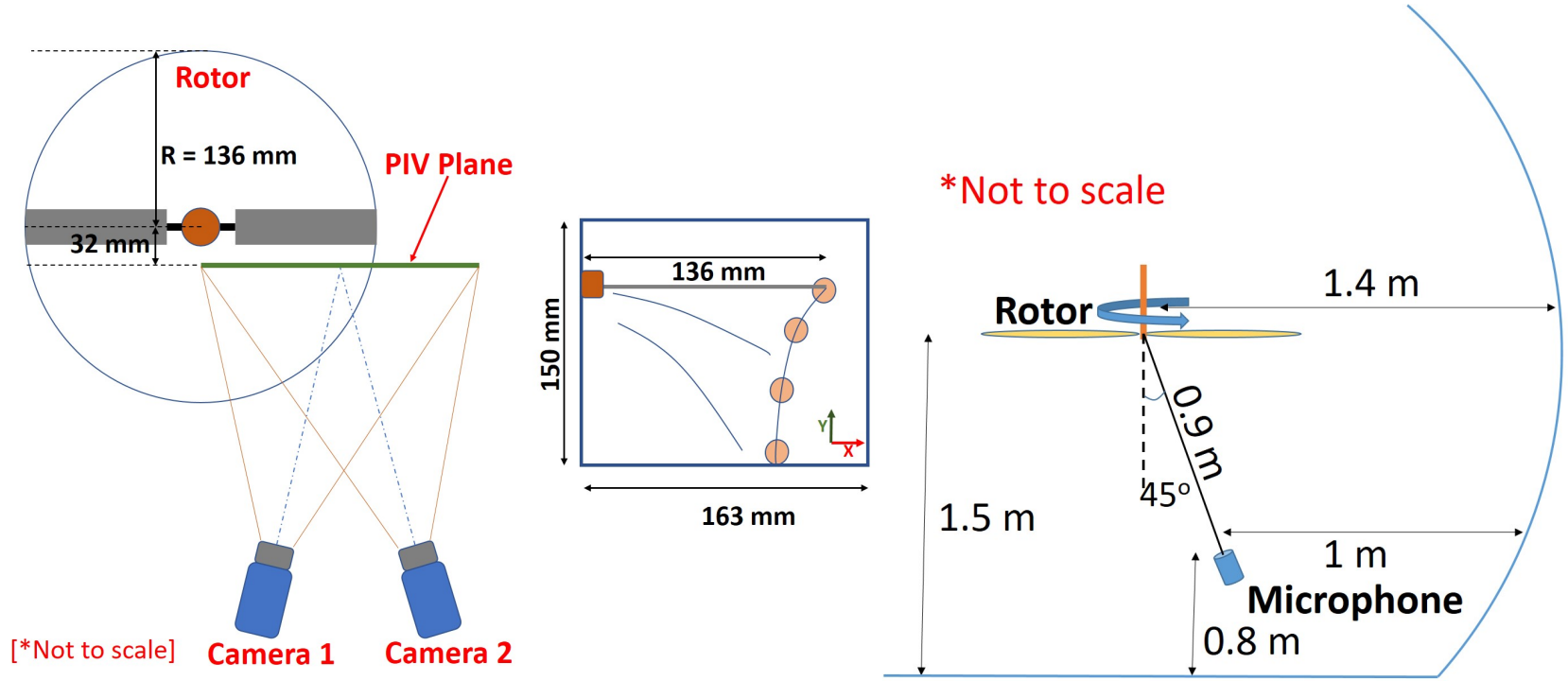

Figure 2.5: (a) PIV measurement location (b) Microphone placement

For PIV measurements, the air was seeded using atomized mineral oil particles of diameter ranging from 5-10 μm. The relaxation time, or the time taken by the seeder particle to follow a step change in air velocity found analytically using Stokes Flow assumptions, is on the order of 0.25 ms. The smallest characteristic time scale in the flow estimated from the vorticity data is on the order of 1-2 ms. Hence, error in the PIV measurements due to seeder particle lag can be neglected. The seeding density was kept uniform by seeding the whole test section well in advance of commencing the PIV tests. No pockets of unseeded or overseeded regions were found in the raw camera images. Each interrogation window of 32 $\times$ 32 pixels covered about 10 to 15 seeder particles everywhere in the PIV plane.

Uncertainty in the velocity vector computation was found using the DaVis software which computes positional disparity of image of seeder particles in two interrogation windows which have been mapped back onto each other [96]. Uncertainties in the instantaneous in-plane velocity components in the area of interest are within 5% of the mean velocity values.

Acoustic measurements

The microphone was placed 0.9 m from the rotor center at an angle of 45° from the rotor axis. This position was chosen to capture the rotor noise perceived on the ground without getting into the rotor wake or coming close to the wind tunnel walls. The motivation of acoustic measurements is to observe basic differences in sound signature and relate those to flow visualization data. A complete characterization of rotor noise would require measurements using multiple microphones at various locations in an anechoic chamber, which is out of the current scope. Figure 2.5(b) depicts the placement of the microphone with respect to the rotor. The 15 seconds data for each case was split into 7 two-second bins. Each of these sub-samples of data was processed separately through fast Fourier transform,

compared for consistency, and then averaged at each frequency. Figure 2.5 supplements the description of PIV and acoustic measurement locations.

Thrust and torque measurements

The 1 kgf load cell for thrust measurements (described in 1.5.3) was installed at the base of the rod hanging from the wind tunnel ceiling, away from the rotor to avoid aerodynamic interactions due to it. For the torque measurements, the BLDC motor + servo blade pitch assembly was mounted to the rod through a frictionless bearing. The rotation about the bearing was restricted by the 0.1 kgf load cell (1.5.3) placed slightly away from the motor axis. This way, all the counter torque necessary to keep the motor mount itself from rotating due to aerodynamic torque on the rotor was provided through the 0.1 kgf load cell, indirectly measuring the aerodynamic torque on the rotor. The torques due to frictional losses in the motor and the variable pitch assembly are internal to the mount and hence they get omitted automatically, saving the efforts of characterizing and subtracting them from the obtained readings.

The small size of the setup, and hence small magnitudes of rotor torques, made torque sensing a challenging task. Even the slightest difference point of load application, or friction in bearings caused a shift in the zero bias of magnitudes as large as 50-100% of the measurements, causing repeatability problems and huge uncertainties in torque readings. Rigidly fixing the load cell onto the test frame used to saturate the load cell output as slight manufacturing imperfections caused overstraining of the delicate load cell. It took many redesigns before the problem could be solved satisfactorily.

Both the load cells were provided with a regulated power supply from a signal conditioner. The signals from them were filtered and amplified to be read by the DAQ. The thrust and the torque data were collected at the rate of 1000 Hz for a span of 60 seconds. The

standard deviation in the thrust and torque measurements for these tests has been found to be within 5% and 3% respectively. The highest standard deviation was observed only at the lowest thrust settings probably because the rotor wake stays near the rotor plane, causing some fluctuations in conditions seen by the rotor. The standard deviation for the other higher thrust cases was closer to 1% and 0.5%. The small deviations from the mean in thrust and torque readings correlated with each other, supporting this reasoning. All high-frequency noise content due to vibrations was filtered using low-pass filters set at 40 Hz. The error due to DAQ resolution is negligible when compared to the standard deviation.

2.3.5 Test Procedure

Following is the test procedure followed for the single rotor experiments. It is assumed that the load cells and the collective pitch are calibrated before these steps.

1. Adjust PIV cameras and laser sheet to be able to capture the region of interest, and calibrate the PIV system using a calibration plate.

2. Bias the load cell readings to zero when the rotor is off.

3. Start the rotor at the intended speed with servo input corresponding to zero pitch and verify that the thrust reading is zero.

4. Increase pitch in small increments, letting the rotor RPM stabilize, until the target thrust/thrust coefficient is obtained. In case the thrust overshoots the desired value, reduce the pitch angle back to zero and start increasing the pitch again to avoid uncertainty due to the play in the pitching assembly.

5. Note the servo input resulting in the desired thrust value and record thrust and torque data over 60 seconds to be able to take a mean over all the small time scale unsteady effects.

6. Switch off the rotor and repeat steps 1 through 5 to verify if the results are consistent.

7. Once the pitch and the loads measurements are verified to be consistent, proceed with the high-speed SPIV measurements, adjusting the parameters such as laser intensity, time difference between frames, etc. ensuring that the software can compute velocity vectors over the whole frame (or at least over the important regions in the frame) using the captured images.

2.4 Results and Discussion

2.4.1 sPIV Measurements

Instantaneous flow field

Figure 2.6 contains the instantaneous vorticity contour plots for 40k and 80k *Re* test cases which are representative of what is found over the whole data set of 200 PIV images for the respective cases. The 60k *Re* cases instantaneous vorticity contour plots resemble those for the other two *Re* cases, and hence are not included in the figure. The plots for the ducted rotor in the figure correspond to the 10 mm tip clearance duct.

The most easily identifiable features in the majority of the cases are the tip vortices having strong positive vorticity, and trailing edge vortex sheet consisting of streaks of discontinuous negative vorticity regions. These are more readily visible in the un-ducted rotor cases. The thick vortex sheet seen in these cases was previously observed by Ramasamy et. al. [104, 106] using smoke flow visualization. Among the un-ducted cases, the constant thrust cases at 60k and 80k *Re* have the tip vortices and vortex sheets tightly packed spatially because of higher frequency of vortex generation at thrust (and hence mean downwash) similar to the 40k *Re* case.

Comparing the ducted and un-ducted rotor cases, one of the biggest differences in the

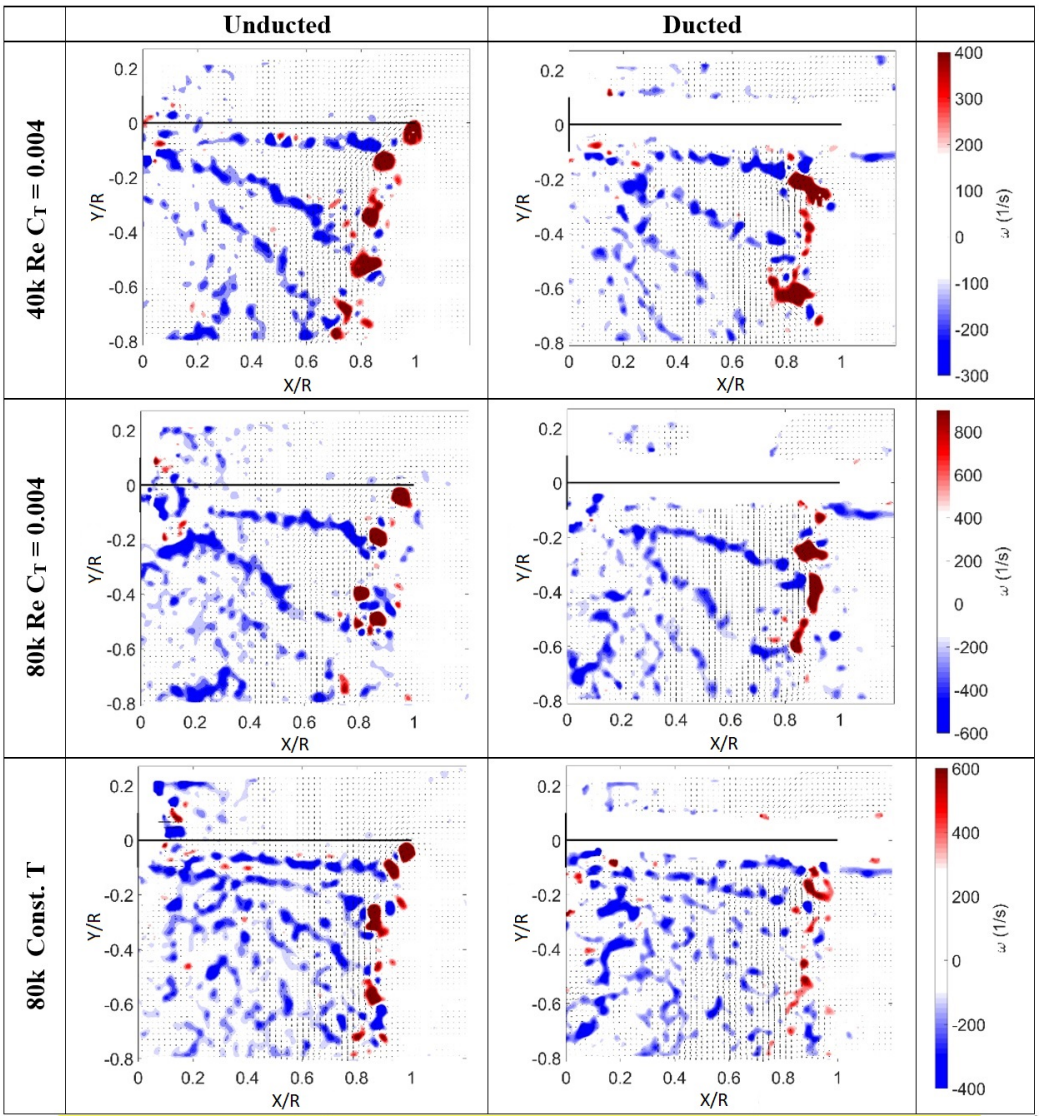

Figure 2.6: Instantaneous vorticity contour plots for 40k *Re* and 80k *Re* test cases

flow field is the shape and integrity of tip vortices. For all the ducted rotor cases, the tip vortices are seen splitting apart and merging chaotically in the wake within $180°$ wake age, whereas the trailing edge vortex sheets maintain their form. On the other hand, the un-ducted rotor tip vortices retain their identity for at least $540°$ wake age for constant C_T test cases. Among the un-ducted rotor instantaneous vorticity plots, the 80k *Re* constant C_T case is unique. The vortices of wake age $540°$ roll up with wake age $360°$ vortex and merge with it. This happens for all consecutive pairs of $540°$ and $360°$ vortices over the whole data set. Figure 2.7 is a representative figure for the observation in Figure 2.6 displaying

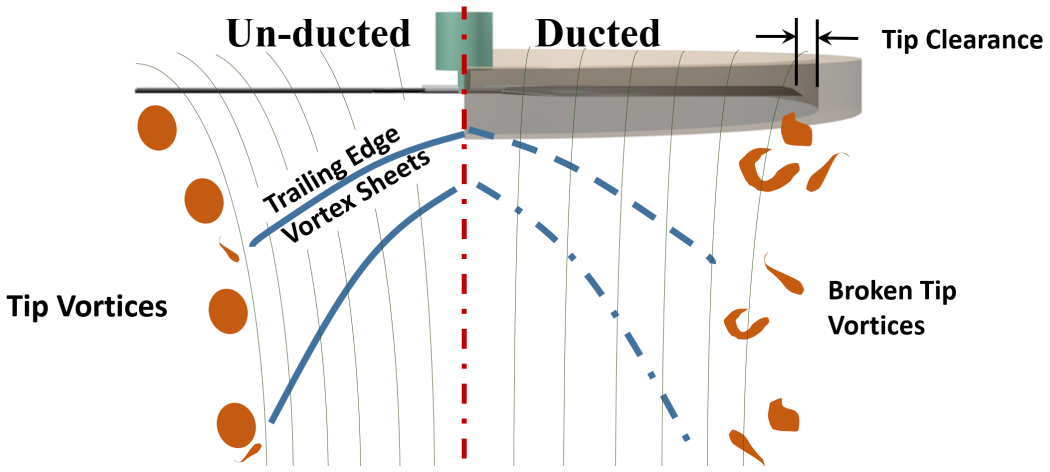

Figure 2.7: Interpretation of instantaneous flow field data

differences in the ducted and un-ducted rotor wakes.

Figure 2.8 contains plots of vortex trajectories of a few consecutive vortices for the un-ducted rotor cases along with the empirical curve fit for high *Re* rotor tip vortices by Landgrebe [110] and Kocurek [111] as the dotted red and black curves, respectively, for a comparison. The vortex centers were identified using the algorithm described by Graftieaux, L. [112]. The algorithm involves defining functions Γ_1 and Γ_2 which characterize the locations of the center and boundary of a large scale vortex by considering the topology of the velocity field. In equations 2.1 and 2.2, P is a fixed point in the measurement domain, S is the area surrounding P, M is a point in S. The functions effectively find the mean angle between position vectors of points neighboring P with respect to P and the velocity vectors of the points in inertial and non-inertial frames respectively. $\Gamma(P) = 1$ corresponds to the case when the flow goes around the point P in perfect circles. Equations 2.1 and 2.2 are the discretized forms of equations for application on PIV data. The PIV velocity fields were spline interpolated to increase the resolution three-folds before using the algorithm to identify vortex centers.

$$\Gamma_1(P) = \frac{1}{S} \sum_{M \in S} \frac{(PM \wedge U_M) \cdot z}{||PM|| \cdot ||U_M||} = \frac{1}{S} \sum_{M \in S} sin(\theta_M) \tag{2.1}$$

$$\Gamma_2(P) = \frac{1}{S} \sum_{M \in S} \frac{(PM \wedge (U_M - \tilde{U}_P)) \cdot z}{||PM|| \cdot ||U_M - \tilde{U}_P||} \tag{2.2}$$

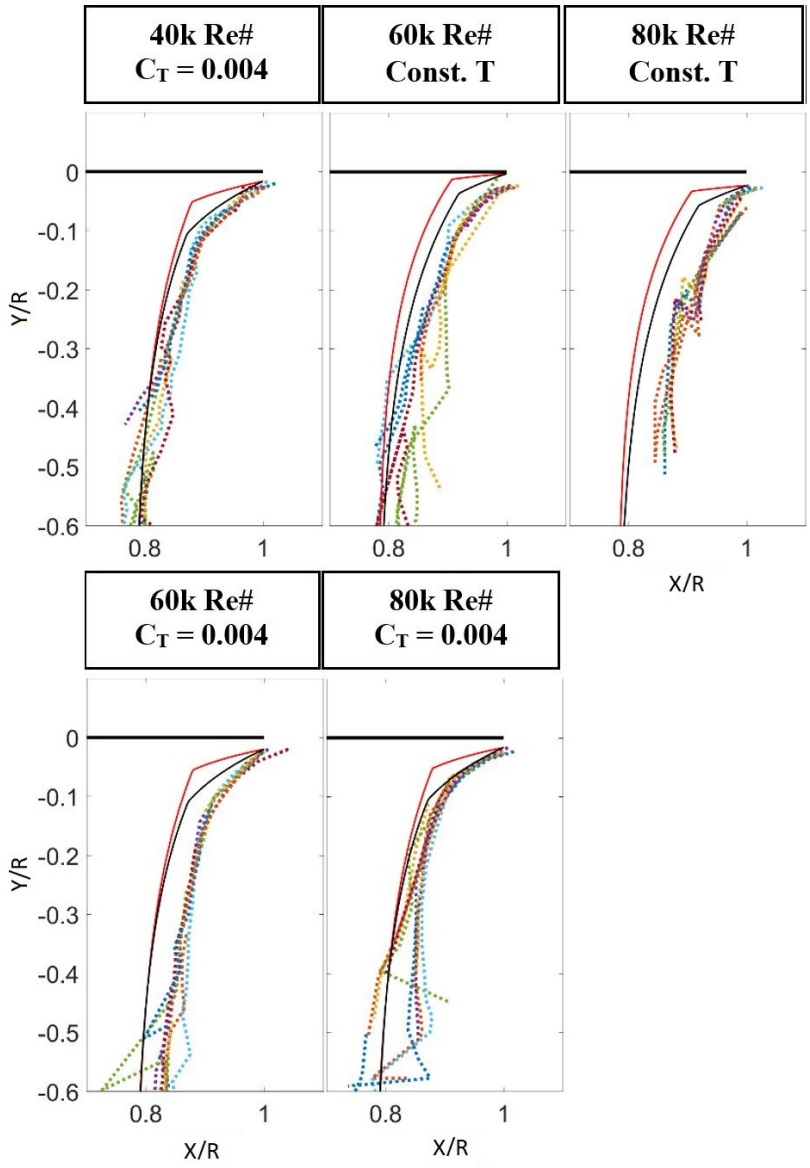

Figure 2.8: Trajectories of five consecutive tip vorticies for each un-ducted rotor case as found from the PIV data. Solid red and black line represent Graftieaux and Kocurek empirical fits for the respective cases

The algorithm is too resource intensive to be used over the whole flow field directly because computing Γ values at each point would require scanning through all other points. Also, the flow fields contain multiple vortices. Therefore, a semi-automatic method was applied wherein the approximate vortex center locations were provided manually based on vorticity contours. The program used these to scan neighboring areas and identify the exact vortex centers. Each vortex was identified uniquely, and its position was observed over the instantaneous frames while coming up with the trajectory plots. Similar vortex trajectory analysis on ducted rotor data is difficult to perform due to frequent vortex splitting and merging induced by interaction with the duct. These affect maintaining correct vortex identity over frames.

Figure 2.8 does capture the roll-up of vortices observed in instantaneous plots for 80k *Re* constant thrust case. The trajectory curves split into two curves below $Y = -0.2R$ representing the roll-up of consecutive vortices for the case. Comparing vortex trajectory plots at $Y > -0.2R$, the 40k *Re* case and the two constant thrust cases have more spread as well as 'roughness' indicating vortex to vortex path deviations and vortex agility respectively. High jitter, especially at low wake ages for low thrust cases, is likely due to lower vortex strength and downwash from the rotor. High downwash velocities help in maintaining the vortex strengths for a longer duration as vortices can feed on shear from a stronger slipstream. Vortices tend to stay along the slipstream for the same reason if the slipstream is strong enough to resist deviations due to external instabilities. Out of the two empirical vortex trajectory curve fits, Kocurek's curve fit is seen to be closer to the recorded vortex trajectories for all the cases. The empirical curve fits contract radially faster than the observed trajectory in the initial 180° of vortex wake age and then straightens downward for all the cases.

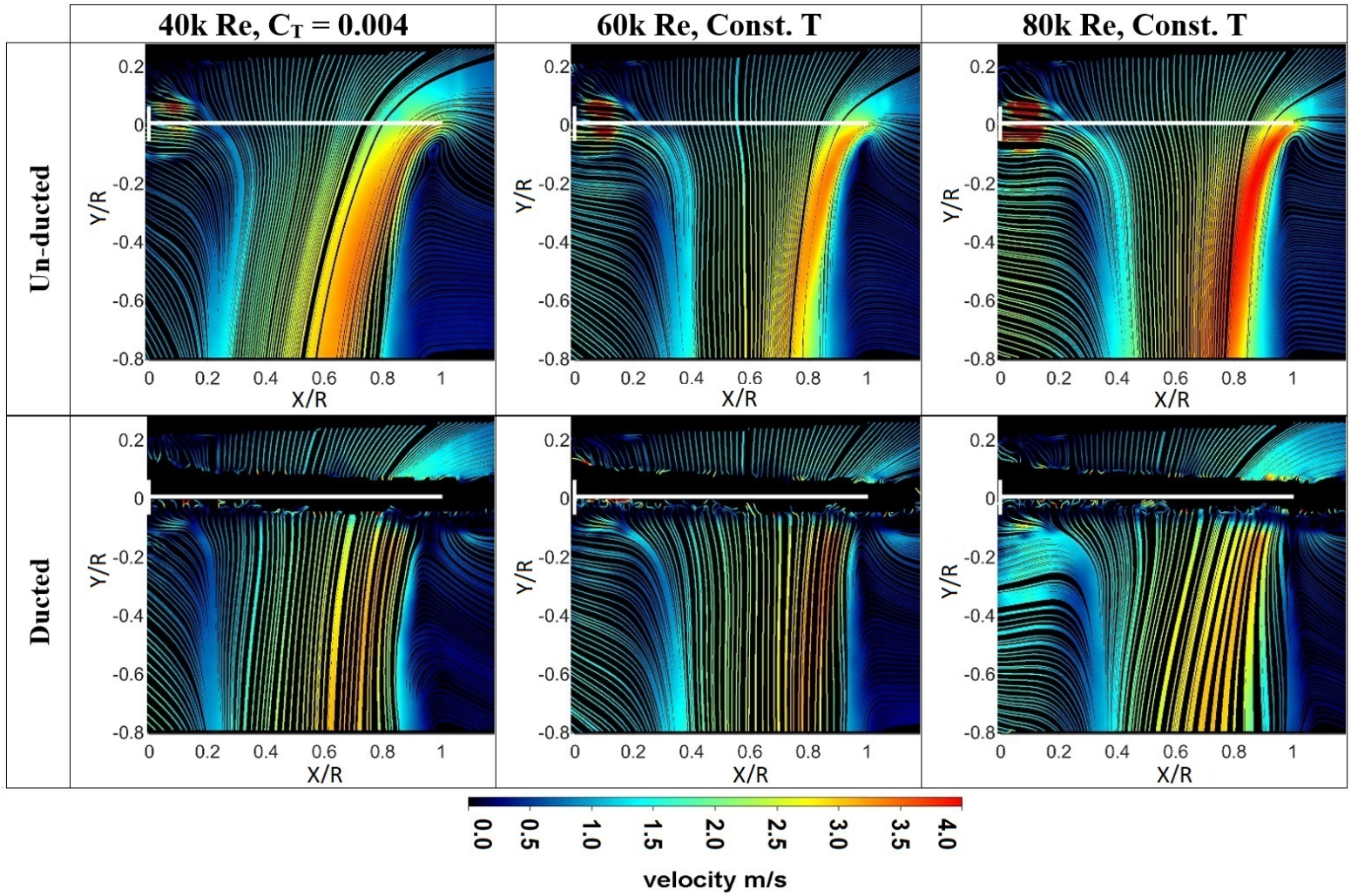
40k Re, C_T = 0.004
60k Re, Const. T
80k Re, Const. T
Un-ducted
Ducted
Y/R
X/R
0.2
0
-0.2
-0.4
-0.6
-0.8
0
0.2
0.4
0.6
0.8
1
0.0
0.5
1.0
1.5
2.0
2.5
3.0
3.5
4.0
velocity m/s

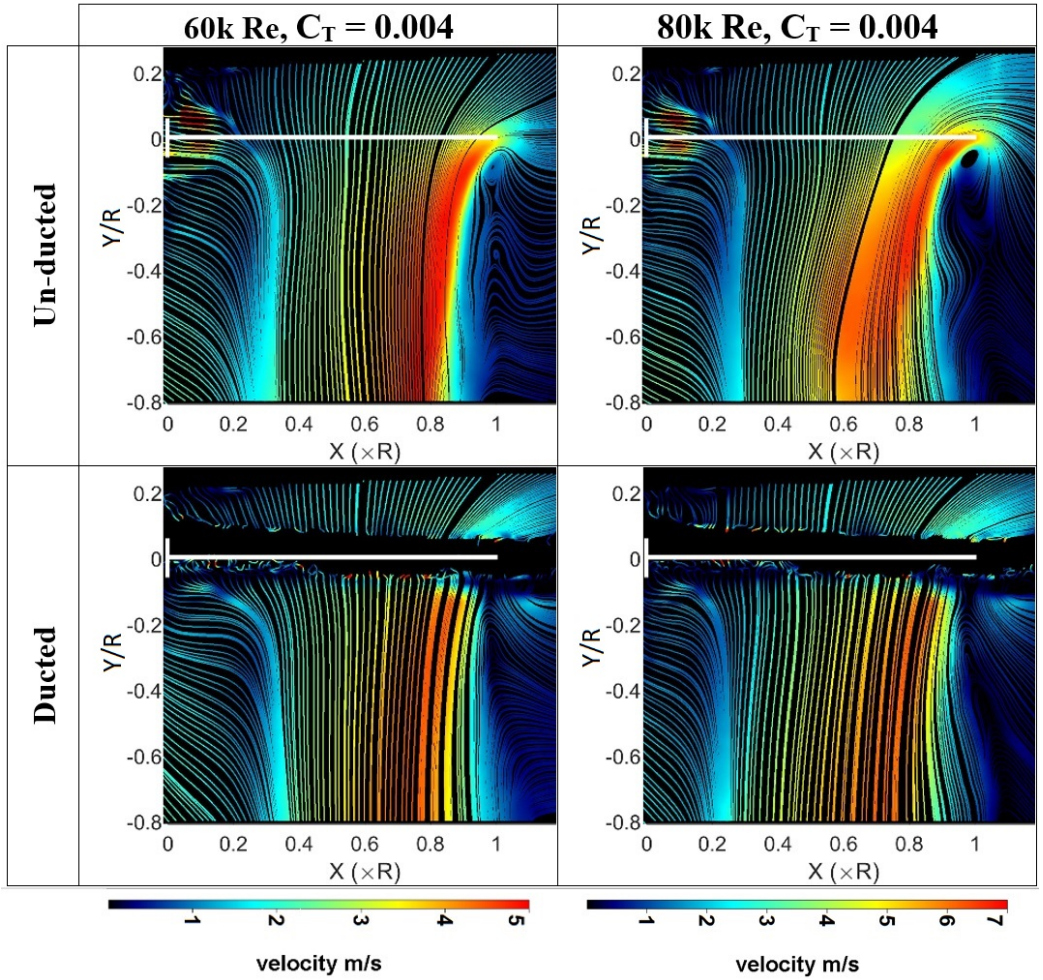

Figure 2.9: Averaged velocity field streamline plots

Mean (time averaged) flow field

Streamline plots of the flow field in Figure 2.9 are averaged over the 200 instantaneous flow field data spanning over 0.5 seconds. The PIV data time duration corresponds to 18 rotations for 40k *Re* cases, 27 rotations for 60k *Re* cases and 36 rotations for 80k *Re* cases. The rotor frequency and PIV frame rate were deliberately kept such that they did not synchronize easily to avoid biasing the mean values towards a narrow set of rotor phases. Therefore, the mean PIV data obtained can be considered to be close to the true mean. The mean velocities for ducted and un-ducted rotor cases are also noticeably different. As seen in Figure 2.9, the flow under a ducted rotor contracts less than an un-ducted rotor wake, making it appear going vertically downward. There is a stronger radially inward velocity component observed for un-ducted rotors. Following the streamline colors, the peak velocity magnitude is higher for the un-ducted rotor.

Figure 2.10 displays mean downward velocity profiles at different planes parallel to the rotor plane. The downward velocity profile corresponding to $H = 0.2R$ can be considered as rotor inflow profile. Rotor inflow data are particularly useful in developing computational models. Downward velocity profiles immediately below the rotor or $H = -0.2R$ can be considered to be the rotor outflow profiles. Differences between the two profiles give information on spanwise thrust generation. Velocity profiles farther down from the rotor, such as at $H = -0.6R$, are important in estimating the rotor downwash or download on UAV support booms, fuselage, payload, etc. below the rotor. From the rotor-box interactions study presented later in the chapter 7, it was found that the performance of the rotor itself improves marginally in the presence of a box blocking significant parts of the wake due to the ground effect like conditions. But the overall performance suffers due to the download losses if the box is part of the vehicle. These provide rotor inflow data for the cases which may be used to develop models tuned specifically for the low-Re regime.

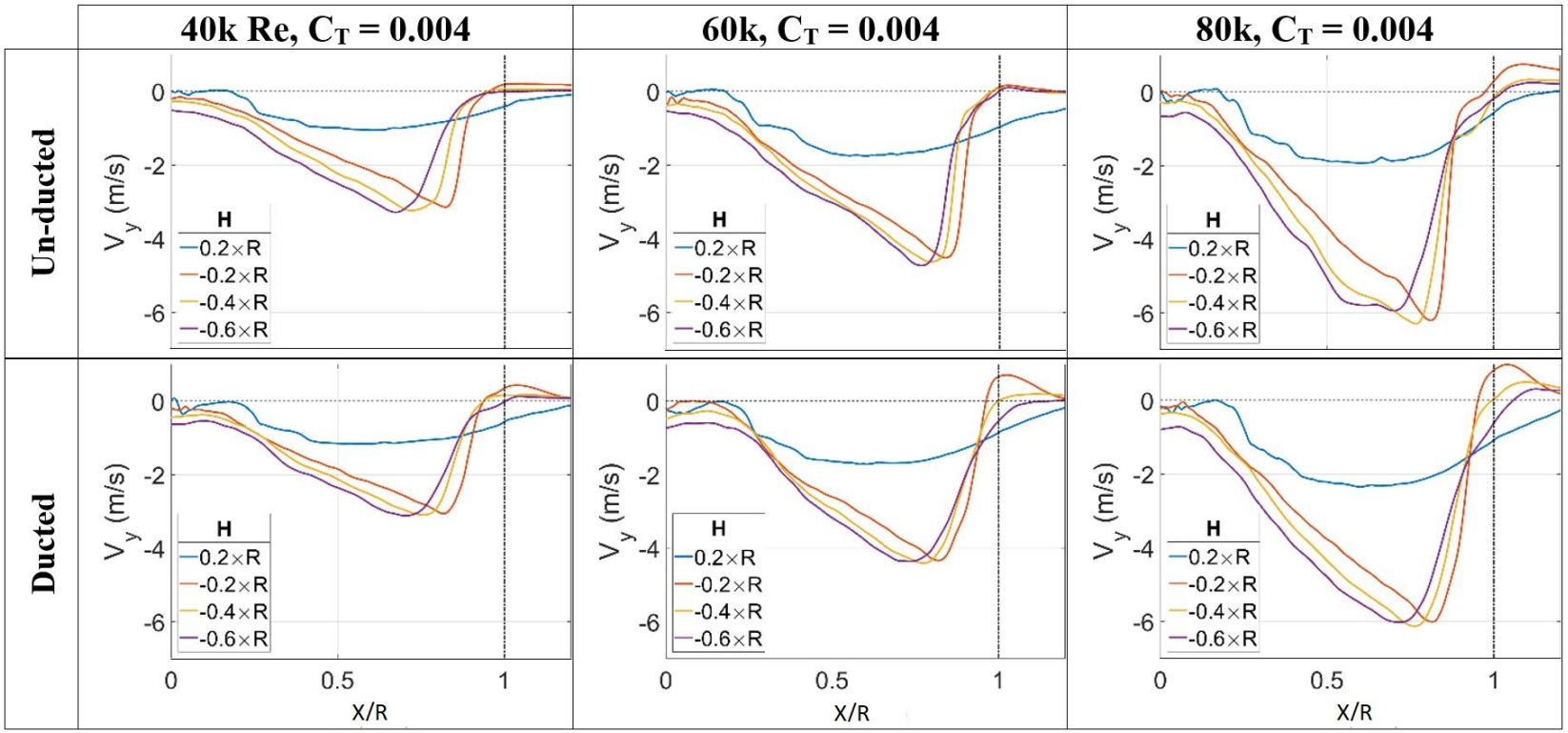

Figure 2.10: Mean downward velocity profiles at planes parallel to the rotor plane. Here 'H' is the vertical distance between the measurement plane and rotor plane.

2.4.2 Thrust and Torque Measurement

Table 2.2 lists load measurement results for all the experiments. The C_T in Table 2.2 are slightly off the target values of 0.004 and 0.006 for some constant C_T cases because of the difficulty in adjusting trim during experiments due to small amplitude instantaneous load signal readout fluctuations and discrete pitch servo settings. However, the FM values are still valid as the slight offset in thrust is followed by torque as well, and FM computation accounts for both. The zero thrust CQ values for 40k, 60k, and 80k *Re* tests are 0.00032, 0.00024, 0.00019 respectively.

Table 2.2: Performance measurement results

Set Condn.	**Re**		C_T	C_Q	**FM**		C_T	C_Q	**FM**		C_T	C_Q	**FM**
C_T = 0.004	40k	**Tip clearance = 5mm**	0.004	0.00061	0.29	**Tip clearance = 10mm**	0.0038	0.00064	0.26	**Un-ducted**	0.0037	0.00071	0.23
	60k		0.004	0.00053	0.34		0.004	0.00056	0.32		0.0041	0.00061	0.31
	80k		0.004	0.00053	0.36		0.0041	0.00053	0.35		0.0041	0.00053	0.35
C_T = 0.006	40k		0.0059	0.00081	0.4		0.0061	0.001	0.33		0.0058	0.00104	0.3
	60k		0.0061	0.00081	0.42		0.006	0.00086	0.38		0.0059	0.00094	0.34
	80k		0.0061	0.00081	0.41		0.0057	0.00081	0.38		0.006	0.00087	0.38
T = 0.27N	60k		0.002	0.00033	0.19		0.0018	0.00033	0.17		0.0019	0.00034	0.17
	80k		0.001	0.00023	0.09		0.0011	0.00024	0.1		0.001	0.00024	0.1

It is noticed that the Figure of Merit (FM) for all cases is much less than that expected for a full-scale helicopter rotor. This is consistent with the findings by Bohorquez [6] who mentioned that small rotors with airfoils and blade geometries similar to those found in full-scale vehicles, like in these experiments, have FM of the order of 0.35. There is a monotonic improvement of rotor performance in terms of FM with an increase in *Re* for ducted as well as the unducted rotor. This is attributed to the viscous profile drag, which does not contribute to lift/thrust, being dominant in low *Re* cases. At higher Re, lift/thrust induced drag takes a larger share of the total rotor torque, bringing the rotor performance closer to the ideal. This argument about thrust induced torque share also applies to the fact that the $C_T = 0.006$ cases have higher FM than $C_T = 0.004$ cases for all corresponding *Re*

and duct conditions.

The ducted rotor performance is consistently seen to be better than that of un-ducted rotor counterparts for all Reynolds numbers. Better FM observed for the ducted rotors correlates with the fact that instantaneous wake structures for ducted rotor cases are significantly different from un-ducted rotors cases. The tip vortices seem to interact with the duct and get destabilized or divided into small pockets of high vorticity immediately after being shed from the rotor tip. This is likely to influence the induced velocity near the blade tip, affecting the induced losses in the form of tip loss. The performance is found to be even better for the smaller tip clearance as the duct is expected to block a bigger fraction of tip vortex core, preventing air near the tip to go over the blade and causing tip losses. However, selecting a duct with small tip clearance from the performance perspective may not be practical for some UAVs where the duct may deform and collide with the rotor blades. Use of small tip clearance duct would require sturdier duct material which may increase duct weight or UAV cost. The performance improvement due to duct is more for $C_T = 0.006$ cases compared to $C_T = 0.004$ cases. This is because the higher C_T cases face higher induced losses, which are limited by the use of a duct.

2.4.3 Acoustic Measurement

Figure 2.11 contains plots of SPL comparing ducted vs un-ducted rotors. The frequency axis is normalized by the respective rotor frequencies to observe the harmonics better. The Table 2.3(a) contains OASPL for the cases integrated over a frequency range of 5 Hz to 15000 Hz. It also contains clear tone quasi-OASPL where the energies in the first 14 rotor frequency harmonics are summed to compare tonal content between ducted and unducted cases. Table 2.3(b) contains OASPL values for non-aerodynamic noise sources such as ambient and motor.

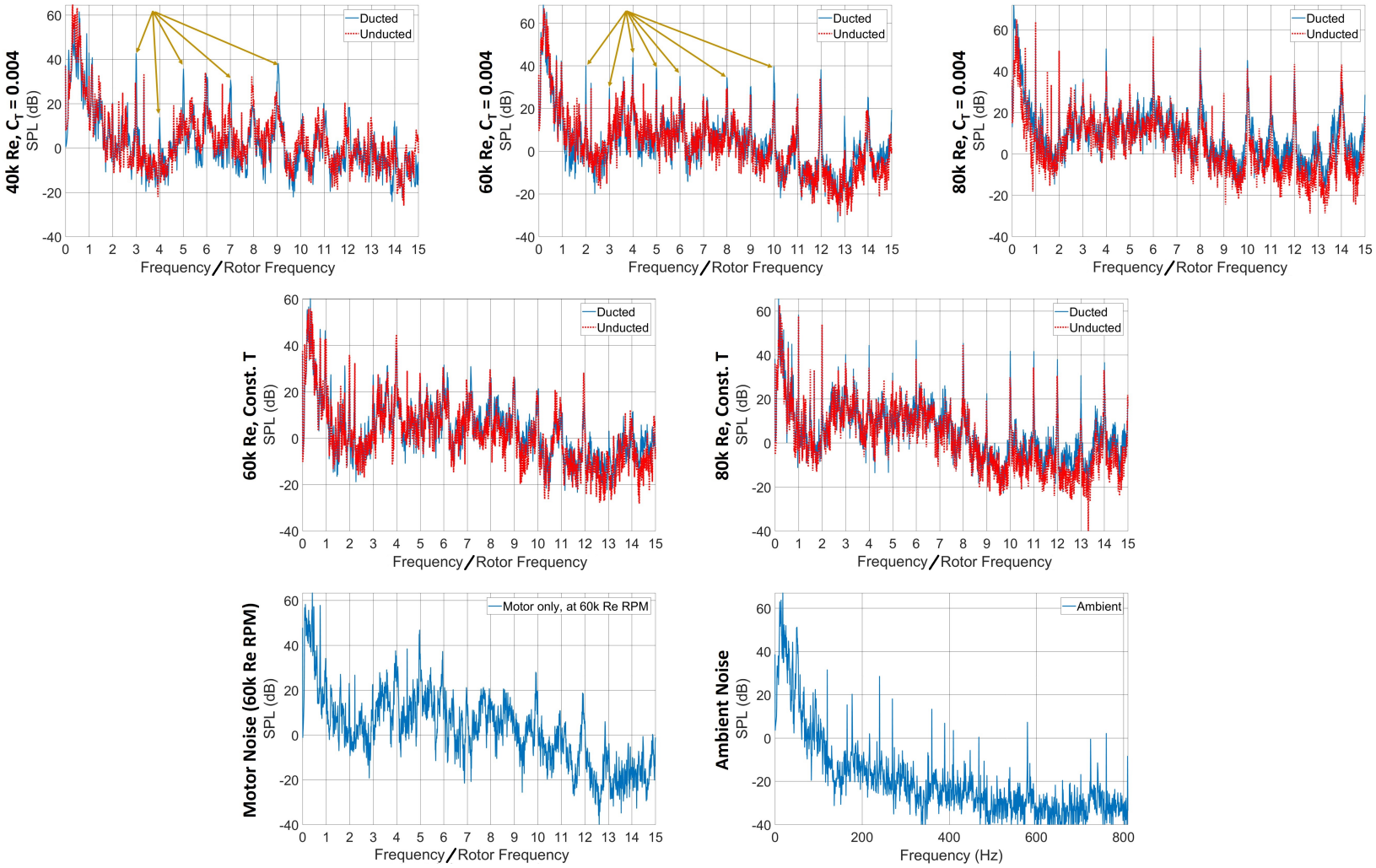

Figure 2.11: Acoustic field spectrum plots for the single ducted and unducted rotor cases

Table 2.3: Overall Sound Pressure Level (OASPL) data for all ducted and un-ducted rotor cases

(a)	OASPL (dB)			Quasi-OASPL (dB)		
Case	**Ducted**	**Unducted**	**Difference**	**Ducted**	**Unducted**	**Difference**
40k Re, C_T = 0.004	85.2	85.2	0	35.8	32.1	3.7
60k Re, C_T= 0.004	92.9	91.9	1	39.8	36.3	3.6
80k Re, C_T= 0.004	98.5	95.9	2.6	43.8	43.2	0.5
60k Re, Const. T	91.9	91.8	0.1	36	36.3	-0.3
80k Re, Const. T	96.2	96.6	-0.4	41.1	40	1

(b)	Case	OASPL (dB)	Quasi-OASPL (dB)
Motor Noise	40k *Re*	82.9	31.2
	60k *Re*	88	31.4
	80k *Re*	93.3	29.8
	Ambient	66.9	-

The Overall Sound Pressure Level (OASPL) for the ducted and un-ducted rotor cases increases with *Re* (or rotor speed) as expected. The OASPL values for the ducted rotor are only marginally higher than those for the un-ducted rotor indicating that the duct is not affecting the overall noise perceived at 45 degrees from the rotor axis significantly. Constant C_T and constant thrust OASPL values for the 60k and 80k *Re* tests are also close to each other and do not have any noticeable trend. This implies that the speed dependent noise dominates over rotor load dependent noise. The ambient and motor noise (with blades removed) spectra and OASPL values reveal that the ambient is responsible for the majority of low-frequency noise, whereas the motor is responsible for majority of high-frequency broadband noise, which increases in magnitude with rotor speed. Apart from the motor, blade thickness noise is also expected to increase with the rotor speed.

Despite OASPL levels being roughly the same for ducted and un-ducted rotors, the sound signature is notably different. In the frequency plots in Figure 2.11, the ducted rotor cases are seen to have relatively higher tonal content at harmonics of the rotor frequency, especially for the 40k and 60k constant C_T test cases. This is easier to notice through

the quasi-OASPL values for the cases in Table 2.3(a) where sound energy in the rotor harmonics is summed. This coincides with the two cases having noticeable performance improvement due to duct compared to the 80K *Re* constant C_T test.

Earlier, it was argued that the positive effect on performance for the two cases was due to vortex cores interacting with the duct, which was probably absent for the 80k *Re* case due to smaller vortex core size. The same argument may hold for this observation. The higher tonal content for the ducted 40k and 60k *Re* cases is very likely due to the tip vortex cores interacting with the duct immediately after generation. The constant thrust ducted 60k *Re* test case does not show higher tonal content like that in the constant C_T case. This is probably because the tip vortices are much weaker in strength and hence the sound signature due to their interaction with the duct is not significant when compared with the existing broadband noise from the motor and the ambient.

2.4.4 Correlating rotor performance with PIV data

The dimension of the core of vortices close to the rotor plane along X (radial direction) would determine if the tip vortex core would interact with the duct if it was present, explaining the observations for the ducted rotor cases. Figure 2.12 features tangential velocity profiles across tip vortices along X for 7 vortices of wake age less than 45° along with the solid black curve denoting the mean profile. Taking the distance between the extrema in the mean profile as vortex core diameter, it is found that the 40k *Re* vortices are about 9.2 mm in diameter whereas 80k *Re* vortices are 7.4 mm in diameter. With the clearance between the rotor tip and the inner duct wall being 10 mm, it is likely that the cores of the tip vortices for the lower *Re* cases collide with the duct due to their larger size. Relatively smaller vortex cores for 80k Re case may limit the duct interaction to only the outer regions of the vortex. This might be the reason for insignificant to non-existing improvement

in performance for 80k *Re* case compared to the other two. Similar improvement in rotor performance due to the duct at lower *Re* was observed by Shukla et. al. [113] for a low *Re* quadrotor setup. The measured vortex core diameter is in the range of 30% to 50% of the blade chord. This is large compared to the 18.2% measured by Heineck [114] for a rotor comparable in geometry at 1.36 million tip *Re* at 0.005 C_T.

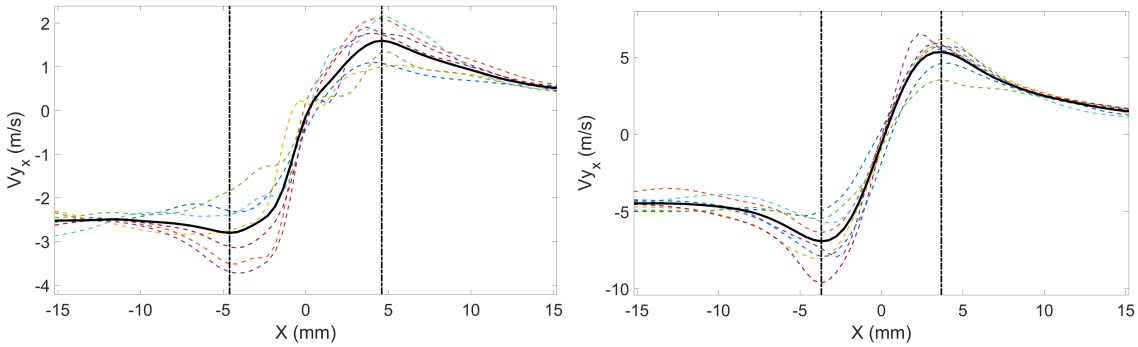

Figure 2.12: Tangential velocity profiles across tip vortices for 7 vortices of wake age less than $45°$ for 40k and 80k *Re* const. C_T cases. Black curve denotes the mean velocity profile and the distance between two black vertical lines denotes vortex size along X axis.

2.4.5 Performance improvement against duct weight penalty

Until now, we observed how having a duct around rotors can be beneficial in terms of rotor performance in a range of operating conditions over and above serving as safety add-on. But before advocating the use of ducts for improving vehicle performance, it is necessary to account for the added weight due to them. To justify adding a duct from a performance perspective only, the weight of the duct must be less than the extra thrust a vehicle can generate at a given power (or torque in hover condition) due to the improvement in efficiency. To get an estimate of the order of magnitude of the extra thrust, we use the 60k Re, $C_T = 0.006$ case. In the expression for FM of a rotor in hover (Equation 5), we keep C_Q as what was obtained for the un-ducted rotor and apply the corresponding FM to find C_T for the ducted and un-ducted rotor cases.

$$FM = \frac{C_T^{3/2}/\sqrt{2}}{C_Q} \tag{2.3}$$

Table 2.4: Thrust benefit calculation outcome for 60k *Re* case at a given power input

	C_Q	**FM**	C_T	**Thrust (N)**
Un-Ducted	0.00094	0.34	0.0059	0.89
Narrow Duct	0.00094	0.42	0.0068	1.03

The extra C_T and thrust due to better FM are 0.00089 and 0.135N respectively from following the calculations in Table 2.4 for the 60k *Re* $C_T = 0.006$ case. It means that if the setup were a flyable vehicle, it could afford to have a duct of not more than 15% of its existing gross weight. This calculation is again very specific to these tests and cannot be applied directly to all rotor designs. Low Reynolds number rotor designs are different from the symmetric airfoil rotor used in this study. The improvement in FM due to duct interaction phenomena observed here is expected to be even more dominant for such rotors as thrust induced torque due to highly cambered airfoils dominate viscous frictional losses, and it is known that vortex duct interaction affects only the induced losses. Hrishikeshavan [109] reported an increase of payload capacity of 20-30 g for his 280-gram vehicle after accounting for the duct weight.

This is encouraging as it allows heavier/sturdier duct structures for the actual UAVs as long as vortex core-duct interaction is ensured. This approach may be more difficult to apply practically for higher Reynolds numbers as vortex core size is smaller and ensuring vortex core-duct interaction would mean smaller clearance between the rotor and the duct, requiring rigid construction to avoid accidental duct scraping by the blades due to vibrations.

The present study is limited to a simple square cross-section duct geometry to keep the focus on understanding low *Re* rotor-duct aerodynamic interaction phenomena. Based on the current observations, it should be possible to come up with a better duct design taking aerodynamic interactions and structural rigidity into consideration.

2.4.6 Low vs High *Re*

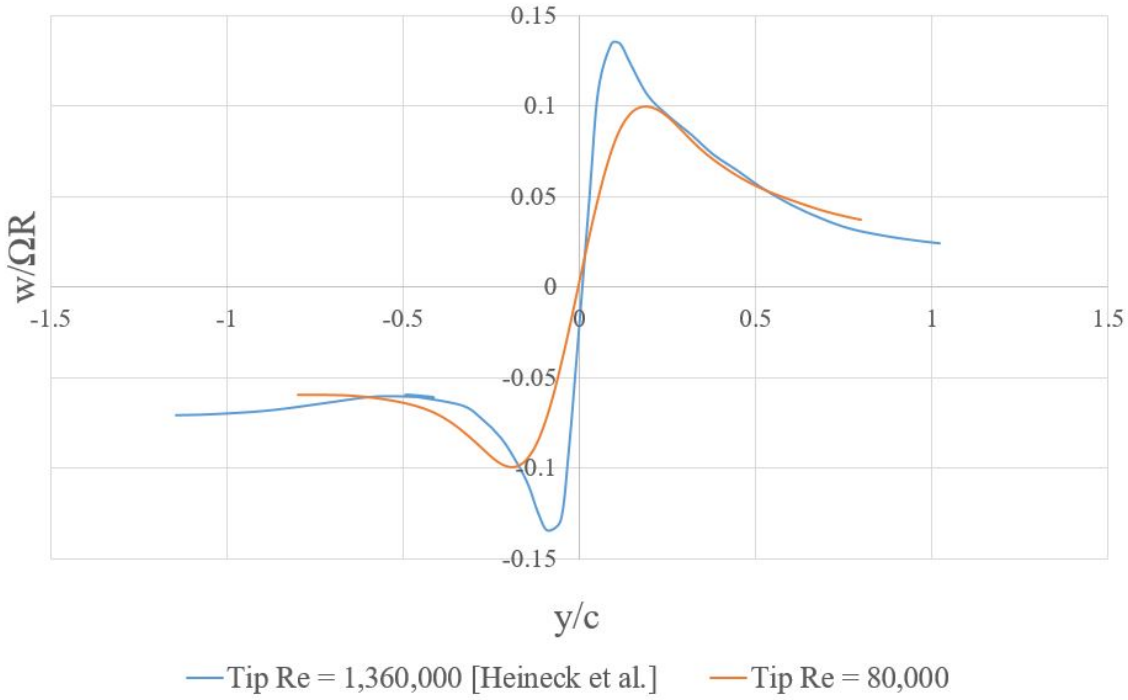

Figure 2.13: Comparing velocity profile of a high *Re* rotor tip vortex by Heineck *et al.* [114] with that observed for the 80k Re case

To address the question about how the low *Re* wake differs from the high *Re* wake, a simple comparison of the non-dimensionalized tangential velocity profiles across a tip vortex is presented in Figure 2.13. In the figure, the high Re velocity profile data are taken from the PIV study by Heineck *et al.* [114] and the low *Re* velocity profile data are from the 80k *Re* unducted rotor case. The high *Re* profile is an average of 486 vortices at wake age of 210° , and the low *Re* profile is an average of 7 vortices at wake age between 10° and 45°.

The data for both the profiles have been scaled and shifted in axes for easier comparison.

It is easy to notice from the plot that the high Re vortex has a smaller core diameter and steeper velocity gradients. The distance between velocity extrema (indicative of the core diameter) for the high and the low *Re* profile plots are 0.181c and 0.388c respectively, where 'c' is the chord length.

2.5 Conclusions

This study showed that the presence of an annular duct around a low *Re* rotor has a positive effect on the rotor performance even if the duct is not designed for thrust generation. The wake features are affected noticeably by the duct and the change is reflected in the instantaneous as well as mean velocity data. The improvement in FM was found to correlate with the likelihood of tip vortex cores interacting with the duct. Further, among the cases where vortex cores interact with the duct, the efficiency change is higher for the cases where thrust induced losses take a larger share of the overall aerodynamic losses. No significant effect of the duct on the overall sound pressure level was observed. However, the cases with a higher possibility of strong vortex core and duct interactions had higher tonal content.

Practical issues such as optical access to the region between rotor tip and duct as well as PIV calibration in such areas make it difficult to observe the tip vortices right when they are interacting with the duct. Seeing that duct interactions can have positive implications on a UAV performance, finding a way around the problem may be of interest and a part of future work. Independent load measurements on the duct can be useful in understanding performance improvement better, and in determining the required duct rigidity for better duct designs.

Summarizing the findings from this work:

1. The cores of tip vortices are larger and trailing edge vortex sheets are thicker for low *Re* rotor compared to a large scale rotor in non-dimensional terms

2. Tip vortices lose their coherent structure after interacting with an annular duct in the ducted rotor cases.

3. Vortex trajectories are generally smoother and repeatable for higher *Re* cases

4. The Duct reduced the mean flow wake contraction for all cases

5. Ducted rotor performs better than un-ducted rotor in terms of FM. Performance improvements were seen to correlate with the extent of vortex core interaction with the duct and the share of lift-induced torque on the rotor.

6. Overall Sound Pressure Level is about the same for ducted and un-ducted rotors.

7. There was higher tonal content in acoustic measurements for cases with higher vortex core-duct interactions.

CHAPTER 3

COAXIAL ROTOR: FORWARD FLIGHT AND HOVER

The first multirotor arrangement being discussed is a coaxial rotor. Two separate setups were made and tested in the effort. The first one was for a preliminary study of coaxial rotors in high advance ratio edgewise flight. This configuration is similar to high-speed compound full-scale helicopters such as Sikorsky S-69 (XH-59), X2, S-97, but at low Reynolds number. The primary motivation for performing experiments on this arrangement was to observe the interaction of the tip vortices due to counter-rotating rotors in the wake. Tip vortices generated by rotor blades at 90° and 270° azimuths due to the two rotors have the same sense of rotation but opposite axial velocity as depicted in Figure 3.1. It was to be seen if the vortices possessing opposite axial velocity 'burst' (sudden increase in core diameter) on interaction with each other in the wake, especially in the low Reynolds number regime where the vortex core diameter is already large compared to their high Reynolds number counterparts.

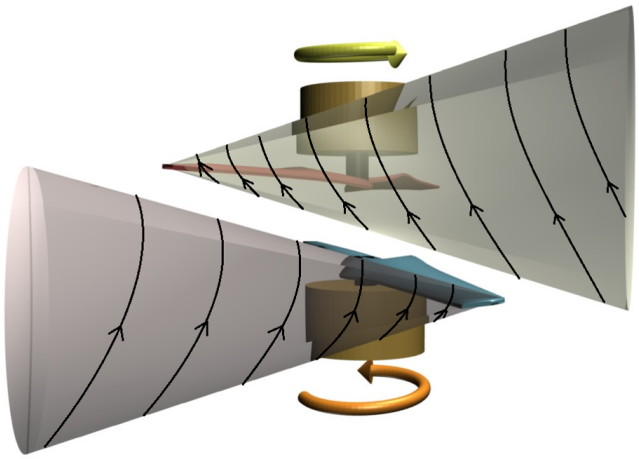

Figure 3.1: Coaxial rotor tip vortex interaction model depiction

The other coaxial rotor setup was developed for a more detailed study, featuring independent thrust and torque measurement, accurate speed control, and collective pitch control capabilities. In this work on low *Re* coaxial rotor covered in [113], some interesting results such as higher than expected FM of the upper rotor and alternating lower rotor tip vortex trajectories are reported. While doing performance measurements on high *Re* rotors at varying vertical separations, Ramasamy *et al.*[115] mention the possible role of swirl recovery in improving coaxial rotor performance, stating that there are no known direct or indirect measurements to validate the hypothesis. Later, Brazinskas *et al.*. [94] report 4% improvement in coaxial rotor efficiency due to swirl, which was estimated by comparing the performance of a counter-rotating coaxial rotor with that of a co-rotating coaxial rotor. However, there is no mention of the effect of swirl on upper rotor performance in either of these high *Re* coaxial rotor studies. On the coaxial rotor flow visualization side, Ma *et al.*[116] studied vortex models, vortex size and trajectories for a high *Re* rotor setup in a water tunnel but without performance measurements.

The current work aims to address the gap in understanding the physics behind the upper rotor in a low *Re* coaxial rotor system performing better than a single isolated rotor (as first observed in [113]), and discovering flow features in low *Re* coaxial rotor wake for use in computational model building and vehicle design. Performance and high-speed stereo PIV measurements were made on a coaxial rotor setup at two vertical separations at three *Re*. The chapter contains performance data on individual rotors of the coaxial system and instantaneous as well as mean high-speed SPIV results. The time-resolved SPIV data and vortex traces help visualize the evolution of the wake and interactions of various prominent flow features. A qualitative vortex - vortex sheet interaction model based on careful observation of hundreds of instantaneous velocity fields from all test cases is also presented here. The model explains the dynamics of these coherent structures in the wake. Rotor inflow, rotor outflow, and swirl velocity computations for all test cases are useful in

understanding coaxial rotor performance from a momentum perspective. Comparison with the performance of high *Re* rotors shows higher profile and induced drag at low *Re* for the same thrust coefficient.

This chapter is divided into two parts. The first part focuses on the preliminary Edgewise flight experiments, and the later part on the detailed hover experiments using the two different setups.

3.1 Previous Forward Flight Coaxial Rotor Studies

Coaxial rotors have been studied extensively since the mid 20th century, with the focus on the performance of full-scale coaxial rotors in hover and low speed forward flight. Some of that work has been cited in subsection 1.3.4.

Yimin Ma *et al.* from Beihang University [116] and Yan-min et at. from Beijing University of Aeronautics and Astronautics [117, 118, 119, 120] performed PIV experiments to observe the flow field around coaxial and single rotor in hover and forward flight in water tunnels to emulate high Reynolds number conditions. J.M. Moschetta *et al.* from ISAE-SupAero conducted hover and forward flight experiments and CFD studies on a short shrouded UAV [121, 122, 123]. A similar study on performance and a CFD study on a long shrouded UAV coaxial rotor were very recently performed by Han Han *et al.* [124]. A detailed aeromechanics study has been performed on high-speed coaxial rotors by Joseph Henry Schmaus in his thesis [125] through simulations and performance measurements on a 2 m diameter coaxial rotor setup. As of now, there are not many PIV studies on low Reynolds number coaxial rotors, especially in high advance ratio Edgewise flight.

3.2 Experimental Setup: Edgewise Flight

3.2.1 Setup description

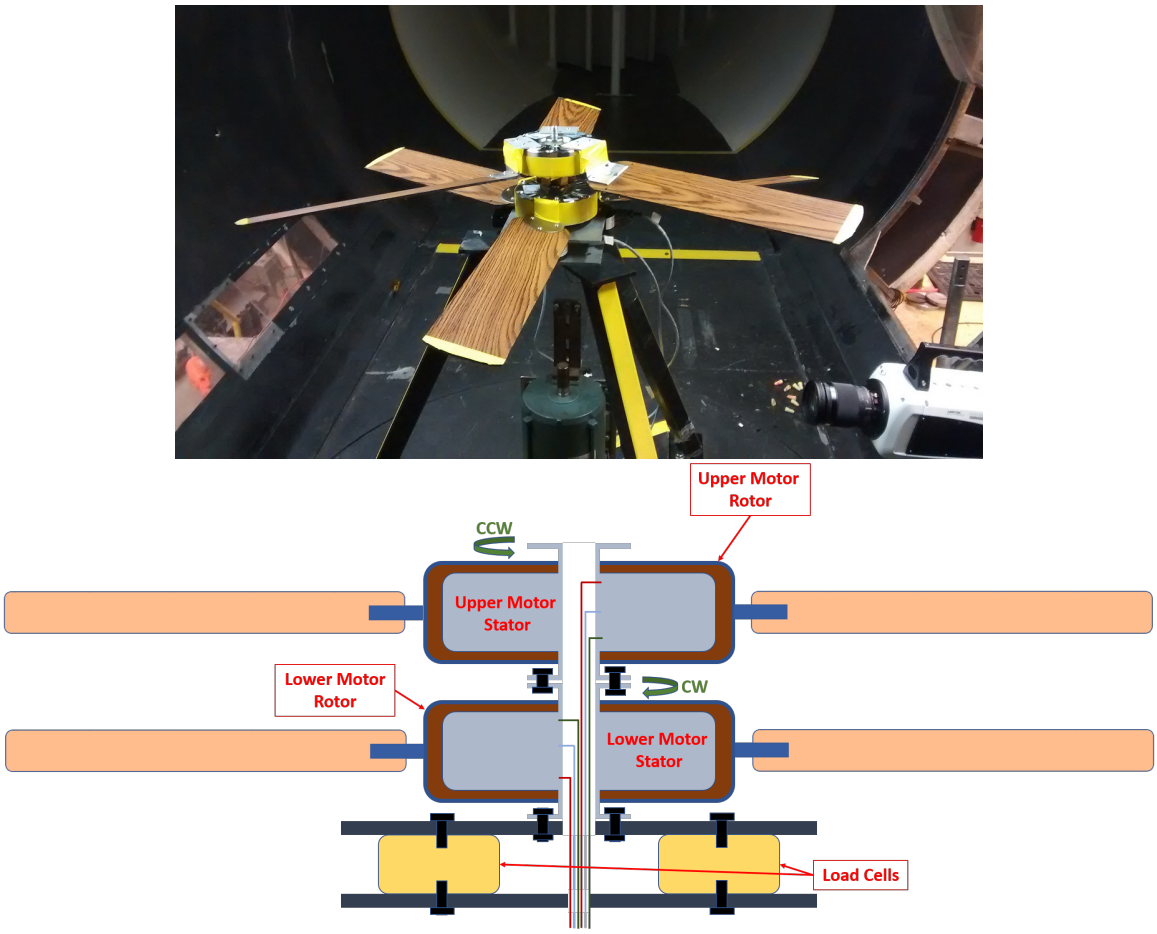

Figure 3.2: Coaxial rotor setup

Figure 3.2 contains a photograph and a schematic of the rotor setup. The coaxial rotor setup was made by attaching two three-bladed rotors one on top of the other. Such an arrangement was realized by using hollow shaft inverted motors for the rotors. Inverted motors, unlike most conventional motors, have a stationary central shaft and rotating outer casing, with the electrical wires attaching to the central stationary shaft. Two such inverted motor shafts were fastened in-line, with electrical wiring for the upper motor (the one away from support) passing through the hollow stationary shaft of the lower motor. The rotor blades were installed on the rotating casing of motors. The upper rotor rotated

counter-clockwise and the lower rotor rotated clockwise. The rotor RPMs and phases are monitored using laser tachometers and controlled using a Variac. This mechanically and electrically decoupled rotor setup allows for independent speed control.

The rotor blades were rectangular, untwisted flat plates with a fixed pitch of 15° and a chord length (c) of 0.12 m. The rotor radius (R) was 0.61 m. The vertical separation between the two rotors (h) was 0.10 m, making the h/D ratio of the coaxial setup 0.08 which is close to that of the Sikorsky S-97 Raider (h/D = 0.07).

3.2.2 Test conditions

The tests were conducted for RPMs ranging from 110 to 170 resulting in tip speed of 7 to 11 m/s and rotor tip *Re* of 57,200 to 87,600. Thrust measurements acquired at μ = 0.19, 0.23, 0.30, 0.46, and 0.64 for the coaxial rotor, and also for both the upper and the lower rotor individually to determine each rotor's contribution and to compare their performance against the coaxial rotor. 2D high speed PIV tests were done at μ = 0.19, 0.23, 0.30. A laser sheet flow visualization was also done for μ = 0.19 case. Table 3.1 gives all the rotor and test parameters for coaxial rotor experiments

3.2.3 Measurements and uncertainty

The coaxial rotor tests involved hi-speed 2D PIV measurements, thrust measurements, and laser flow visualization.

Laser sheet flow visualization

To get the first look of the flow field between the rotors, a laser flow visualization test was done at ψ = 270^0 azimuth as shown in Figure 3.3. A vertical laser sheet, aligned perpendicular to the tunnel axis and near-tip region, was flashed at the rate of 1000 Hz and a

Table 3.1: Coaxial rotor experiments setup specifications and test conditions.

Motor(2)	
Number of Phase	Single Phase
Type	Hollow shaft inverted induction motor
Rated Power	50 W
Rotor(2)	
Radius (R)	0.61 m
# of blades per rotor	3 (Total of 6)
Blade planform	Constant chord, untwisted
Airfoil	Flat Plate
Chord Length (c)	0.12 m
Blade Thickness	0.005 m
Blade edge type	Blunt
Root Cutout	0.09 m
Rotor planes distance	0.10 m
Blade Pitch Angle (α)	15° (fixed)
Hub type	rigid/hingeless
Test Conditions	
RPM range	110 to 170, resulting in rotor tip speeds of 7 to 11 m/s
Rotor tip *Re* Range	57,200 to 87,600
Advance ratios for thrust measurements	0.19, 0.23, 0.30, 0.46, 0.64
Advance ratios for PIV measurements	0.19, 0.23, 0.30

video camera placed three rotor diameters downstream of the rotor recorded at the rate of 60 fps. Since no quantitative measurements were acquired at this stage of the testing, the uncertainty was not quantified.

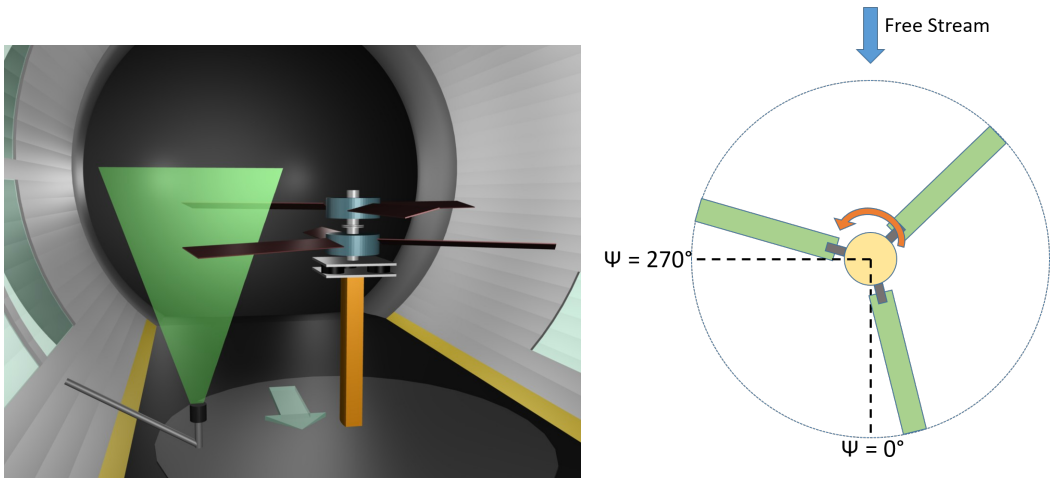

Figure 3.3: Placement of laser sheet for flow visualization and PIV at $\psi = 270°$

Hi-speed PIV measurements

2D high-speed PIV measurements (400 Hz) were done at $\psi = 270^0$ with the aim of capturing the evolution of the swirling motion and its interactions with other rotor blades quantitatively. The laser sheet was placed in a plane normal to the rotor disc planes, at the tip region as shown in Figure 3.3. One hi-speed PIV camera with zoom lens placed about 3 m downstream of the rotors focused on the laser illuminated region. The camera covered a region of 354 mm $\times$ 280 mm. The velocity vector resolution was 2 mm $\times$ 2 mm for all tests.

At $\psi = 270°$, the free stream velocity component is perpendicular to the PIV laser plane, causing the seeder particles to go out of the laser plane before they can be captured in both the frames. Because of this, the instantaneous PIV plots are very patchy, making it difficult to see the frame to frame evolution of the flow. Uncertainty in the instantaneous velocity vector field computed using DaVis is in the range of 0.7 to 1.2 m/s, which is a huge percentage of the computed velocities themselves. Averaging all the 200 instantaneous PIV plots give a much better picture in terms of noise. The uncertainty in the average velocity vector field is within 0.01 m/s for $\mu = 0.19$, $\mu = 0.23$ and within 0.02 m/s for $\mu = 0.30$. Again, higher uncertainty is seen for a higher advance ratio due to the described problem.

The average PIV plots do provide some insights, but the information on wake evolution is lost.

Thrust measurements

The coaxial rotor arrangement is mounted on three DAYTRONIC uniaxial load cells (described in 1.5.3), placed symmetrically about the rotor axis and tunnel axis. All three load cells were provided with a regulated power supply of 12V. The signals from them were filtered and amplified to be read by the DAQ. The thrust data was collected at the rate of 1000 Hz for a span of 60 seconds for each condition. While all the high-frequency noise was filtered using low-pass filters set at 40 Hz, there were oscillations in the collected data about the mean due to variation in thrust as the three-bladed rotors rotate in edgewise free stream.

3.2.4 Test Procedure

Following is the test procedure followed for the high advance ratio coaxial rotor experiments. It is assumed that the load cells are calibrated before these steps.

1. Adjust PIV cameras and laser sheet to be able to capture the region of interest, and calibrate the PIV system using a calibration plate.

2. Bias the load cell readings to zero when the rotor and the wind tunnel are off.

3. Start the wind tunnel and set the desired free stream speed by controlling the RPM of the wind tunnel fan.

4. Start the rotors and adjust the voltage input to them through a Variac until both the rotors are rotating at the same, desired speed. Monitor speed using the laser tachometers.

5. Once the desired rotor speeds and wind tunnel speeds are reached, proceed with the hi-speed PIV measurements, adjusting the parameters such as laser intensity, time difference between frames, etc. ensuring that the software can compute velocity vectors over the whole frame (or at least over the important regions in the frame) using the captured images.

6. Record the thrust data over 60 seconds.

3.3 Results and Discussion: Edgewise Flight

3.3.1 Laser sheet flow visualization

Seeing the captured video frame-by-frame in Figure 3.4, one can observe the seeder particles swirling clockwise (when seen from downstream) just after the passage of a lower rotor blade which is advancing at that azimuth. This swirling motion gets disturbed after the passage of the upper rotor blade, which is retreating at the azimuth. The lower rotor blade, which is in the advancing phase at this azimuthal location is seen to be crossing laser sheet from t = 0 through t = 33.33 ms, causing a clearly visible vortex. This vortex survives until t = 66.67 ms after which the top rotor blade, which is in its retreating phase, disturbs it enough for it to lose its form, bringing the flow back to the initial state seen at t = 0.

3.3.2 2D High-Speed PIV

Figure 3.5 has time-averaged PIV results for $\mu = 0.19$, $\mu = 0.23$ and $\mu = 0.30$ with the position of upper and lower rotors marked using white lines. The average plots are obtained by averaging 200 instantaneous PIV velocity plots spaced by 2.5 ms. The free stream direction is out of the paper

Comparing the time-averaged plots at the three advance ratios, the plot corresponding

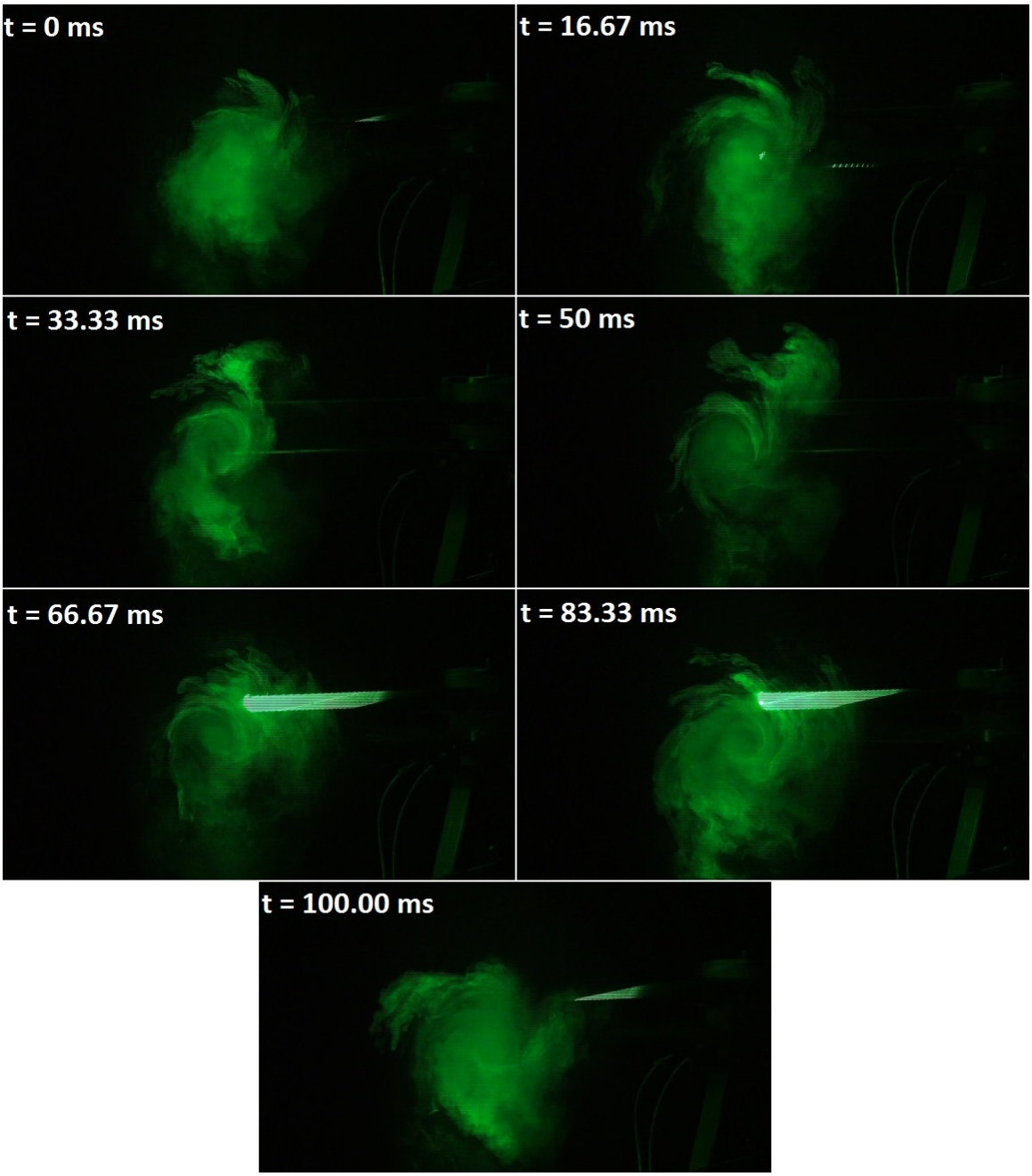

Figure 3.4: Frame-by-frame evolution of a vortex in the coaxial rotor case: ψ = 270^0. Ω = 172 RPM , μ = 0.19

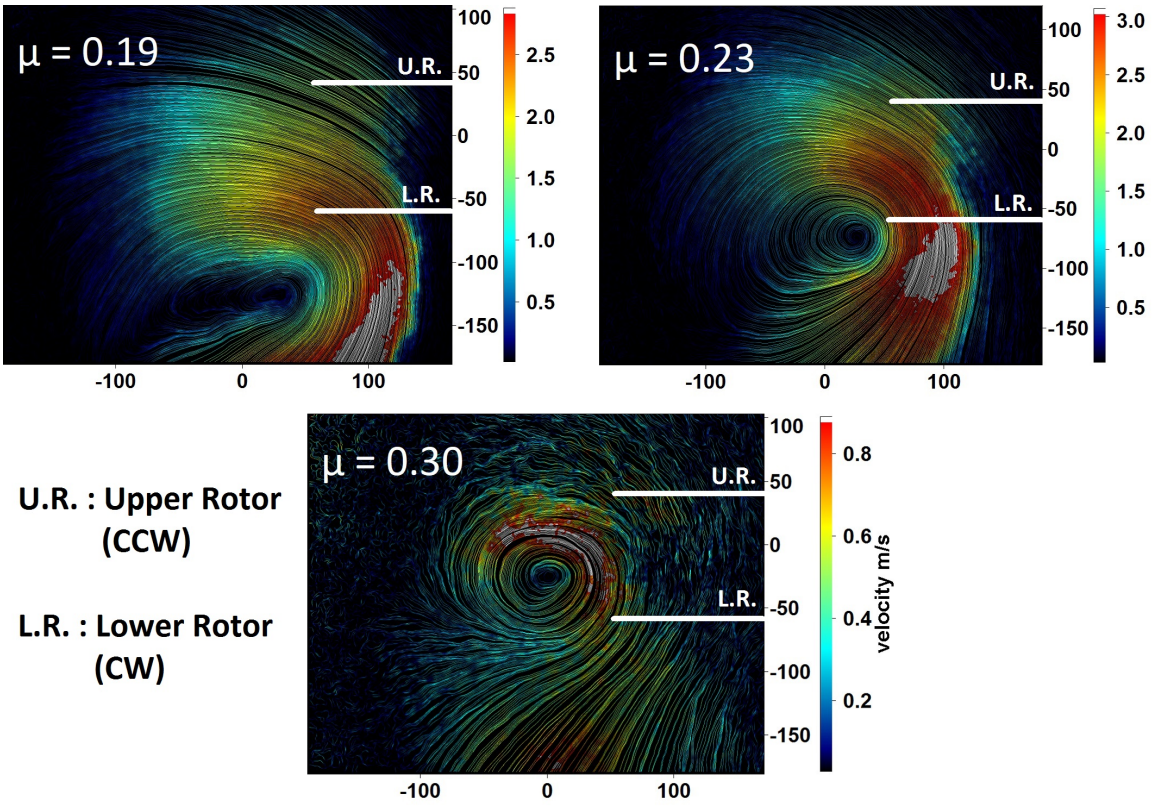

Figure 3.5: Time averaged PIV plot at ψ = 270° AT $\mu = 0.19$, $\mu = 0.23$, $\mu = 0.30$

to the lowest advance ratio appears to have a large, distorted vortex. With an increase in the advance ratio, the vortex becomes smaller in size and rounder. It is reasoned that at the low advance ratios, the tip vortices due to both the upper and the lower rotors are almost equal in strength, but centered at different locations. Hence the resultant average velocity plot appears like a stretched vortex. At higher advance ratios, the advancing rotor generates much stronger tip vortex compared to the retreating rotor because of the higher relative velocity over the advancing side. Due to this, the vortex due to the advancing rotor blade dominates the flow field, causing the resultant average plot to look like that due to a single rotor. The resultant average vortex core shifts up with the increase in advance ratio as downstream convection dominates over rotor downwash.

It is seen from the streamline plots and these velocity profile plots that the tip vortices

generated by the two rotors are indistinguishable from each other and the resultant rotating flow does not have an axis of symmetry. It is reasoned that this is due to the interaction of the core of tip vortices, whose size in this low-Re regime is expected to be on the order of rotor separation.

3.3.3 Thrust measurements

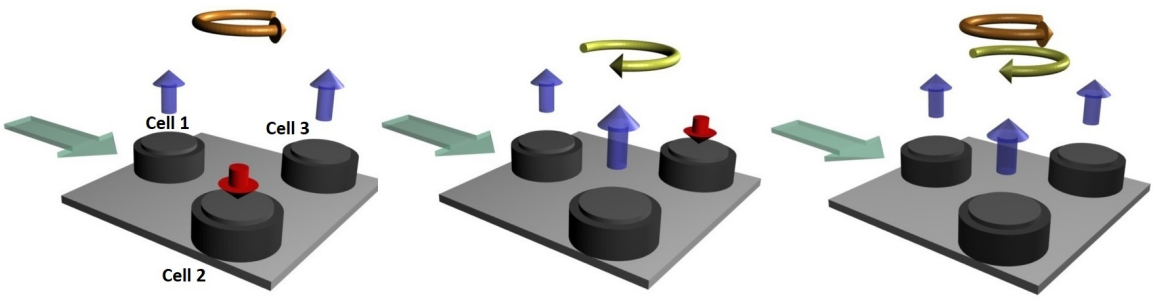

Figure 3.6: Distribution of load among three load cells

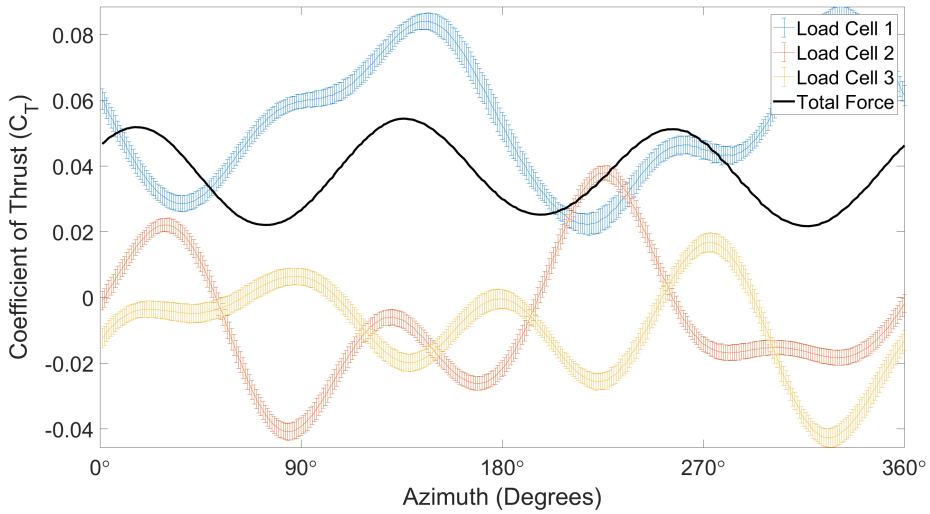

Figure 3.7: Load on each of the three load cells as a function of upper rotor blade azimuth for coaxial rotor at an advance ratio of 0.30

Thrust measurements were acquired at μ = 0.19, 0.23, 0.31, 0.46, and 0.64 for the coaxial rotor and also for both the upper and the lower rotor individually to see each ro-

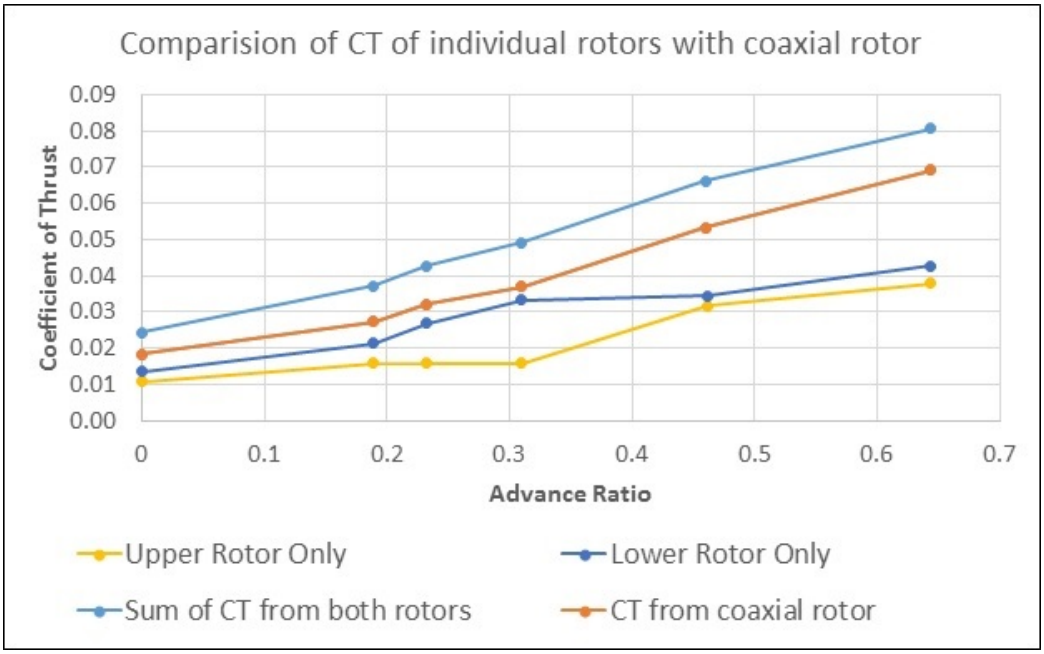

Figure 3.8: C_T vs μ for individual and coaxial rotors

tor's contribution and to compare their performance against the coaxial rotor. Figure 3.6 represents the mean load distribution over the three load cells qualitatively. Figure 3.7 is a representative instantaneous load plot showing how the thrust force varies on each load cell as the rotor rotates a full revolution. The plots contain three peaks as each of the rotors in the setup is three bladed. The error bar signifies cycle-to-cycle variation in loads. The thrust measured by the load cells 2 and 3 is in about equal magnitude range because both the halves (left and right) of the rotor disk have advancing as well as retreating rotor blades. The average thrust coefficient plots are shown in Figure 3.8. It can be noticed that both the individual rotors have almost identical performance except at two intermediate advance ratios, which may be due to some irregularities in the rotors. Comparing C_T of the coaxial rotor with the sum of C_T of the two individual rotors in Figure 3.8, it is seen that both the curves are similar except that the one for the coaxial rotor is shifted down by about 0.01. This is because the lower rotor performs worse in coaxial arrangement due to the downwash from the upper rotor

3.4 Experimental Setup: Hover

3.4.1 Setup description

The coaxial rotor experiments were performed using the modular bi-rotor setup developed for this project. The setup shares some similarities with the setup built by Manikandan Ramasamy[115] in terms of independence of the two rotors, ease of change in configuration, independent rotor RPM and collective pitch control freedom, and independent thrust and torque measurements. The present setup differs in the way the rotors are mounted, installation of torque sensors, dimensions, and range of operation of the rotors

The modular bi-rotor setup described in Figure 3.9(a-c) is very similar to the single rotor setup described in chapter 2 except that this setup has two such independent single rotor rigs, with one of them hung from the wind tunnel ceiling (just as in chapter 2) and the other one mounted on a sliding rail from the wind tunnel floor. The upper rotor (hung from the ceiling) has a telescopic mount, allowing adjustments to the vertical position of the rotor for changing the vertical distance between rotor planes. The sliding rail for the lower rotor allows adjusting the axis shift/rotor overlap between the two rotors.

Both the rotor mounts are equipped with a tilt mechanism at their base, allowing them to be tilted towards the free stream up to 15 degrees in 5 degrees increments for forward flight tests. Almost everything mentioned about the single rotor tests in the sections: Test setup description(2.3) and Measurements and uncertainty(2.3.4) holds true for this bi-rotor setup too as both the rotor modules are exact replicas of the single rotor test stand except for the telescopic and the tilt capability.

Some of the specifications common to this and the single rotor setup are mentioned here again in the Table 3.2 for convenience. Figure 3.10 is pictorial representation of the

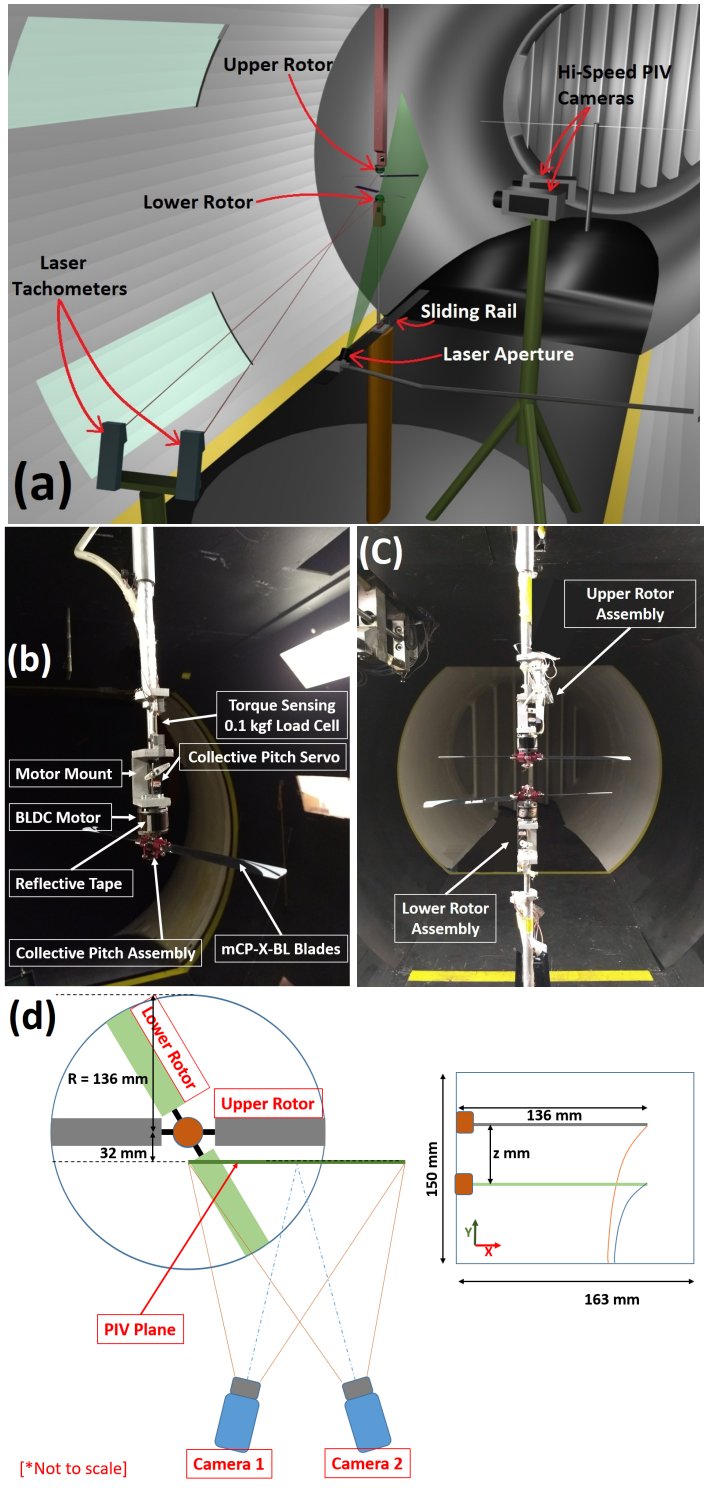

Figure 3.9: (a) Coaxial rotor Setup[113] (b) Individual rotor Construction (c) coaxial rotor setup photo (d) PIV measurement location

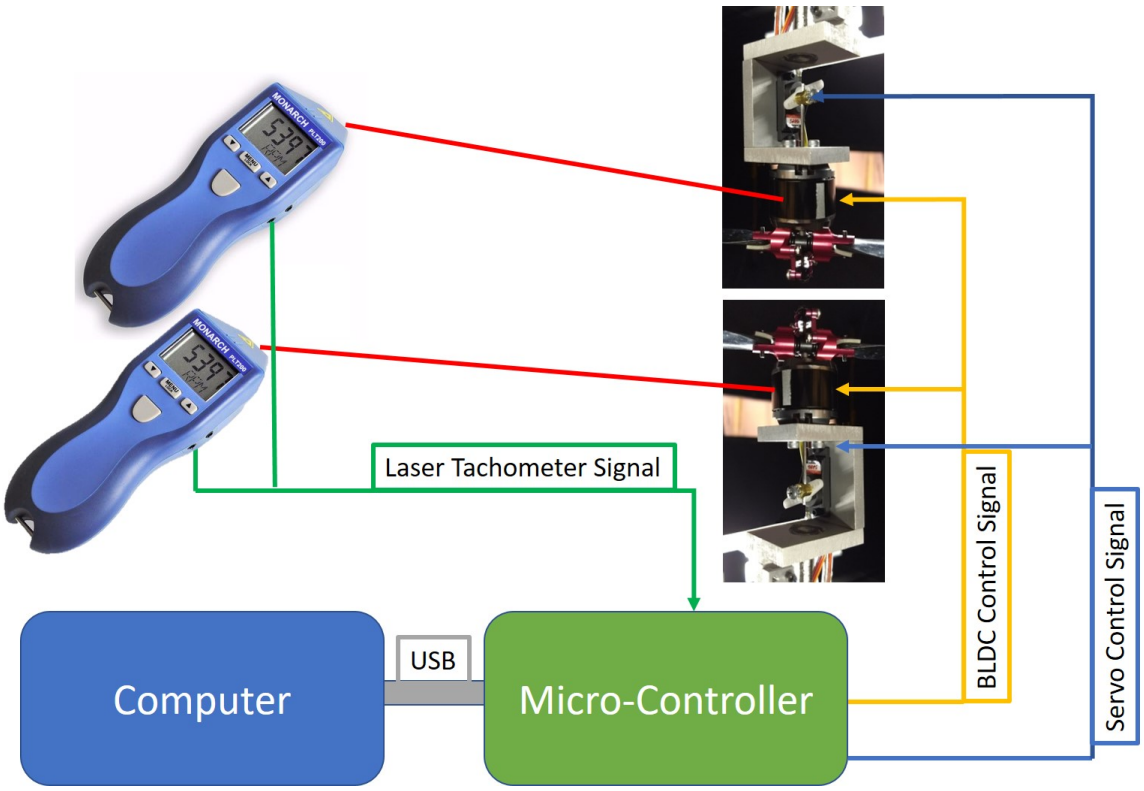

Figure 3.10: Rotor speed and pitch control signal diagram

rotor RPM and pitch control signals.

3.4.2 Test conditions

The coaxial rotor tests were done for three tip Reynolds numbers at two rotor separations. The *Re* was changed by changing rotor RPM, and the rotor separation varied by adjusting the position of the upper rotor. To separate out the effect of rotor loading from the effect due to tip Re, one set of tests was done keeping the C_T constant and the other was done keeping thrust (T) constant while varying Re. The rotor separation of 0.25R and 0.40R was selected based on the range of rotor separations found in commercially available coaxial rotor UAVs such as HAK303, HAK787, Sprite^{TM} [126], WorkFly^{TM} [127] etc. and the minimum achievable rotor separation in the setup. The test matrix for ducted and un-ducted rotor experiments is included in the Table. 3.2.

Table 3.2: Setup and test condition for coaxial rotor experiments

Rotor Specifications	
Number of blades	2
Rotor Radius (R)	136 mm
Root cutout radius	21 mm
Blade planform	untapered, untwisted rectangular blades
Blade chord length	19 mm
Airfoil	NACA 0010
Hub type	rigid/hingeless
Pitch control	collective only
Test Conditions	
Reynolds numbers tested	40k, 60k, 80k
Rotor planes distance	$0.25R$, $0.40R$
C_T for constant C_T tests	0.004 (average per rotor)
T for constant T tests	0.27 N (average per rotor)

The constant C_T experiments were performed at the collective thrust coefficient of 0.008 (i.e an average C_T of 0.004 per rotor) and the constant T experiments were performed at collective thrust value of 0.54 N. The target collective C_T and T along with net torque balance at the RPMs dictated by *Re* were achieved by adjusting collective pitches on the two rotors.

3.4.3 Uncertainty estimates

The modular bi-rotor tests involved hi-speed stereo PIV measurements along with rotor thrust and rotor torque measurements. The hi-speed PIV data were captured at the highest

rate of 400 frames per second at the full camera resolution of 4 megapixels. The resultant physical resolution of the images by the cameras was 0.087 mm x 0.087 mm, as a function of the placement of the cameras w.r.t. PIV plane. For all the PIV, vector computations were done in 4 passes. The first two passes used an interrogation window size of 64 x 64 pixels with 50% overlap, and the next two passes used 32 x 32 pixels with 50% overlap. The computed vector field after the passes has the resolution of 1.375 mm x 1.392 mm, which can be verified to be consistent with the interrogation window size and overlap described above.

The air was seeded using atomized mineral oil particles of diameter ranging from 5-10 μm. The relaxation time, or the time taken by the seeder particle to follow a step change in air velocity found analytically using stokes flow assumptions, is on the order of 0.25 ms. The smallest characteristic time scale in the flow estimated from the vorticity data is on the order of 1-2 ms. Hence, error in the PIV measurements due to seeder particle lag can be neglected. The seeding density was kept uniform by seeding the whole test section well in advance before commencing the PIV tests. No pockets of unseeded or overseeded regions were found in the raw camera images. Each interrogation window of 32 x 32 pixels covered about 9 to 12 seeder particles everywhere in the PIV plane.

The standard deviation in the thrust and torque measurements for these tests has been found to be within 5% and 3% respectively. While all the high-frequency noise was filtered using low-pass filters set at 40 Hz, the collected data still show oscillations about the mean due to vibrations. The uncertainty due to DAQ resolution is negligible when compared to the standard deviation. Uncertainty in the velocity vector computation was estimated using the DaVis software which computes positional disparity of the images of seed particles in two interrogation windows which have been mapped back onto each other[96]. Uncertainties in the instantaneous in-plane velocity components in the area of interest are within 5% of the mean velocity values.

3.4.4 Test procedure

Following are the test procedures followed for hover tests on the modular bi-rotor experiments. It is assumed that the load cells and the collective pitch are calibrated before these steps.

1. Adjust the two rotors to get the desired axis shift and vertical separation.
2. Adjust PIV cameras and laser sheet to be able to capture the region of interest, and calibrate the PIV system using a calibration plate.
3. Bias the load cell readings to zero when the rotors are off.
4. Start the rotors at the intended speed with a servo input corresponding to zero pitch and verify that the thrust readings are zero.
5. Increase the collective pitch of the two rotors in small increments, giving enough time for the rotor RPMs to stabilize back to the set speed. Keep observing the total thrust and difference of torque between the two rotors while increasing the pitch angles. The aim is to reach the target total thrust while keeping the individual torques equal.
6. In case the thrust/torque overshoots the desired value for any of the rotors, reduce the pitch angle back to zero for both the rotors start again.
7. Note the servo inputs for the rotors resulting in the desired thrust and balanced torque, and record thrust and torque data over 60 seconds to be able to take a mean over all the small time scale unsteady effects.
8. Switch off the rotor and repeat the last four steps to verify if the results are consistent.
9. Once the pitch and the loads measurements are verified to be consistent, proceed with the high-speed SPIV measurements, adjusting the parameters such as laser intensity,

time difference between frames, etc. ensuring that the software can compute velocity vectors over the whole frame (or at least over the important regions in the frame) using the captured images.

3.5 Results and Discussions: Hover

The hi-speed PIV was performed on a plane 32 mm offset from the rotor center to avoid motor mount shadows. Only the right half of the rotor setup is covered under the assumption of wake symmetry in hover, to utilize the available camera resolution more optimally. Figure 3.9(d) describes the camera and PIV plane orientation w.r.t the rotors. Hereafter, the test cases corresponding to constant C_T are referred to by their *Re* and vertical separation only without mentioning "Const. C_T". Only the constant T cases are explicitly labeled to show the difference.

3.5.1 Definition and usage of terms

Leishman and Syal [128] derived an expression for Figure of Merit of coaxial rotor system (Eqn. 3.1) which accounts for the unequal thrust due to the two rotors while balancing the torque. Defining Coefficient of Thrust (C_T) and Figure of Merit (FM) for individual rotors in overlapping configurations is difficult. This is because the projected disk area is not simply the sum of the two rotor areas. Also, parts of the lower rotor operating in the wake of the other are effectively in climb condition with highly non-uniform inflow.

In this chapter, the Coefficient of Thrust, Torque, and Figure of Merit for individual rotors in the coaxial arrangement are being defined like the way they are defined for isolated rotors (Eqn. 3.2), ignoring all complexities. This is done only to be consistent with, and be able to compare the results by Ramasamy et al.[115, 129] on high *Re* coaxial and tandem rotor tests. However, it must be understood that $C_{T_L}, C_{T_U}, FM_L, andFM_U$ used in this chapter are not Coefficients of Thrust and Figure of Merit in the true sense.

$$FM_{Coax} = \frac{(T_U^{3/2} + T_L^{3/2})/\sqrt{2\rho A}}{(P_U + P_L)} \tag{3.1}$$

$$FM_U = \frac{T_U^{3/2}/\sqrt{2\rho A}}{P_U}; FM_L = \frac{T_L^{3/2}/\sqrt{2\rho A}}{P_L}; \tag{3.2}$$

$$P_U = Q_U\Omega_U; P_L = Q_L\Omega_L; A = Individual rotor disk area$$

3.5.2 Hover performance measurements

Table 3.3 lists all thrust and torque measurement results in non-dimensional form along with FM of the upper rotor, lower rotor, and that of the combined system. The FM for the coaxial rotor mentioned here is computed using equation 3.1 as given by Leishman et.al [128]. This definition accounts for unequal thrust due to the two rotors while balancing torque.

The table also contains thrust and torque results for baseline single rotor cases for comparison. For the single rotor experiments, only the upper rotor was operated with the lower rotor removed. The zero-thrust C_Q values for both rotors for 40k, 60k, 80k *Re* cases are 0.00024, 0.00021, 0.00019 respectively.

Comparing the overall Figure of Merit (FM) of the constant C_T cases, FM increases with increase in *Re* for all vertical separations. This is just as expected as the viscous parasitic drag losses which do not contribute towards thrust generation are more prominent at low Re, affecting performance. The FM of constant T cases decrease with *Re* because *Re* increase is obtained through increasing rotor RPM. This increases the parasitic drag torque though the thrust demanded is the same. The fraction of parasitic drag torque to the overall torque can be gauged by comparing the readings in the table with the zero-thrust C_Q for the three Re.

Table 3.3: Coaxial rotor thrust and torque measurements in hover

Re 10^3	C_{T_L} 10^{-3}	C_{T_U} 10^{-3}	C_{Q_L} 10^{-4}	C_{Q_U} 10^{-4}	FM_L	FM_U	FM_{Coax}
$VS = 0.25$, Const. C_T							
40	3.6	4.0	6.0	5.7	0.25	0.32	0.28
60	3.3	4.9	6.6	6.7	0.20	0.37	0.29
80	3.1	4.4	5.7	5.7	0.21	0.36	0.29
$VS = 0.25$, Const. T							
40	3.6	4.0	6.0	5.7	0.25	0.32	0.28
60	1.3	2.3	3.5	3.5	0.09	0.22	0.16
80	0.7	1.5	2.4	2.5	0.05	0.16	0.11
$VS = 0.40$, Const. C_T							
40	3.1	5.1	7.0	7.1	0.17	0.36	0.27
60	3.4	4.8	6.5	6.4	0.22	0.37	0.29
80	3.5	4.5	5.8	5.6	0.25	0.38	0.32
$VS = 0.40$, Const. T							
40	3.1	5.1	7.0	7.1	0.17	0.36	0.27
60	1.3	2.1	3.4	3.4	0.10	0.21	0.16
80	0.7	1.5	2.4	2.5	0.05	0.16	0.10
Single Rotor, Const. C_T							
40	-	3.8	-	5.8	-	0.28	-
60	-	3.9	-	5.3	-	0.32	-
80	-	3.8	-	4.7	-	0.34	-

Another easily noticeable trend is that the lower rotor has much lower FM compared to the upper rotor although they are identical in construction. This is due to higher induced losses on the lower rotor as it is operating in the downwash of the upper rotor. The drop in the effective angle of attack of the lower rotor blades makes higher pitch angles necessary, causing the lift generated at each blade section to have a significant component in the drag direction.

While comparing the overall FM of coaxial rotors at the two different vertical separations, the $VS = 0.40$ cases tend to have slightly better performance at higher *Re* as a larger outboard region of the lower rotor experiences flow from the sides. This is because the

upper rotor wake gets more space to contract. This effect is not as sharp at lower Reynolds numbers, likely because of higher viscous effects leading to slower wake contraction.

Another observation is that the divide between the upper rotor performance and the lower rotor performance is greater for the higher separation, which is consistent with findings by Ramasamy *et al.* [115] for much higher *Re* tests. Ramasamy argues that when the vertical separation is low, the lower rotor induces higher inflow through the upper rotor due to the low pressure generated under the upper rotor, increasing induced losses on it (as explained in the previous paragraph). The lower rotor experiences relatively lower downwash from the upper rotor (meaning lower inflow) as the upper rotor is generating lower thrust than what it would have if the vertical separation were greater. This reduces the induced losses on the lower rotor.

For all the coaxial rotor cases, the FM is less than that of the single isolated rotor. Coaxial rotors in this study have effective disk loading twice that of the single isolated rotor. It is well known that higher disk loading leads to higher inflow velocities and induced losses.

It is interesting to note that the upper rotor's FM is much higher than that of the single isolated rotor for all constant C_T cases. One argument supporting this observation is that the upper rotor in a coaxial configuration is operating at a C_T higher than that of the isolated rotor, leading to a higher FM. However, such increase in FM_U due to a higher C_T is not found to be a dominant factor while studying coaxial rotor tests at high *Re* such as those by Ramasamy *et al.*.

Going by what is known from the momentum theory for rotors, higher overall disk loading for coaxial rotors should cause higher inflow velocities above the rotors as a whole. In fact, the upper rotor is responsible for a larger share of thrust and hence is individually facing much higher disk loading than the isolated rotor already, causing higher rotor inflow

velocities. Another way to look at this is that the lower rotor is generating low pressure under the upper rotor, causing more flow through the upper rotor (in other words, higher inflow velocity). Hence, the upper rotor FM should have been lower than the single rotor FM because of the higher induced losses due to higher inflow velocities.

The coaxial rotor tests at high *Re* such as those by Ramasamy *et al.* [115] have always shown the upper rotor performing worse than the isolated rotor, indicating a role of low *Re* effects in the current observations. It is hypothesized that the upper rotor could be benefiting from swirl induced by the lower rotor. A more detailed analysis done on this matter using mean velocity field data from stereo PIV measurements is presented and discussed later in this chapter.

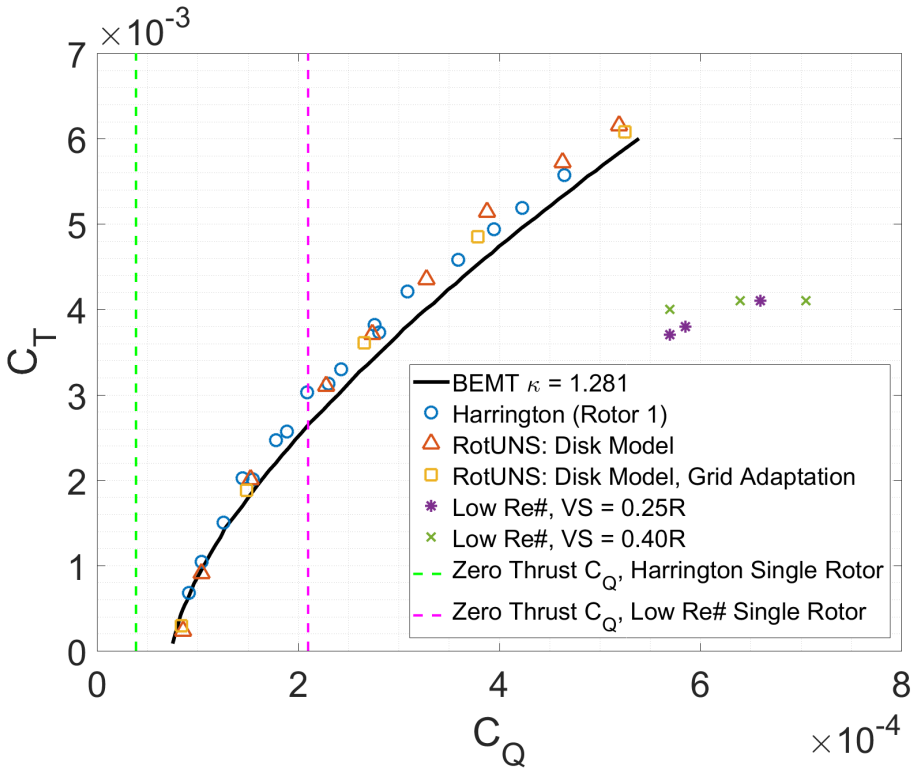

Figure 3.11: Comparison of C_T and C_Q measurements with coaxial rotor data by Harrington [76] and RotUNS CFD data by Schatzman [130]

The thrust and torque measurement outcomes from the current low *Re* coaxial rotor tests are compared with some historical data on a 25-foot-diameter coaxial rotor by Harrington [76] and CFD study on the coaxial rotor by Schatzman [130] in Fig. 3.11. Zero thrust torque coefficients for both the coaxial rotors are also marked on the plot to separate out the contribution of parasitic drag from overall drag. It is seen that the difference in high and low *Re* rotor C_Q is more than the difference between their respective single rotor zero thrust C_Qs. This means that not just profile drag, but induced drag is also higher for low Re rotor. The significant difference in thrust induced torque coefficient may be due to the differences in the way low *Re* rotor wake induces flow over the blades. However, a more precise comparison would need rotors of identical geometries tested at the two significantly different *Re* ranges.

3.5.3 PIV results

Instantaneous velocity field data and wake interactions

Figure 3.12 contains instantaneous vorticity contour plots for constant C_T cases. The red spots in the contour plots correspond to tip vortices, and the coherent blue streaks correspond to the trailing edge vortex sheets. Three instances of the test cases help in understanding the progression of the wake. One can identify the vortices and vortex sheets from the upper and the lower rotor from Figure 3.12 plots by referring to the conceptual depiction of the instantaneous flow field in Figure 3.13 and careful observation.

As the upper and lower rotors in a coaxial rotor rotate in opposite directions, the vortices and the trailing edge vortex sheets form helices of opposite sense of rotation about the rotor axis, but just shifted vertically. The upper rotor tip vortices impinge inboard on the lower rotor disk due to wake contraction, and hence mostly interact directly with the lower rotor trailing edge vortex sheet only above a certain vertical separation between the

rotors. As the upper rotor tip vortices and lower rotor vortex sheets are parts of helices of opposing sense, the separation between the two ranges from zero to a maximum number at any given instant as one looks around the wake. A graphical depiction of the expected rotor wake structure as described above is featured in Fig. 3.14 (a) for aiding visualization. The figure assumes single bladed rotors for clarity, without losing generality.

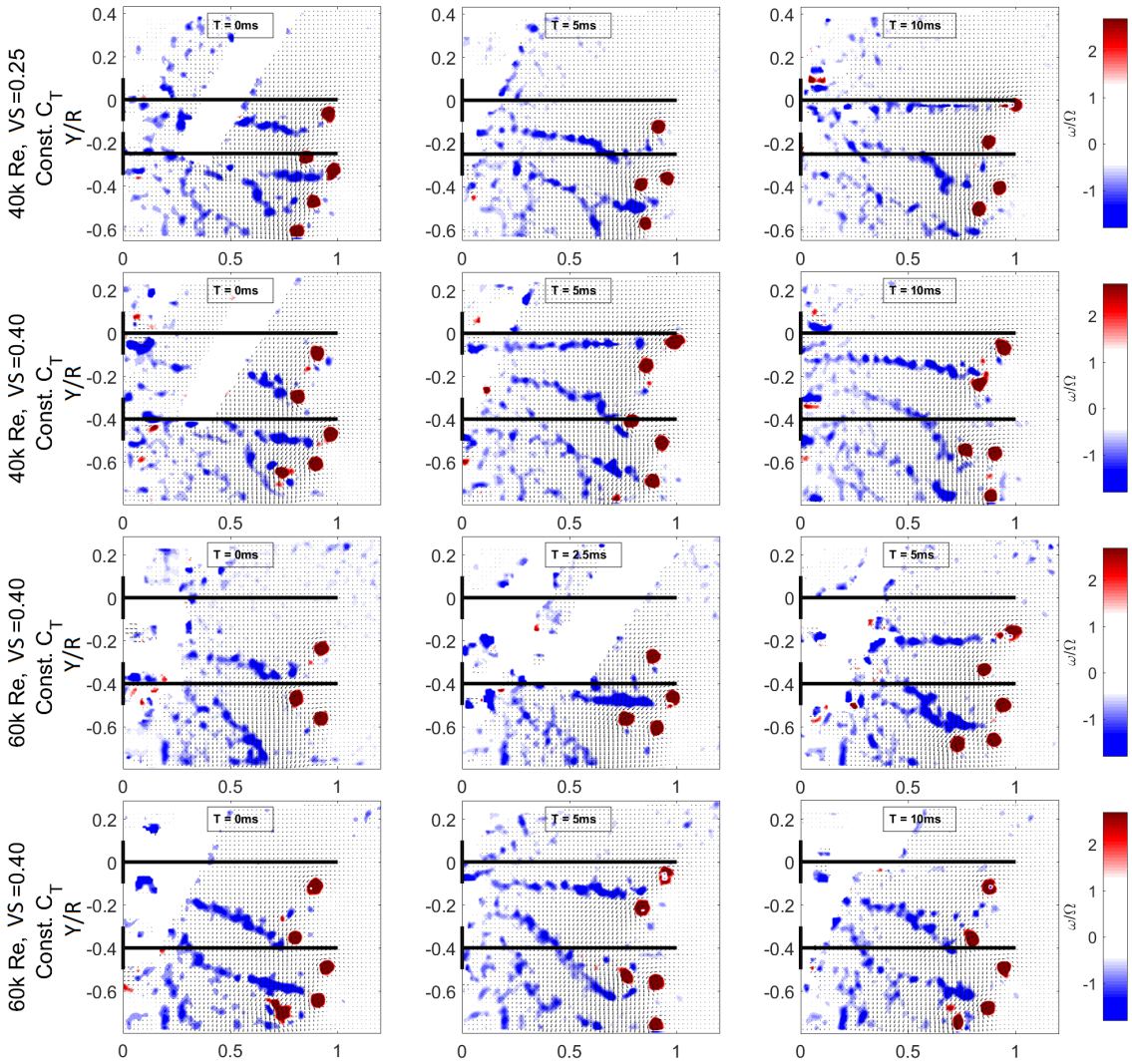

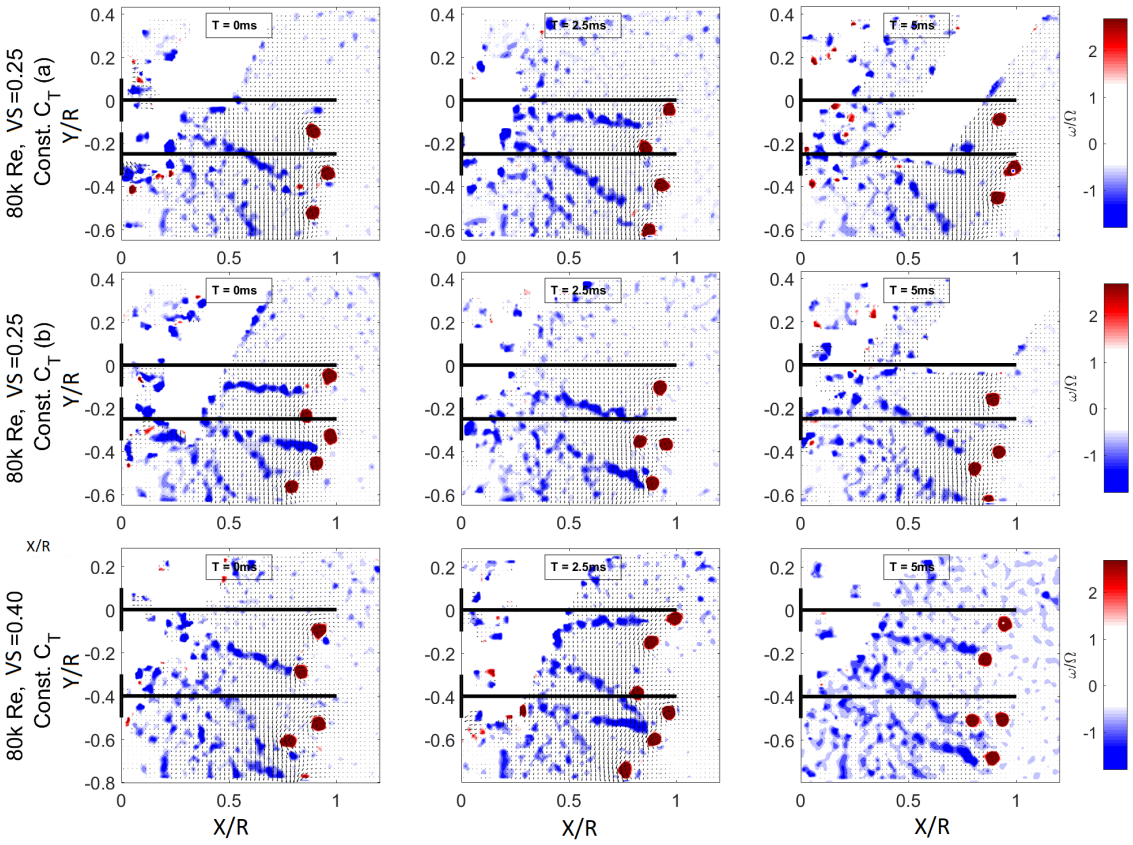

Figure 3.12: Instantaneous vorticity contour plots for hover, coaxial rotor

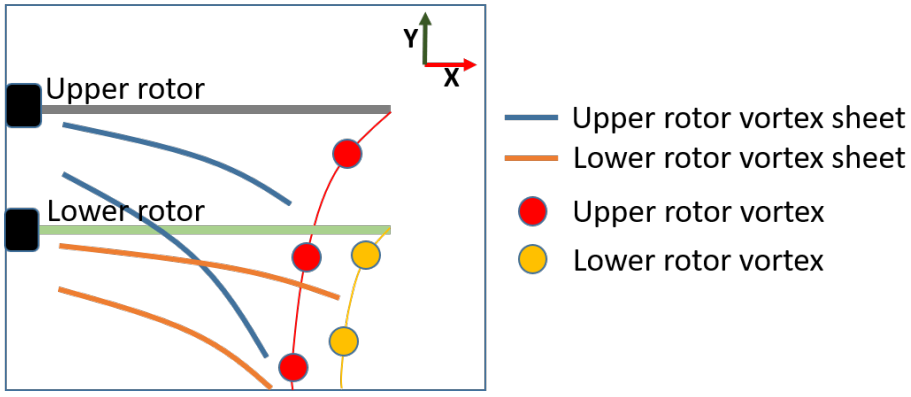

Figure 3.13: Conceptual sketch of instantaneous vorticity contour plots

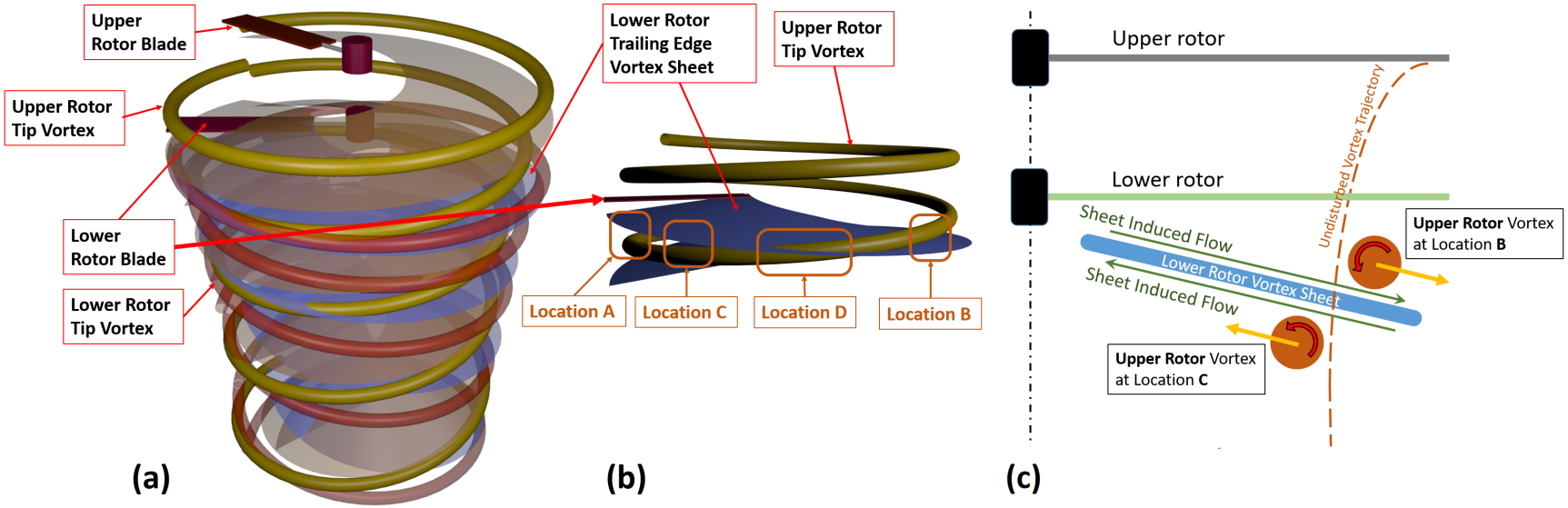

Figure 3.14: (a) Graphical depiction of coaxial rotor wake in hover. (b) Vortex-vortex sheet interaction locations of interest. (c) A graphic explaining vortex-vortex sheet interaction effects at locations B and C.

If the two rotors rotate at the exact same speed, the blade crossings and the vortex-vortex-sheet interactions get locked in azimuth direction. To get a complete picture of the wake all around the coaxial rotor, the speeds of the individual rotors were kept different by 15 RPM while taking the hi-speed PIV images. In hover or axial flight, this has the same effects as slowly moving around the coaxial rotor setup with the cameras to study each vertical sectional plane of the wake.

Interaction mechanisms

Through careful observation of all the instantaneous PIV results for all cases, it was found that there are four specific ways in which the upper rotor wake interacts with the lower rotor wake across the cases. The 4 observed ways correspond to the 4 types of azimuthal locations. Figure 3.14(b) is extracted out from 3.14(a) to show these 4 locations of interaction between the upper rotor tip vortex helix and the lower rotor trailing edge vortex sheet flat helix with more ease. Location A is where the upper rotor tip vortex is approximately in the middle of two consecutive layers of lower rotor vortex sheets. Location B is where the upper rotor tip vortex is just above the vortex sheet, which happens when the lower rotor blade passes right before the upper rotor tip vortex reaches the lower rotor plane. Location C is where the upper rotor tip vortex is just below the vortex sheet, which happens when the lower rotor blade passes right after the upper rotor tip vortex crosses the lower rotor plane. Location D is where the upper rotor merges with the vortex sheet which coincides with the lower rotor blade hitting the upper rotor tip vortex. Though the markers in Fig. 3.14(b) show only a small region, the region actually extends in the vertical direction. This is because the relative positions of the vortices and vortex sheets do not change much with the progression of the wake as the convective speeds are almost the same. The swirl in wake below the coaxial rotor is negligible because of torque cancellation (or swirl recovery). Therefore the wake structures are found to descend vertically down and not spin about

the rotor axis.

At location A, the upper rotor tip vortex trajectory transitions smoothly downwards through the lower rotor disk as the vortices do not have any other structure close to them. The instantaneous vorticity contour plots presented for all the VS = 0.40R cases in Fig. 3.12 are at such location. At location B, the upper rotor vortices being above the vortex sheet, get pushed outboard due to the flow induced by the vortex sheet. On the other hand, the upper rotor vortices at location C being below the vortex sheet, get pulled inboard. The instantaneous vorticity plot series presented for 40k Re, VS = 0.25 case serves as an example for location B, and the series presented for 60k Re, VS = 0.25R for location C. The crude model of interaction effects described above can be understood better by referring to Fig. 3.14(c) where the sheet induced flow above and below vortex sheet is shown to push upper rotor tip vortex away from the original, undisturbed trajectory.

At location D, the upper rotor tip vortex is seen to get destroyed after merging with the vortex sheet or colliding with the lower rotor blade. No trace of the upper rotor tip vortex is found below the lower rotor plane if the collision is complete. Imperfect collisions at small azimuthal distances away from the complete collision result in residual high vorticity pockets which do not have a vortex-like coherent structure. The instantaneous contour plot series labeled "80k Re, VS = 0.25 Const.C_T(a)" is an example for location D.

The upper rotor tip vortex center trajectories for locations A, B, and C were traced for all the cases. Figure 3.15 contains representative vortex trajectory plots for two test cases. For tracing the vortex trajectories, vortex centers were identified using the algorithm by Graftieaux *et al.* [112] described in chapter 2.

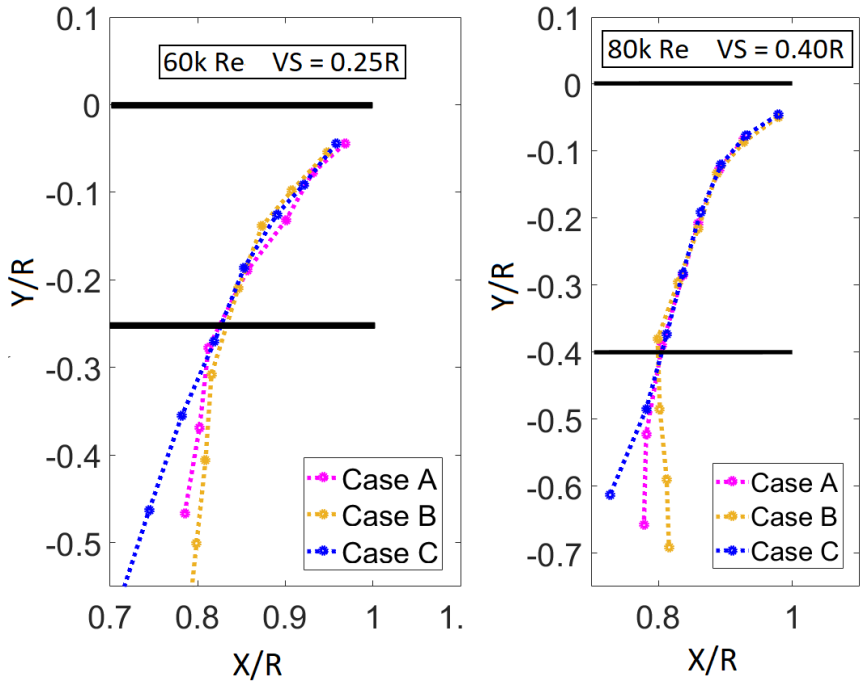

Figure 3.15: Upper rotor vortex trajectories at azimuthal locations marked as A, B, and C in Figure 3.14 for two test conditions

Interaction effects on upper rotor vortices

The effect on the upper rotor tip vortex trajectory due to interaction with the vortex sheet at the different locations is easy to observe through the two plots in Figure 3.15. As expected, the deviations in the trajectories occur only after the vortices cross the lower rotor plane. The effect is independent of vertical separation between rotors, however, the magnitude of trajectory deviation should be a function of vertical separation as vertical separation affects thrust share, downwash from the two rotors, radial location of upper rotor vortices hitting lower rotor plane, vortex sheet strength, etc. The reasons why the upper rotor tip vortex sheet gets affected the most by lower rotor vortex sheet are (1) the radial location of the upper rotor tip vortex matches well with the lower rotor vortex sheet location, and (2) convection speeds of both are comparable, giving more time to the vortex sheets to affect the vortices. The lower rotor vortices convect down much slower than the upper rotor vortices and the vortex sheets.

It is also observed that the upper rotor vortices convecting down at locations A and C retain coherent structure for a much longer duration compared to those convecting down at location B. This is because the vortices at location B are being drawn outboard towards the tip vortices generated by the lower rotor and get disturbed by them. The locations described here are not discrete and they smoothly transition from one to another, which is intuitive through Fig. 3.14(b). Therefore, the vortex trajectories also vary continuously between the extrema as one looks around the coaxial rotor wake. A similar study of tracking rotor tip vortices using PIV, but on high *Re* single rotor was done recently by Karpatne *et al.* [131] where an analytical model was proposed to account for the anisotropic behavior of aperiodic tip vortex motion. Accurate prediction of vortex trajectories and properties is necessary for a refined analysis of rotor performance.

Lower rotor vortices

Now shifting focus to the lower rotor tip vortices, it is found that consecutive vortices tend to have different paths for almost all cases and locations. The lower rotor vortices are affected by the upper rotor wake and get shifted from their usual path either radially outward or inward. In some instances, the consecutive lower rotor vortices which are close to each other due to lower convective speeds get triggered by the disturbance and start to roll about each other. In such scenarios, the divide between the two trajectories is large. Figure 3.16 shows trajectories of two consecutive sets of vortices from the two rotors. The upper rotor tip vortex trajectory does not change noticeably over time as much as it changes over azimuthal location, whereas the lower rotor tip vortex trajectory is different within a range for each vortex. The spread in lower rotor tip vortex trajectories is dependent on radial location. The lowest spread is observed around location B for all cases.

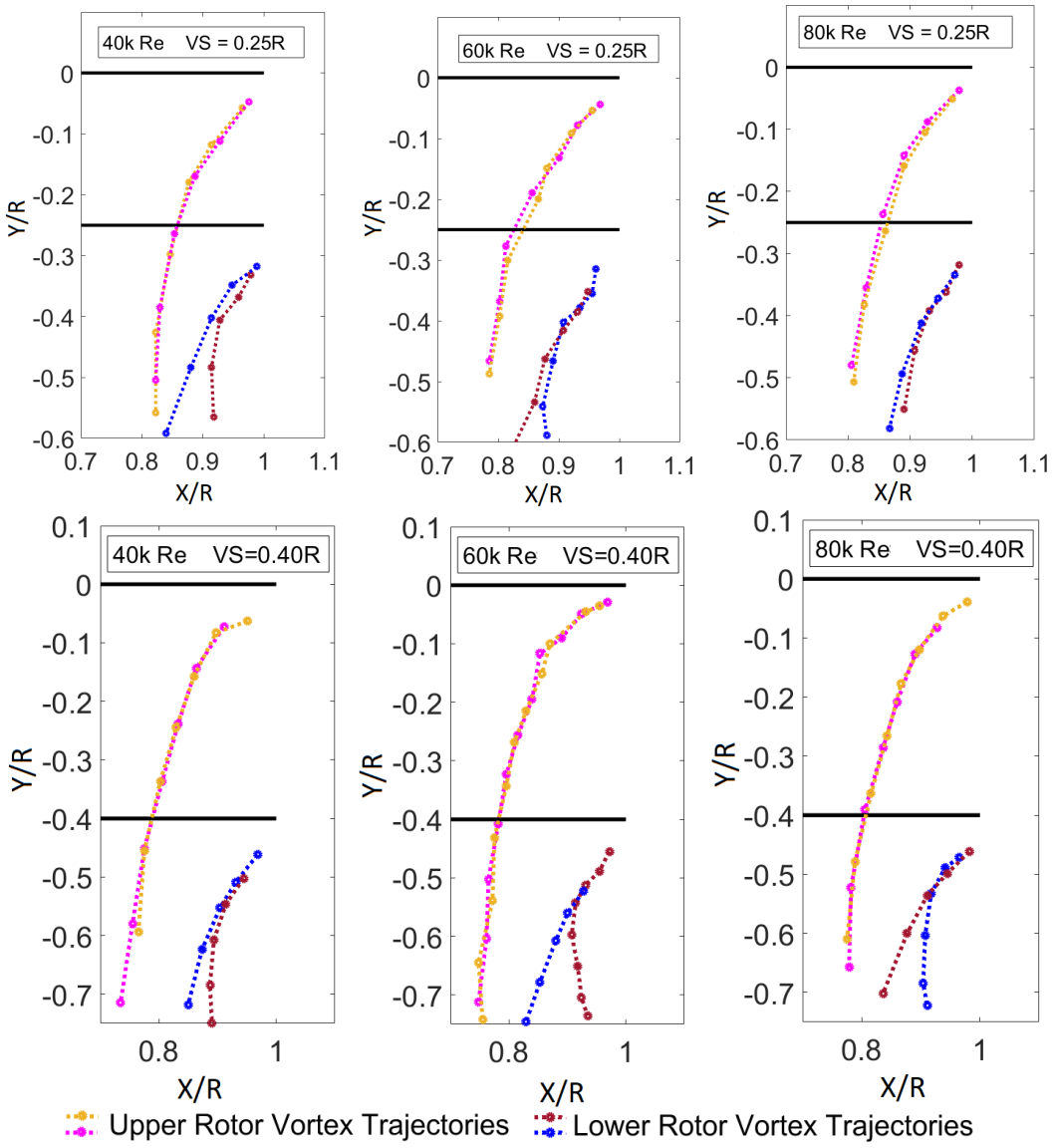

Figure 3.16: Vortex trajectory plots for VS = 0.25R and VS = 0.40R

Significance of wake interactions on performance and design

The upper rotor wake and features directly affect the lower rotor performance through blade-vortex and blade-vortex sheet interactions upon impingement. These vorticity-laden wake structures are expected to have a very strong effect on the spanwise (radial) flow over and under the lower rotor blades depending on the azimuthal locations identified earlier as A, B, C, and D. The spanwise flow is crucial, especially at high C_T conditions where

sections of the lower rotor blades are close to stall. The periodic change in direction and magnitude of the wake-induced spanwise flow can trigger flow separation or reattachment. Factors such as rotor separation, blade geometry, loading, etc. determine the radial location where the wake structures impinge on the lower rotor, also affecting the stall characteristics.

In hover, synchronization of the two rotors to fix bladed crossings is not significantly beneficial in terms of performance because the lower rotor blades have to pass through all the upper rotor wake features as it turns one rotation. However, in forward flight, the synchronized rotors can be tuned to take advantage of favorable or avoid unfavorable blade-wake interactions observed here. The blade-wake interactions have implications on vibrations and noise which may be factors of concern in some applications.

The resultant wake left below the lower rotor generally does not hit the rotors again in case of isolated coaxial rotors. However, the knowledge on the trajectories and strengths of features in the overall wake is important from vehicle design perspective where reducing download on the fuselage and/or payload or reducing gusts on sensors needs to be considered. The results from the wake study are also instrumental in developing high fidelity performance prediction codes for low *Re* rotors along the lines of vortex theory and free wake models for high *Re* rotors.

3.5.4 Mean Velocity Field Data and an Investigation on High Upper Rotor Performance

Figure 3.17 presents mean flow field streamline plots, with $VS = 0.25R$ cases on the left and $VS = 0.40$ cases on the right. The two horizontal white lines in each plot depict rotor planes. The 200 instantaneous velocity fields cover 18 rotor rotations (or 36 blade passings) for the lowest RPM case. The 200 frames cover rotor rotation in 1.8 degrees resolution as the rotor rotates 16.2 degrees between two consecutive instantaneous fields, which is not

a factor of 360. Therefore the mean flow field obtained by averaging 200 instantaneous velocity fields should be well representative of the actual mean flow field.

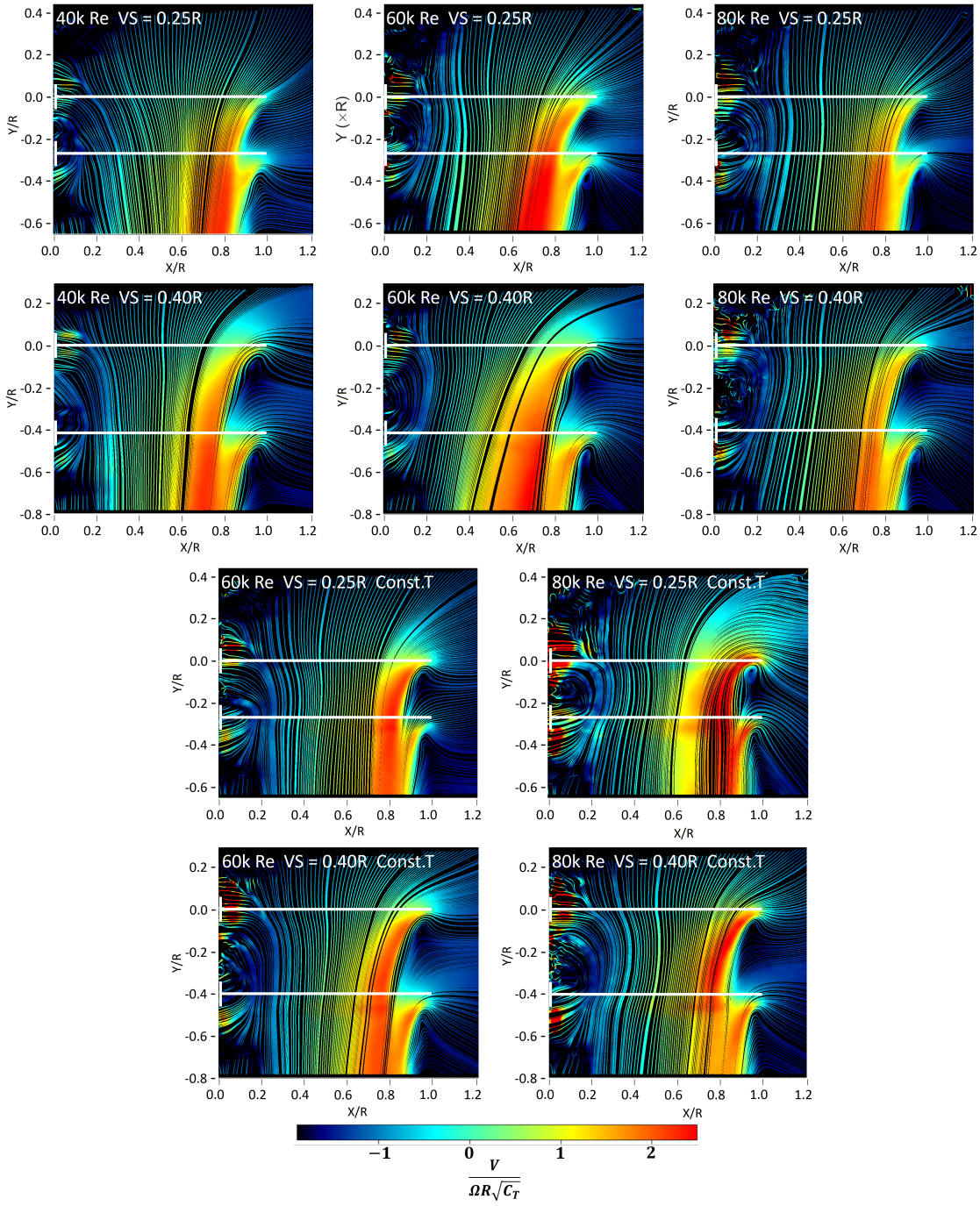

Figure 3.17: Time averaged velocity field streamlines

One simple observation through the plots is that the velocities at the upper rotor slipstream are higher than at the lower rotor slipstream across all cases. This is expected as

the upper rotor generated more thrust, and hence causes stronger downwash. There is a notable difference between streamlines entering the upper rotor for VS = 0.25R and VS = 0.40R constant C_T cases. For all the three *Re*, the streamlines entering upper rotor of VS = 0.25R have a smaller radial component and higher axial component than their VS = 0.40R counterparts. The inflow streamline patterns at the upper rotor for constant thrust cases at both rotor separations also matches that of VS = 0.40R constant C_T cases. This behavior is primarily due to flow induced by the lower rotor at upper rotor plane through suction and/or tip vortices. At smaller rotor separations with a loaded lower rotor, the lower rotor tip vortices are strong and close to induce some flow at the upper rotor plane outside slipstream. Also, the lower rotor creates higher suction below the upper rotor when the separation is low. At higher rotor separations and at low lower rotor loading conditions, the lower rotor suction and tip vortices do not play a significant role in upper rotor inflow.

The effect of the above difference in the upper rotor inflow pattern is visible on the upper rotor performance. The upper rotor is seen to have generally higher FM in VS = 0.40R cases compared to VS = 0.25R cases of constant C_T. This is because the upper rotor in VS = 0.40R cases ingests air from the sides which does not have any significant axial velocities/momentum. In VS = 0.25R cases, the mean downward inflow velocities are higher as the air is pulled from above the rotors, causing relatively higher induced losses.

Figure 3.18 captures inflow and outflow velocity profiles for both rotors for all cases from the time-averaged velocity field. The inflow and outflow data presented here are extracted from a distance of 0.1R above and below the rotors respectively for both the rotors. Here again, the difference in the way flow enters the upper rotor for the two vertical separation cases is apparent from the inflow velocity profile curves. The upper rotor outflow and the lower rotor inflow velocity profiles are very similar. Both of them tend to be further inboard for all VS = 0.40R cases. The lower rotor outflow profile has two peaks because

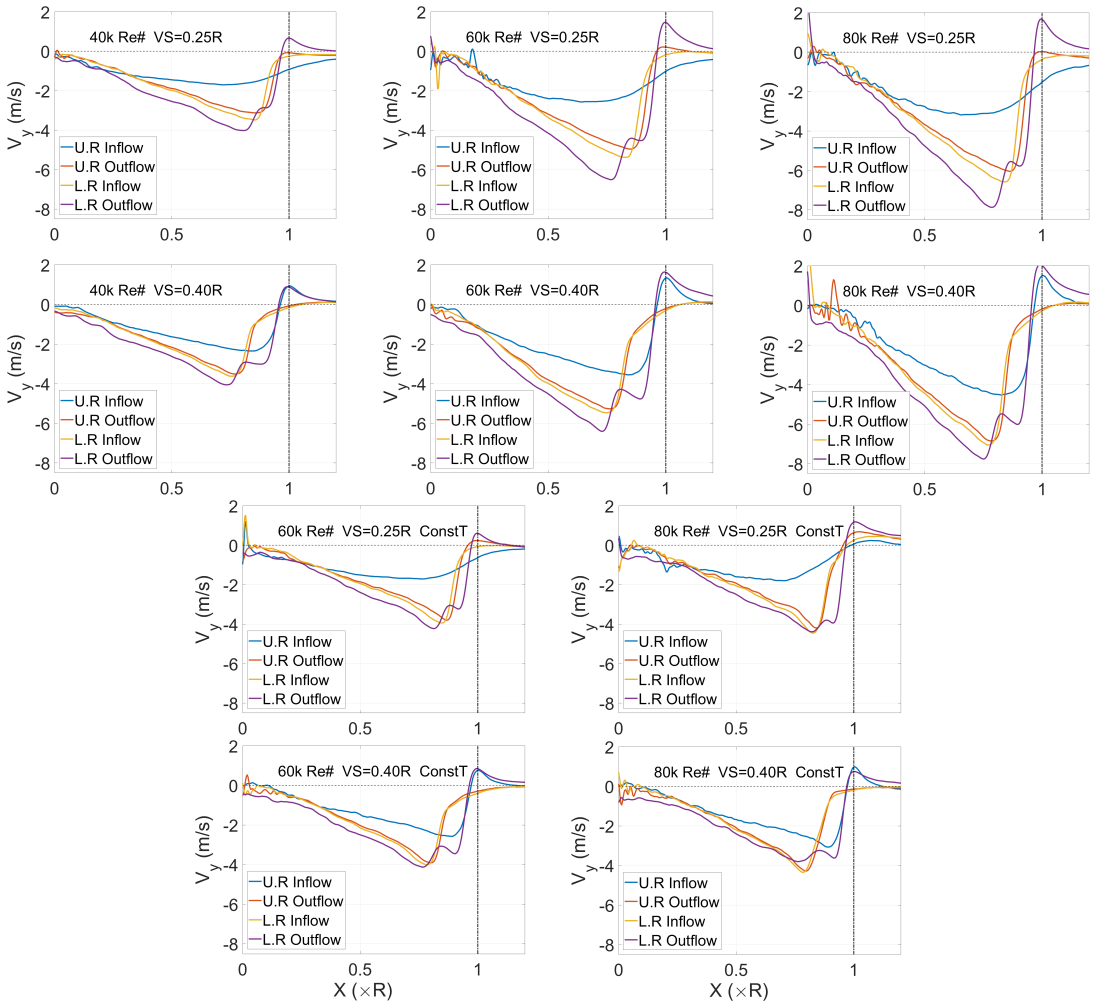

Figure 3.18: Inflow and outflow velocity profiles for upper and lower rotors

there are two slipstreams at this location. The inboard peak is due to the upper rotor slipstream and the outboard peak is due to lower rotor slipstream. The peak corresponding to the upper rotor wake is higher in magnitude as the upper rotor generates more thrust. The divide between radial locations of the peaks is higher for VS = 0.40R cases as expected by observing lower rotor inflow velocity profile.

We now move on to the problem of the upper rotor of a coaxial rotor performing better than an isolated rotor as introduced in the thrust and torque measurement results section. It was hypothesized then that the observation is due to swirl recovery at upper rotor due to the

lower rotor. To verify the hypothesis, the mean tangential (into the plane/swirl) velocities in a region neighboring the upper rotor disk are integrated to find the spatial average for all constant C_T cases and compared with single isolated rotor results. The integration area is 0.2R thick, equally spread on either side of the rotor disk, and 0.8R in length as marked in the Fig 3.19 by the green box. The figure features one single rotor case and one coaxial rotor case for illustration.

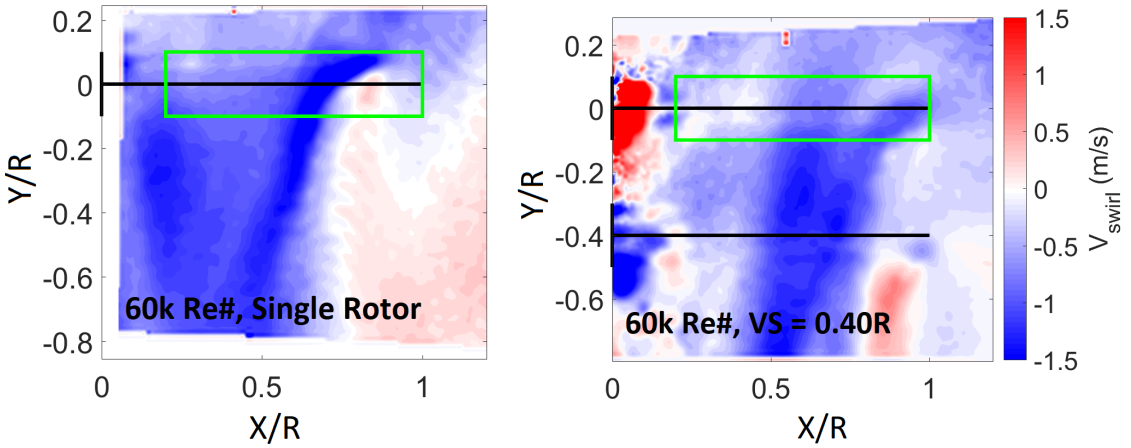

Figure 3.19: Time averaged swirl velocity field plots with integration box marked in green

The effect of the lower rotor on swirl close to the upper rotor cannot be compared by comparing the swirl velocities directly. That is because thrusts and torques at the upper rotor vary across cases, and swirl near a rotor is directly related to the torque applied by the rotor. Hence, the integration averaged swirl velocities around the upper rotor are normalized by the upper rotor torque to account for the effect of rotor torque on swirl before comparing different cases for finding swirl induced by the other rotor.

The normalized results from the aforementioned process are tabulated in the Tab. 3.4. Here it is seen that except for the outlier case of 40k *Re* VS = 0.25R (which may be due to some error in the torque measurements or spurious data in PIV), all other coaxial rotor cases have the normalized swirl velocities smaller (in magnitude) than their single rotor

counterparts. Moreover, the swirl velocity magnitudes for VS = 0.25 cases are smaller than VS = 0.40R cases. This supports the idea that the lower rotor induces counter-swirl on the upper rotor, which can be responsible for performance improvement of the upper rotor compared to a single isolated rotor.

Table 3.4: Integrated normalized swirl velocities

	$V_{Swirl(int)}/(\Omega R)\sqrt{C_Q}$		
Re	**Single Rotor**	**VS = 0.25R**	**VS = 0.40R**
40k	-0.48	-0.48	-0.42
60k	-0.66	-0.32	-0.41
80k	-0.54	-0.21	-0.44

The phenomenon of swirl recovery in a coaxial rotor is not new. However, it is always seen to be benefiting the lower rotor performance, but not the other way around as the flow is from the upper rotor to the lower rotor. It is believed that reverse swirl recovery phenomenon observed here is typical for low *Re* coaxial rotors only because viscous forces which are significant compared to momentum in this regime help in transferring swirl from the lower rotor to the upper rotor against the downward flow.

3.6 Conclusions

The present study on low *Re* coaxial rotors showed that though most arguments made for large size coaxial rotors on performance hold true for low *Re* rotors as well, there are some interesting observations which cannot be explained by what is known from high *Re* rotor aerodynamics.

Just like for high *Re* coaxial rotors, the upper rotor performance is seen to be much better than the lower rotor performance, and the overall coaxial rotor FM is less than that of an

isolated single rotor. However, unlike high *Re* coaxial rotors, the upper rotor was found to have higher FM than the single isolated rotor for all test cases, which goes against what is expected out of typical momentum based approach. It was later found through analysis of swirl velocities from the SPIV data that the better than expected upper rotor performance was due to viscous swirl recovery by the counter-rotating lower rotor. Such viscous swirl recovery is unlikely in high *Re* rotors where strong downwash from the upper rotor does not allow viscous forces to communicate lower rotor swirl in the upward direction.

While comparing the low *Re* coaxial rotor C_T and C_Q data with the historic high *Re* data by Harrington, it is apparent that the parasitic, as well as induced torque coefficients are much higher for the present lower *Re* rotor cases. The higher induced torque is hypothesized to be due to the difference in the way low *Re* rotor wake induces flow over the blades.

The upper rotor vortices are found to interact with the lower rotor trailing edge vortex sheet in four separate ways in each test case, affecting upper rotor tip vortex trajectories and endurance. Upper rotor tip vortices are seen to get pulled inboards, pushed outboards, disintegrated, or stay unaffected after interaction with the lower rotor vortex sheet depending on if the upper rotor tip vortices land below, above, exactly on or far away from the lower rotor vortex sheet at the given azimuthal location. These findings on rotor wake are expected to aid the design of coaxial rotor UAVs and be instrumental in the development of more accurate performance prediction methods for this regime.

Summarizing:

1. The nature of vortex-vortex interaction between the two coaxial rotors in edgewise flight depends on the advance ratio.

2. Thrust generated by a coaxial rotor in edgewise flight is less than the sum of thrust generated by the individual rotors, but follows almost identical trend w.r.t advance ratio.

3. Upper rotor FM is much higher than lower rotor FM. The FM of the overall coaxial system is lower than that of single isolated rotor.

4. FM of the upper rotor is higher than that of the single isolated rotor as well in hover.

5. The better than expected performance of the upper rotor is tracked to viscous swirl recovery, which has not been observed so far for higher Reynolds number coaxial rotors.

6. The torque coefficient is much higher for the same thrust coefficient, at these low Re# cases when compared with the prior experiments on big size rotors. The difference is traced to both a higher profile drag coefficient, and a higher induced drag coefficient.

7. Upper rotor vortices are found to interact with the lower rotor trailing edge vortex sheet in four separate ways in each test case.

8. The nature of interaction affects upper rotor tip vortex trajectories and endurance at the azimuthal location of interaction.

9. A qualitative model is presented to explain the four vortex - vortex sheet interaction scenarios and the observed resultant upper rotor vortex trajectories.

10. Consecutive lower rotor vortices tend to have different trajectories. The spread in trajectories varies on a case to case basis.

11. The coaxial rotor mean flow patterns are noticeably different for the two vertical separations.

CHAPTER 4
QUADROTOR IN HOVER AND EDGEWISE FLIGHT

Quadrotors are currently the most commonly used UAV configuration as they have just the right amount of control for the cheapest construction. All the required motions are achieved by merely changing the speeds of the four rotors. This simplicity makes them a good platform for testing out different navigation and control schemes being developed for UAVs for indoor and outdoor flights. This is also the reason why there are numerous conference and journal articles on quadrotor flight dynamics and control published in the last decade. The huge current and future application potential for quadrotors make them interesting enough to be included in this multirotor aerodynamic interactions study.

4.1 Experimental Setup

4.1.1 Setup description

The Quad-rotor setup consisted of four small two-bladed fixed pitch rotors driven by separate geared DC motors. The speed of the individual rotors was adjusted using independent potentiometers. The rotor RPMs were monitored using the laser tachometers. Two separate sets of experiments were done on the quad-rotor setup with and without duct around the rotors to study how the tip vortices interact with the duct. Rotors located diagonally w.r.t each other had the same direction of rotation and adjacent rotors had the opposite direction of rotation. The whole quad-rotor setup was hung from the wind tunnel ceiling so that the support did not interact with the rotor wakes.

The rotors were 66 mm in radius. Blades were untwisted, tapered and cambered with

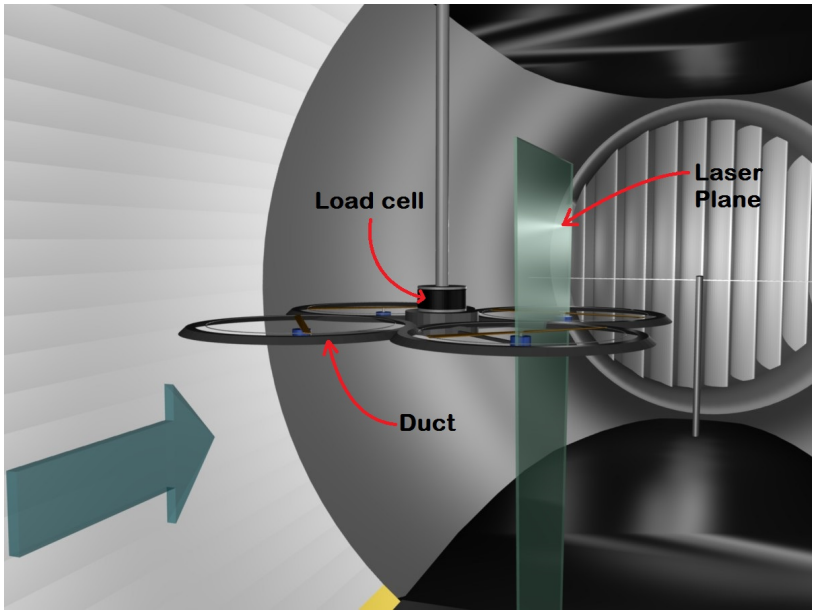

Figure 4.1: Quadrotor setup with laser sheet plane

constant thickness. The inner radius of the duct for the ducted rotor experiments was 73 mm, leaving 7 mm clearance. The rotor blades were cambered and tapered as described in the Table 4.1

4.1.2 Test conditions

The experiments were conducted for hover and edgewise flight cases, with and without duct. The hover tests were performed at two rotor RPMs corresponding to Reynolds numbers 8630 and 16856. Table 4.1 gives all the rotor and test parameters for the quad-rotor experiments. Figure 4.1 shows the setup and placement of the laser plane for the SPIV flow measurements. The duct labeled in the figure was removed from the setup for the un-ducted case.

Table 4.1: Setup and test conditions for quadrotor experiments.

Rotor(4)	
Motor Type	Geared DC
Radius (R)	66 mm
# of blades per rotor	2 (Total of 8)
Blade planform	Untwisted, Tapered
Camber	14%
Chord Length (c)	19.5mm @ r/R = 0.2
	15.3 mm @ r/R = 1
Blade Thickness	7%
Blade Pitch Angle (θ)	10^0
Duct Inner Radius	73 mm
Adjacent rotor axis shift (AS)	160 mm
Test Conditions	
Flight	Hover and edgewise flight of 3 m/s
Configurations	Ducted & Unducted
RPM	1280, 2500, 3500
Tip Speed	8.9 m/s, 17.3m/s, 24.2 m/s
Rotor tip *Re* #	8630, 16856, 23598

4.1.3 Measurements and uncertainty

High-speed PIV measurements

High-speed stereo PIV tests on the quad-rotor were performed for ducted and un-ducted configurations. A baseline case of a single rotor was also studied. PIV data were taken at the rate of 400 frames per second, with both the cameras operating at 800 frames per second at the full resolution of 4 mega pixels. Uncertainty in velocity vectors in all the presented test cases has been found to be under 0.2 m/s everywhere in the PIV plane except close to the blade surface where data is affected due to blade reflections.

Figure 4.1 shows location of the laser plane for PIV measurements with respect to the quadrotor. The laser plane is kept right in the middle of the two adjacent rotors on a side to be able to visualize wake interactions. The cameras covered a region of 200 mm $\times$ 120 mm which included more than half of both the adjacent rotors. The velocity vector resolution was 1.2 mm $\times$ 1.2 mm for all the tests.

Thrust measurements

The thrust measurements on the whole quadrotor setup were done using the ATI Nano load cell (described in 1.5.3), from which the quadrotor was hung. The duct attached to the quadrotor directly, hence any lift generated due to the duct is also accounted for in the thrust measurements. Thrust data was recorded at the rate of 1440 Hz over 15 seconds for each test. The standard deviation in the thrust measurements for these tests has been found to be within 4% for all test cases.

Torque Measurement

Despite ATI Nano being a 6-degree of freedom load cell, it could not be used to measure rotor torque along with the thrust because the 4 rotors rotate in opposite directions, cancelling torque on the vehicle. Directly measuring aerodynamic torque on individual rotor through a torque load cell is challenging due to small setup size hindering installation of a load cell and very low torque values leading to extremely small signal to noise ratio from torque load cells designed for much larger torque range. An indirect approach to measure torque on individual rotors was used. According to the literature, the electric current drawn by a DC motor is proportional to the torque applied by it, independent of motor speed. The 4 rotors are connected to the corresponding motors through a pair of gears, hence independence of the torque-current characteristics to rotation speed had to be verified due to

concerns regarding the contribution of the frictional losses in gears.

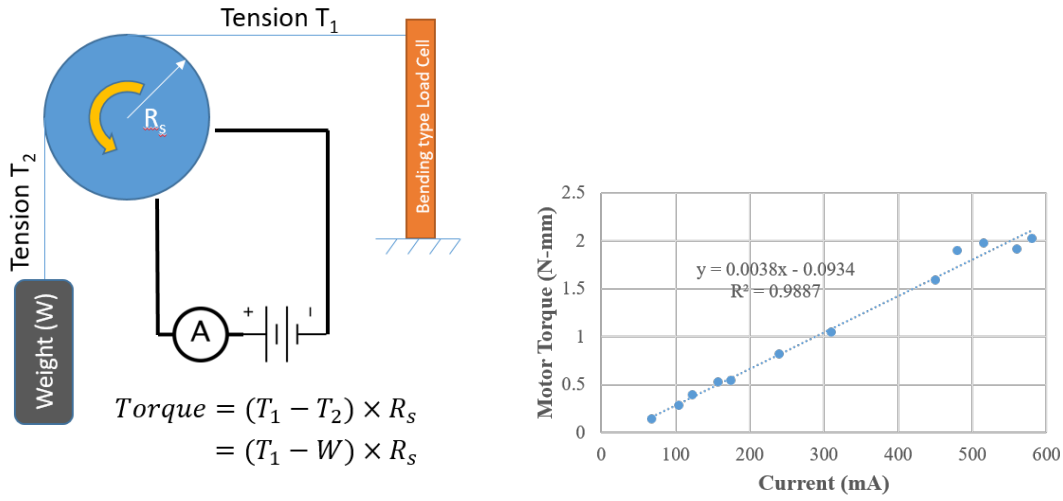

Figure 4.2: (a)A schematic for motor torque-current characteristics test setup (b)Torque-Current plot for the motor

Torque-current characterization experiments were done using a friction dynamometer built in-house for the task. Standard weights were hung from a string tied to a 100 gram force load cell, sliding over the rotor shaft (with blades removed) rotating at set RPMs. The difference in the force measured by the load cell and that applied due to the standard weight gives the tangential force on the rotor shaft, which multiplied by the shaft radius gives the torque applied by the rotor. Different torque values were obtained by changing the standard weight, changing frictional force due to the string on the rotor shaft. The current corresponding to each case was measured using an ammeter with a least count of 10 mA. A schematic for the test setup is provided in Figure 4.2. The torque-current characteristic lines plotted for a range of RPMs from the test data coincided, resulting in the same calibration line for all RPMs. According to the calibration line slope, the least count of torque measurement corresponding to the 10mA least count of the ammeter comes out to 0.038 N-mm.

4.1.4 Test Procedure

Following is the test procedure followed for the quadrotor experiments. It is assumed that the load cells are calibrated before these steps.

1. Adjust PIV cameras and laser sheet to be able to capture the region of interest, and calibrate the PIV system using a calibration plate.

2. Bias the load cell readings to zero when the rotor and the wind tunnel are off.

3. In case of edgewise flight experiments, start the wind tunnel and set the desired speed.

4. Start the rotors and adjust the voltage input to them through the potentiometers until all the rotors attain same, desired RPM. Monitor RPMs using the laser tachometers.

5. Once the desired rotor RPMs and wind tunnel speeds are reached, proceed with the high-speed SPIV measurements, adjusting the parameters such as laser intensity, time difference between frames, etc. ensuring that the software can compute velocity vectors over the whole frame (or at least over the important regions in the frame) using the captured images.

6. Record the thrust data.

4.2 Results and Discussion

4.2.1 High-speed SPIV results

Hover experiments

Figure 4.3 gives instantaneous vorticity contour plots for the ducted and unducted rotor cases at 1280 and 2500 RPM. The four cases look similar in some aspects such as the generation of tip vortices from the rotor blade tips of both the rotors, and their downward convection due to rotor wake. All the cases have a distinct line of trailing edge vortices

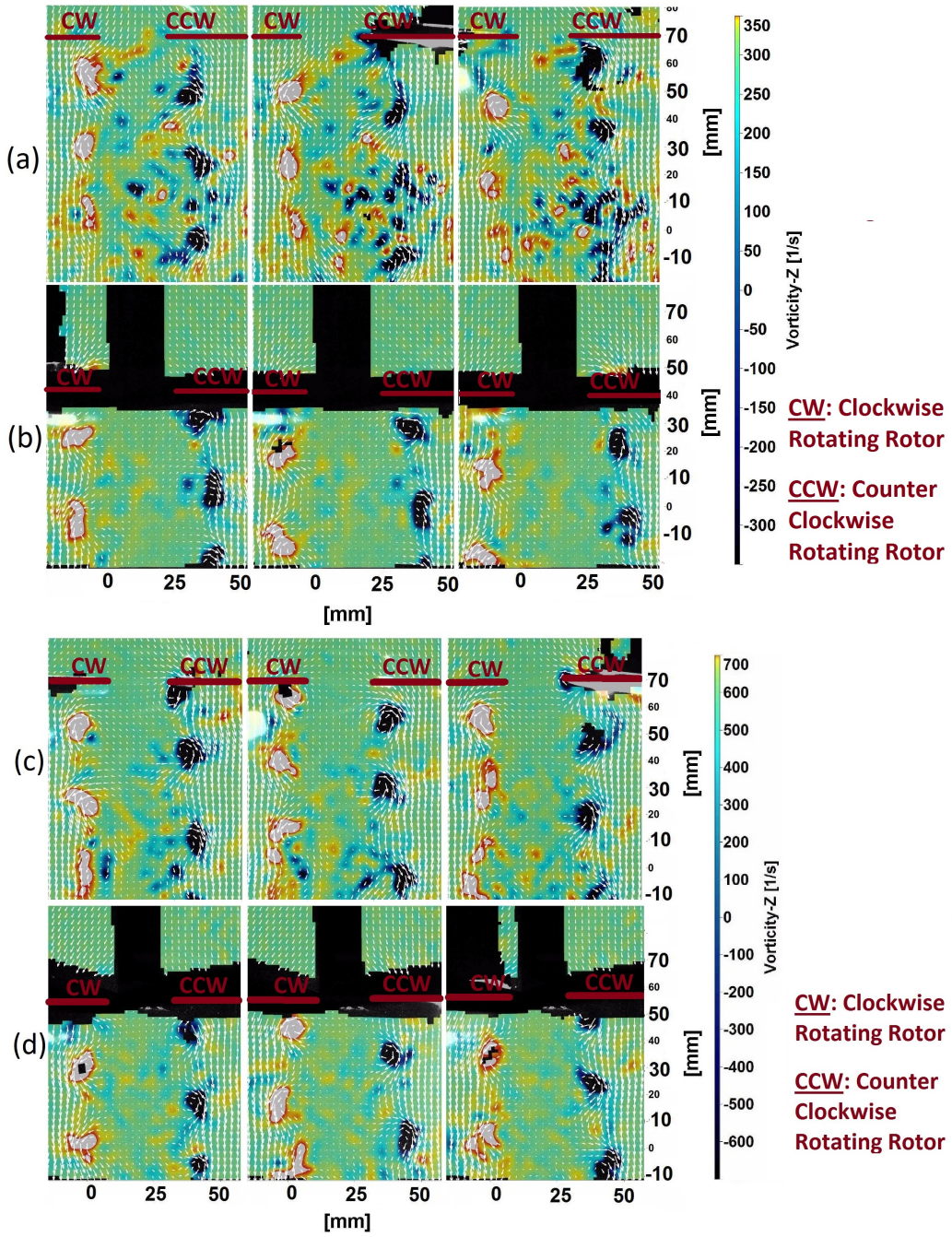

Figure 4.3: Instantaneous vorticity plots spaced 5 ms apart: (a) 1280 RPM, Un-ducted (b) 1280 RPM, Ducted (c) 2500 RPM, Un-ducted (d) 2500 RPM, Ducted (Hover Condition)

(corresponding to the inboard vortex sheet for high-Reynolds number blades) of opposite vorticity. The trailing edge vortices are seen to be generated from the inboard locations of the rotor blade, convecting downward at speeds close to twice the convection speed of the tip vortices. In this low-Reynolds number case, the vortex sheet seems broken up into

several discrete vortices. Especially in the two low Reynolds number cases, these trailing edge vortices close to the tip vortices are seen to get rolled up with the tip vortices after about 2-3 rotor cycles, disfiguring them and often splitting them into two to three smaller and weaker vortices. This is pictorially represented in Fig. 4.4.

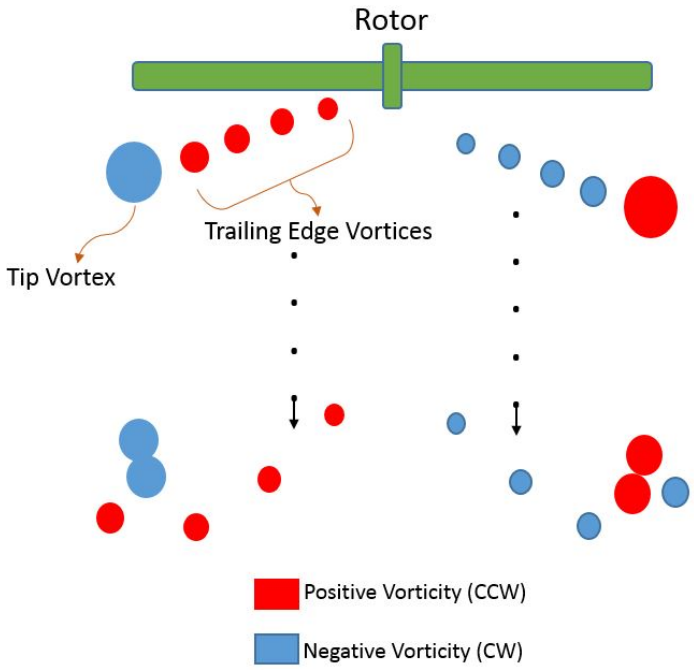

Figure 4.4: Representation of tip and trailing edge vortices (Hover Condition)

The vorticity contour plot for the 1280 RPM un-ducted rotors case is very different when compared with those for the other three hover cases. High vorticity pockets around tip vortices, possibly due to trailing edge vortex sheet, seem to interact with the tip vortices causing them to lose structure and identity within $360^\circ - 540^\circ$ wake age. The plots for ducted 1280 RPM case are much neater and have easily identifiable, prominent tip vortices which maintain their structure at least up to $540^\circ - 720^\circ$ wake age. Both the 2500 RPM cases show features similar to ducted 1280 RPM case where the vortices do not interact as quickly and maintain their form for greater wake age.

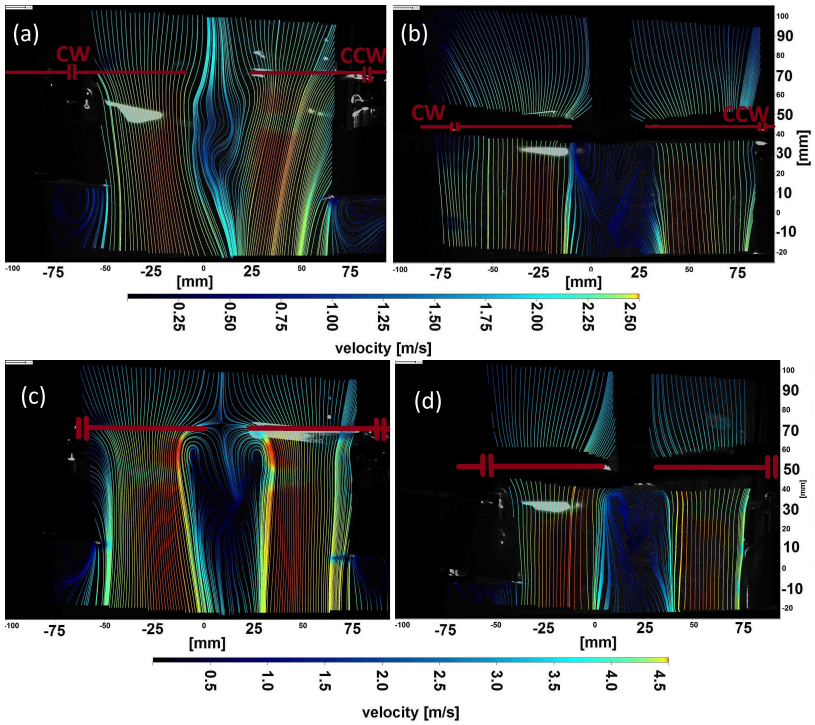

Figure 4.5: Time averaged streamline plots: (a) 1280 RPM, Un-ducted (b) 1280 RPM, Ducted (c) 2500 RPM , Un-ducted (d) 2500 RPM, Ducted (Hover Condition)

Shown in Figure 4.5 are the time-averaged streamline plots over 200 instances for all the four cases. While comparing the un-ducted and ducted rotor cases between the two rotor speeds, the streamline plots for the ducted rotors at both the speeds are very similar, except of course for the wake speed. The streamlines in un-ducted rotor cases spread outwards from rotor centers as they go down. Whereas, in the ducted rotor cases the streamlines barely show any spread. The streamlines due to the two adjacent rotors merge at a very short distance from the rotor disks plane for un-ducted 1280 RPM case. Asymmetry of the streamlines about the center indicates a high level of unsteady flow, which is noticed through the vorticity contour plots too.

This observation may be explained by the following argument. At low rotor speeds, the vortices generated at the rotor tips are weaker in strength, making them more vulnerable to velocity induced due to the neighboring vortex. In presence of a duct, the vortices

from adjacent rotors get insulated from each other during formation. Once these vortices are formed, they get convected down and inwards along with the contracting rotor wake, giving them less opportunity to interact until the wake slows down and vortices expand in size due to viscous effects.

The reason why the 2500 RPM cases show more dominant and coherent vortices is because the vortices have higher strength in terms of local vorticity as well as circulation over a region covering the vortex. Such high strength vortices are relatively more difficult to destabilize. The observation can also be reasoned based on the Reynolds number. The wake and vortices due to the 2500 RPM cases carry more momentum compared to the 1280 RPM cases due to which the effectiveness of viscous forces is tuned down. Even the un-ducted quad-rotor tip vortices are unaffected by the neighboring rotor at 2500 RPM because of higher vortex strength. The duct inhibits inter-rotor wake interactions to some extent at 2500 RPM too.

Table 4.2: Vortex size and convection speeds

Case	**Avg. Vortex Dia. (mm)**	**Avg. Convection Speed (m/s)**
1280 RPM, Un-ducted	8.6	-1.3
1280 RPM, Ducted	8.6	-1.0
2500 RPM, Un-ducted	8.6	-2.4
2500 RPM, Ducted	7.4	-2.3

The velocity profiles across tip vortices in the quad-rotor cases look very similar to that due to the single rotor. Figure 4.6 shows the velocity profile of a tip vortex at six consecutive time instances spaced by 2.5 ms along cuts made in X-direction and Y direction respectively. The average vortex core size estimated from distance between highest and the lowest velocities in the plot and the average vortex center convection speed for these four cases is listed in the Table 4.2. The vortex centers are assumed to be at the center of the

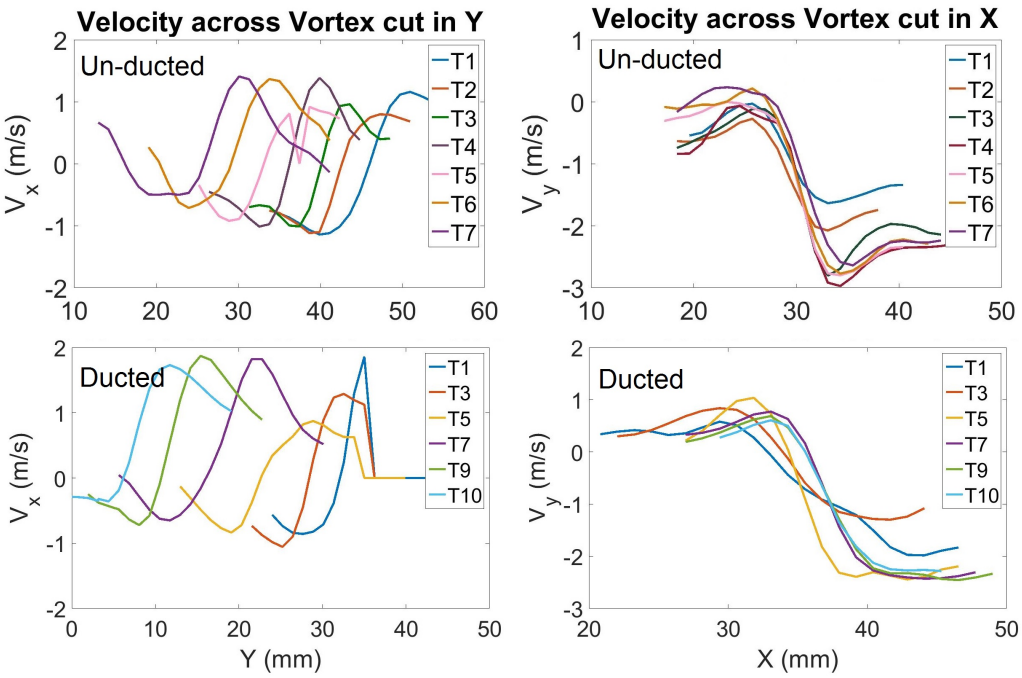

Figure 4.6: Tip vortex velocity plots for 1280 rpm, un-ducted and ducted quad-rotor (Hover Condition)

velocity peaks.

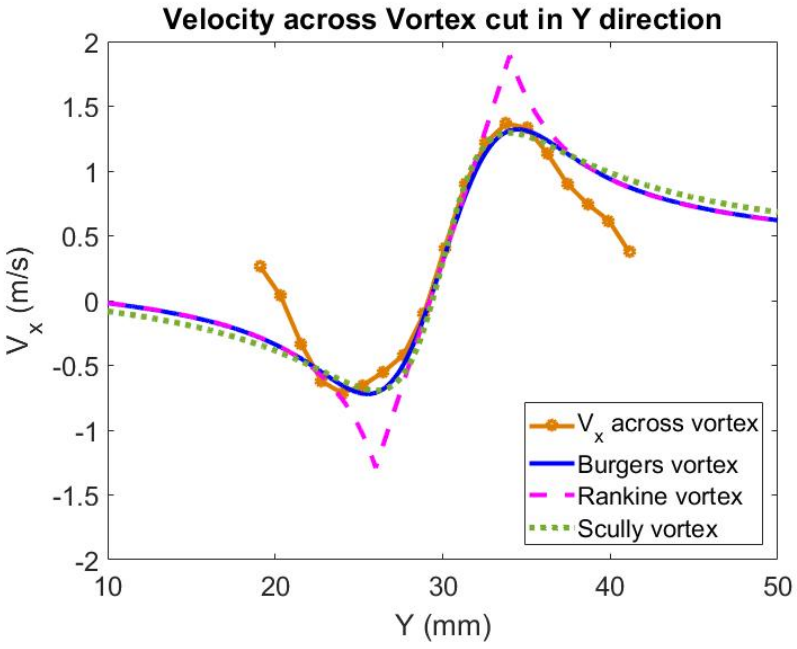

Figure 4.7: Comparison of observed tip vortex velocity profile with Rankine, Burgers, and Kaufmann vortex models

Comparing the velocity profiles across vortices with different vortex models such as Rankine, Burgers, and Kaufmann (Scully) in Figure 4.7, it is seen that the angular velocity in the vortex core region is approximated well by the Burgers and Kaufmann models. But none of the models hold good for the region outside the core as velocity is seen to be dropping much faster than the models. This is possibly due to the influence of neighboring vortices from the same rotor, half rotation older and younger in age. The difference from vortex models would have been lower for a high-Re rotor as the vortex core would have been tighter, giving more space for 1/r shaped decay.

Edgewise flight experiments

The Quadrotor setup was tested in edgewise flow of 3 m/s. This is not a direct representation of a typical forward flight condition, which involves pitch as well. However, the observations from these edgewise flow tests aid understanding of forward flight conditions. SPIV data was gathered with rotors rotating at 2500 RPM. Figures 4.8 and 4.9 contain a sample instantaneous vorticity contour plot, an average streamline plot and an interpretation graphic for unducted and ducted rotor edgewise flight cases respectively. Carefully observing instantaneous vorticity contour plots spaced 2.5 ms sequentially for the edgewise flight experiments, one can notice tip vortices emerging from both sides of the two rotors in the picture, motor wake, and the effect of duct and motor wake on tip vortices. These are difficult to show using a single instantaneous vorticity plot because of vorticity due to motor wake contaminating the flow, and hence a representative image describing the observations is included in the figures.

In the unducted case, the tip vortices due to the leading side (left side) of the left rotor are seen to retain circular shape. Tip vortices due to the lagging side (right side) of the left rotor are coherent when generated, but they soon interact with the tip vortices due to

the leading side of the right rotor, causing the vortices to lose their form within one rotor rotation. The same happens with vortices due to the leading side of the right rotor. The lagging side of the right rotor is out of the PIV frame, but the vortices due to it are expected to behave much like those due to the leading side of the left rotor except that they may interact with the wake due to the right side rotor motor.

In the ducted quadrotor case, almost all tip vortices lose their shape right as they form due to interaction with the duct and its wake. Contrary to the hover cases, the unducted quadrotor in edgewise flight produces more distinct vortices compared to the ducted quadrotor. The duct which used to separate out the flow due to the two adjacent rotors in hover cases now causes the vortices to break up as the edgewise flow pushes them against the duct.

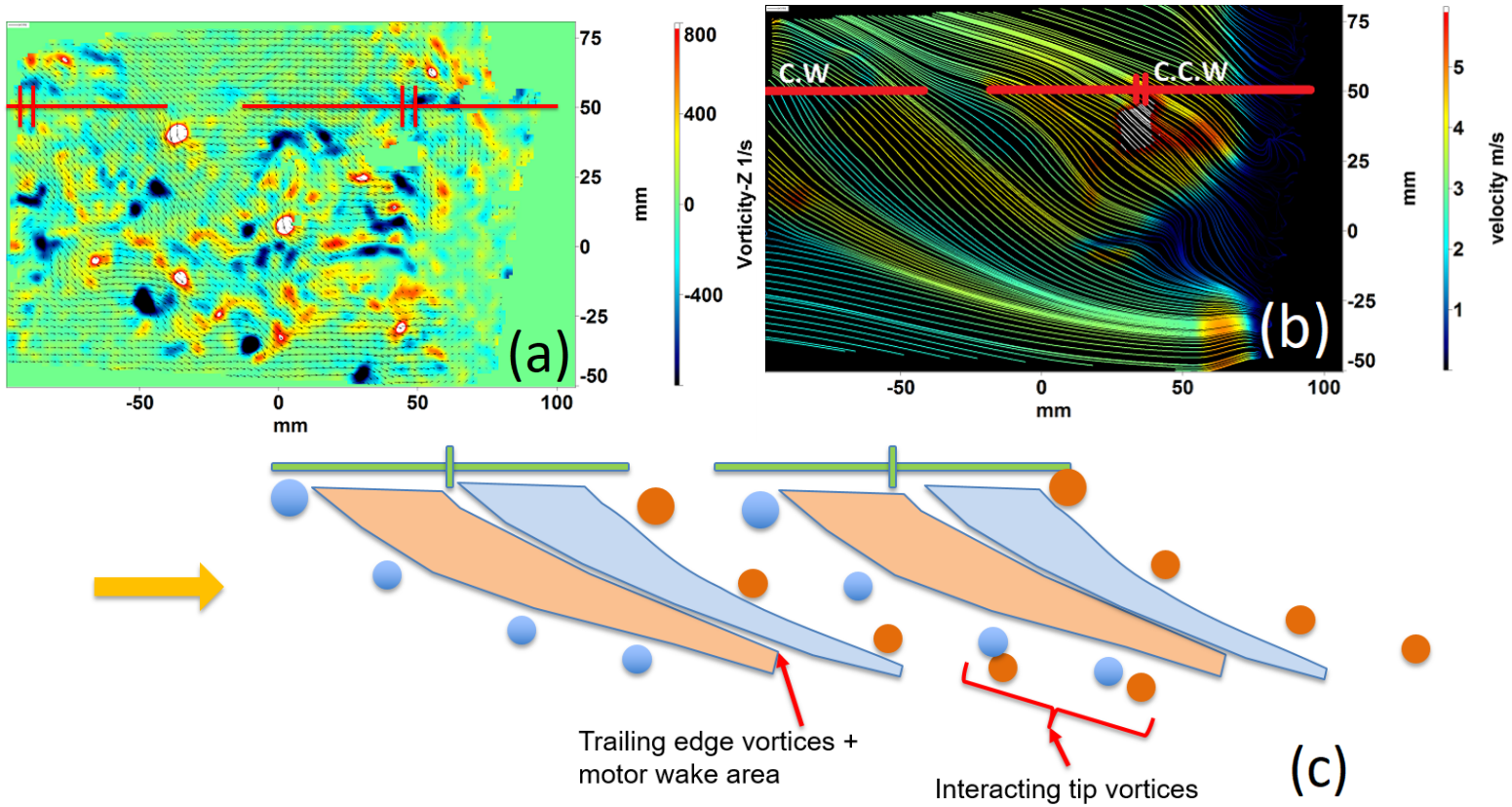

Figure 4.8: Unducted Quadrotor in 3 m/s edgewise flight: (a) Vorticity plot (b) Time averaged streamline plot (c) Interpretation

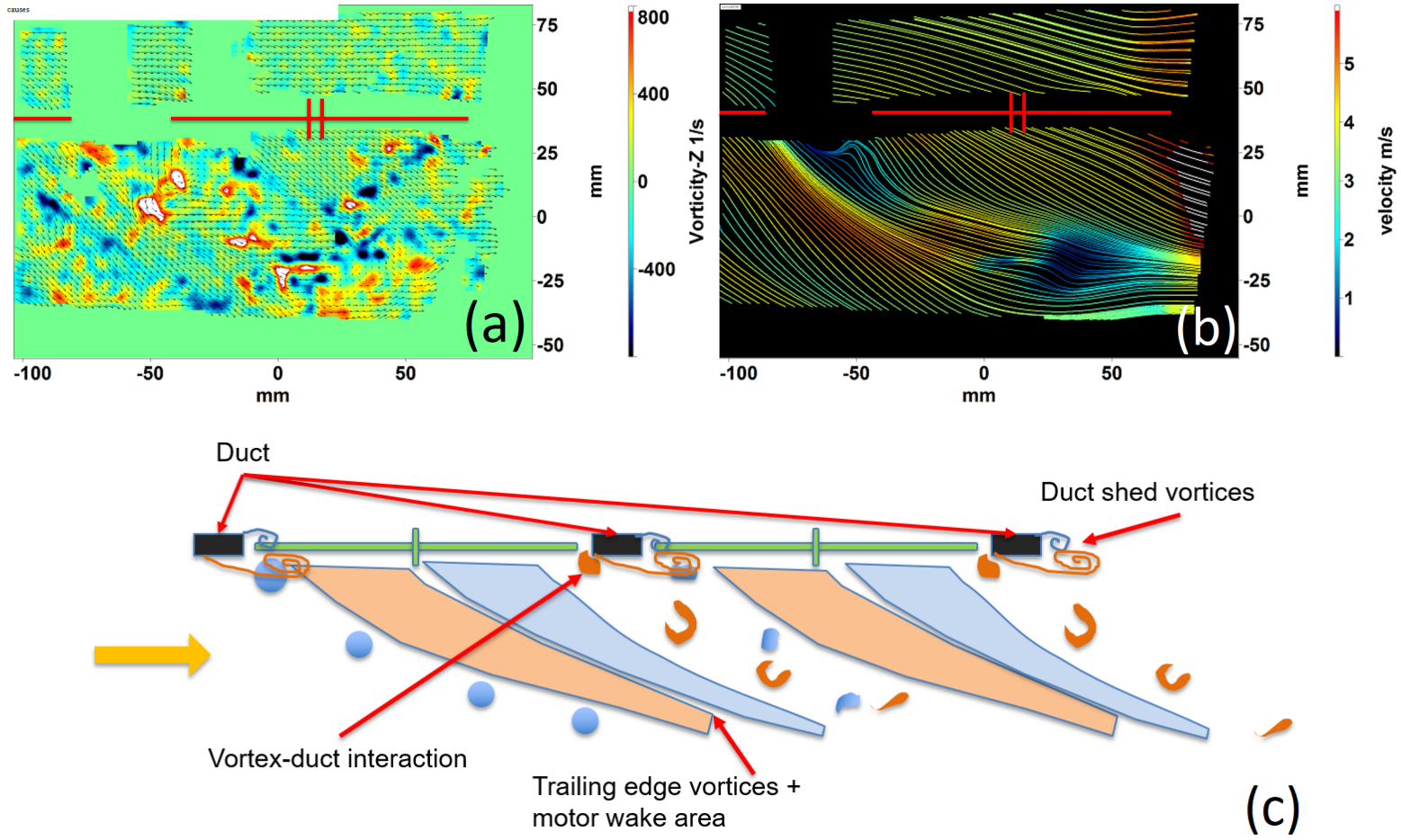

Figure 4.9: Ducted Quadrotor in 3 m/s edgewise flight: (a) Vorticity Plot (b) Time average streamline plot (c) Interpretation

4.2.2 Hover performance measurements

Table 4.3 gives measured average thrust and torque values for all the cases.

C_T found for both the 2500 RPM cases through thrust measurements comes very close to that found for 1280 RPM ducted case, and are higher than the 1280 RPM un-ducted case. Comparing C_Q values, the un-ducted 1280 RPM case has the highest torque among all cases. Therefore, the FM is also lower for the case. This confirms that higher inter-rotor wake interactions seen in Figures 4.3 and 4.5 for the 1280 RPM un-ducted case are responsible for its low C_T, high C_Q and low FM. Load measurements were done for 3500 RPM ducted and un-ducted cases too to confirm that the drastic change in C_T, C_Q and FM going from 1280 RPM to 2500 RPM is primarily due to interactions only and not just a pure *Re* effect.

Another observation while comparing the FM of these quadrotor experiments with the single rotor experiments is that the FM of the highly cambered rotors here is noticeably higher than FM of symmetric, un-twisted rotors used in the single rotor experiments. This is consistent with prior low-*Re* airfoil studies where it is reasoned that high camber increases the lift-induced torque contribution whereas torque due to viscous parasitic drag does not change as much by the change in camber.

Table 4.3: Quadrotor thrust and torque measurements for hover experiments

Case	**Thrust (N)**	C_T	**Torque (N-mm)**	C_Q	C_T/C_Q	**FM**
Un-ducted, 1280 RPM	0.025	0.0192	0.56	0.0065	2.96	0.29
Un-ducted, 2500 RPM	0.118	0.0236	1.85	0.0056	4.23	0.46
Un-ducted, 3500 RPM	0.219	0.0223	3.40	0.0053	4.26	0.45
Ducted, 1280 RPM	0.031	0.0233	0.50	0.0058	4.01	0.43
Ducted, 2500 RPM	0.120	0.0239	1.72	0.0052	4.61	0.50
Ducted, 3500 RPM	0.226	0.0230	3.38	0.0052	4.40	0.47

4.3 Conclusions

1. Quadrotor inter-rotor wake interactions for the 2500 RPM cases are lower than 1280 RPM cases.

2. C_T, C_Q, and FM for all 2500 and 3500 RPM cases match those for ducted 1280 RPM case indicating that high level of inter-rotor wake interactions may be the reason for the performance loss in 1280 RPM un-ducted rotor case.

3. A duct has a significant effect on inter-rotor wake interactions and wake spread in hover.

4. Vortices due to neighboring rotors interact even at higher *Re* for quadrotor in edge-wise flight.

5. The presence of a duct disturbs tip vortices due to all rotors on a quadrotor in edge-wise flight.

6. Under high thrust conditions, interactions between rotors are less.

CHAPTER 5
SIDE-BY-SIDE ROTORS IN HOVER

In-plane multirotor UAVs such as Quadcopters, hexacopters, and octocopters are popular platforms for various commercial and recreational applications. Chapter 4 included flow visualization and performance measurements on a small size quadrotor setup as a special case of in-plane multirotor. This chapter is more generalized for use in any in-plane multirotor configuration. All in-plane multirotors can be interpreted as pairs of rotors placed side-by-side. Hence studying one pair of side-by-side rotors at a range of conditions should provide a fair idea about all possible in-plane configurations. This study includes high-speed stereo particle image velocimetry and performance measurements on a setup comprising two counter-rotating side-by-side rotors. Some instantaneous and mean flow field results are presented here for a range of test conditions along with analysis and discussion.

The uncertainty estimates and the test procedure for these experiments are identical to those mentioned for the coaxial rotor hover experiments in chapter 3 as the setup is the same. Hence, these are not repeated here.

5.1 Experimental Setup

5.1.1 Setup description

The setup used here is the same as that described in chapter 3 for hover experiments. The upper rotor setup attached from the ceiling was telescoped down to the level of the lower rotor. The lower rotor assembly being on a sliding rail, it was moved around to achieve a range of axis shifts. The SPIV plane was kept 32 mm off the plane of the rotor axes towards the cameras to avoid laser shadows and obstructions due to the rotor mounts, as depicted in

Figure 5.1. The left-hand side rotor rotated counter-clockwise and the right-hand side rotor rotated clockwise when seen from above.

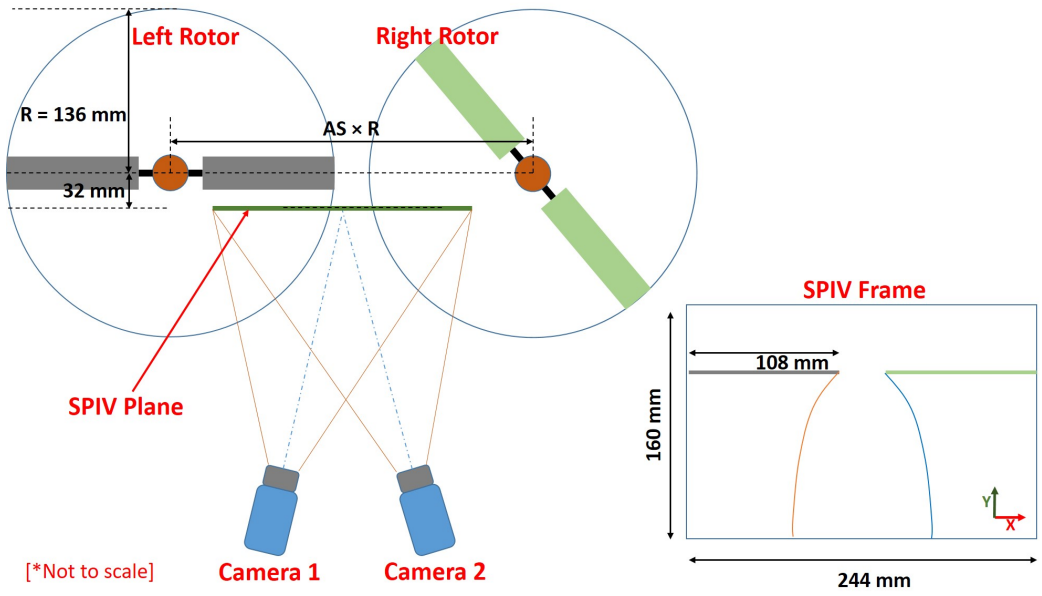

Figure 5.1: SPIV measurement plane locations

5.1.2 Test conditions

The experiments were performed at two separate rotor blade tip Reynolds numbers (Re) of 40,000 (40k) and 80,000 (80k). Rotor RPM was varied to change the Re. The rotors were operated at a constant average coefficient of thrust (C_T) of 0.004 and the torques on both were matched to depict steady hover flight condition by adjusting blade pitches. The distance between the rotor axes or axis shift (AS) was varied from 2.1 $\times$ R to 2.5 $\times$ R. Table 5.1 lists test conditions.

Table 5.1: Test conditions for bi-rotor experiments

Test Conditions	
Rotor tip *Re*	40,000, 80,000
AS	2.1, 2.2, 2.3, 2.4,
	2.5 (performance only)
C_T	0.004 (average per rotor)

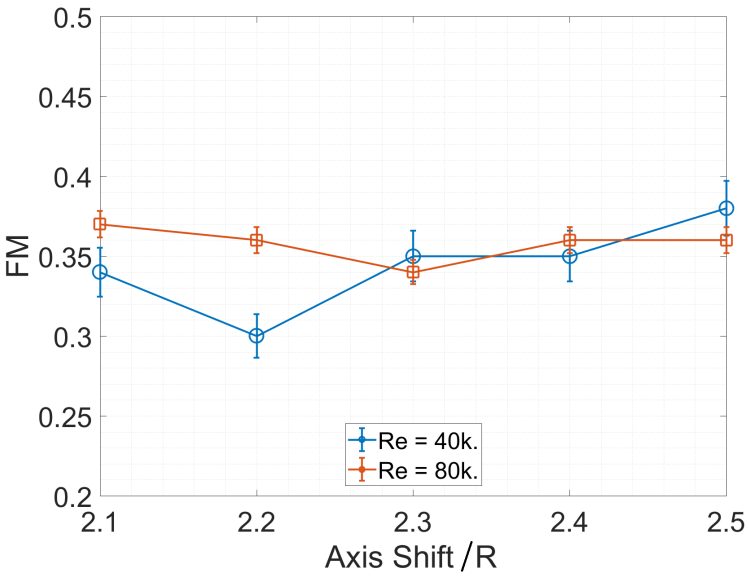

Figure 5.2: Figure of Merit plot for all side-by-side rotor hover test cases

5.2 Results

5.2.1 Performance measurements

Performance of the rotors in hover is evaluated using thrust and torque measurement results. The load cell readings in Newtons and Newton-meters for thrust and torque, respectively, are converted to the non-dimensional Coefficient of Thrust (C_T) and Coefficient of Torque (C_Q) form to account for the variations in rotor speed and dimensions while comparing among cases. The coefficients of thrust and torque are used to find Figure of Merit (FM) which is a measure of efficiency (or power requirement) of a rotor compared to the theoretical best found using the momentum theory. Here we compare the rotor performance among all cases using FM. The expression used for computing FM of the bi-rotor setup is

given in equation (5.1). Figure 5.2 is a plot of FM for the rotor tests performed at two *Re* at a range of axis shifts.

$$FM_{Combined} = \frac{(C_{T_L}^{3/2} + C_{T_R}^{3/2})/\sqrt{2}}{(C_{Q_L} + C_{Q_R})} \tag{5.1}$$

5.2.2 Instantaneous flow fields

Figure 5.3 shows how the instantaneous flow field looks like for each of the test cases. The vorticity contour plots in the figure help in identifying tip vortices and trailing edge vortex sheets which are the most prominent features in a rotor wake. When following the wake from the left-hand side rotor, red circular spots correspond to tip vortices and coherent blue streaks correspond to trailing edge vortex sheets. Similarly, when following the right-hand side rotor wake, blue circular spots correspond to vortices and coherent red streaks correspond to trailing edge vortex sheets. The horizontal black lines in the plots represent rotors.

5.2.3 Mean flow fields

The mean velocity field presented here was obtained after time averaging 200 instantaneous velocity fields. The streamline plots for all cases in Figure 5.4 show how the overall flow develops around the rotors. The white lines in the plots represent the rotors.

Figure 5.5 contains plots of non-dimensionalized inflow and outflow velocity profiles extracted at a distance of 0.1R from the rotor plane. Here, outflow velocity is being referred to the axial flow right below the rotors, indicating flow going out of the rotor plane. The three velocity field components from SPIV measurements were interpolated three folds increasing the resolution by a factor of three before extracting the profile for obtaining smoother curves. The red and black vertical dotted lines mark the location of the left and

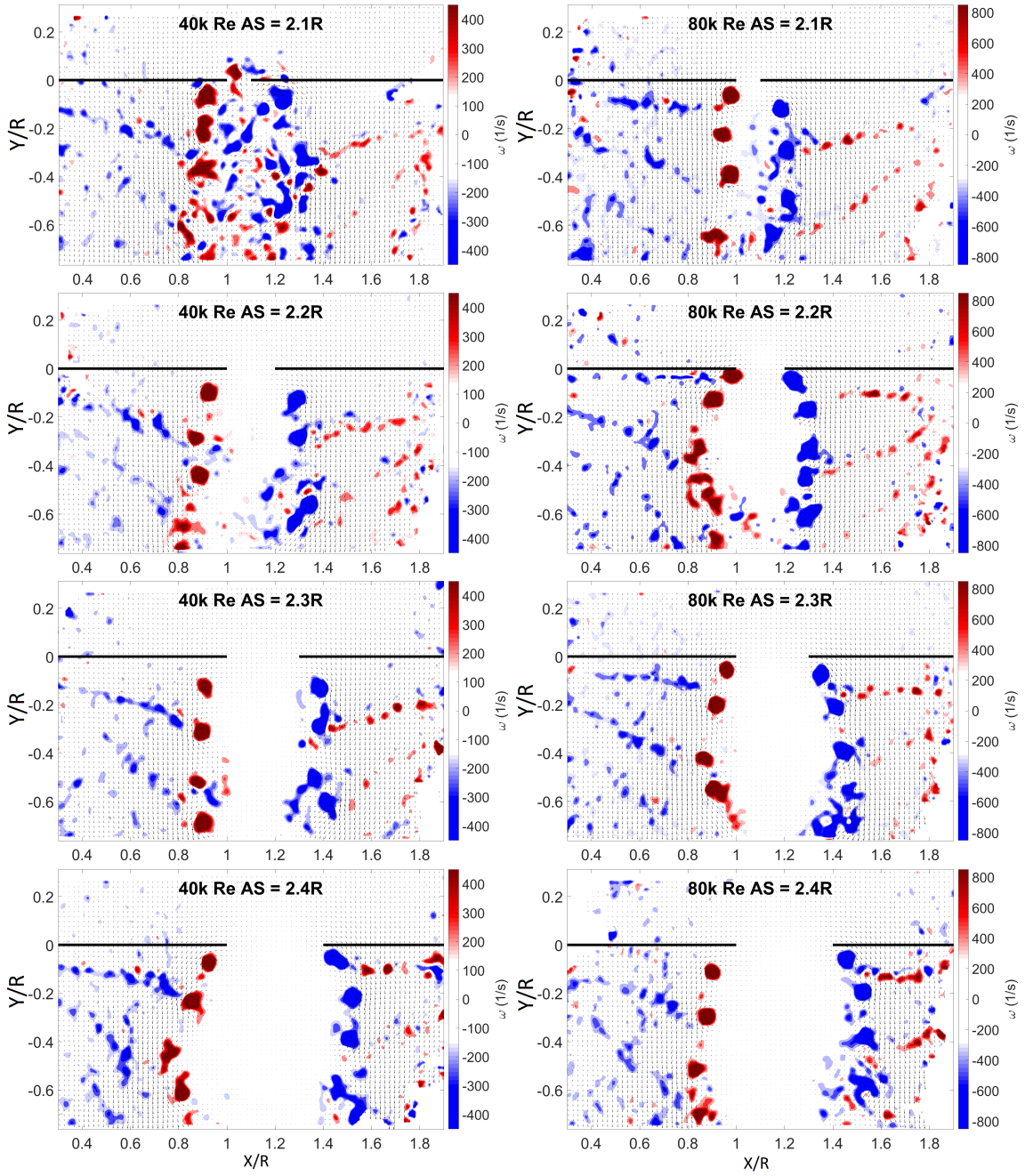

Figure 5.3: Instantaneous vorticity contour plots for hover, side-by-side rotors

right rotor edges to help understand the velocity profiles w.r.t. location of the rotors. Inflow and outflow velocity profiles are useful in estimating the contribution of different sections of rotor disk in imparting momentum to the flow, and hence in generating thrust.

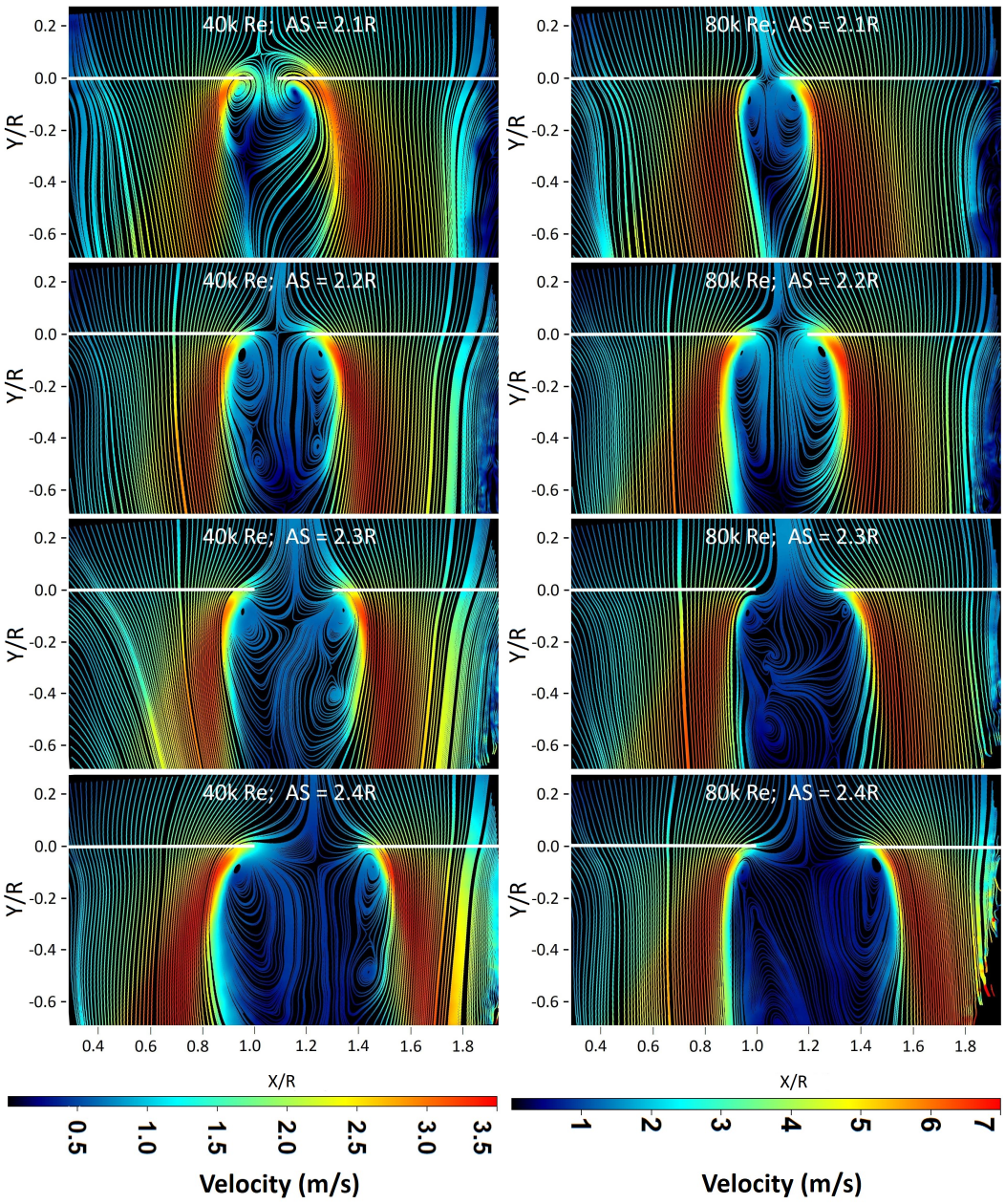

Figure 5.4: Time averaged flow field streamline plots for side-by-side rotor configuration.

5.3 Discussion

Starting with the Figure of Merit plot in Figure 5.2, it is seen that the 80k *Re* cases do not show any noticeable variation in FM over the range of axis shifts. However, the FM of 40k *Re* cases tends to increase slightly with an increase in distance between the rotors. This slight increase for 40k *Re* cases too is significant only for AS $\leq$ 2.3R after which it is

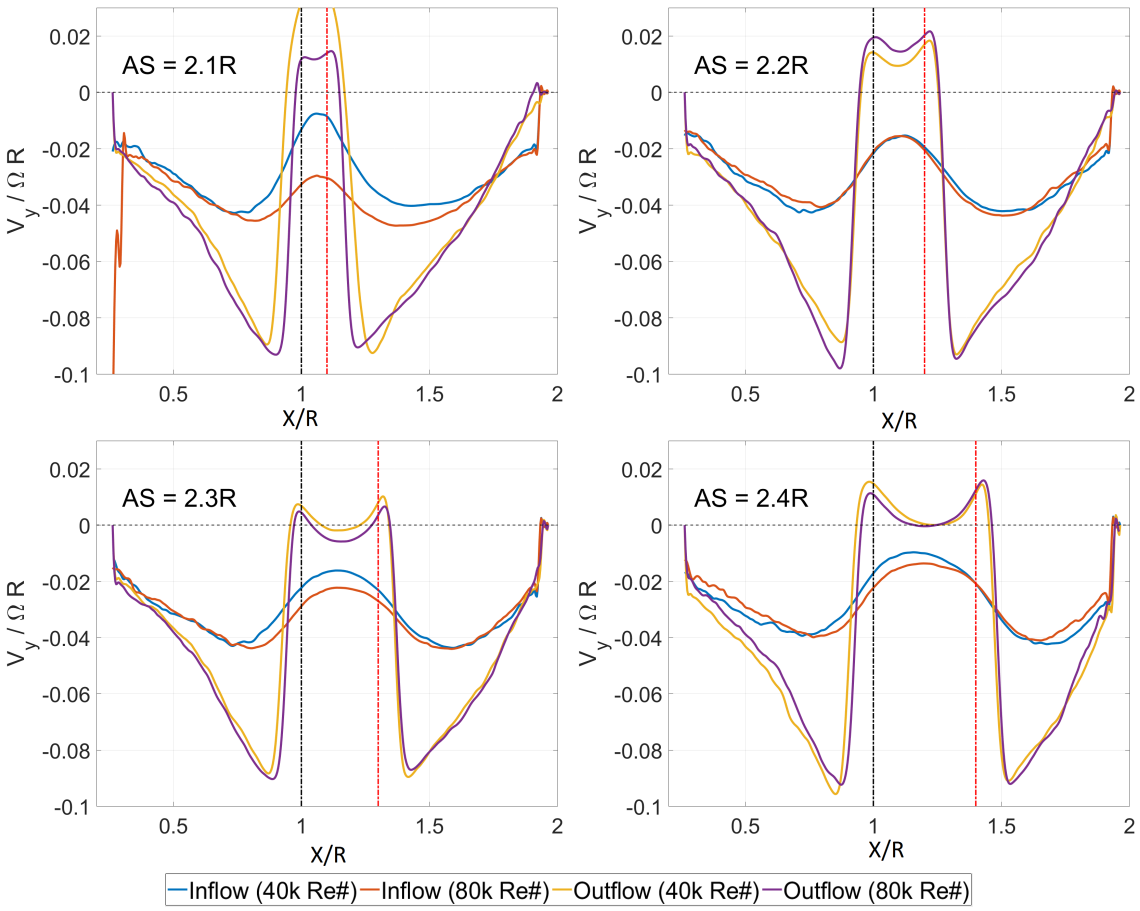

Figure 5.5: Time averaged flow field inflow and outflow velocity profiles for side-by-side rotor configuration.

approximately similar to 80k *Re* cases.

Studying the instantaneous vorticity contour plots in Figure 5.3, it is observed that the rotor tip vortices due to the two adjacent rotors interact with each other for small axis shift values. The tip vortices are seen to deviate from the trajectories expected in a typical rotor wake. They lose their coherent structure in about a rotor rotation and get split into small spots of high vorticity in the region between the rotor wakes. Very often, consecutive tip vortices from the same rotor are seen to roll about each other after getting disturbed from their trajectory by velocity induced by vortices from the neighboring rotor. The direction of vortex roll-up is the same as the direction of vorticity in the vortices. These pairs of

vortices eventually merge and then split into spots of high vorticity soon after.

Such wake interactions are relatively higher for 40k *Re* ca•ses compared to 80k *Re* cases. With an increase in axis shift, the trajectories of tip vortices tend to get more predictable and the region between rotor wakes become free of sporadic flow. Lesser wake interactions at higher axis shifts are in a way obvious and expected as velocity induced by vortices decay with the distance outside the solid body rotation core area. The wake should in principle become like that of a single isolated rotor as axis shift tends to infinity. Figure 5.6 contains explanatory sketches for the instantaneous vorticity contour plots in Figure 5.3, depicting behaviour of major wake features under a separate range of conditions.

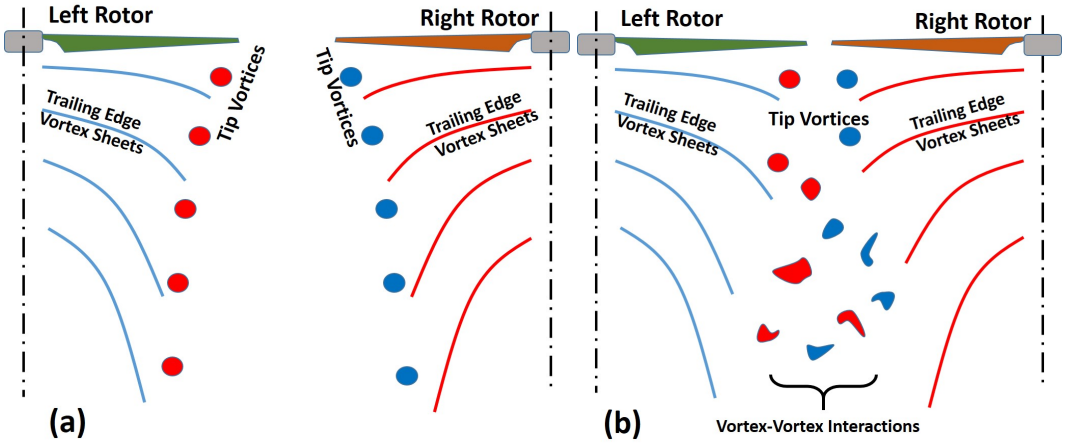

Figure 5.6: Instantaneous flow field plot concept sketches for (a) High *Re* or large axis shifts (b) Low *Re* or small axis shifts

The low *Re* cases have more wake interactions, probably because the tip vortices are weaker in terms of circulation and the downwash convecting them downward is also low. These slow-moving vortices with low circulation are more vulnerable to velocities induced by flow features in close proximity such as vortices from the neighboring rotor. At high *Re* (and hence higher thrust values), the vortices are stronger and they also get less time to get affected by other disturbances due to stronger downwash. The relative strength of

vortices can be judged by comparing vorticity magnitudes in the instantaneous vorticity contour plots. The time-averaged rotor outflow velocity gradient near the rotor tip is apparent through the plots in Figure 5.5, which is also indirectly indicative of the vortex strengths in the two Re cases.

Similar observations were made regarding relatively higher wake interactions for low *Re* cases of the quadrotor in chapter 4. There, the *Re* 8630 test case (1280 RPM) showed significantly higher wake interactions compared to *Re* 16856 case (2500 RPM) as seen in the Figure 5.7. The FM for the lower *Re* case was also much lower than the other two higher *Re* cases (see Table 5.2) just like it is in the current study where the FM is lower for 40k *Re* cases at low AS. It is possible that the poor rotor performance at small axis shifts at low *Re* is because of flow that is induced over the blades by interaction with tip vortex cores of the adjacent rotor. Tip vortex cores are known to be larger in size for low *Re* rotors [105]. If interactions of rotor blades with adjacent rotor tip vortices is a factor, then the phase difference between the rotors should also play an important role in performance. Verifying that will require a setup where the rotors are mechanically linked to allow locking their phase with respect to each other. Here for the two-bladed rotors, the phase difference can be defined as the acute angle between the lines connecting rotor blades of the two adjacent rotors rotating at the exact same speed.

Comparing FM data of the current bi-rotor tests in Figure 5.2 with those from the tests on quadrotor in Table 5.2, it can be noticed that rotors in the current tests perform worse than the quadrotor rotors despite being operated at a much higher Re. The biggest difference between the two setups (other than size) is blade geometry (which is described in Table 5.3). The blades used in this setup are symmetric and more like those for large scale helicopters whereas the quadrotor blades are highly cambered. Such highly cambered blades are ideal for low Reynolds number rotors only where the viscous skin friction drag is

high enough to afford highly cambered airfoil designs which otherwise would have caused a much larger share of pressure drag.

Table 5.2: FM for quadrotor tests taken from chapter 4.

Case	**FM**	**Case**	**FM**
Un-ducted, 1280 RPM	0.29	Ducted, 1280 RPM	0.43
Un-ducted, 2500 RPM	0.46	Ducted, 2500 RPM	0.50
Un-ducted, 3500 RPM	0.45	Ducted, 3500 RPM	0.47

It is noticed from the streamline plots in Figure 5.4 that the mean rotor wakes from the two rotors tend to stay farther away from each other for 80k *Re* cases, suggesting lower wake interactions at higher *Re*, which are apparent from the instantaneous vorticity contour plots as well. As the axis shift increases, the flow around the rotors slowly tend to be similar to that expected for an isolated rotor, with 80k *Re* cases leading the change. The streamline plot for *Re* 40k, AS = 2.1R is noticeably different from the rest. The first plot shows high-velocity magnitudes in the region between the two rotor wakes due to inter-rotor wake interactions, and the streamlines in the last plot (Re 40k, AS = 2.4R) are as if results from two isolated rotors are put side-by-side. All other cases in between show how the interactions between the rotors evolve with axis shift and *Re* into two isolated rotors in terms of the mean flow.

The inflow and outflow profile plots in Figure 5.5 contain some common features among cases. Outflow profiles under both rotors are wedge-shaped with velocity magnitude increasing while going from rotor hub to tip, and dropping back to zero steeply right before the tip. The peak in outflow velocity profile is consistently found close to r = 0.9R span-wise location for both rotors for all cases except *Re* 40k AS = 2.1R, where it is seen to be slightly inboard (close to the hub). Such a wedge-shaped feature is common for most rotors, especially if the blades are simple rectangular blades like the ones in this study. As mentioned earlier, inflow and outflow profiles provide an estimate of thrust generated by

Table 5.3: Description of the quadrotor setup used in experiments in chapter 4.

Parameter	**Value**	**Parameter**	**Value**
Radius (R)	66 mm	Blade planform	Untwisted, Tapered
Camber	14%	Chord length (c)	19.5mm @ r/R = 0.2 15.3 mm @ r/R = 1
Blade thickness	7%	Blade pitch angle (α)	10^0
Adjacent rotor axis shift (AS)	160 mm	Duct radius	73 mm

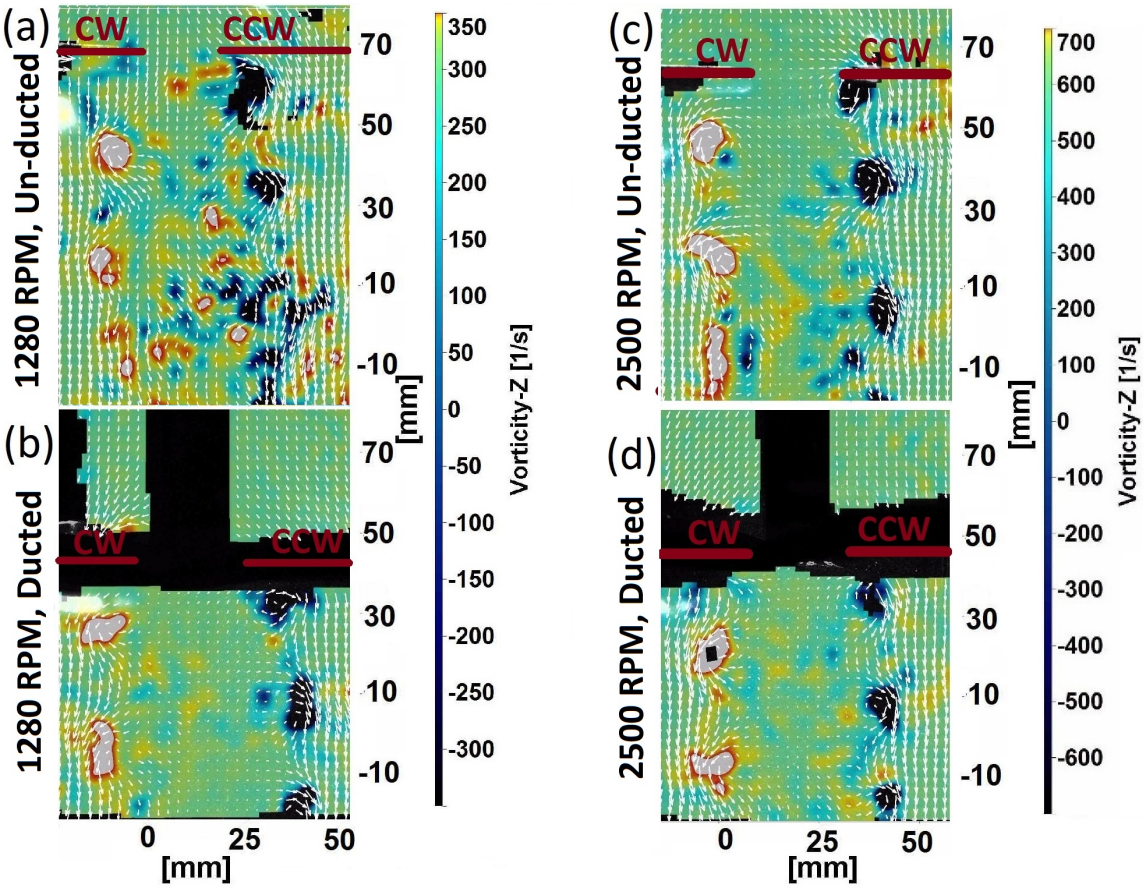

Figure 5.7: Instantaneous vorticity contour plots for quadrotor tests in chapter 4

different sections of the rotor, and hence their shape is dependent on rotor blade geometry (taper and twist). Inflow velocity profiles peak around r = 0.75R (and slightly inboard for *Re* 40k AS = 2.1R case). The outflow velocity profile peaks are much sharper than the inflow velocity peaks due to a sudden drop in thrust near the blade tip and the resultant tip vortices.

It should be noted that the velocity profiles, which are non-dimensionalized using rotor tip speed, are almost exactly the same for the two *Re* for AS = 2.2R, 2.3R, and 2.4R. This may mean that at least in this *Re* range, *Re* does not have any significant effect on the way inflow and outflow velocities get induced when the rotors are farther than 2.2R. Out of the two cases on the AS = 2.1R plot, the 80k *Re* curves still look similar to the other axis shift cases but the 40k *Re* plots have higher upward directed inflow and outflow velocities between the rotors. But for all cases within the range, it should be possible to come up with a rough estimate of the velocity profiles, and hence span-wise thrust distribution on side-by-side rotors based on the presented results. Figure 5.8 is a sketch of a typical side-by-side rotor inflow and outflow velocity profiles based on the mean velocity profiles for the test cases presented in Figure 5.5.

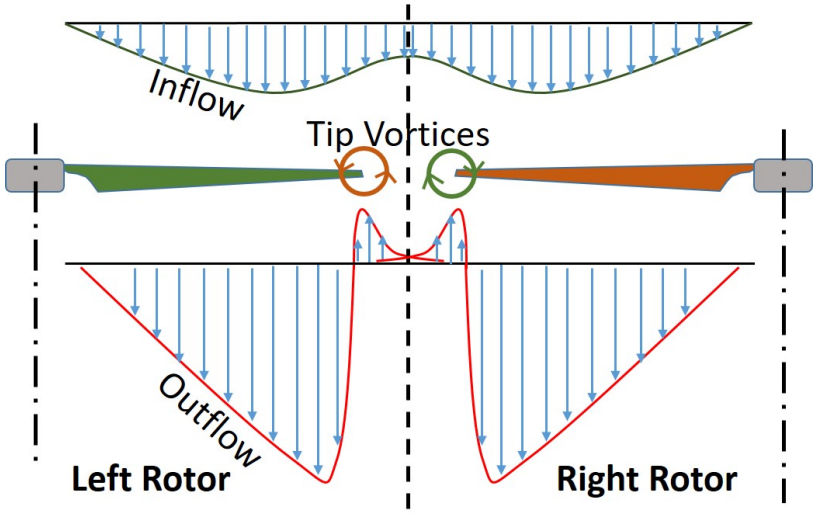

Figure 5.8: Mean inflow and outflow concept sketches.

The information on outflow or downwash velocity profiles is also instrumental in deciding on fuselage and payload placement under a UAV while designing it. The objective here is to minimize download on the rest of the structure and payload from the rotor downwash to reduce rotor thrust lost in internal force.

5.4 Conclusions

The interactions between the wakes of two side-by-side rotors as a function of the distance between the rotors and their *Re* were studied from both instantaneous and mean flow field perspectives in this study. A dip in performance was observed for cases with rotors very close to each other at low Re. It was hypothesized that the interaction of rotor blades with the tip vortex cores of the neighboring rotor blades at small axis shifts could be a reason for the effect on efficiency. However, more focused tests are needed to confirm this. The instantaneous flow field measurements indicated high inter-rotor wake interactions for small axis shifts causing rotor wake features to distort, lose coherent form and deviate from their typical trajectories.

The time-averaged streamline and inflow-outflow velocity profiles brought out commonality among the range of tests in this study. Prominent instantaneous flow features and mean velocity profile traits were identified for the test cases which are expected to guide rotor wake and performance estimates on a wider range of vehicle designs and flight conditions.

Briefly summarizing the key findings:

1. Rotor hover performance is adversely affected when adjacent rotors are in close proximity to one another.

2. Blade-vortex interactions are hypothesized to be a reason behind the noticed effect on performance.

3. High inter-rotor wake interactions were observed for close proximity rotors at low Reynolds numbers.

4. Similarities observed in instantaneous and mean flow fields for the range of tested conditions were useful in extending the understanding to a wider range of vehicle configurations.

CHAPTER 6
TANDEM ROTORS IN HOVER

The rotor configurations studied so far in the thesis are single rotor, single rotor with duct (chapter 2), coaxial rotor (chapters 3), quadrotor (chapter 4), and in-plane multirotors (chapter 5). This chapter's focus is on tandem rotors, which may be considered as a superset of most other multirotor configurations such as coaxial and in-plane multirotors. Here, performance and flow field observations are made for tandem rotors over a range of overlaps. All major flow interaction phenomena found in multirotors have been identified and characterized to some extent. The intention is to come up with a generalized approach which can be applied to any possible multirotor configuration for a large range of conditions.

The setup and test method used here is same as that for the coaxial and side-by-side rotor experiments. Hence setup description, uncertainty estimates, and test procedure are not being repeated here in this chapter.

6.1 Previous Studies

As of now, there has been only one experimental study aimed at measuring performance for a wide range of two-rotor configurations. Manikandan Ramasamy [115] created a two rotor setup where both rotors were supported independently, and could be shifted with respect to each other to give different axis shifts and vertical separation. The experiments were done at the tip Reynolds numbers of 275,000 and 325,000 for twisted and untwisted blades respectively. That study did not include any flow visualization or PIV. The results obtained through the low Reynolds number experiments can be compared with those by Ramasamy for understanding effects due to Reynolds number.

6.2 Experimental Setup

6.2.1 Test conditions

The tandem rotor SPIV and performance tests were conducted at two vertical separations, two Reynolds numbers and a range of axis shifts (AS) as listed in Table 6.1. The average C_T of the two-rotor setup was kept constant at 0.004 for all cases. This is similar to assuming fixed vehicle weight across all configurations at a given rotor speed (and *Re*) for a fair comparison of performance. Another condition set for the trim was torque balance, which is a must for steady hover in a vehicle. Reynolds number changes were achieved by changing rotor RPM. For attaining the described trim conditions, the collective pitches of both rotors were adjusted until the total target thrust was met and the rotor torques equalized.

Table 6.1: Test conditions for tandem rotor experiments

Test Conditions	
Rotor tip *Re*	40k, 80k
Rotor planes distance (VS)	$0.25R$, $0.40R$
Rotor axis shift (AS)	-0.25R, 0.25R, 0.50R, 0.75R,
	1.00R, 1.25R, 1.50R, 1.875R, 2.00R
	$0.00R, 2.50R$: Performance measurements only
Average C_T per rotor	0.004

6.3 Results and Discussion

Across all the SPIV cases, the cameras and the laser optics were kept fixed. The PIV frame covered the right half of the upper rotor, which could be moved up or down to change the

vertical separation between the rotor planes. The lower rotor assembly could slide on the rail to vary axial separation between the two rotors. Figure 6.1 describes the camera and PIV plane orientation w.r.t the rotors.

6.3.1 Definition and usage of terms

The performance terms such as C_T, C_Q, FM used here are defined in the same fashion as they were for the coaxial rotors in hover in . Hence, $C_{T_L}, C_{T_U}, FM_L, and FM_U$ are not Coefficients of Thrust and Figure of Merit in the true sense. This must be kept in mind while comparing the results presented here with other studies.

6.3.2 Performance measurements in hover

The thrust and torque measurement results for all the cases are consolidated to FM and presented in the form of plots in Figure 6.2 in the interest of space. The figure also includes results from similar performance measurement study on high *Re* tandem rotors by Ramasamy et al. [115] for a comparison. The expression used for finding FM of the combined system is the same as that used for coaxial rotor hover experiments in chapter 3.

Observing Figure 6.2, it is seen that the combined FM of tandem rotors increases gradually with an increase in axis shift, and the lower rotor is a bigger contributor in this change. This is because as axis shift increases, the rotor overlap decreases causing a smaller fraction of the lower rotor to experience downwash from the upper rotor. Downwash from the upper rotor causes an increase in the inflow through the lower rotor leading to higher induced losses at the lower rotor. Hence, the lower rotor performance is worst for the coaxial arrangement (AS = 0), where the lower rotor is fully under the upper rotor with a huge fraction of its disc area facing downwash. The lower rotor performance is seen to match the upper rotor performance between AS = 1 and AS = 1.5. A similar trend for lower rotor performance is noticed in Ramasamy's data, too.

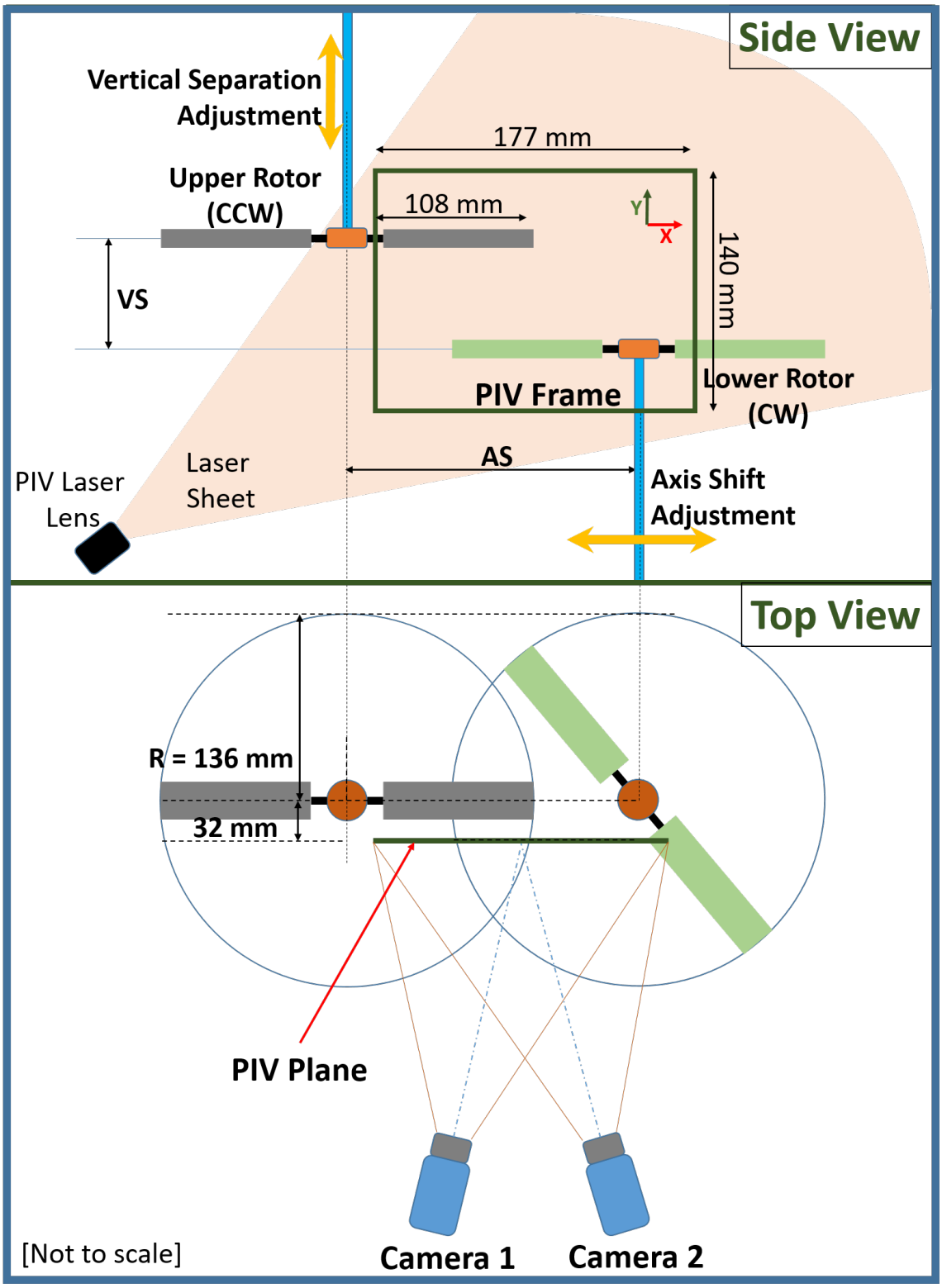

Figure 6.1: Schematic diagram of the tandem rotor setup and PIV plane

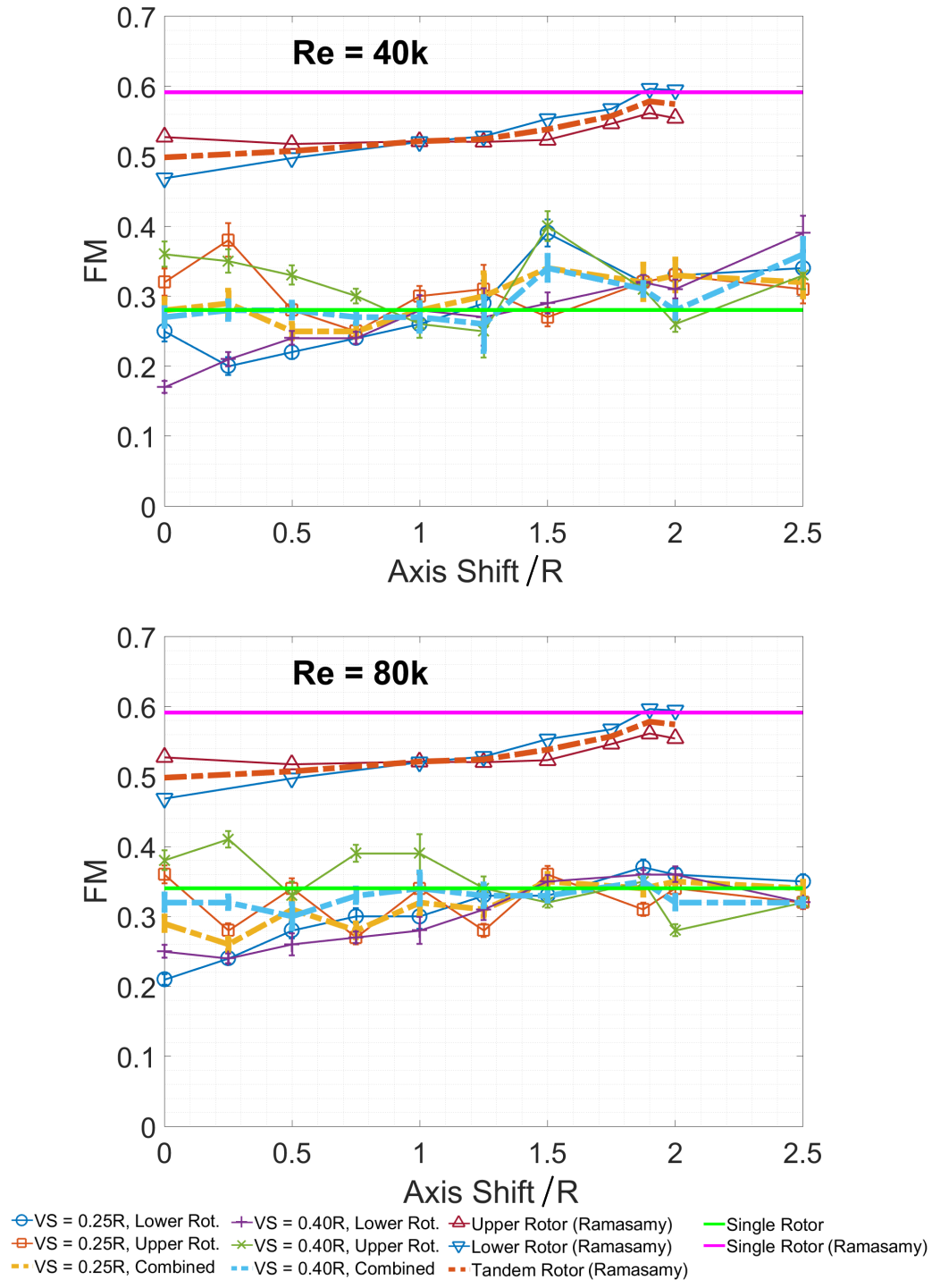

Figure 6.2: FM of individual rotors and combined system at the range of tested configurations and conditions. Comparison with data for 3-bladed twisted rotor setup at 183k *Re* by Ramasamy *et al.* [115]

Performance anomaly and explanation

Just like in the case of coaxial rotors in hover, here too we find the upper rotor performing better than the single isolated rotor for cases with significant overlap. This again can be due to the same viscous swirl recovery effect described in 3.5.4.

The performance trends for the current low Re cases are not monotonic like those by Ramasamy for high *Re* tandem rotors. This is probably because the wake features such as vortices and trailing edge vortex sheets are larger in size (relative to rotor dimensions) at low *Re* due to viscous effects, making the flow induced at the rotor blades due to these features highly sensitive to the relative rotor locations and phases over the whole range of axis shifts. In full-scale rotors, the tip vortex cores are very small compared to the blade span, and hence very small portions of the rotor blade actually get impinged by them, limiting the impact that such interactions have on the overall performance. A synchronized rotor setup can be useful in investigating the observation and the hypothesis, as rotor blade interactions with the wake features can be precisely controlled.

The FM of the present low *Re* rotors tests are much lower than Ramasamy's high *Re* tests, mostly because of higher viscous profile drag losses and also because of the difference in rotor geometry affecting induced losses. The zero lift torque coefficient for Ramasamy's untwisted two-bladed rotors was about 0.00014, whereas that for the current rotors at 40k *Re* is 0.00021.

6.3.3 Mean velocity field rotor inflow and outflow profiles

The time-averaged flow fields were computed using 200 instantaneous PIV frames. The average velocity fields were found to be within 2% of those obtained using 150 frames and within 0.5% of those obtained using 175 frames for all cases, indicating a convergence of

the results.

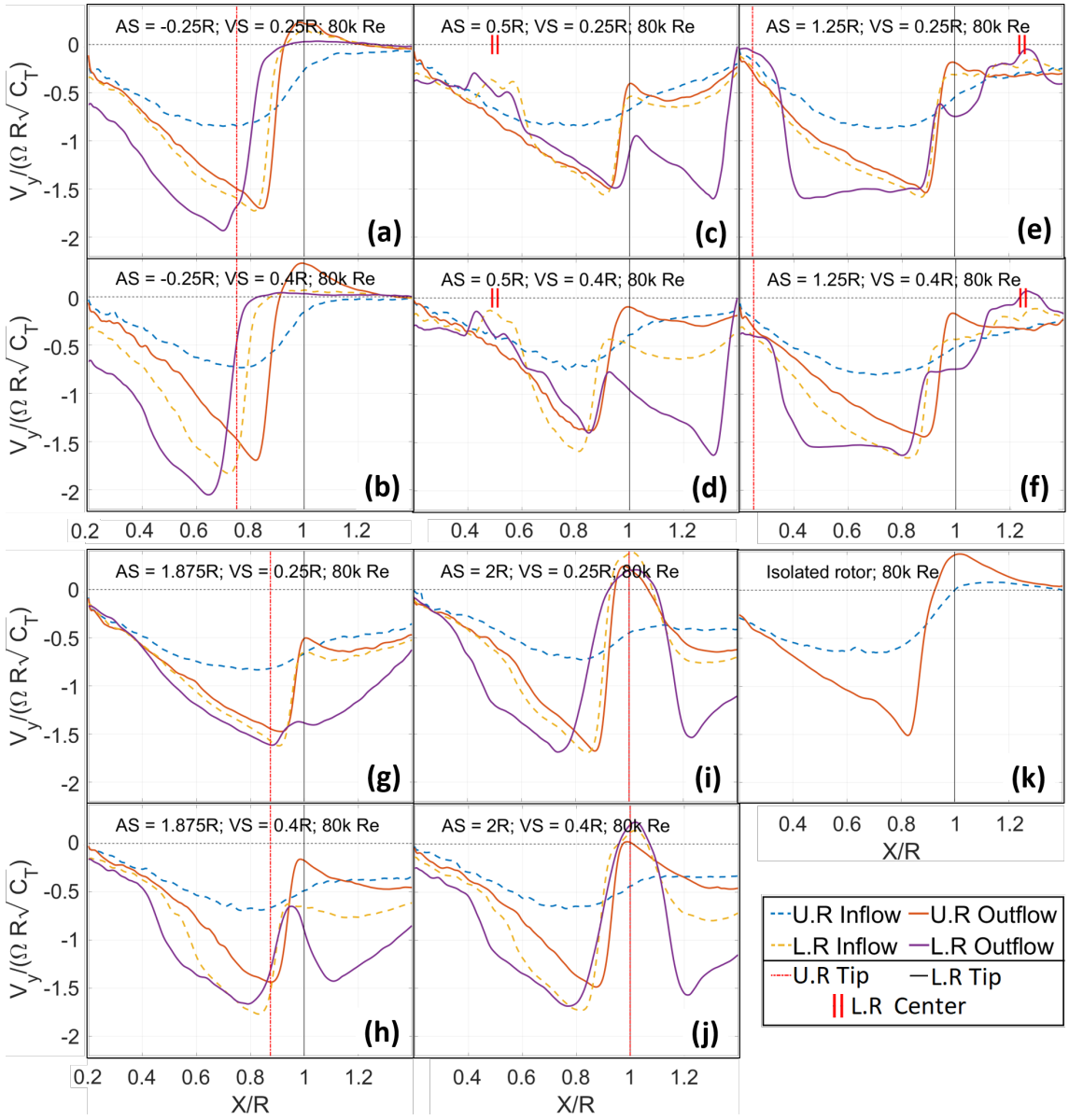

Figure 6.3: Inflow and outflow velocity profiles for the upper and lower rotors for selected cases

Figure 6.3 contains plots for rotor inflow and outflow for both rotors for all cases. The inflow and outflow data presented here are extracted from a distance of 0.1R above and below the rotors, respectively, for both rotors. The red and black vertical dotted lines mark locations of the lower and upper rotor edges, and the double red lines mark the lower rotor center to help understand the velocity profiles with respect to the rotor locations. These

profiles give a picture of the downward momentum imparted by the individual rotors at the plane of interest. For all configurations, the plots for 40k Re and 80k Re cases have similar trends and vary only in magnitude and sharpness of features. Therefore, only 80k Re cases have been presented here.

Comparing the plots of all VS = 0.40R cases with corresponding VS = 0.25R cases, VS = 0.40R cases are found to be similar to VS = 0.25R cases at slightly lower axis shifts. This is because the upper rotor wake constricts more as it reaches the lower rotor plane at higher vertical separations. Thus, the results presented here can be applied for a range of vertical separations for obtaining approximate results if corrections are made to account for the wake constriction.

Outflow velocity profiles for the upper rotor are triangular in shape for all cases, with downward velocity increasing gradually while going from the hub towards the tip of the upper rotor and dropping back to zero sharply right before the tip. This is similar to the profile due to an isolated rotor presented in Figure 6.3(k). The downwash profile shape of an isolated hovering rotor depends on the thrust generated by each section of the rotor blade, and hence on the blade geometry (twist and taper). The downwash profile of a typical rectangular untwisted blade rotor looks like the one shown here for the isolated rotor case because thrust generation increases with radial location until location close to the rotor tip where thrust generation is zero. The downwash profile also gets reflected in the shape of trailing edge vortex sheets (presented later in the paper) and evolve below a rotor as they convect with the downwash.

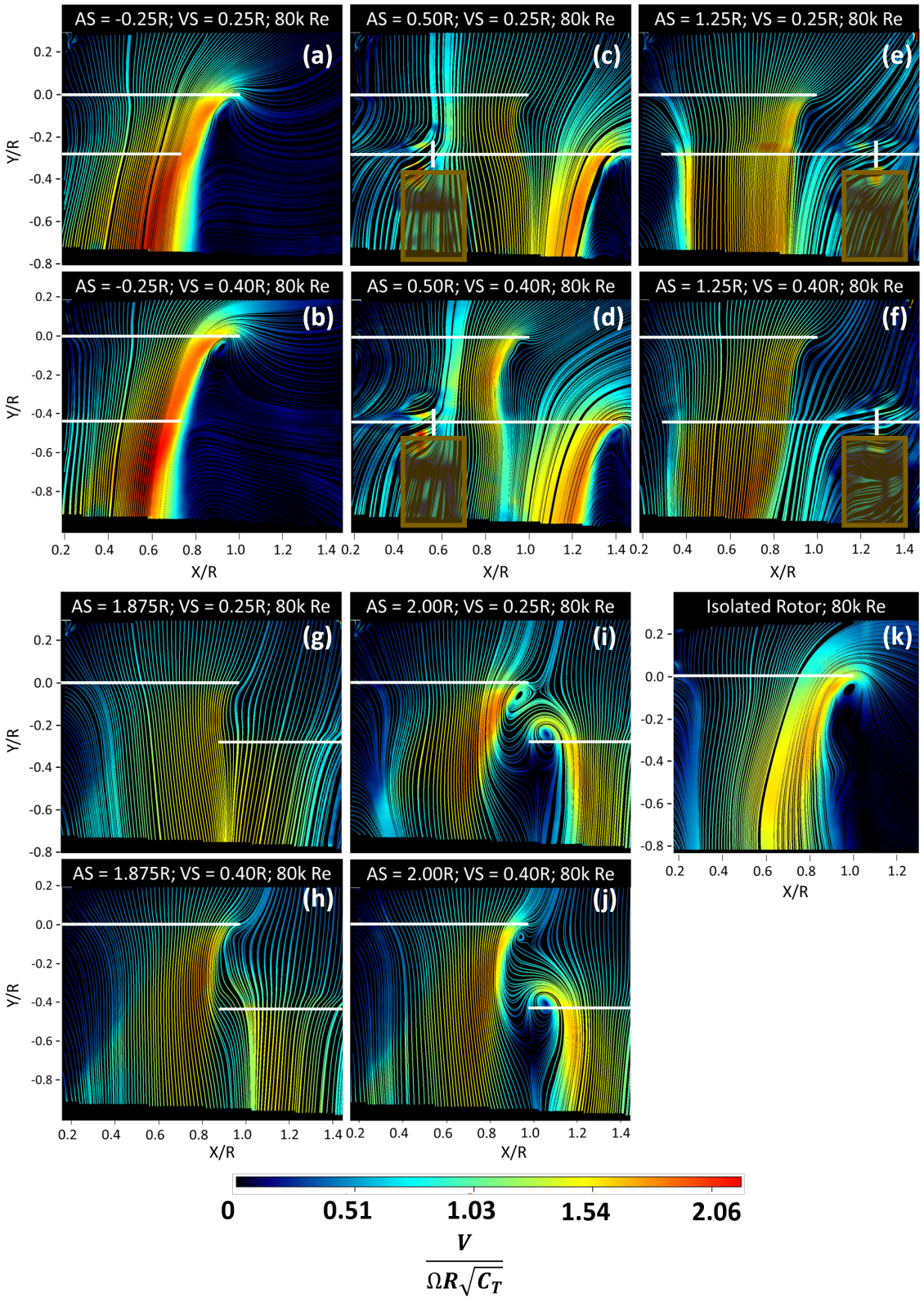

Figure 6.4: Time averaged velocity field streamline plots for selected cases

AS = -0.25R

The AS = -0.25R lower rotor outflow profiles (Figure 6.3(a,b)) comprise of just one identifiable peak as the lower rotor wake and slipstream approximately aligns with those due to the upper rotor as evident from the corresponding streamline plots (Figure 6.4(a,b)). The alignment is close for VS = 0.40R cases, resulting in the highest velocity peak among all test cases. This can be seen as triangular downwash profiles due to both rotors getting superimposed with their peaks aligned. With an increase in AS, the triangular downwash profile due to the lower rotor shifts outboard, causing two peaks in the lower rotor (or final) outflow profile plot as noticed in Figure 6.3(c,d). Of course, the final outflow profile is not a direct sum of the isolated rotor downwash profiles shifted in axis and only the profile shapes resemble addition. Outflow velocity magnitudes are highly dependent on individual rotor inflow and thrust.

AS = 0.50R to 2.00R

For AS between 0.5R and 1.00R, the inflow and outflow profiles for the lower rotor have a wavy segment due to obstruction by the lower rotor motor and mount as in Figure 6.3(c,d). Beyond 1.00R, the lower rotor mount is out of direct downwash from the upper rotor, and the left half of the lower rotor disk comes totally under the right half of the upper rotor disk. This changes the final outflow profile noticeably. The axis shifts between 1.00R and 1.50R have an almost flat final outflow profile region between the two rotors. The width of this region is directly related to the extent of wake overlap between the rotors.

The reason behind such uniform outflow profile in the section is as follows: Looking at the left half of the lower rotor, the triangular downwash profile from it is flipped compared to that due to the right half of the upper rotor. Adding these mutually flipped downwash profiles forms a trapezoidal profile. The resultant trapezoid is closer to a rectangle at higher

overlaps (like for AS = 1.00R, 1.25R) as in Figure 6.3(e,f). The trapezoidal profile starts resembling an isosceles triangle as axis shift increases to about AS = 1.875R (Figure 6.3(g)), where the lower rotor tip gets in line with the upper rotor slipstream as seen in Figure 6.4(g). The final outflow profile deviates from the ideal trapezoid or isosceles triangle as downwash profiles due to the two rotors are not identical in magnitude and the lower rotor inflow is strongly influenced by the upper rotor outflow/downwash.

The AS = 2.00R cases are similar to what one would expect for two side-by-side rotors, except that the magnitudes of thrust due to both are different, causing asymmetry. The difference in thrust indicates that the upper rotor affects lower rotor performance even when the lower rotor is not directly in the upper rotor's wake. The streamline plots for the cases in Figure 6.4(i,j) show interaction between the upper and lower rotor flows near the tips affecting lower rotor thrust.

6.3.4 Investigation of the high upper rotor performance

The hypothesis claiming viscous swirl recovery as a reason behind the better-than-expected upper rotor performance at high overlaps is verified using the swirl (out of plane) component of the mean flow field like in chapter 3. The time-averaged swirl velocity field in a $0.8R \times 0.2R$ region neighboring the upper rotor is integrated to find a spatial average. The integration area is marked by green boxes in Figure 6.5, which features two cases for illustration. The swirl velocities are normalized using $(\Omega R)\sqrt{C_Q}$ which follows the upper rotor torque. This is to separate out the swirl due to the upper rotor itself, for observing the effects due to the lower rotor while comparing cases with different upper rotor torques.

The normalized results from the process are tabulated in Table 6.2. Here, it is seen that except for the outlier case of AS = 0R, VS = 0.25R, the other three high overlap rotor

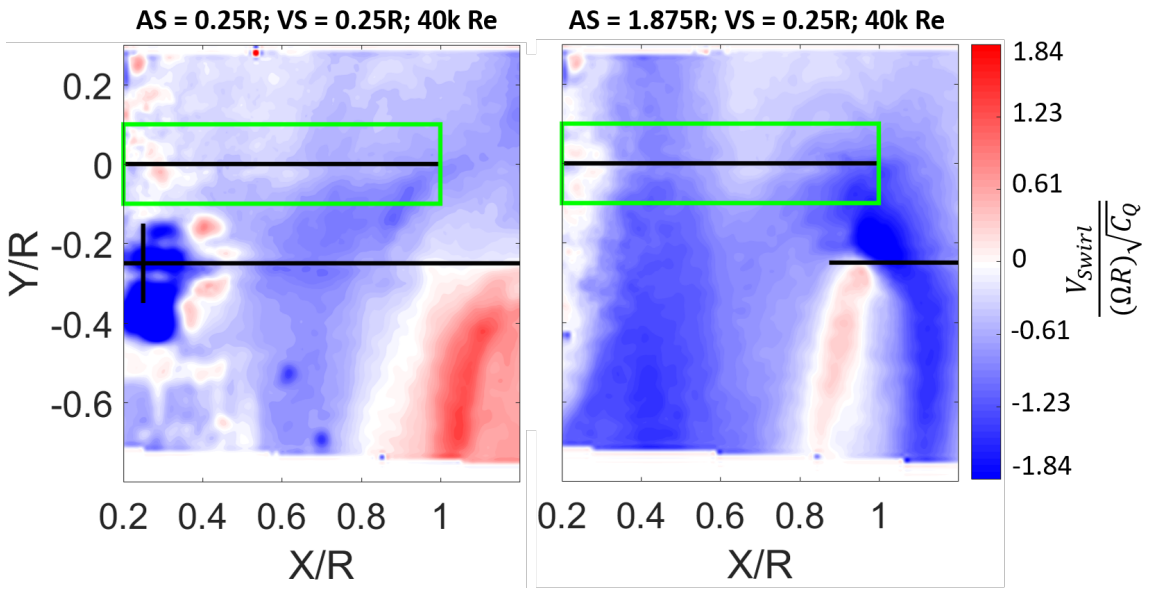

Figure 6.5: Time averaged velocity field streamline plots for selected cases

cases (AS = 0R, VS = 0.40R; AS = 0.25R, VS = 0.25R; AS = 0.25R, VS = 0.40R) have the normalized average swirl velocities smaller (in magnitude) than that for an isolated rotor. On the other hand, the normalized average swirl velocities for the cases with lower rotor overlap (especially in the AS = 0.75 to AS = 2.0 range where overlapping parts of the rotors move into the plane) are much higher than that for an isolated rotor. This supports the hypothesis that the lower rotor induces swirl on the upper rotor, which may be responsible for the observed effect on upper rotor performance.

Table 6.2: Integrated normalized swirl velocities at the upper rotor for selected 40k *Re* cases

$V_{Swirl(int)}/(\Omega R)\sqrt{C_Q}$				
Isolated Rotor		**AS = 0R**	**AS = 0.25R**	**AS = 1.875R**
-0.482	**VS = 0.25R**	-0.485	-0.408	-0.683
	VS = 0.40R	-0.42	-0.434	-0.597

6.3.5 Instantaneous flow field

Figure 6.6 presents typical instantaneous flow fields observed for some test cases in the form of vorticity contour plots. Vorticity contour plots make it easy to visualize vortices and trailing edge vortex sheets generated by the rotors. When following the wake from the right half of a rotor, red circular spots correspond to tip vortices and coherent blue streaks correspond to trailing edge vortex sheets. Similarly, when following the wake from the left half of a rotor, blue circular spots correspond to vortices and coherent red streaks correspond to trailing edge vortex sheets. The horizontal black lines in the plots represent rotor disks and the brown translucent boxes represent the motor. Again, only 80k *Re* cases are shown here as the results and the observations for 40k *Re* cases are similar.

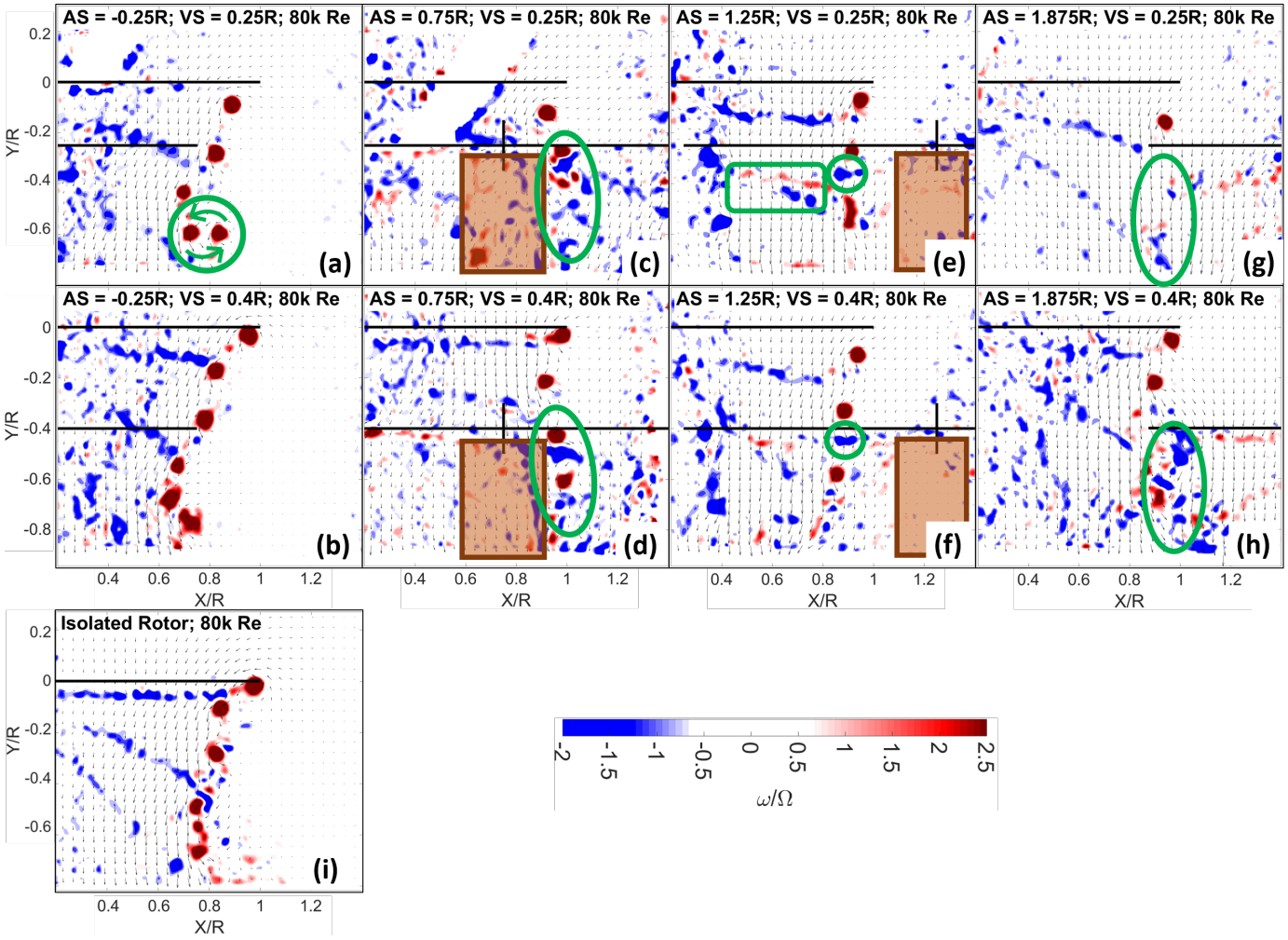

Figure 6.6: Instantaneous vorticity contour plots for selected cases

AS = -0.25R

In the AS = -0.25R cases shown in 6.6(a,b), the upper rotor and lower rotor vortices are seen to be in close proximity. This happens as the upper rotor slipstream converges inboards and passes near the lower rotor tip region where the tip vortices are being generated. The lower rotor vortex is almost always weaker in terms of circulation than the upper rotor vortex as the lower rotor tip at this location is in strong downwash from the upper rotor. For instance, for the AS = -0.25R cases, the circulation in lower rotor tip vortices was found to be about 40% lower than that of the upper rotor tip vortices near the lower rotor disk. Circulation of the vortices was computed by integrating vorticity layer by layer around the vortex center until the circulation value became independent of further inclusion of region.

The vortices due to the two rotors interact with each other in two different ways depending on their positions and strengths with respect to each other. One is when the upper rotor vortex hits almost exactly at the lower rotor tip where a vortex is forming. In such cases, the vortices due to the two rotors merge and the lower rotor vortex is not seen in the wake distinctly. The combined vortices are generally not very stable and may get disturbed within 360° wake age below the lower rotor. The second and more common way of interaction between vortices at this rotor overlap is when the vortices are close enough from each other to change each other's trajectories. The directions in which the vortices get pushed depends on the directions from which they approach each other. In this second way of vortex-vortex interaction, the magnitude of trajectory change of a vortex is inversely dependent on its convection velocity and directly related to the time for which it stays in the vicinity of the other vortex. Two vortices close to each other and convecting down at almost the same speeds are likely to roll about each other as they continuously push each other tangentially. This behavior is evident in the plot presented for the 80k *Re* VS = 0.25R case (6.6(a)) at this rotor overlap.

AS = 0.00R to 0.50R

The AS = 0R, 0.25R and 0.50R cases have a few similarities. In these cases, the upper rotor tip vortices are seen to interact with the lower rotor trailing edge vortex sheet only. After studying all the instantaneous high-speed PIV frames for these cases, four specific vortex-vortex sheet interaction scenarios were identified. These scenarios correspond to the four possible ways the upper rotor vortices can be located with respect to the lower rotor vortex sheets. They are: above vortex sheets, below vortex sheets, between the consecutive vortex sheets, and coinciding with the vortex sheets. The occurrence of these four relative positions is again dependent on where the blade crossings occur, or more precisely, the position of lower rotor blades when the upper rotor tip vortex approaches the rotor plane. The upper rotor tip vortices would land above the lower rotor vortex sheets if the lower rotor blades pass the azimuthal location right before the upper rotor vortices reach the rotor plane. Similarly, the tip vortices would land below vortex sheets if the lower rotor blades pass right after the upper rotor vortices pass the rotor plane. These vortex-vortex sheet interactions affect the vortex trajectories and endurance. For cases where the vortices are seen above the vortex sheet, the vortices get pushed outboard due to the velocity induced by the vortex sheet. Vortices below vortex sheets get pulled inboard, again due to the sheet induced velocities. Vortices between two consecutive sheets do not experience much change in their trajectories, whereas vortices coinciding with vortex sheets are most often broken down into incoherent pockets of high vorticity. AS = 0R cases have some commonality with AS = -0.25R cases in terms of vortex-vortex interactions, especially at lower vertical separations. The vortex-vortex interactions at AS = 0R are primarily of the type where the vortices due to the two rotors roll about each other without merging.

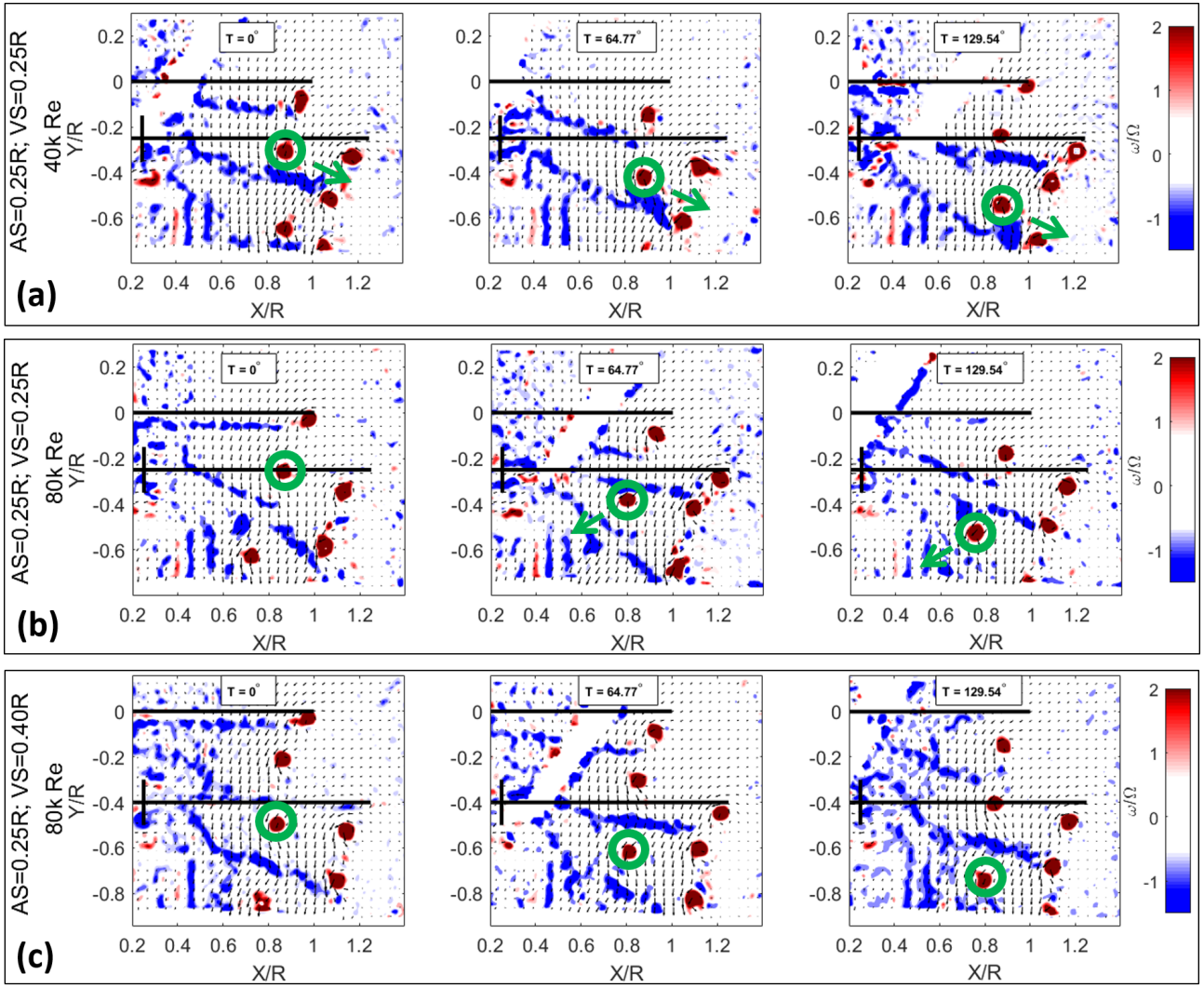

Figure 6.7: Instantaneous vorticity contour plots for AS = 0.25R cases showing the evolution of wake with time at three vortex-vortex sheet interaction scenarios: (a) upper rotor vortex above vortex sheets, (b) upper rotor vortex below vortex sheets, and (c) upper rotor vortex in between vortex sheets.

6.7(a) depicts the condition where the upper rotor vortex (marked by a green circle) lands above the lower rotor vortex sheet and gets pushed outwards. The opposite can be seen in 6.7(b) where the vortex gets pulled inward by the vortex sheet. The effect is clearer by comparing vortex trajectories plots for these two cases (6.8(a,b)) with that for the third case (6.7(c), 6.8(c)) where the vortices are approximately between two consecutive sheets. The vortex trajectories of two consecutive vortices are almost identical, indicating that the wake is fairly periodic provided the two rotor speeds are exactly the same. The algorithm used here for tracing tip vortices is the same as that described in chapter 2.

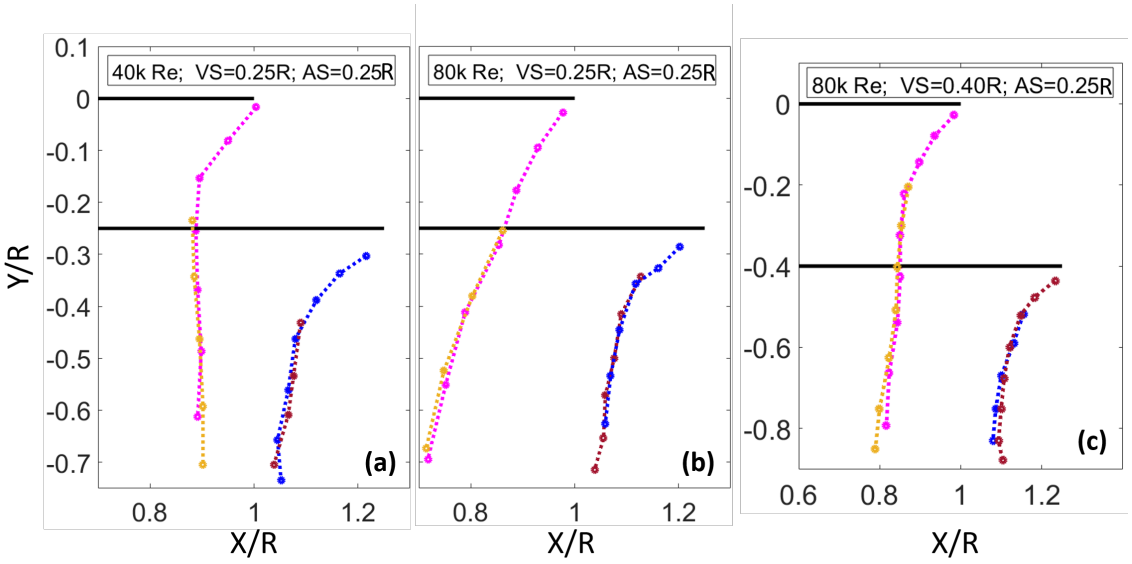

Figure 6.8: Vortex trajectory plots for two consecutive vortices at the three vortex-vortex sheet interaction scenarios seen in Figure 6.7

AS = 0.75R to 1.50R

In the AS = 0.75R and 1.00R cases for VS = 0.25R (6.6(c)), the upper rotor tip vortices are seen to hit the lower rotor hub, motor, mount, etc. and get broken down into high vorticity pockets. For VS = 0.40R cases (6.6(d)), the vortices are seen to avoid the lower rotor mount by moving outboard or inboard for AS = 0.75R and AS = 1.00 R respectively.

This is probably due to the centrifugal effect of the lower rotor, drawing air above the rotor radially outward.

The lower rotor trailing edge vortex sheets in AS = 1.00R, 1.25R, and 1.50R cases are found to stay horizontal while descending downward in the region below overlap as seen for AS = 1.25R in 6.6(e), marked by a green box. The upper rotor vortex sheets maintain the inclination they get before passing through the lower rotor plane. This is an indication of uniform to near uniform downwash below the overlap region and correlates with the observation made using the downflow plots in Figure 6.3(e,f).

For AS = 1.25R and 1.50R, vortices of vorticity and circulation comparable to the lower rotor tip vortices get generated out of the lower rotor vortex sheet where it intersects the upper rotor slipstream. These vortices have the same sense of rotation as lower rotor tip vortices, and hence the opposite of what is expected for the lower rotor vortex sheet. The trajectory of these vortices is dependent on their position with respect to the upper rotor tip vortex, just as described for vortex-vortex interaction in AS = -25R cases. Such vortices have been circled in the 6.6(e,f) for easy identification.

AS = 1.75R to 2.00R

Tests for AS = 1.875R were planned especially to observe vortex-vortex interactions between vortices of opposite sense of rotation. From 6.6(h), it is apparent that such vortex-vortex interaction leads to vortices losing their coherent structure, resulting in a rather chaotic wake. In a special case when the upper rotor vortices hit exactly on the lower rotor tip, the lower rotor tip vortex cancels out the upper rotor vortex and no vortices are seen in the wake following that. The vorticity plot for 80k Re VS = 0.25R (6.6(g)) is an example of this. The wake of AS = 2.00R resembles single rotor wakes, except that the vortices due

to the two rotors disturb or break each other because of close proximity like in AS = 1.875 cases. Figure 6.9 summarizes some typical interactions observed over four tandem rotor overlap ranges through the instantaneous flow plots in Figures 6.6 and 6.7.

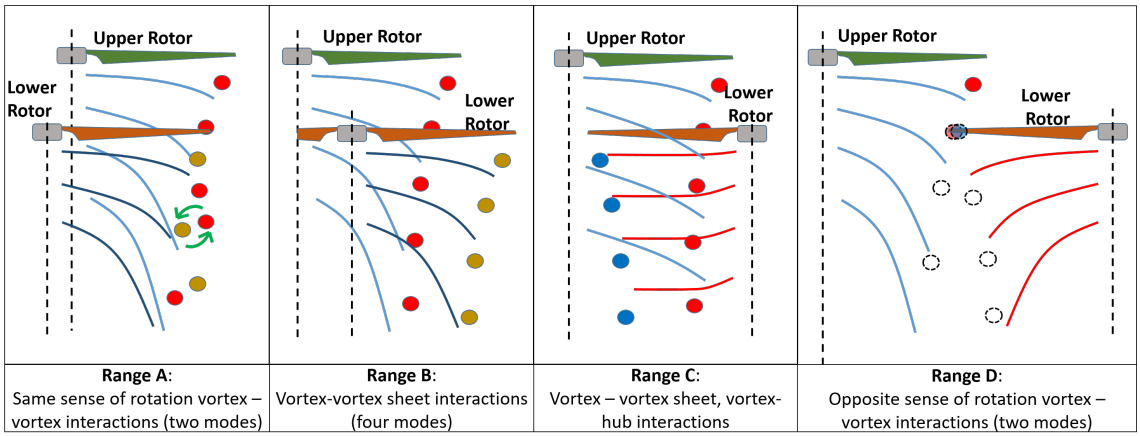

Figure 6.9: Tandem rotor instantaneous wake interactions summary

6.3.6 Generalizing findings

Though these experiments were conducted at discrete configurations and conditions, the observations made here can be easily extended to any configuration within the range. This is possible by tying all the important components of tandem rotor wake interactions discovered and discussed above through logical arguments. For instance, the kind of vortex-vortex interactions found at AS = -0.25 should be common to all combinations of AS and VS where the slipstreams or vortices from the same sides of the rotors come close to each other. Similarly, the vortex-vortex sheet interactions seen at AS = 0.25 and 0.50 and resultant effects on vortex trajectories are expected to be found for all cases where the upper rotor tip vortices cross lower rotor plane away from tip and hub. Vortex-vortex interactions observed at AS = 1.875R cases should again be common to all conditions where tip vortices of opposite sense of rotation come very close to each other.

The wake interaction phenomena can be generalized to coaxial rotors of equal or unequal radius as well. The vortex-vortex sheet interactions found at AS = 0.25R can be found for coaxial rotors with the lower rotor radius equal to or larger than upper rotor radius. The vortex-vortex interactions such as those at AS = -0.25R would be common for coaxial rotors with the lower rotor smaller than the upper rotor. The only difference will be that the flow interaction phenomena discovered at the plane connecting axes of the tandem rotors will be found at all radial planes of such coaxial rotor.

While operating in forward flight conditions, the rotor wake gets an additional edgewise component which changes the trajectories of vortices and vortex sheets. Though the effect of edgewise flow on low *Re* rotors is not investigated in this study, the basic components of tandem rotor interactions should still be valid for low advance ratios (forward flight speed/rotor tip speed) after accounting for the added velocity component.

It may be possible to extend some of these findings to large scale rotors as well, keeping in mind the difference in relative vortex core size and vortex sheet thickness as found by Ramasamy et al. [104]. As the large *Re* rotors are expected to have much stronger and tighter tip vortices (as a fraction of rotor radius), merging and splitting of tip vortices from the two rotors should be a rare event. The vortex-vortex interactions may still contain vortices spinning about each other as found in low *Re* cases here. The effect on upper rotor vortex trajectory due to interaction with the lower rotor vortex sheet may be limited at high *Re*, as the vortex sheet is much thinner and its influence may not extend out far.

6.4 Conclusion

The present study helped in discovering some major wake interaction phenomena that occur over a range of tandem rotor configurations and conditions. These include two types

of vortex-vortex interactions of tip vortices with the same and opposite sense of rotation, four types of vortex-vortex sheet interactions affecting the trajectory of vortices, and interaction of tip vortices with the rotor hub and mount. Observing the mean inflow and outflow velocity profiles for all configurations and conditions led to the identification of the basic components of mean downwash velocity and an understanding of how downwash due to a multirotor configuration can be seen as a combination of these components.

The findings on wake interactions can be extended to tandem and other multirotor configurations not tested in this study. This is because the instantaneous and mean flow features discretely identified and explained here can be applied logically, accounting for rotor geometry and position to provide a first-hand estimate. Some of the current results can be applied for high *Re* rotors as well, after correcting for the differences in tip vortex and vortex sheet geometry.

Performance measurement results for low *Re* tandem rotors show similar overall trend as high *Re* tandem rotor test done by Ramasamy *et al.* [115]. The higher than expected upper rotor performance in some low-*Re* cases was hypothesized to be due to viscous swirl recovery. Analysis of the mean swirl velocity component near the upper rotor provided some evidence on the lower rotor affecting swirl at the upper rotor, supporting the hypothesis.

CHAPTER 7
ROTOR-BOX INTERACTIONS

Multirotor Unmanned Aerial Vehicles (UAVs) are a promising means of package delivery. Such applications generally involve carrying bulky payloads under the vehicle. The placement of these with respect to the rotors becomes a critical design decision affecting the vehicle's performance in terms of range, endurance, and speed. Most rotor UAV designs have their payload located below the rotor plane considering vehicle stability and ease of in-flight package loading and unloading. This leads to concerns about the rotor wakes interacting with the payload and adversely affecting overall vehicle performance. Understanding the aerodynamic interaction effects of payloads on the vehicle is key to designing such systems, in the low Reynolds number regime of small UAVs. In this chapter, a setup comprising of a rotor and a cubic box used to investigate rotor-box interactions and configurations typical of multirotor UAVs. The findings from single rotor-box interaction study can be extended to a range of multirotor UAV configurations after accounting for rotor-rotor interactions.

In the present investigation, rotor performance and box download (downward force on the box due to rotor downwash/wake) measurements have been made at a range of positions of the box with respect to the rotor at two *Re* values. High-speed stereo Particle Image Velocimetry (SPIV) was used to study the instantaneous flow interactions and the mean flow features associated with the performance and load measurement observations. The performance and PIV results are presented here with interpretation and important findings have been highlighted.

7.1 Related prior work

Some prior studies related to the problem are on rotor-fuselage interactions on helicopters where the fuselage is right under the rotor. Helicopter rotor-fuselage interactions have been studied very extensively over the decades to understand and mitigate the associated adverse effects on helicopter efficiency.

Lober *et al.* [132] developed a computational method for the unsteady aerodynamic interaction between a helicopter rotor, wake, and fuselage by combining lifting line-prescribed wake rotor analysis and source panel fuselage analysis codes. Renaud *et al.* [133, 134] did a CFD study on Dauphin 365N helicopter with the aim of fuselage performance prediction and rotor-fuselage interaction using actuator disk models to simulate the rotor downwash. Nam *et al.* [135] studied the interaction by simulating the condition using unstructured adaptive mesh, dividing the computational domain into a moving zone rotating with the blades, and a stationary zone containing the fuselage. Other computational studies on the problem are by Kenyon and Brown [136], Steijl and Barakos [137], Lee and Kwon [138], and many more.

On the experimental front, Blanch [139] did an extensive experimental investigation of interactions between the main rotor, fuselage and tail rotor of a helicopter in hover. Leishman [140] conducted wind tunnel experiments on an isolated fuselage, isolated rotor, and on the rotor and fuselage combination obtaining independent load measurements along with unsteady pressure measurements on the fuselage. Mineck and Gorton [141] also performed pressure measurements on a fuselage model in the presence of a rotor for providing validation data for CFD studies on the topic. More recent studies on rotor-fuselage interactions are by Xu *et al.* [142], Jiao *et al.* [143], Açıkgöz *et al.* [144], and Quackenbush *et al.* [145].

All of the above work for helicopters assumes a relatively streamlined fuselage located under the rotor through its center. However, multirotor UAVs such as quadcopters, hexarotors, octorotors, etc. typically have their fuselage/payload at the center of the vehicle with the rotors in the periphery. Therefore the position of payload with respect to a rotor and hence associated rotor-payload aerodynamic interactions are very different from the kind of rotor-fuselage interactions studied so far. There is also a big difference in the order of magnitude of *Re* in which helicopters and small multirotor UAVs operate, making simplifying assumptions used for helicopter rotor analysis invalid for the problem at hand.

7.2 Experimental Setup

7.2.1 Test Setup

The test setup consisted of the single rotor assembly used for rotor-duct interaction study in chapter 2, and a box. The box was cubic with each side equal to the rotor radius. It was supported by a height-adjustable stand arm through a 100 gm load cell for measuring rotor downwash force (or download) on the box. The stand arm was mounted on a carriage which could slide on a rail to allow adjusting the horizontal distance of the box from the rotor.

All three load cells (one for thrust, one for torque, and one for download on the box) were provided with regulated power supply from a signal conditioner. The signals were filtered and amplified to be read by a DAQ. The data were collected at the rate of 1000 Hz for a span of 60 seconds. Figure 7.1(a) is a labeled photograph of the setup.

The high-speed PIV was done on a plane 32 mm offset from the rotor center to avoid motor mount shadows. Only the right half of the rotor setup was captured where the box is

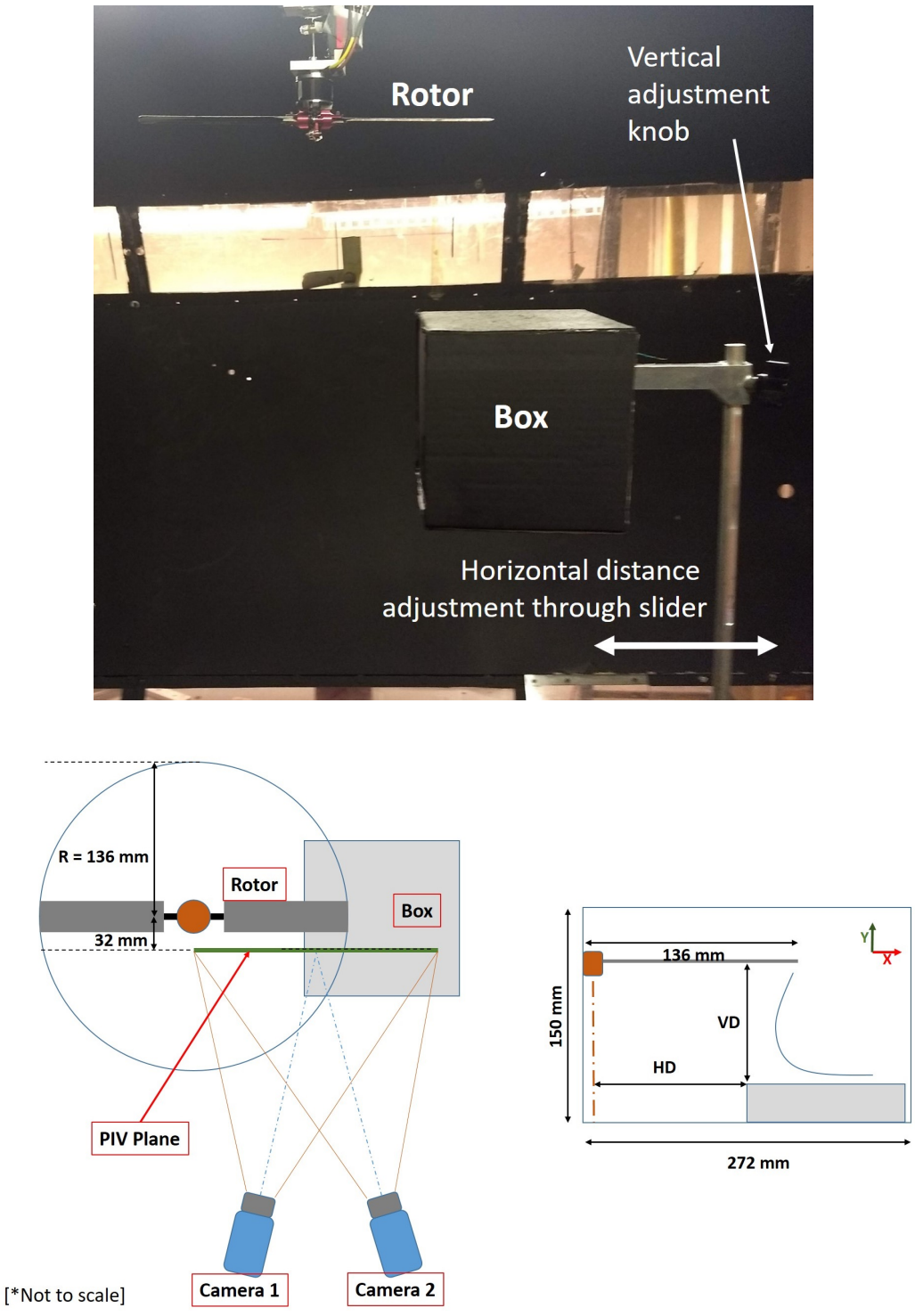

Figure 7.1: (a) A labeled photograph of the setup (b) PIV measurement location

introduced, for optimal use of the available camera resolution. Figure 7.1(b) describes the camera and PIV plane orientation w.r.t the rotor and the box.

7.2.2 Test Conditions

The tests were done for two tip Reynolds numbers at four vertical separations and four horizontal distances of the box with respect to the rotor center in hover. The *Re* was changed by changing rotor RPM. Vertical and horizontal distances of the box from the rotor were varied using the height-adjustable stand and horizontally sliding carriage. The test matrix for these experiments is included in the Tab. 7.1.

The experiments were performed at the overall thrust coefficient of 0.004, accounting for the thrust generated by the rotor, as well as downward force or the download experienced by the box. This is to mimic the real vehicle condition where the box is being carried along, and hence the forces on it have to be adjusted for by the rotors.

Table 7.1: Setup and test condition for coaxial rotor experiments

Box dimensions	$0.136m \times 0.136m \times 0.136m$
Rotor tip *Re*	40000, 80000
Box vertical distance (VD)	0.54R, 0.79R, 1.04R, 1.29R*
Box horizontal distance (HD)	0.56R, 0.68R, 0.81R, 1.06R
$C_{T(Overall)}$	0.004

*Performance measurements only

7.3 Results and Discussion

7.3.1 Rotor Performance and Load Measurements

The rotor thrust and torque measurement results are presented in the form of Figure of Merit (FM) in Figure 7.2 for compactness. The performance of the overall rotor-box system has been represented using a pseudo overall Figure of Merit (FM^*) computed using

a pseudo overall coefficient of thrust (C_T^*) defined in the equation 7.1. It must be noted that C_T^* and FM^* are not coefficient of thrust and Figure of Merit in a strict sense, but are defined in this fashion only for some convenience in comparison of results. Download on the box is presented in the form of a percentage of rotor thrust.

$$C_T^* = \frac{T_{Rotor} - Download}{\rho(\pi R^2)(\Omega R)^2}; FM^* = \frac{(C_T^*)^{3/2}}{\sqrt{2}C_Q} \tag{7.1}$$

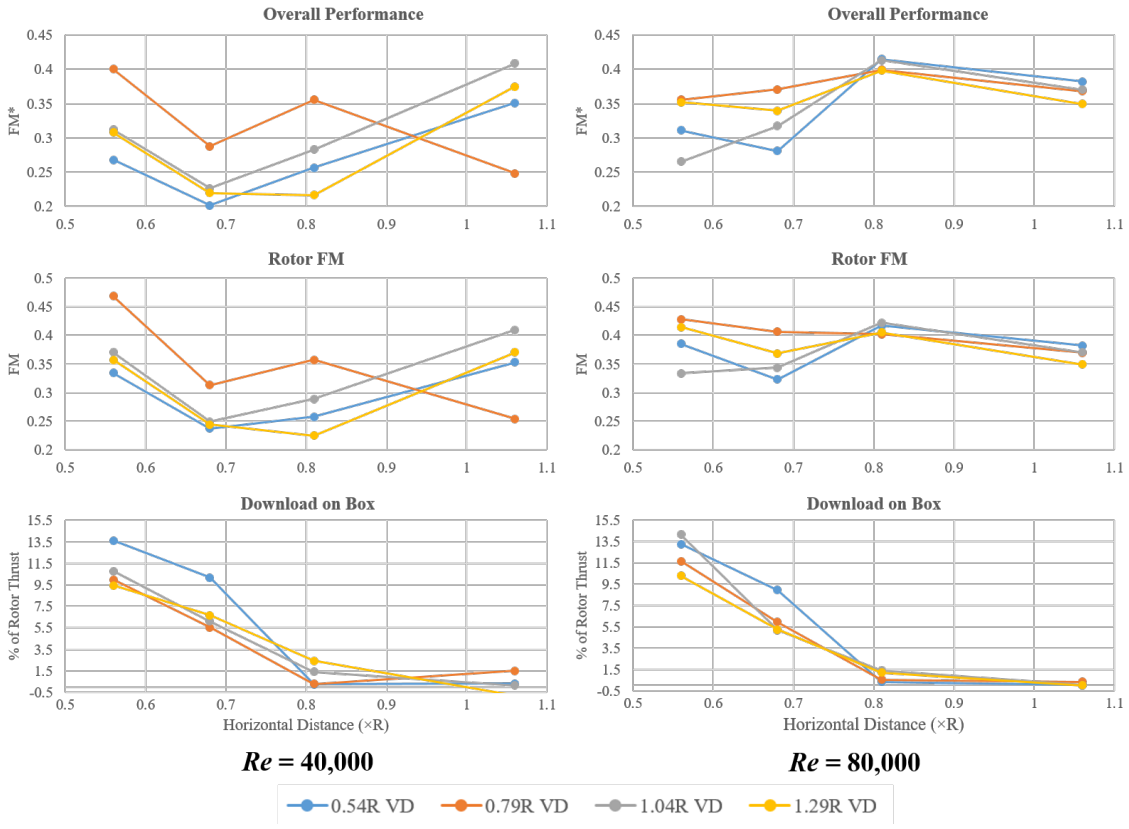

Figure 7.2: Rotor performance and load measurement results

In the following, horizontal distances are denoted as HD and vertical distances as VD. Observing the performance plots, it is apparent that there is a significant difference in the effect the box has on the rotor at the two *Re* for the range of box positions. The spread in FM between different vertical distances is more at 40k *Re* compared to 80k *Re*. This is likely to be due to unsteady wake getting re-ingested by the rotor after interacting with the

box, causing large variations in the results. The 40k *Re* cases are more vulnerable to such interactions as the velocity magnitudes in the wake are smaller due to lower thrust. Though 80k *Re* cases are much steadier, more spread in the data is observed for the high overlap conditions of HD = 0.56R and 0.68R. This again may be attributed to the unsteady wake ingestion due to the presence of the box.

Good rotor performance is observed at the highest overlap (or the smallest horizontal distance) conditions of HD = 0.56R which may be attributed to the ground-effect like situation created by the upper surface of the box. The rotor at HD = 0.68R conditions has noticeably lower FM than at neighboring conditions of HD = 0.56R and 0.81R instead of varying monotonically with HD. 80k *Re*, HD = 1.06R cases are expected to show behavior closer to that of an isolated rotor as the wake does not interact with the box (evident from zero download on the box and the PIV data plots presented later). The fact that the rotor, as well as overall performance for 80k *Re* HD = 0.81R cases are better than HD = 1.06R cases is interesting as it suggests that the box caused improvement in the isolated rotor performance. The box experiences almost no downward force due to the rotor wake at HD = 0.81R too, as apparent from the download plot.

Download on the box decreases with increase in HD as expected. However, change in VD does not affect download to such an extent. At HD = 0.56R and 0.68R, larger spread in download with the change in vertical distance is observed as the fraction of the high momentum wake impinging on the box varies with wake deflections due to side-way perturbations. The 40k *Re* cases of HD = 0.81R show higher download percentage than 80k *Re* cases, likely due to wider wake at 40k *Re* (or more constricted wake at 80k *Re*). Excepting HD = 0.81R, the percentage of rotor download in 40k and 80k *Re* cases have very similar magnitudes.

7.3.2 Mean Velocity Field Data

Figure 7.3 presents mean flow field streamline plots for some cases selected based on uniqueness in observed flow. The 40k and 80k *Re* streamline plots are very similar, and hence only 80k Re plots have been featured. The observations and discussions made for these plots hold true for the 40k Re cases as well. The horizontal white line in each plot depicts the rotor disk. The mean flow field was obtained by averaging 200 instantaneous velocity fields separated by 2.5 ms. The 200 frames cover rotor rotation with 1.8 degrees resolution as the rotor and PIV frames are not synchronized in frequency. Hence the mean flow field should be well representative of the actual mean flow field. The plots are non-dimensionalized by $\Omega R\sqrt{C_T}$. X and Y axes are normalized by rotor radius.

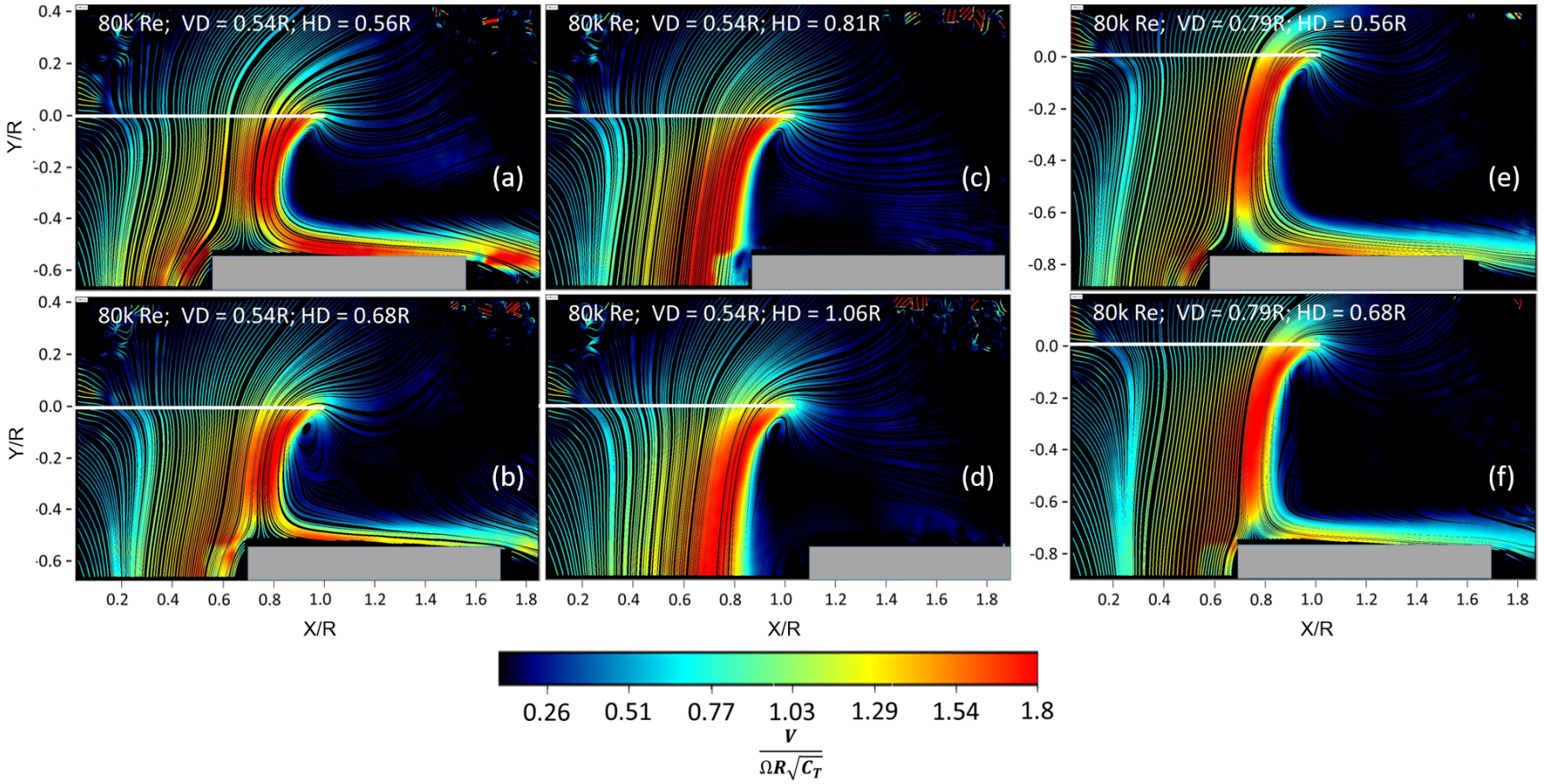

Figure 7.3: Streamline plots for selected 80k Re cases

HD = 0.56R & 0.68R

In HD = 0.56R and HD = 0.68R cases (Figure 7.3 (a,b)), high velocity flow below the rotor tip (seen as red-colored streamlines) is found to be impinging on the upper surface of the box. The difference between the two cases is the location of impingement and subsequent deflection. In HD = 0.56R case, the volume and strength of flow deflected inboard is significant. This is expected to cause a higher static pressure under the rotor, assisting rotor thrust (mimicking ground-effect). In case of HD = 0.68R, majority of the inboard rotor wake is unaffected by the box and only a small volume of flow gets deflected inwards. The flow deflected outwards due to box, in this case, is found to result in weak recirculation near the rotor tip. A smaller volume of wake getting deflected inward means lower static pressure under the rotor (compared to HD = 0.56R cases), and hence a low-to-no benefit to the rotor through ground-effect. Instead, recirculation near the rotor tip would increase induced losses, and adversely affect rotor performance. This explains why the rotor performance for HD = 0.68R cases is worse than the neighboring cases for almost all VD and both *Re*. The reason for the decrease in download on the box going from HD = 0.56R to HD = 0.68R is obvious by noting the fraction of rotor wake deflected by the box and the size of the near-stagnation region on box surface.

HD = 0.81R & 1.06R

The mean high-velocity rotor wake is found to just miss the box edge for HD = 0.81R cases, and the clearance between the high-speed wake and the box is obviously even more for the HD = 1.06R cases (Figure 7.3 (c,d)). The effect of this is apparent from the plot on download on the box in Figure 7.2 where the download is close to zero for HD = 0.81R and 1.06R. The box being very close to the rotor wake at HD = 0.81R, blocks recirculation of air back into the rotor to some extent and hence may be responsible for the slight increase in rotor performance observed for all HD = 0.81R cases at 80k *Re*. At 40k Re, relatively

higher spread in the instantaneous wake causes some flow to impinge on the box surface (as evident from the non-zero download on the box in Figure 7.2) and move back to the rotor.

Vertical distance variation

The increasing vertical distance between the rotor and the box has a rather weaker effect on the way the wake interacts with the box. This may be seen by comparing plots for HD = 0.56R and HD = 0.68R at VD = 0.54R and 0.79R in Figure 7.3 (a,e,b,f). With an increase in VD, the wake trajectory becomes more vulnerable to external disturbances, affecting the precise location where the wake impinges on the box. This leads to uncertainty in predicting download forces on the box and also rotor performance as observed in Figure 7.2 for HD = 0.56R and HD = 0.68R.

7.3.3 Instantaneous Velocity Field Data and Wake Interactions

Figure 7.4 contains instantaneous vorticity contour plots for selected test cases. Instantaneous flow fields at 40k and 80k *Re* was found to be approximately similar in nature, and hence only 80k Re cases of significance are being presented here for brevity. The instances presented in these plots have been selected after studying all 200 frames of the PIV data for each case to bring up typical instantaneous flow field at these conditions. The length scales are non-dimensionalized using rotor radius and vorticity is non-dimensionalized using rotor angular speed (Ω). The rotor disk is depicted by a horizontal black line and the box is shown in grey. The coherent red spots in the contour plots correspond to tip vortices and the coherent blue streaks correspond to the trailing edge vortex sheets owing to their sense of vorticity. The figure also features empirical curve fits modeled by Landgrebe[110], and Kocurek and Tangler[111] for tip vortex trajectory of an isolated rotor, computed for the

present cases. These are for comparing the observations with existing models for isolated rotors.

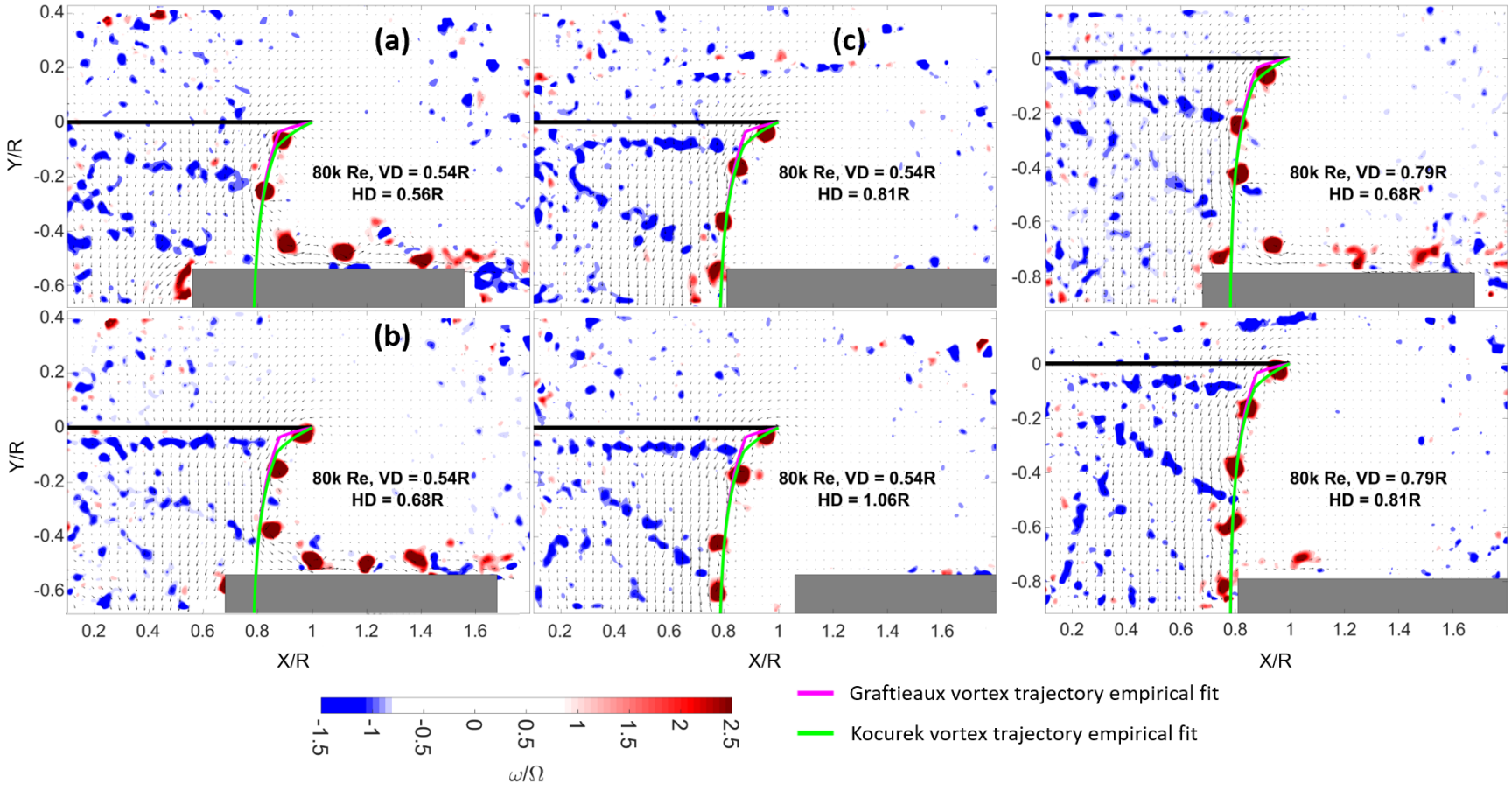

Figure 7.4: Instantaneous vorticity contour plots for selected 80k Re cases

HD = 0.56R & 0.68R

Looking at the VD = 0.54R, HD = 0.56R case (Figure 7.4(a)), it is observed that the tip vortices go radially outward along the box's upper surface as they approach it. The vortices do not actually contact the box surface immediately as there is a layer of air from the region just inboard of the vortex stream, which is also flowing along the horizontal box surface and keeping the vortices away. This 'layer of air' includes parts of trailing edge vortex sheets, which invariably get broken into small pockets of high vorticity on being stretched outward in this fashion. A recirculation zone is observed on the vertical surface at the edge of the box. The size of this region fluctuates at blade passing frequency. It increases in size when trailing edge vortex sheets approach and interacts with the box. Instantaneous flow at VD = 0.54R, HD = 0.68R cases (Figure 7.4(b)) is similar to VD = 0.54R, HD = 0.56R cases except that the vortices come much closer, or actually interact with the horizontal box surface and lose their shape sooner. The vertical wall recirculation zone also appears smaller.

HD = 0.81R & 1.06R

At VD = 0.54R, HD = 0.81R (Figure 7.4(c)), the tip vortices just avoid hitting the horizontal surface of the box and go beside the vertical surface. This correlates with the observation made for the case through a streamline plot in Figure 7.3(c). The region above the box is generally calm in the absence of any significant flow. There is no noticeable separation region near the box edge, but some vortices get disturbed by the edge as they come close and interact with it. At VD = 0.54R, HD = 1.06R (Figure 7.4(d)), the box is clearly away from the rotor wake and there is almost no visible interaction between the two.

Vertical distance variation

With an increasing vertical distance of the box from 0.54R to 0.79R at HD = 0.56R and 0.68R, the tip vortices get weaker (in terms of circulation, due to viscous effects and age) by the time they come closer to the box. Hence they lose their form soon after slightest interaction. In 80k *Re* cases, the consecutive vortices roll around each other in pairs as they descend from the rotor. Due to this, one vortex of the pair gets pushed outboard (radially) and the other inboard before they come close to the box. The vortices pushed outboard stay away from the box and the vortices pushed inboard get closer to the surface and generally get disintegrated soon after. In HD = 0.68R (Figure 7.4(e)) case, the vortices pushed inboards tend to terminate at the box edge, affecting the separation region on the vertical surface.

Observations at VD = 0.79R for HD = 0.81R and 1.06R are similar to those for the corresponding cases at VD = 0.54R. For the 80k Re case of VD = 0.79R, HD = 0.81R, it is seen that occasionally a tip vortex pushed outward due to the roll-up would land on the horizontal surface after encountering the edge and travel horizontally. One such instant is shown in the contour plot for the case (Figure 7.4(f)).

7.4 Generalizing findings

Based on the observations here, it is possible to categorize the rotor-box interactions roughly into three modes as shown in Figure 7.5. Mode A type interactions are seen when the rotor-box overlap is high, mode C type interactions are seen when the box is out of the rotor wake, and mode B type interactions are expected at conditions between those for mode A and mode C where the box edge is very close to the wake boundaries. In mode B, the vortices neither fully avoid the box, nor impinge on the horizontal surface far enough from the edge.

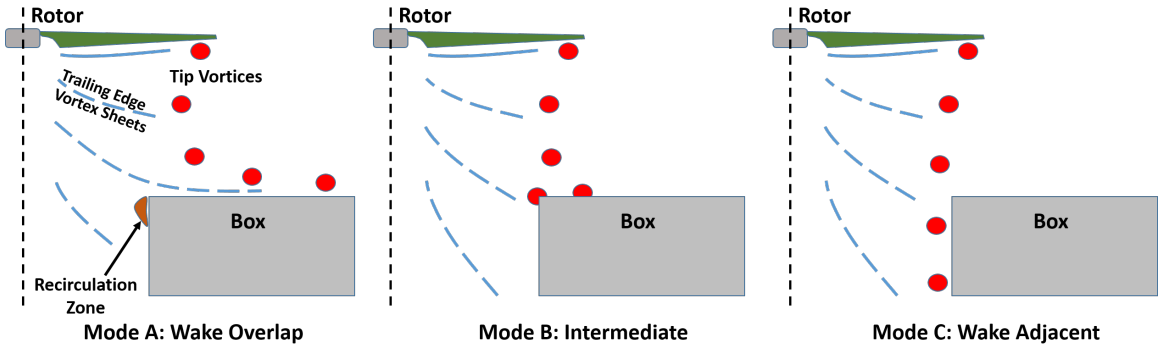

Figure 7.5: Modes of Rotor-box aerodynamic interactions based on box position

Out of the two vortex trajectory empirical fit models plotted on the instantaneous vorticity contour plots in Figure 7.4, the one by Kocurek and Tangler is seen to be better near the rotor plane. However, both of them merge at some distance below the rotor. It is interesting to note that the tip vortices do follow the empirical fits approximately for the cases where the rotor wake does not impinge on the box. As observed earlier, the vortices turn radially outward on encountering the box for cases with high overlap (such as at HD = 0.56R and 0.68R) and hence naturally depart the empirical model trajectories. The vortex trajectories in such high overlap cases visually seem to be comparable to that expected in the wake of a helicopter rotor hovering in ground effect. Of course, the empirical fits do not account for vortex-to-vortex variations in trajectories and rolling of consecutive vortices in pairs as seen for some 80k *Re* cases.

The fact that the tip vortices follow Kocurek and Tangler's empirical trajectory even at such low *Re* for mode C type conditions is exciting and useful. It is so because now one can simply compute the empirical trajectory based on C_T and rotor solidity and get an idea on which of the three modes of interaction depicted in Figure 7.5 should be expected for a given location of a box/fuselage/payload. Knowing that vortex core size is (inversely) related to *Re* [105], it is being hypothesized that *Re* plays a role in the extent of horizontal

distances for which mode B type of interactions are found. There is little doubt about the empirical fit not working at high *Re* as it was developed observing high *Re* rotor wakes. Hence the approach discussed here should be valid for a vast range of *Re* and vehicle sizes.

The following is a summary of characteristics observed or expected at the three modes of interaction depicted in Figure 7.5:

Mode A: Wake Overlap

- High rotor download on the box.
- Ground-effect-like conditions for the rotor.
- High rotor performance but low overall performance compared to an isolated rotor.
- Dominantly periodic box download signature expected as all the vortices and trailing edge vortex sheets impinge on the box almost identically.

Mode B: Intermediate

- Moderate rotor download on the box.
- No significant ground-effect-like conditions for the rotor.
- Low rotor and overall performance due to recirculation near rotor tip.
- Large deviations from periodicity expected in the box download signature as each vortex and vortex sheet impinges differently on the box.

Mode C: Wake Adjacent

- No rotor download on the box
- No ground-effect-like conditions
- Slightly higher rotor and overall performance due to restricted wake recirculation.

In the previous studies done at this lab on helicopter rotor-airframe interaction [146, 147], it was found that the effects of the presence of the airframe on the rotor velocity field is as large in magnitude as the rotor induced velocity itself. The tests were done in forward flight using a cylindrical fuselage under the rotor. The downward velocity was seen to be reduced due to airframe blockage. The rotor inflow was not affected by the airframe itself, hinting that interactions could be computed based on isolated rotor calculations. The measurements were periodic with the frequency the same as the blade-passing frequency in spite of the airframe at the advance ratio of 0.1. The flow field around the airframe saw large periodic and time-averaged effects due to the rotor wake, and the presence of the cylinder caused significant changes in the rotor vortex structures, which appeared to get broken up into several different structures.

Comparing findings from the present work with the above, significant changes in the rotor velocity field are noticed only at high overlap configurations. The decrease in downward velocities also happens at similar conditions where the box is marginally or significantly in the rotor wake. Unlike the previous study, some effect of the box on rotor inflow and performance is noticed here as the rotor wake is not convected away as it would have in the forward flight case. Higher effect on rotor inflow is expected in these low *Re* cases, also due to larger relative size of wake features. Through the same argument, slight aperiodicity in the rotor flow is expected in the current regime. The effect of the rotor on forces and flow around the box is obvious from the PIV and load measurement plots. Breaking up of vortex structures near the box surface is also evident from the instantaneous vorticity contours for some cases.

7.5 Conclusions

This study showed how a box or box-shaped payload being carried by a multirotor vehicle would affect the rotor wake and vehicle performance depending on its position with respect to the rotor. Ground-effect like conditions develop below the rotor for high overlap configurations causing improvement in rotor FM, but at the expense of higher download on the box and generally lower overall performance. Configurations, where the box is just out of the rotor wake, are interesting as they indicate better overall performance compared to an isolated rotor.

Rotor performance and download on the box are highly susceptible to external disturbance to the rotor wake as it changes the fraction of the wake impinging on the box surface. Changing vertical distance between the rotor and the box does not change download on the box as a clear trend (for the vertical distances tested here) due to the same reason.

The mean flow streamlines results provide explanations for the performance and load measurement observations. The rotor-box interactions were characterized into three distinct modes based on relative positions of the rotor and the box. The flow and performance attributes expected at the three modes were highlighted. A definitive approach for predicting the mode of interaction based on an existing empirical vortex trajectory model for isolated rotors and *Re* was proposed. Mode A type interactions corresponding to high rotor-box overlap result in high rotor download on the box, ground effect, high rotor performance but low overall performance. Mode B type interactions cause moderate rotor download, aperiodic wake and loads, and poor rotor as well as overall performance. Mode C type interactions do not see any rotor download and the overall performance is found to be marginally better than isolated rotor due to restricted flow recirculation near the rotor tip.

The comparison of the present low *Re* rotor-box interactions in hover with the older findings on high *Re* rotor-airframe interactions in forward flight brought forth some similarities and differences due to configuration, *Re*, and flight condition.

CHAPTER 8
PREDICTION TOOL DEVELOPMENT EFFORTS

There is an ongoing effort to use the knowledge obtained about the flow field through the experiments to develop methods for predicting characteristics of low *Re* multirotor vehicles. The work on this front has begun with comparing the experimental results with those obtained using two state-of-the-art rotor codes. The codes are RotCFD and GT Hybrid. The objective here is to first understand the extent by which the flow phenomena observed through the experiments are captured by these codes originally developed for high *Re* rotors. This understanding will then help augment the tools to predict low *Re* multirotor characteristics better. This chapter describes the two rotor codes briefly and presents some computational results obtained using them for a single rotor case from the present experiments. The single rotor CFD study will be followed by multirotor simulations once there is enough confidence. There are plans on using the experimental and the validated CFD results to develop inflow model based prediction method which will cut down the computation time for use in vehicle controls and design optimization.

8.1 RotCFD

RotCFD is a CFD tool developed at Iowa State University [90] with the goal of reducing setup and run times for rotor computations. RotCFD models rotor blades as momentum sources. The rotor momentum sources are primarily a function of the local velocity of the flow and the two-dimensional airfoil characteristics of the rotor blades. The Navier-Stokes equations and the blade element theory are coupled implicitly to yield a self-contained method for generating performance, as well as the near and far wake including all the aerodynamic interference inherent in a situation. The classical blade element theory yields the

Table 8.1: Performance data comparison between RotCFD and experiments

	C_T	C_Q	**Pitch**
Experiment	0.004	0.00057	7.3°
RotCFD	0.004	0.00067	9.6°

correct forces on the rotating blades once the local vector velocity field is known. The numerical algorithm that solves the Navier-Stokes equations provides the flow field near the rotor blades which also includes the rotor induced momentum sources.

RotCFD is capable of simulating complete rotorcraft and aerodynamic interactions with other aircraft or bodies. The tool has shown good to reasonable agreement with experimental data for rotor performance and rotor-body interference studies[90].

Table 8.1 contains performance results obtained using RotCFD and experiments. It is observed that for the set Coefficient of Thrust of 0.004, RotCFD predicts a higher torque and a higher pitch setting. Figure 8.1 compares the wake computed using RotCFD's unsteady flow solver with that obtained experimentally through PIV. RotCFD does not resolve the tip vortices and the vortex sheets well enough to observe and compare the resultant instantaneous wake structure.

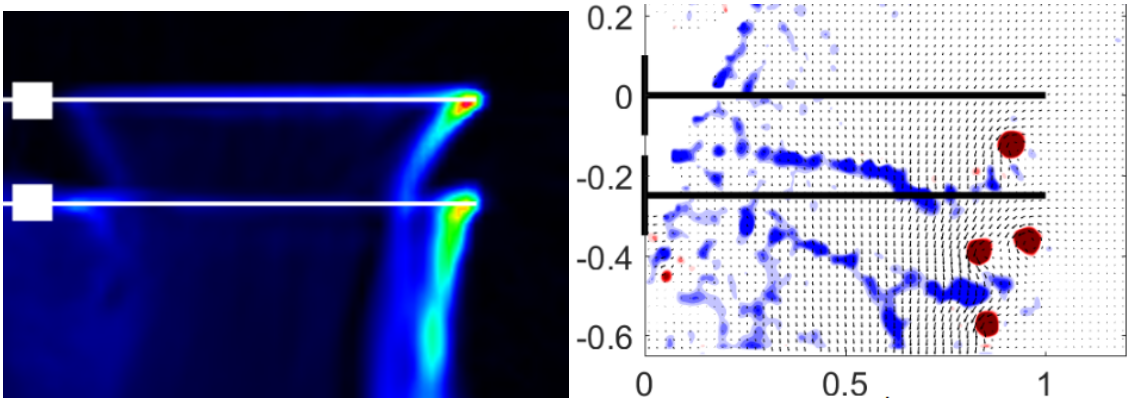

Figure 8.1: Coaxial rotor wake vorticity plot from RotCFD and experiments

8.2 GT-Hybrid

GT-Hybrid is a three-dimensional unsteady viscous compressible flow solver for rotors [148]. The flow is modeled using the Reynolds Averaged Navier-Stokes(RANS) methodology. A time accurate, finite volume scheme is used to solve the three-dimensional unsteady Navier-Stokes equations on a curvilinear body-fitted coordinate system around the rotor blades.

The code uses a Lagrangian wake approach to model vortex wake, with a collection of piece-wise linear geometric vortex elements. The trailing elements are released from the rotor blade trailing edge and are convected downstream by a combination of the free-stream velocity and the bound and trailing vortex self-induced velocities. In a way, GT Hybrid's approach is opposite to that of RotCFD.

The GT-Hybrid simulations were performed by Po-Wei Chen, a graduate student of Prof. Lakshmi Sankar at Georgia Tech. Figure 8.2 shows the wake generated by GT-Hybrid for the single rotor case, consisting of tip vortex and trailing edge vortex sheet elements. Normal velocity profiles obtained through GT-Hybrid simulation are compared against those from the experiments in Figure 8.3. It is seen that the rotor inflow velocity profile (0.2R) by GT-Hybrid matches very well with the experimental data. However, the velocity profile extracted from the rotor plane is off. GT-Hybrid result indicates a much tighter vortex structure than observed, which may be due to viscous effects not getting captured effectively in this low *Re* case. Further comparisons of performance and wake for single and multirotor cases are ongoing.

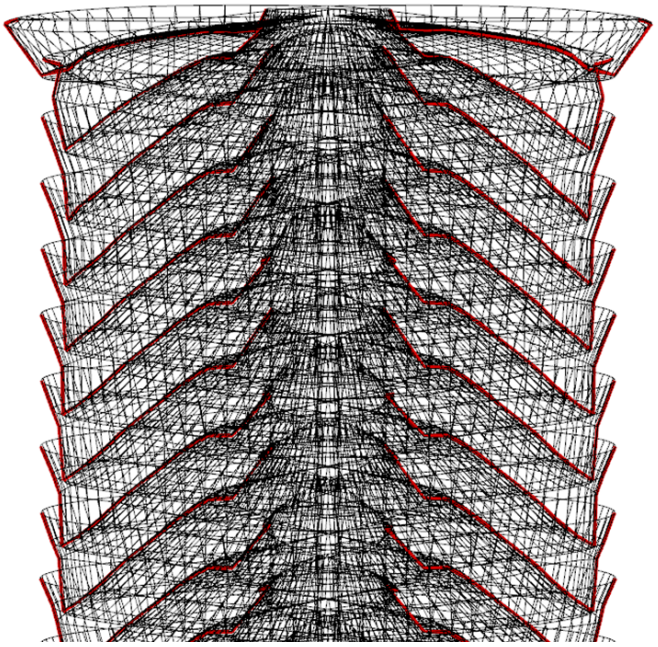

Figure 8.2: Single rotor wake from GT Hybrid

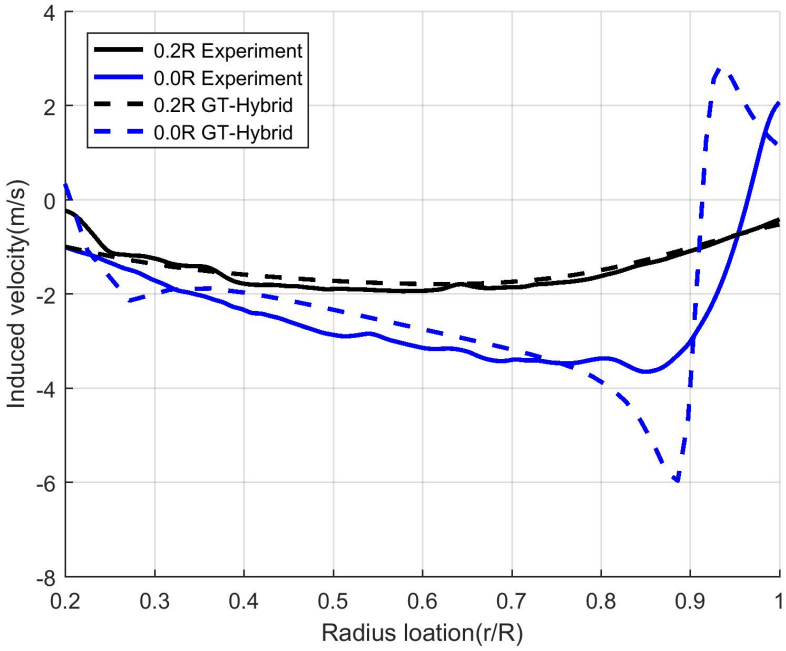

Figure 8.3: Comparison of normal velocity distributions at the rotor disk and on a plane 0.2R above the rotor

CHAPTER 9
CONCLUSION

This thesis explored low Reynolds number multirotor aerodynamic interactions at a large variety of configurations using multiple setups. The objective was to discover and understand important flow interaction phenomena relevant to small size multirotor vehicles to aid the development of better vehicle analysis, design and optimization methodologies and tools. The setups utilized in this study were selected carefully such that the findings are applicable to all possible and relevant multirotor vehicle configurations. The exploratory work presented here serves as a platform over which further detailed studies into specific aspects of the whole problem can find inspiration.

This chapter summarizes findings over all the chapters and proposes recommendations for further work in the area.

9.1 Summary of key findings and their significance

1. Tip vortex core size and vortex sheet thickness are inversely related to *Re* when scaled using rotor dimensions. This means that at low *Re*, these wake features affect much larger sections of the other rotor blades on interaction, causing a larger impact on the blade loading and hence rotor performance.

2. Performance of rotors at low *Re* is significantly lower than that of rotors at high *Re*. This is because of the significantly greater share of viscous parasitic losses which do not contribute to thrust generation. For instance, the blade geometry and C_T used in the single rotor experiments here are comparable to a full-scale helicopter rotor, but the maximum observed FM of 0.38 at 80000 *Re* is about half of what is typical for helicopter rotors. Most modern rotors designed for low *Re* are thin and

highly cambered to increase thrust at a given rotor speed at the expense of higher lift induced drag. The performance of such a rotor is better than that of a typical helicopter type rotor because the share of viscous parasitic drag is now relatively smaller. Comparing the highest FM of 0.50 of the cambered quadrotor setup rotors at 16850 *Re* with the highest FM of the symmetric blade single rotor at 80000 *Re* supports this point.

3. Presence of an annular duct around the rotor improves rotor performance, even if the duct is not designed for thrust generation. This is associated with tip vortex core interacting with the duct. The size of the tip vortex cores with respect to tip clearance is an important factor determining the magnitude of performance gain. Combined with the knowledge on vortex core size dependence on *Re*, this suggests that the tip clearance does not need to be as small for low *Re* as for high *Re* rotors to see some performance improvement. This is evident from the performance gains for the three *Re* cases tested in the study, too. The tip vortices lose their coherent structure after interacting with an annular duct and the overall wake contracts less. Vortex core interaction with the duct causes tonal acoustic signature comprised of rotor frequency harmonics. However, the Overall Sound Pressure Level values for the ducted and unducted rotor cases are still similar.

4. Inter-rotor wake interaction is dominant in low *Re* side-by-side rotor cases. The large tip clearance rotor ducts in the quadrotor setup experiments limited inter-rotor wake interactions by shielding tip vortices of one rotor from the other during their generation. Higher inter-rotor wake interactions correlated with lower rotor performance for most cases. This suggests that ducts around rotors are useful in limiting performance losses associated with close proximity side-by-side inter-rotor wake interactions. Low tip clearance is not necessary for the rotor-rotor wake isolation, but it is still useful in improving the individual rotor performance as noted in the previous

point. The similarities observed in the instantaneous flow field and mean velocity profiles for the tested range of rotor separations and speeds are useful in extending the findings to a wider range of in-plane rotor vehicle configurations.

5. In the low *Re* coaxial and high overlap tandem rotor hover cases, the upper rotor performs better than the baseline isolated rotor. This is contrary to what is expected from a momentum-based approach and such behavior is not seen in comparable high *Re* studies in the past. Viscous swirl recovery at the upper rotor due to the lower rotor was hypothesized to be the reason behind the observation. Effect of the lower rotor on the swirl velocities at the upper rotor was confirmed using SPIV data, supporting the hypothesis. High upper rotor performance in low *Re* coaxial rotors translates to FM of the overall coaxial rotor system being close to that of an isolated rotor, which is difficult for high *Re* rotors. The comparison here is only with the isolated rotor of the same geometry, loading, and *Re*. Overall FM of a low *Re* coaxial rotor is still expected to be lower than that of a comparable high *Re* coaxial rotor due to viscous losses.

6. The tandem rotor wake study led to the discovery of a variety of wake interaction phenomena happening over a range of tandem rotor configurations and conditions. These include two ways of vortex-vortex interactions of tip vortices with the same and opposite sense of rotation, four types of vortex-vortex sheet interactions affecting the trajectory of vortices, and interaction of tip vortices with the rotor hub and mount. The basic components of mean rotor downwash were identified and an approach to look at any multirotor downwash as a combination of these basic components was presented. The findings on wake interactions can be used to provide first-hand estimates for many other multirotor configurations and conditions by applying the instantaneous and mean flow features discretely identified and explained here. Observing the instantaneous flow interactions, rotor blade performance, vibrations and noise are

expected to be highly sensitive to the relative rotor phasing.

7. Three primary modes of rotor-box interaction were observed in an effort aimed at understanding rotor-payload aerodynamics relevant to UAV based package delivery. The first type of interactions corresponding to high rotor-box overlap results in high rotor download on the box, ground effect like conditions at the rotor, high rotor performance, but low overall performance. The second and the intermediate type of interactions cause moderate rotor download, aperiodic wake and loads, and poor rotor as well as overall performance. The third type of interactions corresponding to box a positioned just outside the rotor wake do not see any rotor download and the overall performance is found to be marginally better than isolated rotor due to restricted flow recirculation near rotor tip. A definitive approach for predicting the mode of interaction based on Kocurek's [111] empirical vortex trajectory model for isolated rotors and *Re* was proposed. Rotor performance and download on the box are highly susceptible to external disturbance to the rotor wake as it changes the fraction of the wake impinging on the box surface. Changing the vertical distance between the rotor and the box does not change download on the box as a clear trend (for a finite range of vertical distance) due to the same reason.

Table 9.1 lists the key findings and their location in the thesis.

9.2 Recommendations for future work

1. Single rotor simulations using a Navier-Stokes wake solver can be useful in checking if the experimental observations regarding the trajectory and size of vortices and vortex sheets get captured.

2. Similarly, comparison of rotor performance, inflow and outflow velocity profiles, trajectories of multi-rotor wake features, etc. from a few different CFD simulation codes with the experimental data is an important step for completeness of the problem. It

is of interest to identify which flow interaction phenomena are captured by the codes and what additional work is needed to simulate low *Re* multirotor flows better. Once a reasonable agreement is attained, CFD simulations will be instrumental in studying regions of the flow field not covered in the present SPIV measurements.

3. The inflow and outflow velocity data for the rotors can be used to create reduced-order models to predict multirotor performance. Such models can serve as great tools for preliminary multirotor vehicle design and optimization as they will inherently be much faster and cheaper than CFD simulations.

4. There is some scope for exploration on positive rotor-rotor interference due to the unique nature of low *Re* rotor flows. If successful, the knowledge will be useful in designing better performance multirotor UAVs.

5. Studying acoustic signatures related to the interaction modes discovered in the present effort will be useful in mitigating noise issues.

6. It is meaningful to do some performance measurements, flight tests and CFD simulations on a multirotor UAV, and compare results from those with the predictions made using the findings from the current bi-rotor experiments. Aiding the development of such prediction capability for multirotor vehicles has been the primary motivation for this work.

7. In recent times, the concept of urban passenger vehicles employing large numbers or small rotors are being discussed widely. Hence, characterizing the performance of vehicle platforms with a large number of rotors will be valuable. Some work on that front has already started. A 16 rotor UAV has been made by combining four quadrotors and flight tests on it are underway. The aim is also to develop a way to combine any number of identical UAVs to address different mission requirements (such as payload or range), which is relevant to package delivery applications. Such an ap-

proach will help reduce the costs associated with owning and maintaining different UAVs for different missions. Figure 9.1 is a photograph of the 16 rotor UAV.

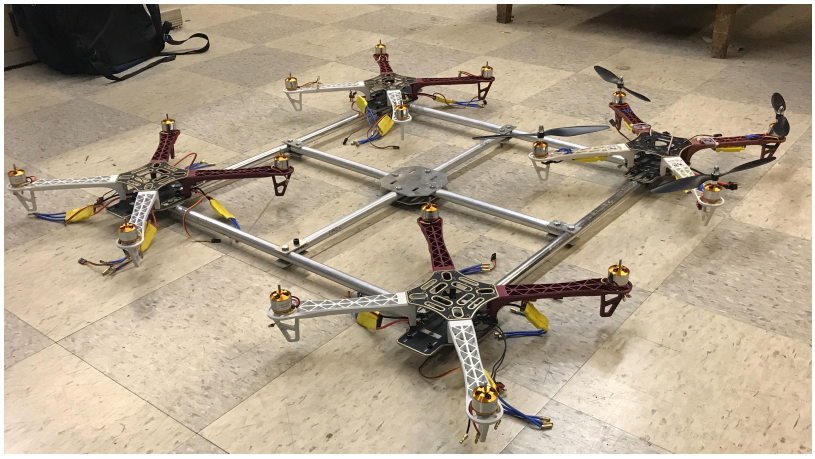

Figure 9.1: The quad-quad rotor UAV made using four quadrotors

8. Wind tunnel experiments and flight tests with a payload tethered at a few different distances under an actual UAV will be useful in studying vehicle wake-payload interactions and performance. This can be seen as an extension of the rotor-box study here where the predictions based on current findings can be verified.

Table 9.1: A list of key findings from the thesis

	Finding	**Section**
1	Tip vortex core size are inversely related to *Re* when scaled using rotor dimensions.	2.4.4, 2.4.6
2	Performance of rotors at low *Re* is significantly lower than that of rotors at high *Re*.	2.4.2
3	Low *Re* rotor blade design is different from high *Re* rotor blades and performs better than high Re rotor blades at low *Re*	2.4.2, 4.2.2
4	Presence of an annular duct around rotor improves rotor performance	2.4.2
5	The size of the tip vortex cores with respect to tip clearance is an important factor determining the magnitude of performance gain.	2.4.4
6	Vortex core interaction with the duct causes tonal acoustic signature comprising of rotor frequency harmonics.	2.4.3
7	Inter-rotor wake interaction is dominant at low *Re* side-by-side rotor cases.	4.2.1, 5.2.2
8	The rotor ducts limit inter-rotor wake interactions in side-by-side rotor arrangement by shielding tip vortices of one rotor from the other during their generation.	4.2.1
9	Higher inter-rotor wake interactions correlated with lower rotor performance for most cases.	4.2.2, 5.3
10	The upper rotor in low *Re* coaxial and high overlap tandem rotor hover cases performs better than the baseline isolated rotor	3.5.2, 6.3.2
11	Effect of the lower rotor on the swirl velocities at the upper rotor was confirmed using SPIV data	3.5.4, 6.3.4
12	A variety of wake interaction phenomena happening over a range of tandem and coaxial rotor configurations and conditions were discovered	3.5.3, 6.3.5
13	Three primary modes of rotor-box interaction were observed in the effort aimed at understanding rotor-payload aerodynamics.	7.4

Appendices

APPENDIX A

BLADE PITCH ANGLES DATA

Table A.1: Collective blade pitch angles for single, coaxial and tandem rotor cases. ($\pm 0.5^{\circ}$ uncertainty)

VS/R	**AS/R**	***Re***	T_L **(N)**	T_U **(N)**	Q_L **(N-mm)**	Q_U **(N-mm)**	$Pitch_L$	$Pitch_U$
Single Rotor		40,000	-	0.27	-	5.243	-	6.06
		80,000	-	1.088	-	18.28	-	6.06
0.25	0	40,000	0.24	0.27	5.5	5.2	7.43	6.75
		80,000	0.82	1.18	20.9	20.8	9.08	6.75
	0.25	40,000	0.22	0.35	6.0	6.4	7.98	8.20
		80,000	1.00	1.08	24.0	23.6	9.67	7.44
	0.5	40,000	0.23	0.28	5.7	6.1	7.26	7.44
		80,000	1.01	1.13	21.3	20.8	8.63	6.86
	0.75	40,000	0.25	0.26	6.0	6.2	7.43	7.61
		80,000	1.07	0.99	21.8	21.5	8.63	7.20
	1	40,000	0.26	0.27	5.8	5.5	7.15	7.61
		80,000	1.02	1.10	19.9	19.8	8.25	6.75
	1.25	40,000	0.27	0.28	5.7	5.7	7.15	7.61
		80,000	1.11	0.98	20.4	20.5	8.41	6.86
	1.5	40,000	0.31	0.24	5.2	5.0	6.58	6.75
		80,000	1.08	1.16	19.8	20.1	8.08	6.40
	1.875	40,000	0.28	0.28	5.4	5.6	6.58	7.32
		80,000	1.11	0.99	18.7	18.3	7.54	6.18
	2	40,000	0.29	0.29	5.4	5.4	6.58	7.32
		80,000	1.11	1.06	18.8	18.9	7.54	6.18
	2.5	40,000	0.28	0.26	5.2	5.2	5.99	6.75
		80,000	1.10	1.01	19.1	18.7	7.70	6.18
0.4	0	40,000	0.21	0.34	6.4	6.5	8.25	8.20
		80,000	0.94	1.21	21.3	20.3	9.08	6.75
	0.25	40,000	0.23	0.31	6.0	5.8	7.98	7.44
		80,000	0.92	1.28	21.4	20.9	9.08	7.03
	0.5	40,000	0.26	0.32	6.6	6.4	7.87	7.61
		80,000	0.93	1.09	20.1	20.0	8.52	6.75
	0.75	40,000	0.26	0.29	6.5	6.3	7.70	7.61
		80,000	0.94	1.20	19.6	19.7	8.08	6.75
	1	40,000	0.27	0.25	5.8	5.7	7.15	7.03
		80,000	0.96	1.20	19.6	19.9	7.98	7.03
	1.25	40,000	0.26	0.24	5.7	5.4	6.87	6.75
		80,000	1.00	1.08	19.1	19.3	7.98	6.46
	1.5	40,000	0.26	0.33	5.6	5.4	6.58	7.03
		80,000	1.08	1.04	19.1	19.1	7.54	6.18
	1.875	40,000	0.28	0.27	5.5	5.4	6.81	7.03
		80,000	1.07	1.06	18.1	18.4	7.92	6.40
	2	40,000	0.27	0.23	5.2	5.2	6.11	6.29
		80,000	1.11	0.94	19.0	19.1	7.54	6.29
	2.5	40,000	0.31	0.28	5.2	5.4	6.58	7.03
		80,000	1.00	0.98	18.6	18.0	7.65	6.23

REFERENCES

[1] *Principles of helicopter aerodynamics (by Gordon Leishman).*

[2] W. Pearce, *Dorand Gyroplane G.20 (G.II)*, https://oldmachinepress.com/2015/03/28/dorand-gyroplane-g-20-g-ii/.

[3] D. A. Day, *Piasecki: The Dogship and the Flying Banana, U.S. Centennial of Flight*, https://web.archive.org/web/20111219125310/http://www.centennialofflight.gov/essay/Rotary/Piasecki/HE4.htm.

[4] *Germany's secret weapons in World War II (by Roger Ford).*

[5] D. Joshi, *Commercial Unmanned Aerial Vehicle (UAV) Market Analysis – Industry trends, companies and what you should know*, 2017.

[6] F. Bohorquez, "Rotor hover performance and system design of an efficient coaxial rotary wing micro air vehicle," 2007.

[7] S. Miley, "On the design of airfoils for low Reynolds numbers," in *AIAA, MIT, and SSA, International Symposium on the Technology and Science of Low Speed and Motorless Flight, 2 nd, Cambridge, Mass, Army-supported research*, vol. 11, 1974.

[8] R. Liebeck, "Low Reynolds number airfoil design at the Douglas Aircraft Company," *Aerodynamics at low Reynolds numbers Re greater than 10 to the 4 th and less than 10 to the 6 th*, p. 7, 1986.

[9] M. S. Selig and J. J. Guglielmo, "High-lift low Reynolds number airfoil design," *Journal of aircraft*, vol. 34, no. 1, pp. 72–79, 1997.

[10] I Kroo and P Kunz, "Analysis and Design of Airfoils for Use at Ultra-Low Reynolds Numbers," *Fixed and Flapping Wing Aerodynamics for Micro Air Vehicle Applications, edited by TJ Mueller, Progress in Astronautics and Aeronautics, AIAA, Reston, VA*, p. 503 517, 2001.

[11] P. J. Kunz, "Aerodynamics and design for ultra-low Reynolds number flight," PhD thesis, Stanford University, 2003.

[12] P. Kunz and I Kroo, "Analysis and Design of Airfoils for Use at Ultra-Low Reynolds Numbers, Fixed and Flapping Wing Aerodynamics for Micro Air Vehicle Applica-

tions, Mueller, TJ ed," *Progress in Astronautics and Aeronautics*, vol. 195, pp. 35–59,

[13] R. H. Liebeck and A. I. Ormsbee, "Optimization of airfoils for maximum lift," *Journal of Aircraft*, vol. 7, no. 5, pp. 409–416, 1970.

[14] R. Eppler and D. M. Somers, "A computer program for the design and analysis of low-speed airfoils," 1980.

[15] M. S. Selig, "Multi-Point Inverse Design of Isolated Airfoils and Airfoils in Cascade in Incompressible Flow," PhD thesis, Ph. D. thesis, The Pennsylvania State University, College Park, Pennsylvania, 1992.

[16] M. S. Selig and M. D. Maughmer, "Multipoint inverse airfoil design method based on conformal mapping," *AIAA Journal*, vol. 30, no. 5, pp. 1162–1170, 1992.

[17] ——, "Generalized multipoint inverse airfoil design," *AIAA Journal*, vol. 30, no. 11, pp. 2618–2625, 1992.

[18] A. B. Bauer, "The Laminar Airfoil Problem," in *Eighth National Free Flight Society Symposium*, National Free Flight Society Lake Charles, CA, 1975, pp. 40–45.

[19] D. Volkers, "Preliminary results of windtunnel measurements on some airfoil sections at Reynolds numbers between 0.6 x 10ˆ 5 and 5.0 x 10ˆ 5," Delft University of Technology, Tech. Rep., 1977.

[20] A Bruining, "Aerodynamic characteristics of a curved plate airfoil section at Reynolds numbers 60000 and 100000 and angles of attack from-10 to+ 90 degrees," 1979.

[21] M. Drela and M. B. Giles, "Viscous-inviscid analysis of transonic and low Reynolds number airfoils," *AIAA Journal*, vol. 25, no. 10, pp. 1347–1355, 1987.

[22] R. J. McGhee, B. S. Walker, and B. F. Millard, "Experimental results for the Eppler 387 airfoil at low Reynolds numbers in the Langley low-turbulence pressure tunnel," 1988.

[23] M. S. Selig, J. F. Donovan, and D. B. Fraser, "Airfoils at low speeds,"

[24] D. M. Somers, "Subsonic natural-laminar-flow airfoils," in *Natural Laminar Flow and Laminar Flow Control*, Springer, 1992, pp. 143–176.

[25] S. Sunada, A. Sakaguchi, and K. Kawachi, "Airfoil section characteristics at a low Reynolds number," *Journal of Fluids Engineering*, vol. 119, no. 1, pp. 129–135, 1997.

[26] T. J. Mueller and S. M. Batil, "Experimental studies of separation on a two-dimensional airfoil at low Reynolds numbers," *AIAA journal*, vol. 20, no. 4, pp. 457–463, 1982.

[27] T. J. Mueller, "The influence of laminar separation and transition on low Reynolds number airfoil hysteresis," *Journal of Aircraft*, vol. 22, no. 9, pp. 763–770, 1985.

[28] M Brendel and T. J. Mueller, "Boundary-layer measurements on an airfoil at low Reynolds numbers," *Journal of aircraft*, vol. 25, no. 7, pp. 612–617, 1988.

[29] J. J. Guglielmo and M. S. Selig, "Spanwise variations in profile drag for airfoils at low Reynolds numbers," *Journal of Aircraft*, vol. 33, no. 4, pp. 699–707, 1996.

[30] T. J. Mueller, "Aerodynamic measurements at low Reynolds numbers for fixed wing micro-air vehicles," DTIC Document, Tech. Rep., 2000.

[31] E. Laitone, "Wind tunnel tests of wings at Reynolds numbers below 70 000," *Experiments in Fluids*, vol. 23, no. 5, pp. 405–409, 1997.

[32] A. Pelletier and T. J. Mueller, "Low Reynolds number aerodynamics of low-aspect-ratio, thin/flat/cambered-plate wings," *Journal of Aircraft*, vol. 37, no. 5, pp. 825–832, 2000.

[33] S Sunada, T Yasuda, K Yasuda, and K Kawachi, "Comparison of wing characteristics at an ultralow Reynolds number," *Journal of aircraft*, vol. 39, no. 2, pp. 331–338, 2002.

[34] S Sunada and K Kawachi, "Effects of Reynolds number on characteristics of fixed and rotary wings," *Journal of aircraft*, vol. 41, no. 1, pp. 189–192, 2004.

[35] D. Althaus, *Profilpolaren für den Modellflug. 1*. Neckar-Verlag, 1980.

[36] B. Carmichael, "Low Reynolds number airfoil survey, volume 1," 1981.

[37] J. Van Ingen and L. Boermans, "Aerodynamics at low Reynolds numbers: a review of theoretical and experimental research at Delft University of Technology," in *Conference on Aerodynamics at Low Reynolds Numbers, October, London*, 1986.

[38] S. J. Miley, "A catalog of low Reynolds number airfoil data for wind turbine applications," 1982.

[39] M. S. Selig, *Summary of low speed airfoil data*. SoarTech, 1995, vol. 1.

[40] E. Laitone, "Aerodynamic lift at Reynolds numbers below 7 x 10ˆ4," *AIAA Journal*, vol. 34, no. 9, pp. 1941–1942, 1996.

[41] M. Lowson, "Aerodynamics of Aerofoils at Low Reynolds Numbers," in *UAVs-14th Unmanned Air Vehicle Systems International Conference, United Kingdom*, 1999.

[42] C. Van Den Berg and C. P. Ellington, "The three–dimensional leading–edge vortex of a 'hovering' model hawkmoth," *Philosophical Transactions of the Royal Society of London B: Biological Sciences*, vol. 352, no. 1351, pp. 329–340, 1997.

[43] C. Ellington and J. Usherwood, "Lift and drag characteristics of rotary and flapping wings," *Progress in Astronautics and Aeronautics*, vol. 195, pp. 231–248, 2001.

[44] M. Okamoto and A. Azuma, "Experimental study on aerodynamic characteristics of unsteady wings at low Reynolds number," *AIAA Journal*, vol. 43, no. 12, pp. 2526–2536, 2005.

[45] M. H. Dickinson, "Unsteady mechanisms of force generation in aquatic and aerial locomotion," *American zoologist*, vol. 36, no. 6, pp. 537–554, 1996.

[46] M. H. Dickinson, F.-O. Lehmann, and S. P. Sane, "Wing rotation and the aerodynamic basis of insect flight," *Science*, vol. 284, no. 5422, pp. 1954–1960, 1999.

[47] S. E. Rogers and D. Kwak, "Upwind differencing scheme for the time-accurate incompressible Navier-Stokes equations," *AIAA Journal*, vol. 28, no. 2, pp. 253–262, 1990.

[48] A. P. Singh, S. Winoto, D. Shah, K. Lim, and R. E. Goh, "A Computational Study on Airfoils at a Low Reynolds Number," *ASME-PUBLICATIONS-FED*, vol. 253, pp. 405–412, 2000.

[49] M. I. Kellogg and W. J. Bowman, "Parametric Design Study of the Thickness of Airfoils at Reynolds Numbers from 60,000-150,000," in *42nd AIAA Aerospace Sciences Meeting and Exhibit*, 2004, pp. 6508–6515.

[50] M. Drela, "XFOIL: An analysis and design system for low Reynolds number airfoils," in *Low Reynolds number aerodynamics*, Springer, 1989, pp. 1–12.

[51] Y. Shum and D. Marsden, "Separation bubble model for low Reynolds number airfoil applications," *Journal of aircraft*, vol. 31, no. 4, pp. 761–766, 1994.

[52] F. Bohorquez and D. Pines, "Hover performance of rotor blades at low Reynolds numbers for rotary wing micro air vehicles," *An experimental and cfd study. AIAA Paper*, vol. 3930, p. 2003, 2003.

[53] B. R. Hein and I. Chopra, "Hover performance of a Micro Air Vehicle: Rotors at low Reynolds number," *Journal of the American Helicopter Society*, vol. 52, no. 3, pp. 254–262, 2007.

[54] P. J. Kunz and R. C. Strawn, "Analysis and design of rotors at ultra-low Reynolds numbers," in *40th AIAA Aerospace Sciences Meeting, Reno, NV*, 2002.

[55] V. K. Lakshminarayan, B. L. Bush, K. Duraisamy, and J. D. Baeder, "Computational investigation of micro hovering rotor aerodynamics," in *24th AIAA Applied Aerodynamics Conference*, 2006, pp. 5–8.

[56] V. K. Lakshminarayan and J. D. Baeder, "Computational investigation of micro hovering rotor aerodynamics," *Journal of the American Helicopter Society*, vol. 55, no. 2, pp. 22 001–22 001, 2010.

[57] V Gupta and J. Baeder, "Low Mach Number Preconditioning for Tiltrotor Rotor-Wing Interaction," in *AHS 4th Decennial Specialist's Conference on Aeromechanics, San Francisco, CA*, 2004.

[58] E. J. Schroeder and J. D. Baeder, "Using computational fluid dynamics for micro-Air vehicle airfoil validation and prediction," in *23rd AIAA Applied Aerodynamics Conference, Toronto, Ontario, Canada*, 2005.

[59] E. J. Schroeder, *Low Reynolds Number Flow Validation Using Computational Fluid Dynamics With Application To Micro Air Vehicles*. University of Maryland, 2005.

[60] O. Rubio, F. Gutiérrez, J. C. Zuñiga, and M. Funes-Gallanzi, "Low-Re μUAV Rotor Design," in.

[61] F. Bohorquez, D. Pines, and P. D. Samuel, "Small rotor design optimization using blade element momentum theory and hover tests," *Journal of aircraft*, vol. 47, no. 1, pp. 268–283, 2010.

[62] T. J. Mueller, "Low Reynolds number vehicles," DTIC Document, Tech. Rep., 1985.

[63] R. J. Foch and P. L. Toot, "Flight testing Navy low Reynolds number (LRN) unmanned aircraft," in *Low Reynolds Number Aerodynamics*, Springer, 1989, pp. 407–417.

[64] R. Foch and K. Ailinger, "Low Reynolds number, long endurance aircraft design," Tech. Rep., 1992.

[65] P Samuel, J Sirohi, L Rudd, D Pines, and R Perel, "Design and development of a micro coaxial rotorcraft," in *Proceedings of the AHS Vertical Lift Aircraft Design Conference, American Helicopter Society, Alexandria, VA*, 2000.

[66] L. Lipera, J. D. Colbourne, M. B. Tischler, M. H. Mansur, M. C. Rotkowitz, and P. Patangui, "The micro craft iSTAR micro air vehicle: control system design and testing," in *Annual Forum Proceedings-American Helicopter Society*, Citeseer, vol. 57, 2001, pp. 1998–2008.

[67] S. J. Morris, "Design and flight test results for micro-sized fixed-wing and VTOL aircraft," in *Proceedings of the First International Conference on Emerging Technologies for Micro Air Vehicles, Georgia Institute of Technology, Atlanta, GA*, Citeseer, 1997.

[68] J. M. Grasmeyer, M. T. Keennon, *et al.*, "Development of the black widow micro air vehicle," *Progress in Astronautics and aeronautics*, vol. 195, pp. 519–535, 2001.

[69] F. Bohorquez, P. Samuel, J. Sirohi, D. Pines, L. Rudd, and R. Perel, "Design, analysis and hover performance of a rotary wing micro air vehicle," *Journal of the American Helicopter Society*, vol. 48, no. 2, pp. 80–90, 2003.

[70] J. Sirohi, M. Tishchenko, and I. Chopra, "Design and Testing of a Micro-Aerial Vehicle with a Single Rotor and Tuming Vanes," in *Annual Forum Proceedings-American Helicopter Society*, American Helicopter Society, INC, vol. 61, 2005, p. 1957.

[71] I. Kroo, F. Prinz, M. Shantz, P. Kunz, G. Fay, S. Cheng, T. Fabian, and C. Partridge, "The Mesicopter: A miniature rotorcraft concept–phase ii interim report," *Stanford university, USA*, 2000.

[72] I. Kroo and P. Kunz, "Mesoscale flight and miniature rotorcraft development," in Fixed and Flapping Wing Aerodynamics for Micro Air Vehicle Applications," in *of Progress in Astronautics and Aeronautics*, Citeseer, 2001.

[73] L. A. Young, E. Aiken, J. Johnson, R. Demblewski, J. Andrews, and J. Klem, "New concepts and perspectives on micro-rotorcraft and small autonomous rotary-wing vehicles," in *AIAA 20th Applied Aerodynamics Conference, St Louis, MO*, 2002.

[74] M. Woods, J. Henderson, and G. Lock, "Energy requirements for the flight of micro air vehicles," *Aeronautical Journal*, vol. 105, no. 1045, pp. 135–149, 2001.

[75] D Baxter and R East, "A survey of some fundamental issues in micro-air-vehicle design," in *Proceedings 14th UAVs-Unmanned Air Vehicle Systems International Conference, United Kingdom*, 1999, pp. 12–14.

[76] R. D. Harrington, "Full-scale-tunnel investigation of the static-thrust performance of a coaxial helicopter rotor," DTIC Document, Tech. Rep., 1951.

[77] R. C. Dingeldein, "Wind-tunnel studies of the performance of multirotor configurations," no. 3236, 1954.

[78] T Nagashima and K Nakanishi, "Optimum performance and wake geometry of co-axial rotor in hover," in *DGLR Seventh European Rotorcraft and Powered Lift Aircraft Forum 17 p(SEE N 82-18119 09-01)*, 1981.

[79] S. Sunada, K. Tanaka, and K. Kawashima, "Maximization of thrust-torque ratio of a coaxial rotor," *Journal of aircraft*, vol. 42, no. 2, pp. 570–572, 2005.

[80] C. P. Coleman, "A survey of theoretical and experimental coaxial rotor aerodynamic research," 1997.

[81] J. G. Leishman and S. Ananthan, "Aerodynamic optimization of a coaxial proprotor," in *Annual Forum Proceedings-American Helicopter Society*, American Helicopter Society, INC, vol. 62, 2006, p. 64.

[82] S Saito and A Azuma, "A numerical approach to co-axial rotor aerodynamics," *1981. 19*, 1981.

[83] M. Andrew, "Co-axial rotor aerodynamics in hover," in *(European Rotorcraft and Powered Lift Aircraft Forum, 6 th, Bristol, England, Sept. 16-19, 1980.) Vertica,*, vol. 5, 1981, pp. 163–172.

[84] H. Zimmer, "The aerodynamic calculation of counter rotating coaxial rotors," 1985.

[85] A. Bagai and J. G. Leishman, "Free-Wake Analysis of Tandem, Tilt-Rotor and Coaxial Rotor Configurations," *Journal of the American Helicopter Society*, vol. 41, no. 3, pp. 196–207, 1996.

[86] D Griffiths, "A study of dual-rotor interference and ground effect using a free-vortex wake model," in *AHS International, 58 th Annual Forum Proceedings-*, vol. 1, 2002, pp. 592–612.

[87] A Radhakrishnan and F Schmitz, "An experimental investigation of a quad tilt rotor in low speed forward flight," in *Proceedings of the 4th Decennial Specialists' Conference on Aeromechanics, American Helicopter Society, San Francisco, CA*, 2004.

[88] V. Gupta and J. D. Baeder, "Quad Tilt Rotor Aerodynamics in Helicopter Mode," in *Annual Forum Proceedings-American Helicopter Society*, AMERICAN HELICOPTER SOCIETY, INC, vol. 61, 2005, p. 416.

[89] J. Lee, K. Yee, and S. Oh, "Aerodynamic characteristic analysis of multi-rotors using a modified free-wake method," *Transactions of the Japan Society for Aeronautical and Space Sciences*, vol. 52, no. 177, pp. 168–179, 2009.

[90] R. G. Rajagopalan, V. Baskaran, A. Hollingsworth, A. Lestari, D. Garrick, E. Solis, and B. Hagerty, "RotCFD-A Tool for Aerodynamic Interference of Rotors: Validation and Capabilities," in *Future Vertical Lift Aircraft Design Conference, San Francisco, CA*, 2012.

[91] S. Driessens and P. E. Pounds, "Towards a more efficient quadrotor configuration," in *2013 IEEE/RSJ International Conference on Intelligent Robots and Systems*, IEEE, 2013, pp. 1386–1392.

[92] S Yoon, T. Pulliam, and N. Chaderjian, "Simulations of XV-15 rotor flows in hover using OVERFLOW," in *fifth decennial AHS aeromechanics specialists' conference, San Francisco, CA*, 2014, pp. 22–24.

[93] S. Yoon, H. C. Lee, and T. H. Pulliam, "Computational Analysis of Multi-Rotor Flows," in *54th AIAA Aerospace Sciences Meeting*, 2016, p. 0812.

[94] M. Brazinskas, S. D. Prior, and J. P. Scanlan, "An Empirical Study of Overlapping Rotor Interference for a Small Unmanned Aircraft Propulsion System," *Aerospace*, vol. 3, no. 4, p. 32, 2016.

[95] L. Young, *Conceptual Design Aspects of Three General Sub-Classes of Multi-Rotor Configurations: Distributed, Modular, and Heterogeneous*, 2015.

[96] A. Sciacchitano, D. R. Neal, B. L. Smith, S. O. Warner, P. P. Vlachos, B. Wieneke, and F. Scarano, "Collaborative framework for PIV uncertainty quantification: comparative assessment of methods," *Measurement Science and Technology*, vol. 26, no. 7, p. 074 004, 2015.

[97] D. S. Jenney, J. H. Olson, and A. J. Landgrebe, "A Reassessmemt of Rotor Hovering Performance Prediction Methods," *Journal of the American Helicopter Society*, vol. 13, no. 2, pp. 1–26, 1968.

[98] D. W. Boatwright, "Three-Dimensional Measurements of the Velocity in the Near Flow Field of a Full-Scale Hovering Rotor," Mississippi State Univ Mississippi State Dept of Aerophysics and Aerospace Engineering, Tech. Rep., 1974.

[99] G. K. Yamauchi, L. Lourenco, J. T. Heineck, A. J. Wadcock, A. I. Abrego, and E. W. Aiken, "Application of Three-Component PIV to a Hovering Rotor Wake," 2000.

[100] P. B. Martin, G. J. Pugliese, and J. G. Leishman, "High resolution trailing vortex measurements in the wake of a hovering rotor," *Journal of the American Helicopter Society*, vol. 48, no. 1, pp. 39–52, 2003.

[101] K. W. McAlister, "Rotor wake development during the first revolution," *Journal of the American Helicopter Society*, vol. 49, no. 4, pp. 371–390, 2004.

[102] A. J. Wadcock, G. K. Yamauchi, E. Solis, and A. E. Pete, "PIV measurements in the wake of a full-scale rotor in forward flight," in *Proceedings of the AIAA 29th Applied Aerodynamics Conference, Honolulu, HI, USA*, 2011.

[103] M. Ramasamy and J. G. Leishman, "A generalized model for transitional blade tip vortices," *Journal of the American Helicopter Society*, vol. 51, no. 1, pp. 92–103, 2006.

[104] ——, "A Reynolds Number-Based Blade Tip Vortex Model," *Journal of the American Helicopter Society*, vol. 52, no. 3, pp. 214–223, 2007.

[105] M. Ramasamy, J. G. Leishman, and T. E. Lee, "Flowfield of a rotating-wing micro air vehicle," *Journal of aircraft*, vol. 44, no. 4, pp. 1236–1244, 2007.

[106] M. Ramasamy, B. Johnson, and J. G. Leishman, "Understanding the Aerodynamic Efficiency of a Hovering Micro-Rotor," *Journal of the American Helicopter Society*, vol. 53, no. 4, pp. 412–428, 2008.

[107] J. L. Pereira, "Hover and wind-tunnel testing of shrouded rotors for improved micro air vehicle design," Maryland Univ College Park Dept of Aerospace Engineering, Tech. Rep., 2008.

[108] A. Akturk, A. Shavalikul, and C. Camci, "PIV measurements and computational study of a 5-inch ducted fan for V/STOL UAV applications," in *47th AIAA Aerospace Sciences Meeting including The New Horizons Forum and Aerospace Exposition*, 2008, p. 332.

[109] V. Hrishikeshavan, "Experimental investigation of shrouded rotor micro air vehicle in hover and in edgewise gusts," PhD thesis, 2011.

[110] A. J. Landgrebe, "An analytical and experimental investigation of helicopter rotor hover performance and wake geometry characteristics," United Aircraft Research Labs East Hartford CT, Tech. Rep., 1971.

[111] J. D. Kocurek and J. L. Tangler, "A prescribed wake lifting surface hover performance analysis," *Journal of the American Helicopter Society*, vol. 22, no. 1, pp. 24–35, 1977.

[112] L. Graftieaux, M. Michard, and N. Grosjean, "Combining PIV, POD and vortex identification algorithms for the study of unsteady turbulent swirling flows," *Measurement Science and technology*, vol. 12, no. 9, p. 1422, 2001.

[113] D. Shukla, N. Hiremath, and N. M. Komerath, "Low Reynolds Number Aerodynamics Study on Coaxial and Quad-Rotor," in *2018 Applied Aerodynamics, AIAA Aviation and Aeronautics Forum and Exposition*, 2018, p. 4118.

[114] J. T. Heineck, A. J. Wadcock, G. K. Yamauchi, L. Lourenco, and A. I. Abrego, "Application of three-component PIV to a hovering rotor wake," NASA Moffett Field CA Ames Research Center . . ., Tech. Rep., 2000.

[115] M. Ramasamy, "Measurements comparing hover performance of single, coaxial, tandem, and tilt-rotor configurations," in *69th AHS Annual Forum, Phoenix, AZ*, 2013.

[116] Y. Ma, M. Chen, X. Zhang, and Q. Wang, "Scale-model tests of coaxial rotors in water tunnel via particle image velocimetry technique," *Proceedings of the Institution of Mechanical Engineers, Part G: Journal of Aerospace Engineering*, vol. 230, no. 3, pp. 426–443, 2016.

[117] Y. S. D. Yanmin, "PIV measurements in the wake of coaxial-rotor in water tunnel [J]," *Journal of Beijing University of Aeronautics and Astronautics*, vol. 6, p. 001, 2007.

[118] S.-m. YU and Y.-m. DENG, "PIV measurement of water tunnel for the flow field of a hovering coaxial-rotor," *Journal of Aerospace Power*, vol. 11, p. 012, 2007.

[119] H. Zeng-long and D. Yan-min, "Experimental Investigation of Coaxial-Rotor Induced Velocity in Water Tunnel Using PIV," *Aircraft Design*, vol. 1, p. 002, 2008.

[120] Y.-c. Ma, S.-m. Yu, and Y.-m. Deng, "PIV experimental investigation of coaxial rotors' induced velocity field in hover," *J Exp Fluid Mech*, vol. 1, pp. 16–20, 2012.

[121] C. Thipyopas, R. Barènes, and J.-M. Moschetta, "Aerodynamic analysis of a Multi-Mission Short-Shrouded coaxial UAV: part I–Hovering flight," in *26th AIAA Applied Aerodynamics Conference*, 2008, pp. 18–21.

[122] C. Thipyopas, S. Poutriquet, R. Barènes, and J. M. Moschetta, "Aerodynamic analysis of a multi-mission short-shrouded coaxial UAV: Part II–translation flight," in *48th AIAA Aerospace Sciences Meeting*, 2010, pp. 4–7.

[123] G. Grondin, C. Thipyopas, and J.-M. Moschetta, "Aerodynamic Analysis of a Multi-Mission Short Shrouded Coaxial UAV: Part III–CFD for Hovering Flight," in *28th*

AIAA Applied Aerodynamics Conference, AIAA E-library Chicao, vol. 10, 2010, pp. 6–2010.

[124] H. Han, C. Xiang, B. Xu, and Y. Yu, "Experimental and computational analysis of microscale shrouded coaxial rotor in hover," in *Unmanned Aircraft Systems (ICUAS), 2017 International Conference on*, IEEE, 2017, pp. 1092–1100.

[125] J. H. Schmaus, "Aeromechanics of a High Speed Coaxial Helicopter Rotor," PhD thesis, University of Maryland, College Park, 2017.

[126] Kickstarter, *Sprite: portable and rugged. A totally different drone.* `https://www.kickstarter.com/projects/ascentaerosystems/sprite-the-portable-rugged-totally-different-small`.

[127] C. Drone, *WorkFly: Datasheet.* `http://www.civicdrone.com/our-rpa/datasheet-of-drones-c10114.html`.

[128] J. G. Leishman and M. Syal, "Figure of merit definition for coaxial rotors," *Journal of the American Helicopter Society*, vol. 53, no. 3, pp. 290–300, 2008.

[129] M. Ramasamy, "Hover performance measurements toward understanding aerodynamic interference in coaxial, tandem, and tilt rotors," *Journal of the American Helicopter Society*, vol. 60, no. 3, pp. 1–17, 2015.

[130] N. L. Schatzman, "Aerodynamics and Aeroacoustic Sources of a Coaxial Rotor," PhD thesis, Georgia Institute of Technology, 2018.

[131] A. Karpatne, J. Sirohi, S. Mula, and C. Tinney, "Vortex ring model of tip vortex aperiodicity in a hovering helicopter rotor," *Journal of Fluids Engineering*, vol. 136, no. 7, p. 071 104, 2014.

[132] P. F. Lorber and T. A. Egolf, "An Unsteady Helicopter Rotor-Fuselage Aerodynamic Interaction Analysis," *Journal of the American Helicopter Society*, vol. 35, no. 3, pp. 32–42, 1990.

[133] T. Renaud, D. O'Brien, M. Smith, and M. Potsdam, "Evaluation of isolated fuselage and rotor-fuselage interaction using CFD," Office National D'etudes Et De Recherches Aerospatiales Chatillon (France), Tech. Rep., 2004.

[134] ——, "Evaluation of Isolated Fuselage and Rotor-Fuselage Interaction Using Computational Fluid Dynamics," *Journal of the American Helicopter Society*, vol. 53, no. 1, pp. 3–17, 2008.

[135] H. J. Nam, Y. M. Park, and O. J. Kwon, "Simulation of Unsteady Rotor-Fuselage Aerodynamic Interaction Using Unstructured Adaptive Meshes," *Journal of the American Helicopter Society*, vol. 51, no. 2, pp. 141–149, 2006.

[136] A. R. Kenyon and R. E. Brown, "Wake Dynamics and Rotor-Fuselage Aerodynamic Interactions," *Journal of the American Helicopter Society*, vol. 54, no. 1, pp. 12 003–12 003, 2009.

[137] R Steijl and G. Barakos, "Computational study of helicopter rotor-fuselage aerodynamic interactions," *AIAA Journal*, vol. 47, no. 9, pp. 2143–2157, 2009.

[138] J.-K. Lee and O. J. Kwon, "Predicting aerodynamic rotor-fuselage interactions by using unstructured meshes," *Transactions of the Japan Society for Aeronautical and Space Sciences*, vol. 44, no. 146, pp. 208–216, 2002.

[139] D. T. Balch, "Experimental study of main rotor/tail rotor/airframe interaction in hover," *Journal of the American Helicopter Society*, vol. 30, no. 2, pp. 49–56, 1985.

[140] J. Leishman and N.-p. Bi, "Aerodynamic interactions between a rotor and a fuselage in forward flight," *Journal of the American Helicopter Society*, vol. 35, no. 3, pp. 22–31, 1990.

[141] R. E. Mineck and S. A. Gorton, "Steady and periodic pressure measurements on a generic helicopter fuselage model in the presence of a rotor," NASA Hampton VA Langley Research Center, Tech. Rep., 2000.

[142] H.-Y. Xu, S.-L. Xing, Z.-Y. Ye, and M.-S. Ma, "A simple and conservative unstructured sliding-mesh approach for rotor–fuselage aerodynamic interaction simulation," *Proceedings of the Institution of Mechanical Engineers, Part G: Journal of Aerospace Engineering*, vol. 231, no. 1, pp. 163–179, 2017.

[143] L. R. Jiao, D. Peng, X. Wen, Y. Liu, and J. W. Gregory, "Experimental Study of the Interaction between Rotor Wake and a Cylinder in Hover," in *2018 Applied Aerodynamics Conference*, 2018, p. 4214.

[144] M. B. Açıkgöz and A. R. Aslan, "Dynamic Mesh Analyses of Helicopter Rotor–Fuselage Flow Interaction in Forward Flight," *Journal of Aerospace Engineering*, vol. 29, no. 6, p. 04 016 050, 2016.

[145] T. R. Quackenbush, G. R. Whitehouse, and M. K. Yu, "Analysis of Rotor/Airframe Interaction in Hover and Near-Hover Flight Conditions," in *AIAA Scitech 2019 Forum*, 2019, p. 0596.

[146] S. Liou, N. Komerath, and H. McMahon, "Velocity measurements of airframe effects on a rotor in a low-speed forward flight," *Journal of Aircraft*, vol. 26, no. 4, pp. 340–348, 1989.

[147] ——, "Velocity Field of a Cylinder in the Wake of a Rotor in Forward Flight," *Journal of aircraft*, vol. 27, no. 9, pp. 804–809, 1990.

[148] T. A. Egolf, N Rajmohan, E Reed, and L. Sankar, "A hybrid cfd method for coaxial rotor performance prediction in forward flight," in *AHS Specialist's Conference on Aeromechanics*, 2010.

VITA

Dhwanil Shukla was born and brought up in Ahmedabad, a city in India. He got his bachelor's degree in mechanical engineering from Indian Institute of Technology, Gandhinagar in 2014. He is a three-time recipient of Academic Excellence Scholarship and is an awardee of the Institute Gold medal for his academic achievements at IIT Gandhinagar.

Dhwanil joined Georgia Tech's School of Aerospace Engineering for doctoral study in 2014. He is a two-time recipient of the Vertical Flight Foundation scholarship by Vertical Flight Society. During his time at Georgia Tech, he has worked on a variety of research projects ranging from bluff body aerodynamics, to high-speed helicopters, to multirotor drones.

His research interests include aerodynamics, rotorcraft, drones, and fluid dynamics. Outside research and academics, he also volunteers for Asha for Education, which is a philanthropic organization funding education of the underprivileged children and women.